A Preliminary Study of Slurry Pipeline Erosion Using a Toroid Wear Tester

by

Nitish Ranjan Sarker

A thesis submitted in partial fulfillment of the requirements for the degree of

Master of Science

Department of Mechanical Engineering
University of Alberta

Abstract

Wear-related reliability issues, especially slurry erosion has become one of the principal concerns for the process industries that use slurry pipelines for coarse particle transport. The study and development of an appropriate wear model for slurry pipelines is, therefore, essential from the commercial perspective. The mechanism of slurry erosion is not well understood, and yet, the amount of pipeline wear data for accurate prediction of wear rate is limited. Since actual pipeline wear tests are slow and expensive, laboratory-scale wear testers are widely used, but in most cases, the particle-wall interactions are not similar to an operating pipeline. Limited, but favorable comparisons between pipeline wear and the Toroid Wear Tester (TWT) results have been stated in the literature. No detailed studies of the hydrodynamics or the performance of the TWT have been completed to date.

In this study, a TWT was fabricated and used to investigate erosion under conditions meant to simulate slurry flows in a pipeline. Qualitative flow observations were made to better understand the slurry flow behavior and particle-coupon contact mechanisms. Controlled slurry erosion experiments were also conducted to evaluate the TWT performance. A preliminary assessment of the TWT hydrodynamics was completed by analyzing the surface roughness of test coupons and also from CFD analysis of a TWT containing only air and water. These results suggest that the TWT is a reasonable approach for some types of tests, e.g. capable of determining slurry abrasivity; however, it exhibits very different hydrodynamic behavior than a pipeline. The strength and limitations of the TWT were identified and reported in this preliminary study as a foundation for a more detailed hydrodynamic future analysis of the TWT.

Dedicated to my family and friends

Acknowledgements

First and foremost, I would like to express heartfelt thanks and gratitude to my supervisors Dr. Sean Sanders and Dr. Brian A. Fleck for their excellent supervision, encouragements and guidance throughout my MSc program. Their insights, excellence in research, and advising was truly inspiring for me. Despite being tremendously busy with their works, they helped me a lot to learn about experimental works and evaluating results in a proper manner and made me a better researcher. I will always cherish these experiences and will be forever grateful to them.

I am also thankful to Terry Runyon for her limitless assistance throughout my research. I would like to extend my thanks to my colleagues in the Pipeline Transport Process Research Group at the University of Alberta for their helpful conversations and valuable feedbacks on my research work. Special thanks go to Md. Ashraful Islam, David Breakey, Ameneh Shokrollahzadeh, Marzieh Saadat and Osama Ahmed for their support, friendship and help during this research.

I would like to express my gratitude to Imperial Oil Limited (IOL) and NSERC for providing financial support for this project. My appreciation also goes to Paterson and Cooke Consulting Engineers (PCCE), especially Dr. Robert Cooke, for sharing their design and valuable insights on the topic of this study.

My sincere appreciation goes to my friends for their cooperations and for making my life joyful. Finally, I would like to thank my family for their commendable encouragement, inspirations, and support, which helped me to complete my thesis smoothly and productively.

Table of Contents

List of Tables

List of Figures

Nomenclature

Symbol	Description	Unit
A_S	Surface area of a test coupon	mm^2
$A_{\alpha\beta}$	Interfacial area density	-
b/l	Particle aspect ratio	-
C_v, C_S	Volumetric solids concentration	-
C_w	Solids concentration by weight	-
C_1	Total in-situ volume fraction solids	-
C_{lim}	Total volume fraction of solids in lower layer of a settling slurry	-
C_{max}	Maximum solids concentration in a packed bed	-
d_{50}	Mass median particle diameter	mm
d_p	Particle size	mm
D_{CS}	Diameter of the TWT central shaft	mm
DO	Dissolved oxygen level	PPM
E	Erosive wear rate	mm/year
h	TWT channel height	mm
k	Coefficient for erosion model	-
L_{CS}	Length of the TWT central shaft	mm
M_I	Initial weight of a test coupon	g
M_F	Final weight of a test coupon	g
M_L	Material lost from a test coupon	g
$M_{c,t=0}$	Calibration specimen mass before experiment	g

Symbol	Description	Unit
$M_{c,t}$	Calibration specimen mass after experiment	g
M_α	Interfacial momentum transfer term acting on phase α	kg-m/s^2
N	Wheel speed	RPM
n_1	Particle size exponent	-
n_2	Bulk velocity exponent	-
n_3	Solids concentration exponent	-
OD	Toroid wheel outer diameter	mm
p	Pressure	Pa
r_α	Volume fraction of phase α	-
r	Flow channel radius	mm
$SPHT$	Particle sphericity	-
$Symm$	Particle symmetry	-
S_{MS_α}	User specified mass sources (CFX)	-
T_L	Thickness lost from a test coupon	mm
$T_{L,avg}$	Average thickness lost	mm
t	Time	s
t_{TR}	Total run time of experiment	s
t_{DT}	Total downtime during experiment	s
t_{ERT} , t_{TRT}	Total effective run time of the TWT	s
t_{SRI}	Slurry replacement interval	s
t_{sb}	Sliding bed thickness	mm
$\mathbf{U}_\alpha$	Velocity of phase α	m/s
u_*	Wall frictional velocity	m/s
V	Bulk flow velocity	m/s
V_1	Velocity of upper layer	m/s

Symbol	Description	Unit
V_2	Velocity of lower layer	m/s
V_x	Water velocity in X-direction	m/s
W_s	Maximum wear rate in straight section of a pipeline	mm/year
W_b	Maximum wear rate in a 90° bend section	mm/year
w_L	TWT channel width (for A, B, C)	mm
w_s	TWT channel width (for D)	mm
y / H	Normalized channel height	-
z / H	Normalized channel width	-

Greek letter	Description	Unit
α	Continuous phase	-
$\Gamma_{\alpha\beta}$	Interphase mass transfer	-
μ_α	Dynamic viscosity of phase α	Pa-s
μ_f	Dynamic viscosity of carrier fluid	Pa-s
ρ	Bulk carrier fluid density	kg/m^3
ρ_α	Density of phase α	kg/m^3
ρ_s	Density of test coupons	kg/m^3
σ_{SL}	Normal stress	Pa
τ_{wall}	Wall shear stress	Pa

Chapter 1
Problem Statement

1.1 Introduction

Slurry pipelines are used in many process industries, especially in the mineral and mining sectors, as an effective and environmentally sensitive means of transport for mined raw materials [1, 2]. The oil sands mining and processing sector in Alberta provides one of many excellent examples of the industrial application of slurry pipelines. In the Alberta oil sand industry, the reliability of a slurry pipeline represents a significant challenge since failures may lead to an unplanned, prolonged shutdown, loss of human life, environmental damage, and may increase the plant operating cost [3, 4]. Erosive-corrosive wear has been identified as one of the major problems that occur in slurry pipelines, and affect the hydraulic and mechanical performance of the system. The extent of the problem is such that more than $1 billion is spent on wear-related reliability issues each year in Canada's oil sand industry [3]. As a solution to this problem, conservative maintenance approaches, i.e. pipe section replacement and rotation are being employed, which also significantly increase plant operating costs [2]. An erosion model to predict pipeline wear will be very beneficial for process industries who use the conservative maintenance strategies. Therefore, for the design and economic evaluation of slurry pipeline systems, accurate prediction of the wear rate is very important [3, 5].

Pipeline erosion is the continuous and progressive removal of material from the pipe as the moving particles impact on the internal surface [5–8]. The mechanism governing erosive wear is complex and not yet well understood. There is no accurate model to predict slurry

erosion and wear profile in hydrotransport pipelines [2]. Although single particle based erosion models exist, it is impractical to use these for predicting the erosion damage in industrial scale slurry pipelines [7], because macroscopic parameters like flow velocity, particle properties and solids volume concentration play important roles in industrial scale pipelines [7]. Corrosion often plays an important role in the overall pipeline wear mechanism and the synergistic effect of erosion-corrosion together typically leads to higher wear rates than either mechanism working alone [9]. Numerous research studies have been conducted to further the understanding of erosive wear, but very few controlled studies have been conducted using pipelines, and the amount of pipeline wear data available in the literature is still inadequate [5].

1.2 Pipeline Wear Experiments

Wear tests for slurry pipelines are essential to evaluate slurry abrasivity and to designate the necessary wear allowances for new pipelines, especially when they are designed for long distance or underground operation [5]. Wear studies are also important in order to evaluate new pipeline materials and to obtain performance data under actual pipe flow conditions [3]. To accomplish these targets, the best method available currently is to monitor wear performance of pipe spools installed in an actual operating slurry pipeline [3, 5]. Although this method gives performance data in real "field" condition, it is almost impossible to regulate macroscopic parameters such as solids concentration, velocity, particle size, shape, and size distribution within the pipeline and then quantify their effects on the overall wear behavior. It is also uneconomical since the sample collection and measurement procedure will add downtime in the production process [3]. Introducing new materials into actual operating pipelines also comes with the risk of those materials failing prematurely or unexpectedly.

An alternative way of evaluating materials in slurry pipelines is to conduct pilot scale recirculating pipe loops tests. They have the advantage of accurately producing pipeline flow conditions [3, 5]. The hydrodynamics of a recirculating pipe loop and an actual pipeline are similar and macroscopic control parameters can be easily changed to suit the investigation. For example, Schaan *et al.* [10] investigated erosion in a straight section and in a 90° bend section of an actual operating pipeline and reported the ratio (W_s/W_b) between maximum wear in the straight section to the maximum wear at 90° bend to be 0.38. Fotty *et al.* [3] repeated similar experiments using a recirculating pipe loop in the Alberta Innovates – Technology Futures (AITF) facility and reported the ratio (W_s/W_b) to be 0.30, suggesting that the recirculating pipe loop has the potential to provide the same wear mechanisms as can be found in an actual pipeline. However, it has been also reported that a large amount of 'fines' (d_{50} <44 μm) was found after an 800-hour test using the AITF recirculating pipe loop [3], which is a combination of degraded sand particles and accumulated iron oxide from the worn pipe. The slurry pump that recirculates the slurry in the pipe loop causes the degradation of particles in the slurry and makes it difficult to investigate the effect of control parameters on wear rate. Therefore, periodic and systematic replacement of slurry is required for material loss studies using a recirculating pipe loop. Another difficulty in working with pipe loops is that a large volume of slurry is required for any given series of experiments.

To evaluate the wear properties of materials, other laboratory-scale test methods are often used (e.g. impinging jet wear tester, slurry pot tester, and Coriolis tester) [7, 8, 11–13]. In laboratory wear testers, the test specimens are exposed to erosive conditions over a particular time period, and the material loss from the test specimens is quantified to determine local erosion

rate and ranking of materials. The impinging jet wear tester is suitable for understanding particle impact based wear and studying the effect of impact angle and velocity on the wear rate. In a slurry pot, coupons are exposed to both sliding and impact erosion that can predict local erosive wear on pipe surfaces with reasonable accuracy under very specific or limited conditions [8]. Although these methods provide an accelerated way of evaluating the erosion resistance of materials, they are hydrodynamically dissimilar to a pipe loop and therefore, cannot be generally used to understand the fundamentals of slurry erosion mechanism in an actual pipeline.

1.3 Toroid Wear Tester

In comparison with expensive and time-consuming pipe loop wear tests, many laboratory wear testers provide an accelerated mode to study erosion wear and rank materials, but the flow hydrodynamics in those testers are quite dissimilar to an actual operating pipeline. The Toroid Wear Tester (TWT) has been identified as another useful method of pipeline wear testing, as favorable comparisons between pipe wear and TWT results have been reported [5]. Figure 1.1 shows a schematic diagram of a TWT built by Paterson and Cooke Consulting Engineers (PCCE) for wear experiments. The TWT consists of four hollow toroidal wheels with wear test plates attached at the outer circumference of the wheel. Approximately one-third of each toroid wheel is filled with slurry and the wheel rotates while the slurry remains relatively stationary at the bottom. The TWT has been developed based on the previous works of Traynis (1977), Truscott (1975) and Henday (1988) as reported by Cooke *et al*. [5]. This particular laboratory tester is advantageous over other lab-scale wear testers mainly because [5]:

- A relatively small volume of slurry is required

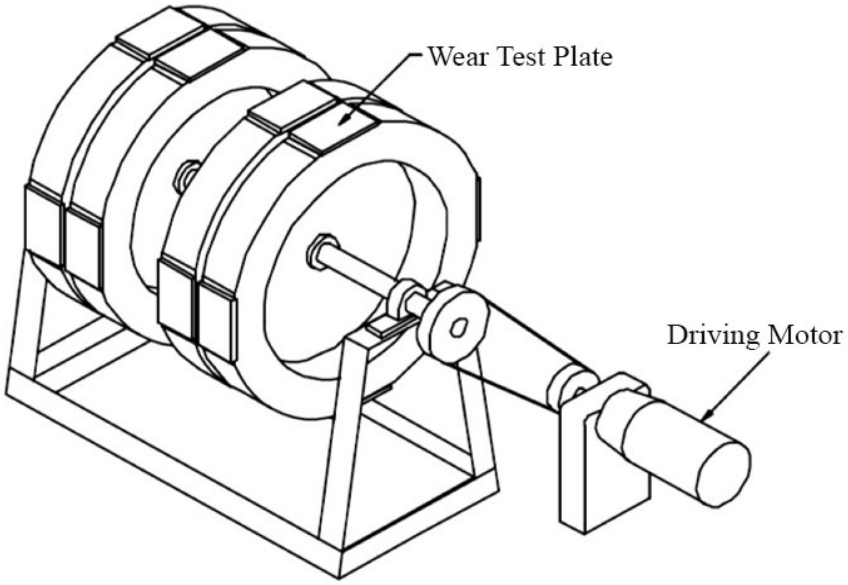

Figure 1.1. PCCE's Pipeline Wear Tester

- The particle-coupon contact in the TWT is similar to that occurs at the pipeline bottom wall. Therefore, the coupons in the TWT are exposed to a wear mechanism analogous to that occurring on the bottom of a pipeline (highest wear zone in straight pipelines)
- The particle degradation that occurs during a wear experiment is less severe than that which occurs in recirculating pipe loops (see Table 1.1).

Table 1.1. Comparison of particle degradation between different slurry pipeline wear testers [5]

Tester name	**Test duration (hours)**	d_{50} **(mm)**	
		Before test	**After test**
Recirculating Pipe Loop	5	12.5	8.6
Toroid Wheel	100	12.5	9.5

However, the TWT rotates in a vertical plane and the rotation of the wheels may make the slurry move along the wall and tumble down due to gravity after reaching the slurry-air interface. The slurry behavior in the rotating TWT is complex and suggests that the comparison of wear in a pipe loop with wear in a TWT may not be direct. For example, it has been observed that under some operating conditions, generally accepted wear trends (say, effect of particle size or solids concentration) do not appear to hold during toroid tests. Very little work has been performed to look further into this matter and to characterize wear mechanisms in a TWT. A better fundamental understanding of the hydrodynamics within a toroid wear tester is therefore required. In order to accurately predict erosive wear in industrial slurry pipelines, the key research objective is to determine the absolute wear rate from TWT experiments and compare the results to wear rates obtained using recirculating pipe loop experiments. A hydrodynamic analysis (both experimental and CFD analyses) on the TWT is also necessary to understand the slurry behavior in the TWT.

1.4 Research Objectives

The primary objective of this study is to develop a standard methodology for the measurement of material loss rates using a TWT under conditions meant to simulate dense slurry flows in a pipeline. The major activities required to meet this objective are:

- Flow observation inside a TWT to better understand and characterize the flow patterns inside the TWT;
- Analysis of the performance of a TWT as a laboratory apparatus that has the potential to predict pipeline erosion, and to identify the strength and limitations of this wear measurement technique;

- CFD analysis of the hydrodynamics of an air-water multiphase system in a rotating TWT to predict and analyze the velocity field and wall shear stress distribution inside it.

1.5 Thesis Outline

Chapter 1 presents the motivation for the study of erosive wear using a TWT, the specific research objectives and an outline of the thesis. A critical literature review on slurry pipeline wear is outlined in Chapter 2. Chapter 3 describes the materials and equipment used during this study. It also presents the experimental procedures and experimental program in detail. Chapter 4 discusses the commissioning and evaluation of the newly built TWT experimental set up fabricated for the present study. Chapter 5 contains the results and analysis of the experiments completed using the TWT in detail and focuses on the strength and limitations of the TWT as a laboratory wear tester. Chapter 6 presents more insights on the hydrodynamics analysis of the TWT through CFD analysis. Finally, the conclusions of this study and recommendations for future work are discussed in Chapter 7.

1.6 Author's Contribution

In this study, a new TWT was built, and the author was involved the installation and commissioning of the new TWT. The author directly contributed in every flow observation, repeatability, and parametric experiments reported in this study, and presented a detail uncertainty analysis for material loss measurement using a TWT. The author developed standard procedures for test coupon cleaning and erosive wear experiments using the TWT with the help of Dr. Ashraful Islam. The slurry replacement interval (SRI) experiments for absolute erosive wear determination, as mentioned by Cooke *et al.* [5], were successfully executed by the author with the guidance and help of Dr. Ashraful Islam and Osama Ahmed. The sensitivity of the SRI

experiment results was analyzed by the author, based on the frequency of slurry replacement. Carrier fluid samples were collected after each SRI experiments, and the viscosity and fines concentration of the samples were measured with the assistance of Ameneh Shokrollahzadeh. The author also completed a preliminary study on the TWT hydrodynamics by measuring and analyzing the surface roughness of test coupons using a Contracer. A simplified CFD analysis was also conducted by the author to understand water flow behavior in the TWT. Particle shape properties were evaluated with the help of a CAMSIZER in the facility of Alberta Innovates Technology Future and using the scanning electron microscopy (SEM) facilty of the Biological Science Department at University of Alberta. The author would like to thank Dr. David Breakey, who helped the author to organize the contents of this study through his valuable reviews on the dissertation. Thanks also go to Terry Runyon for constantly providing the author with valuable administrative and logistics support.

Chapter 2
Literature: Understanding Slurry Pipeline Wear

2.1 Introduction

The transport of a particle laden carrier fluid by means of slurry pipelines is a key industrial process [4]; however, during recent years, wear in slurry pipelines has been identified as one of the most significant limiting factors for pipeline service or lifetime [14]. Although the nature of wear in slurry pipelines is complex [15], a better fundamental understanding of wear in slurry pipelines is necessary. The pipe material loss in a slurry pipeline can be caused by erosion or corrosion or a combination of the two mechanisms. Wear due to erosion is the main focus of this chapter and throughout this study.

A typical oil sand hydrotransport system involves slurry consisting of crushed oil sands and hot water flowing to the extraction site [3], and most oil sand slurries contain coarse particles (d_{50} > 44 μm) that range between 0.18 and 150 mm [10]. These coarse particles form a heterogenous (settling) slurry system [2]. Several studies have indicated that the maximum wear occurs at the bottom of a pipeline because of the settling of the coarse particles [5, 10, 16, 17]. Heterogenous slurry flow patterns and slurry erosion mechanism are discussed in the following sections to convey the basic principles of slurry erosion in pipelines transporting settling slurries.

2.2 Flow Pattern: Heterogeneous (Settling) Slurries

During coarse particle transport, the so-called settling or heterogeneous flow situation occurs as the larger particles settle quickly and tend to form stationary deposits at specific

velocities [18, 19]. The 'Two Layer Model', proposed and improved with follow-up investigations by Gilles *et al.* [20, 21], provides a semi-mechanistic description to characterize the kinematic and Coulombic frictions associated with these flows.

The general assumption of the two layer model is that the particles in the slurry can be divided, theoretically, into a 'contact load' and a 'suspended load'. The contact load portion of the particles directly contribute to the sliding friction at the pipe wall and the immersed weight of the suspended load is transferred to the carrier fluid itself [20, 22]. The concentration and velocity distributions are non-uniform and are represented as step-change functions as shown in Figure 2.1. The upper layer with a low volumetric solids concentration of C_1 moves at a velocity V_1. The volumetric flow rate of the bottom layer is lower and has a higher solids concentration of $C_{\lim}$, designated as the loose-packed bed concentration. Fluid turbulence does not affect the loose-packed bed of particles significantly and the immersed weight of these particles is conveyed to the pipe wall by particle-particle interaction producing a high frictional resistance to flow at the pipe wall [23]. Erosive wear in this situation can result from a combination of kinematic (velocity-dependent) friction and Coulombic (velocity independent) friction i.e. the weight and density of particles times a coefficient of friction [18, 19, 24].

2.3 Slurry Erosion Mechanism

While prediction of essential flow parameters like pressure drop and deposition velocity for coarse particle slurry flows are well understood, wear rates in slurry pipelines remain difficult to predict accurately because of the complexity of the wear process [15] and its dependence on particle-wall interaction. As discussed above, the particles in a settling slurry flow are either in

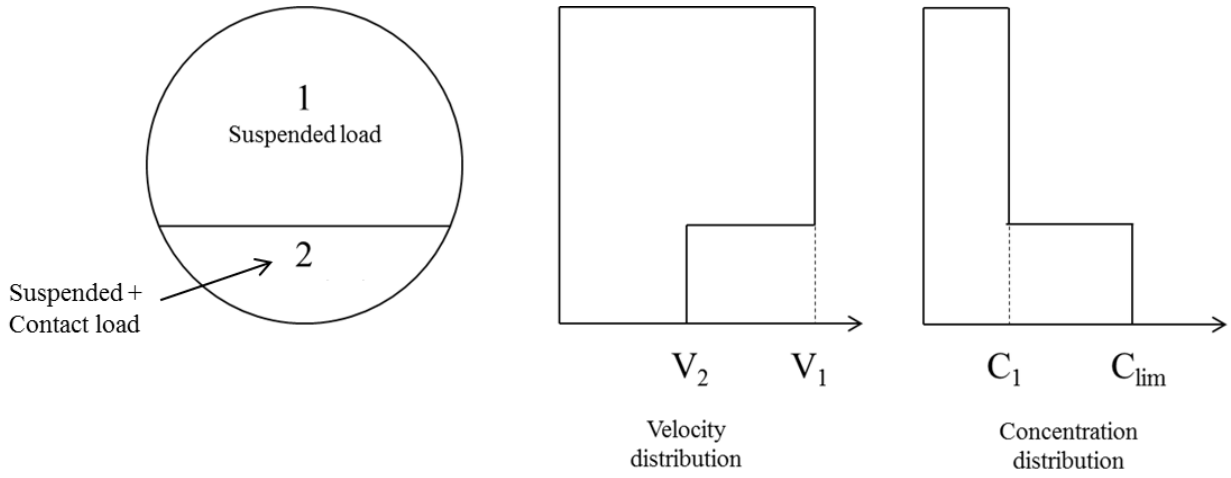

Figure 2.1. Asymmetric velocity and concentration distributions in a slurry without deposition; represented as step-change functions in the Two-Layer Model [20]

turbulent suspension or being supported by contact with other particles or sliding along the bottom of the pipe. Therefore, the particles interact with the wall if [23]:

- Convective flow velocity components move particles toward the wall,
- Fluid turbulence and particle-particle interactions at high volumetric solids concentration $(C_v > 5\%)$ produce fluctuating particle velocities near the wall
- Particles near the pipe invert are transported as a sliding bed, pressing their weight as a normal load on the bottom surface.

Several investigations have characterized the material removal procedure at the contact zone between a particle and a target surface, and the most accepted wear theories are abrasive wear, adhesive wear, delamination wear, rolling wear, fretting wear, plastic deformation and fatigue wear [25]. Erosion damage in pipelines results from particle-wall interactions when local stresses at the point of contact exceed the yield stress of the material. The mode of failure can be ductile, brittle, or a combination of both. Based on the possibilities of particle-wall interaction

presented above, the erosion process in dense slurry flow can be considered to have three components [23]: (a) directional impingement of solid particles, (b) impingement of particles due to fluctuating turbulent motion and (c) sliding bed friction pressing onto the wall (see Figure 2.2). During coarse particle transport using a slurry pipeline the solid particles, which cannot be maintained in a suspension by the hydrodynamic forces, slide on the bottom pipe wall, transmitting a normal stress (σ_{SL}). On the remaining part of the pipe wall, the directional and random impact based erosive wear mechanisms remain dominant.

2.4 Wear Loss Measurement Techniques

In order to quantify the erosion damage in slurry pipelines, a number of wear measurement techniques have been reported [3, 14] such as gravimetric measurement, surface activation, metrology, electrical capacitance, ultrasonic gaging, physical wear profile measurement and post-mortem physical measurement. The reliability and applicability of these methods are important as these measurements are used not only to evaluate erosion damage occurring within an actual pipeline (at commercial or laboratory scale) but are also needed for

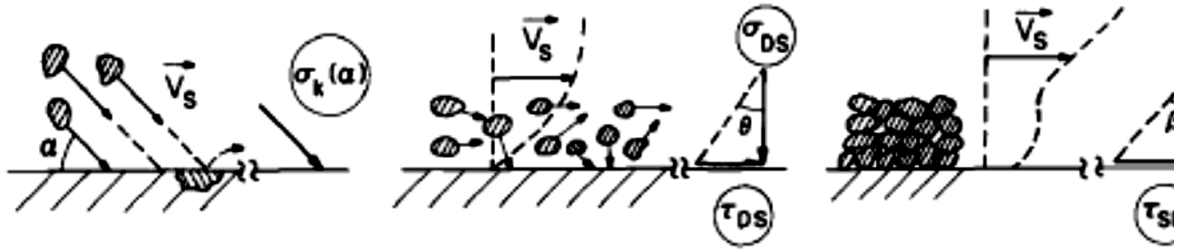

(a) Directional Impact **(b) Random Impact** **(c) Wear by friction**

Figure 2.2. Schematic of particle-wall interaction in dense slurries; (a) directional impingement (b) random impingement (c) Coulombic friction [23] **(Reused with permission)**

the calibration and assessment of relative erosion data and simulation results. A comparative study of gravimetric measurement, surface activation, and electrical capacitance measurement, done by Baker *et al.* has been reported in the review of Summer *et al.* [14], which involved detection of 0.025 m of material loss over 10 hours. The Baker *et al.* study indicated that weighing, surface activation (change in measured radiation with the change in radioactive test surface thickness) and electrical capacitance methods (change in electrical capacitance with the change in wall thickness) have potential as valuable measurements of slurry pipeline erosion. However, the electrical capacitance method needs considerable development due to problems with wall thickness and water absorption, and surface activation is relatively complicated and is not applicable to plastic pipes. Fotty *et al.* [3] have reported the advantage and disadvantages of the ultrasonic gauge measurement, gravimetric measurement, physical wear profiling and post-mortem physical measurement methods. The ultrasonic gauge is simple, non-destructive and does not require access to both sides of the pipe surface for thickness measurement. The main drawback of this method is its inability to measure thickness in non-homogeneous piping systems (i.e. overlays, polymer liners). However, it is currently being used for industrial scale actual pipeline wear measurement [10, 17] for its simplicity. The physical wear profiling and post-mortem physical measurements both can quantify the wear profile of the test coupon, but physical profiling strongly depends on the accuracy and sensitivity of the profiling sensor or stylus, and the post-mortem technique is destructive in nature and test coupons cannot be used for further experiment or analyses. Weighing or the gravimetric method has been found as the most effective yet simple measurement approach from both of the studies mentioned above. In this experimental study, the gravimetric measurement method has been implemented to calculate

the material loss along with physical surface profiling to quantify the wear pattern and will be discussed in Chapter 3.

2.5 Reports of Erosion in Slurry Pipelines

Parent *et al.* [17] studied slurry erosion in two existing oilsand hydrotransport lines of Suncor Energy Inc. and reported that wear on the X65 Carbon Steel piping is dominated by the sliding bed friction mechanism. Table 2.1 shows the operating conditions for the two pipelines reported. The pipeline thickness was measured with an ultrasonic thickness gauge at 12 circumferential positions around the pipes at 30 m intervals. The erosion-dominant wear rate reported at the bottom of the first pipeline was about 4 mm/year, whereas the general wear rate in the upper region of the pipe was about 1 mm/year. This indicates that wear due to sliding bed of particles is more aggressive than the wear due to the directional and random impact of particles near the wall. The erosion-based wear found on the second pipeline suggested the same trend; pipeline wear at the bottom was found to be 3 mm/year, while the general material loss in the remaining sections was about 2 mm/year.

Table 2.1. Operating conditions for two Suncor hydrotransport lines transporting Athabasca Oil Sands [17]

Operating Conditions	Pipeline 1	Pipeline 2
Pipe Diameter (OD)	710 mm	710 mm
Pipe Length	1 km	3 km
Velocity	3.5 – 4.5 m/s	3.5 – 4.5 m/s
d_{50}	180 μm	180 μm
Elevation gain	15 m	200 m
Specific gravity	1.5	1.5

The Schaan *et al.* study on erosion damage in Syncrude's 'Aurora Mine' also displayed a wear map at different circumferential positions for an oil sands hydrotransport pipeline transporting oil sands [10]. Table 2.2 shows the operating conditions for the Syncrude hydrotransport pipeline studied. The wall thickness at 12 positions along the pipe circumference was measured using an ultrasonic thickness gauge at different axial locations of the pipeline. Figure 2.3 shows the measured wear rates along the pipeline circumference taken over two different operating periods: February-June (2005) and August-Sept (2006). It indicates that the maximum erosive wear occurs at the pipe invert, near the 180° position from the vertical. For example, during the operating period of Feb-June (2005), the measured wear rates at the bottom and at the remaining sections pipeline were about 1.3 mm/1000 hours and 0.5 mm/1000 hours, respectively. However, the wear rate at the pipe invert increased sharply by about 40% for the period of Aug-Sep (2006). Schaan *et al.* studied the properties of the slurries being hydrotransported, and reported an increase in the contact load fraction from 0.001 to 0.01 for the oil sand slurries during the period of Aug-Sep (2006), which partially explains the increase in the wear rate.

Table 2.2. Operating conditions for Syncrude's Aurora Mine hydrotransport lines [10]

Operating conditions	**Pipeline**
Pipe Diameter (OD)	737 mm
Pipe Distance	5 km
Velocity	3.0 – 5.5 m/s
d_{50}	180-300 μm
Elevation gain	15 m
Solid concentration	> 35% (by volume)

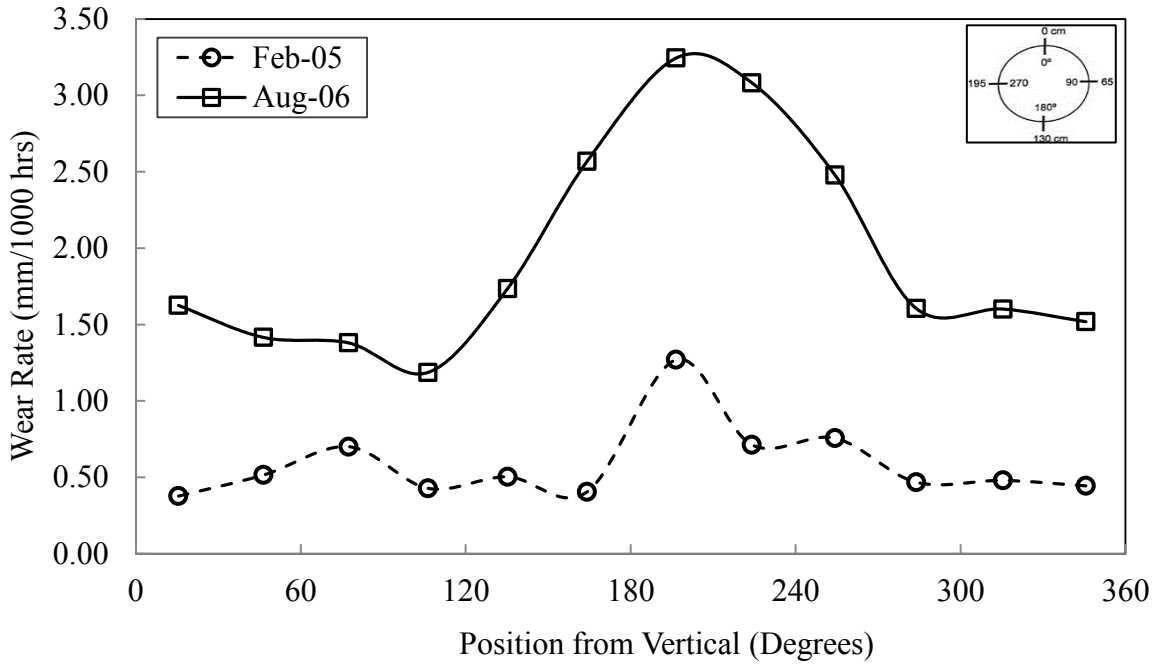

Figure 2.3. Absolute wear measurements in the Aurora Oil Sand Hydrotransport pipeline (Regenerated); Feb-June (2005) and Aug-Sept (2006) [10]
(Reused with permission)

Goosen *et al.* [6] worked with boiler bottom ash disposal slurry transport line and compared the absolute wear rate obtained from the pipeline with a recirculating pipe loop experiment, which was within 5% of each other. They installed a three-meter long PVC pipe with 332 mm inside diameter in the ash disposal line and made 16 ultrasonic gauge measurements around the circumference, at three different axial locations. The material loss rate for a mean flow velocity of 2.2 m/s was measured, and again the bottom of the pipeline was the zone of highest wear.

2.6 Characterization of Erosive Wear

Erosion damage in slurry pipelines depends on a large number of interrelated parameters (such as flow hydrodynamics, properties of erodent and target material), and these parameters

characterize deformation and cutting wear mechanisms differently [13]. In 1963, Bitter [26] suggested two different theoretical models for deformation and cutting wear for gas-solid flows and discussed their combined effect on the target surface. Alternatively, investigators have also attempted to characterize and develop correlations for estimating erosive wear rate based on results using bench-scale test apparatus like slurry pot testers, recirculating pipe loops, and jet impingement testers [3, 8, 12, 13]. Only pipe loops could be expected to allow for the study of wear due to a sliding bed. The parameters that govern erosion damage of materials due to Coulombic friction are mainly particle size, shape, bulk slurry velocity, carrier fluid viscosity, solids concentration, pipe diameter and target material properties [4].

2.6.1 Effect of Particle Size and Shape

Many investigators [4, 8, 13, 27–29] have used the mass median diameter (d_{50}) of particles as the characteristic size of the erodent particles and reported a power-law relationship with the erosion rate:

$$E \ \alpha \ \ d_p^{\,n_1} \qquad 2.1$$

Here, E is the rate of erosion and d_p is the particle size. The exponent n_1 was reported to vary from 0.3 – 2.0 and this variance is mainly attributable to experimental conditions, material properties, and particle size distribution. The increase in the particle size increases the kinetic energy of particles and therefore more energy is available for erosion during a particle-wall collision. Elkholy [27] completed a systematic study on the effect of particle size on erosion using jet impingement and found the value of the exponent n_1 to be 0.616. Gupta *et al.* [8] used a slurry pot tester and found the exponent value to be approximately 0.3. Gandhi *et al.* [13] also experimented with a slurry pot tester to see the effect of particle size for three different

velocities, while ensuring a parallel flow situation over the test coupons. They reported the exponent to be 0.85. However, Clark *et al.* [29] experimented with aluminum particles ranging from 14 to 780 μm using a slurry pot tester. They observed that smaller particles (<100 μm) at lower velocities get trapped in the boundary layer near the wall. The particle-coupon contact in this situation is parallel to the coupon and the exponent value n_1 found at this condition was approximately 2.0. Girish *et al.* [28] have reported similar observation for particles below 200 μm and reported the value of n_1 as 0.92.

Previous experimental studies [30, 31] focusing on particle shape reported that angular particles are more erosive in nature than rounded or spherical particles. Woldman *et al*. [30] conducted a comprehensive study to investigate the influence of particle size and shape on abrasive wear behavior using a 'dry sand – rubber wheel' test rig. They used six different types of particles and modeled erosive wear based on particle size, shape and feed rate or, velocity together. Overall it is clear that the effect of particle shape needs to be taken into account in case of erosion modelingl.

2.6.2 Effect of Bulk Velocity

The bulk velocity of the slurry has a major impact on the erosion damage. Studies [4, 8, 13, 32–34] have shown that the absolute erosion rate is proportional to velocity, i.e.:

$$E \ \alpha \ V^{n_2} \qquad 2.2$$

Here, V indicates the bulk flow velocity. Karabelas [33] completed a systematic study on erosive wear by using machined brass wall inserts inside a sand slurry pipeline. He reported that n_2 was within the range 1.2 to 2.7 for sands having d_{50} < 138 μm. Elkholy [27] worked with the

jet impingement method and reported $n_2 = 2.39$. Gandhi *et al.* [13] used a modified slurry pot tester with special fixtures to ensure parallel flow over the test coupon and they reported an average exponent value of 2.56 in their erosion model. The parallel flow wear experiments were conducted for three different particle sizes, i.e. 0.22, 0.45 and 0.89 mm, and in each case, the wear rate increased with the velocity in a similar manner.

Huang *et al.* [4] developed a phenomenological model of erosion damage in pipelines and reported that n_2 not only depends on a particle's random impact due to fluid turbulence but also on its settling velocity. The two limiting values for the exponent n_2 are 2.0 and 3.575, respectively. They have compared the predicted erosion damage from their model with Karabelas' [33] experimental data at the top, middle and bottom position of a pipeline; all of them are in good agreement. Figure 2.4 shows a comparison between the predicted value from the model with Karabelas experimental data at the bottom of the pipe and the good agreement can be seen.

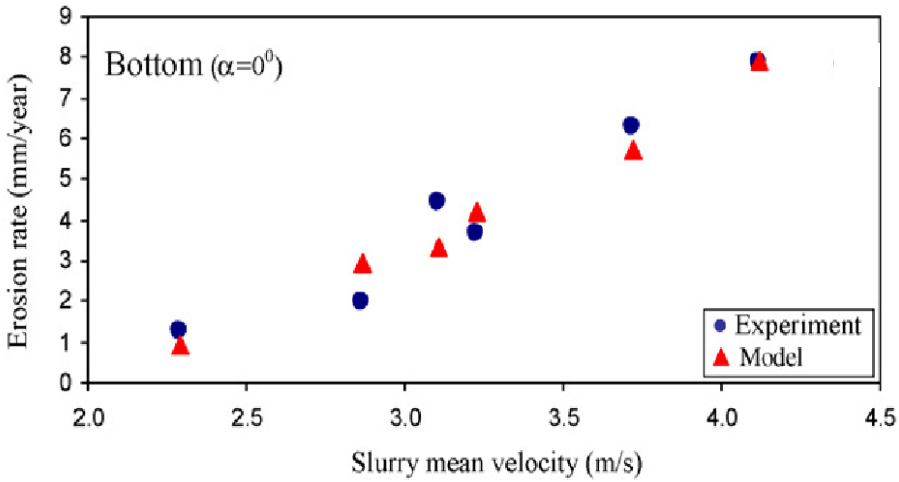

Figure 2.4. Comparison of Huang et al. wear rate predictions with Karabelas experimental data at the bottom of the pipeline [4] (Reused with permission)

2.6.3 Effect of Solids Concentration

It is also reported in the literature [4, 5, 8, 13] that the erosive wear rate increases with the slurry solids concentration of particles in the slurry. Gupta *et al.* [8] worked with four solid concentrations (% by weight) of a slurry sample, namely 15, 25, 35 and 45%, and three operating velocities, 3.9, 5.5 and 8.1 m/s. They described the erosive wear dependence on solids concentration as a power law relationship as shown in equation 2.3 and found the exponent to be approximately 0.55.

$$E \ \alpha \ C^{n_3} \qquad 2.3$$

Here, C is the solids concentration. Gandhi *et al.* [13] reported the exponent n_3 to be 0.83 for wear rate from a parallel flow situation. Cooke *et al.* [5] worked with 70 μm particles at 3.0 m/s velocity with a TWT and found that the wear rate increases slightly with increasing solids concentration. A power law fit of the experimental results reveals the exponent value to be 0.13 in their study.

2.6.4 Erosive Wear Models

Based on the properties discussed above, previous researchers modelled erosion damage [4, 8, 13, 26, 27, 34–36] using a general form correlation:

$$E = k d_p^{n_1} V^{n_2} C^{n_3} \qquad 2.4$$

Here, E is the erosive wear rate, V is velocity, d_p is particle diameter, C is solids concentration (% by volume) in the slurry. The coefficient k and exponents n_1, n_2 and n_3 are constants which depend on the erodent and the target material properties. In the case of the

sliding wear system, the flow of particles is parallel to the surface and therefore the effect of particle impact angle is neglected in the general formulation. Gupta *et al.* [8] and Gandhi *et al.* [13] presented wear models based on this formulation where the coefficient k value was reported to be 0.2 and 2.57, respectively. Huang *et al.* [4] derived a phenomenological model for slurry erosion based on turbulent theory and a single particle based erosion model that incorporates the effect of settling velocity of particles in the slurry pipeline. The model showed reasonable agreement with existing pipe loop experiment and indicated that erosion is not only a power law function of the bulk flow velocity, solids concentration and particle size but also weakly depends on liquid viscosity and pipe diameter. Additionally, Oka *et al.* [34, 36] incorporated mechanical properties of the target material as a key parameter for estimating erosion damage. They investigated using aluminum, copper, carbon steel and stainless steel test coupons and added another power law based term derived from material hardness.

Sections 2.1 and 2.2 of this chapter clearly identified that during coarse particle transport the flow situation inside the slurry pipeline can be considered as a heterogeneous and the sliding particle bed on the pipe invert results in a higher wear rate due to Coulombic friction. Almost all the erosion models reported in the literature based on laboratory scale experimental studies (i.e. using slurry pot wear tester, jet impingement methodology etc.) and phenomenological modelling are not focused on the modelling of erosive wear rate due to sliding friction. The hydrodynamics and wear mechanism that can be attained using a simple slurry pot tester or using the jet impingement method are quite different than the actual pipeline situation. Also, phenomenological modelling of erosion damage based on the single particle based model is inappropriate, as it fails to incorporate the effect of particle-particle interaction during sliding friction. To mitigate the shortcomings of the existing erosion models and to better understand

erosion damage due to Coulombic friction, experimental studies incorporating the sliding friction based wear mechanism are necessary.

2.7 Study of Slurry Erosion using the Toroid Wear Tester (TWT)

In the Pipeline Transport Processes Research Group at the University of Alberta, a number of laboratory scale test devices have been used to study erosive wear mechanisms and related parameters, which includes a slurry pot tester [7] and several recirculating pipe loops [37–39]. As discussed in Chapter 1, to reproduce the sliding bed condition in a slurry pipeline, it is thought that two techniques can be used confidently, the recirculating pipe loop and the toroid wear tester (TWT). Although the pipe loop is capable of nearly reproducing the flow hydrodynamics found in actual operating slurry pipelines, there are several disadvantages, such as a higher amount of particle degradation, the requirement of a large volume of slurry and the requirement of some scale-up basis to compare with larger diameter actual pipelines. On the other hand, the TWT has very different geometry and kinematics than straight pipelines [40], but it appears to be possible to study wear that occurs at the slurry pipeline invert [5]. The use of a TWT also has the advantage of lower particle degradation rate and a smaller volume of slurry is required for each experiment.

2.7.1 Previous Studies

The first TWT test rig was developed by Worster *et al.* [41] to study coal degradation in pipelines and was known as the ring pipe. The diameter of their TWT was 1.2 m with a flow channel area of 150 mm^2. Coal-water slurry was used to fill three-quarters of the volume of the ring-shaped TWT, and when the TWT was rotated, the slurry remained approximately stationary

relative to the pipe (see Figure 2.5). The relative velocity was assumed to be very similar to the velocity in a coal hydrotransport pipeline. The work of Traynis (1977) on the particle (coal) degradation of slurry and the hydraulic drag of slurries was also reviewed by Cooke *et al.* [5] and they reported that the quantity of fines formed in horizontal pipelines and the Ring Pipe is almost identical. Truscott surveyed abrasive wear in was also reviewed by Cooke *et al.* [5] and they reported that the quantity of fines formed in horizontal pipelines and the Ring Pipe is almost identical. Truscott surveyed abrasive wear in hydraulic machinery and suggested the TWT as the best simulation apparatus for pipeline wear was also reviewed by Cooke *et al.* [5] and they reported that the quantity of fines formed in horizontal pipelines and the Ring Pipe is almost identical. Truscott surveyed abrasive wear in hydraulic machinery and suggested the TWT as the best simulation apparatus for pipeline wear [32]. The British Hydromechanics Research Association (BHRA) had developed a toroid wheel for wear measurement that produced similar

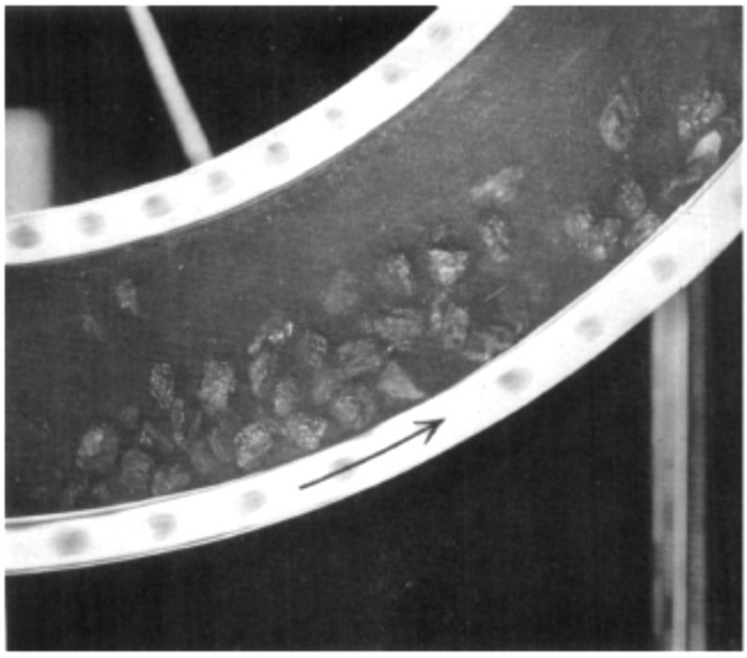

Figure 2.5. Part of ring pipe used for measuring coal degradation [41] **(Reused with permission)**

wear distributions as found in actual pipelines, as mentioned by Cooke *et al.* [5] in their review on the TWT. To overcome the drawbacks of the erosion damage analysis in pipe loops, Paterson and Cooke Consulting Engineering (PCCE) also designed a small-scale TWT (see Figure 1.1) [5]. In PCCE's TWT, four square section toroidal wheels were mounted on a shaft driven by an electric motor. Each toroid can hold four flat test coupons at their outer circumference with a clamping mechanism (see Figure 2.6). A modification of that particular design has been fabricated and used in this study, and will be discussed in Chapter 3. One major advantage of PCCE's TWT is the use of flat sample plates at the circumference which makes the curvature correction principle for ring pipes unnecessary. The sliding friction on top of the flat plates is thought to be similar to that present on the bottom of a pipeline. Major disadvantages are the upper and lower speed limit of operation during the experiment. Cooke *et al.* [5] reported an upper limit for the toroid RPM, above which the slurry inside the toroid starts to carry over to the other side of the wheel and termed it 'carry-over'.

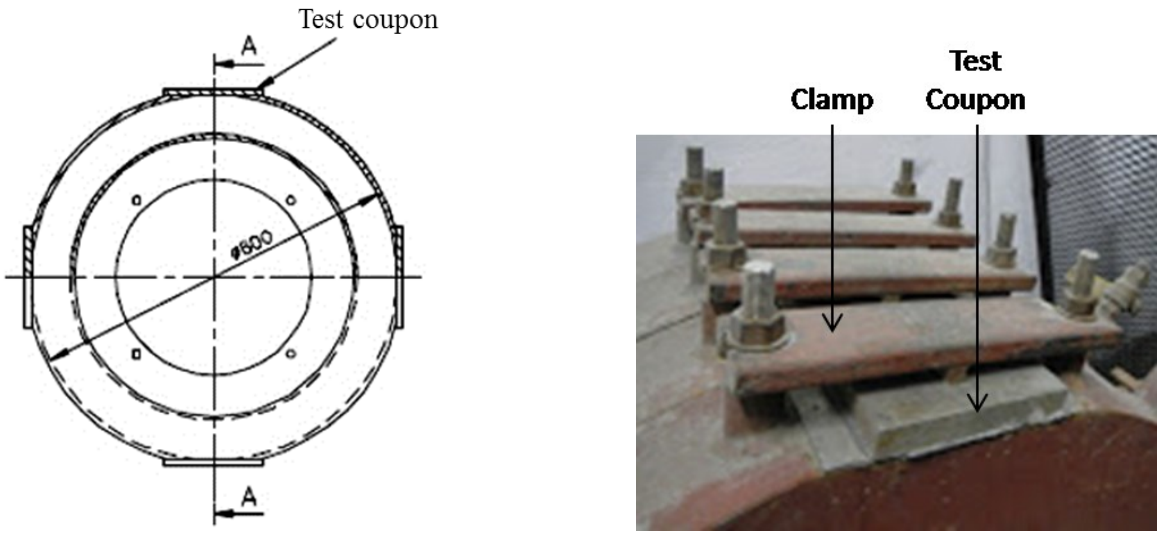

(a) Dimensional details of PCCE's TWT **(b) Coupon clamping mechanism**

Figure 2.6. PCCE Pipeline Wear Tester Design Details [5]

2.7.2 Accounting for Particle Degradation

The abrasivity of the slurry depends on the particle size, shape, hardness and friability. Shook *et al.* [42] observed that although the slurry in a recirculating system is replaced on a regular schedule, the particle shape changes significantly. This degradation of particles decreases the abrasivity of the slurry and needs to be taken into account for the correct determination of the absolute wear rate. Similar observations were reported in other studies [3, 5, 6] as well, which requires a method to account for the particle degradation problem in laboratory scale slurry erosion studies. Cooke *et al.* [5] presented a procedure to account for the effect of particle degradation. The procedure is as follows:

- Conduct a wear test over a period of 96 hours while the slurry will be replaced every 48 hours. Determine the wear rate.
- Conduct similar wear tests changing the slurry replacement interval to 8, 12 or 24 hours. Determine the wear rate for each of the tests.
- Plot the variation of the wear rate against the slurry replacement interval (as shown in Figure 2.7). By fitting an exponential curve to the data, the wear rate for fresh slurry i.e. zero hours of slurry replacement interval can be extrapolated.

2.7.3 Predicted Wear Rate vs Actual Wear Rate

A reasonable correlation between the predicted data using a toroid wear tester and field data from an actual operating pipeline has been reported by Cooke *et al*. [5]. The predicted wear rate using fine tailings of slurry inside a toroid wear tester was found to be approximately 0.60 mm/year, whereas the actual fine tailing conveying pipeline reported a wear rate between 0.88

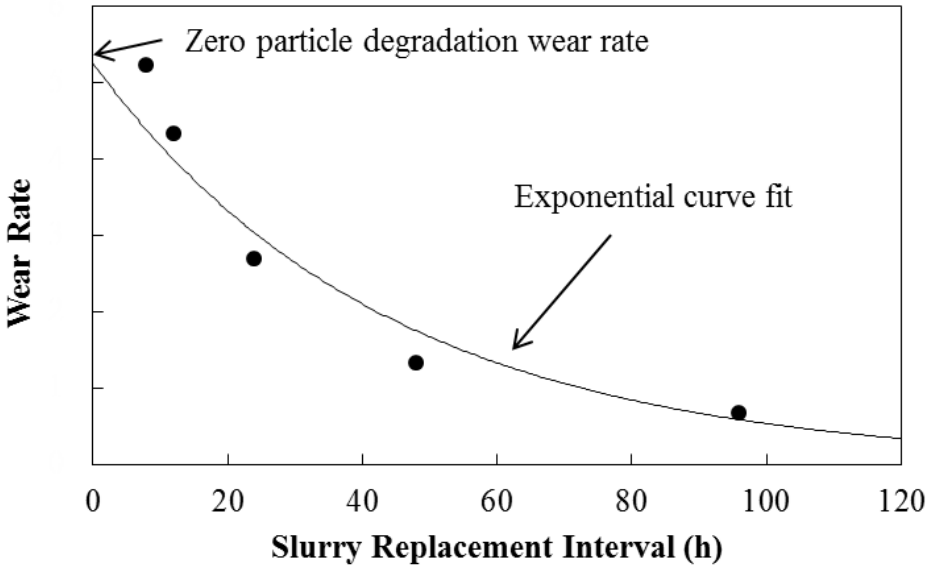

Figure 2.7. Effect of Slurry Replacement Interval on Wear Rate [5]

and 1.23 mm/year. Based on their findings, Cooke *et al.* suggested their toroid wear tester as a potential design tool for future work and emphasized the need for further experimental work so that the data from the TWT can be practically applied with confidence to the design and evaluation of slurry pipeline systems.

2.8 Summary

From the literature reviews presented here, it is quite clear that the sliding bed erosion in heterogenous slurry pipelines cannot be evaluated using most laboratory-scale wear testers. Measurement of wear in actual slurry transport pipelines is possible, however, these measurements cannot easily be used for the characterization of erosive wear or development of wear models. Several studies used laboratory scale test methods to characterize and model pipeline wear, but both the wear mechanism and flow hydrodynamics in most of the laboratory testers are different than an actual pipeline. In the TWT, test coupons wear appears to be

analogous to the wear at the bottom of a pipeline; in slurry pipelines, the pipeline remains stationary and coarse particles move with the flow, and in the TWT, the coarse particles are assumed to be settled and relatively stationary while the test coupons slide across them. The TWT, however, may induce a slurry flow within the system creating a tumbling action of the particles within the slurry domain. The slurry behavior in the TWT is complex and very few studies involving the TWT can be found. Therefore, based on the designs and specifications provided by PCCE, a TWT was built for detailed experimental study and erosion modeling. To determine the experimental operating and limiting conditions (i.e. wheel speed, solids concentration) through qualitative flow observation, a transparent acrylic toroid wheel was manufactured as well. Details of the experimental setup and experiments completed are discussed in Chapter 3.

Chapter 3
Experimental Method

3.1 Introduction

Based on the provided by Paterson and Cooke Consulting Engineers (PCCE), a toroid wear tester (TWT) with four hollow toroid shaped wheels was fabricated for this study. For qualitative flow observations, an additional acrylic wheel was also fabricated. The materials and equipment used in this study, detailed design of the newly built TWT, and the slurry erosion experiment procedures maintained throughout this study are featured in this chapter. Sections 3.2 and 3.3 of this chapter describe the materials and equipment used in this study. Sections 3.4 through 3.6 describe the design of the TWT and experiment procedures. The calculations necessary for the material loss measurement are also demonstrated in Section 3.7. Finally, the experimental matrix is presented in Section 3.8.

3.2 Materials Used

3.2.1 Particles

In this study, different particles were used, which were chosen based on their size, shape and density. The mass median diameter (d_{50}) of the particles was considered as the average particle diameter and used to characterize the particle size in this study. Particles with different d_{50} values (ranging from 0.125 mm to 2.0 mm) were selected for tests to characterize the slurry flow inside the TWT, and also to understand the effect of particle size during erosion tests. Table 3.1 shows the detailed properties and sources of the particles used in this study.

Table 3.1. Properties of particles used (supplier information)

Product Name	Manufacturer/Supplier	Density (kg/m^3)	d_{50} (mm)
LM 125	Lane Mountain Company	2650	0.125
SIL 1	SIL Industrial Minerals	2650	0.250
A.F.S. Testing Sand 50-70	U.S. Silica	2650	0.250
SIL 4	SIL Industrial Minerals	2650	0.420
Fused Aluminum Oxide (Alodur®)	Treibacher Industrie Inc.	3950	0.425
Silica Gravels	Target Products Ltd.	2650	2.0

The shape of the particles was also qualitatively analyzed by scanning electron microscopy (SEM). Figure 3.1 shows SEM micrographs of five of the six particle types used in the current study. No SEM images of the gravels were taken. It can be seen from the SEM images that the U.S. Silica sand particles (see Figure 3.1 (c)) are almost spherical, but the other particles are relatively more angular. The Aluminum Oxide particles (see Figure 3.1 (e)) are very angular and have more sharp edges than the SIL 4 sand particles (see Figure 3.1 (d)), which has the same d_{50}. For this particular reason, the Aluminum Oxide particles were chosen to study the effect of abrasivity of erodent particles on test coupons. The 2.0 mm gravels are the largest among the particles used and these particles were chosen to study the effects of large particles on erosion rates.

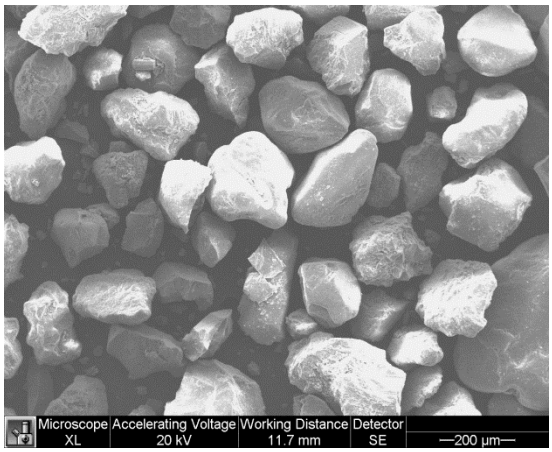

Figure 3.1(a) LM 125 SEM image;
Magnification: 200x, d_{50} = 0.125 mm

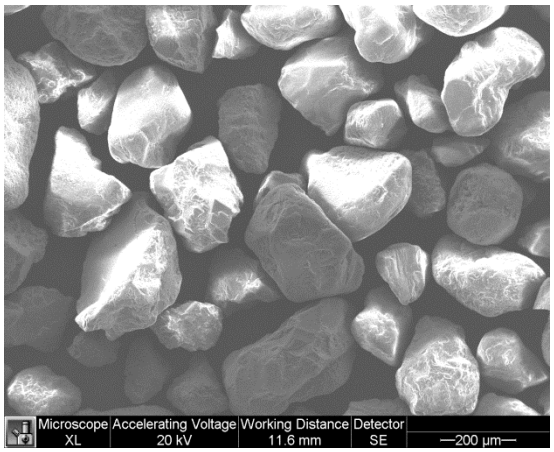

Figure 3.1(b) SIL 1 SEM image;
Magnification: 200x, d_{50} = 0.25 mm

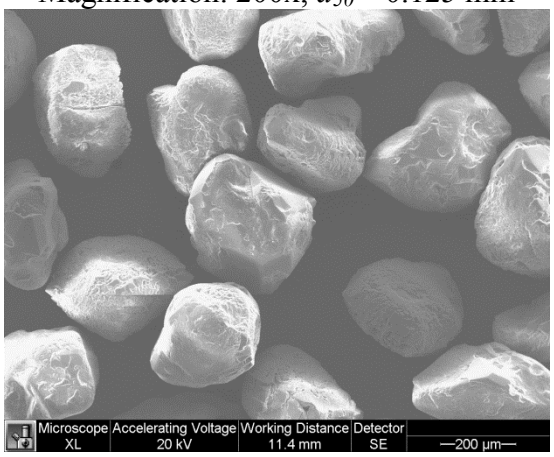

Figure 3.1(c) U.S. Silica SEM image;
Magnification: 200x, d_{50} = 0.25 mm

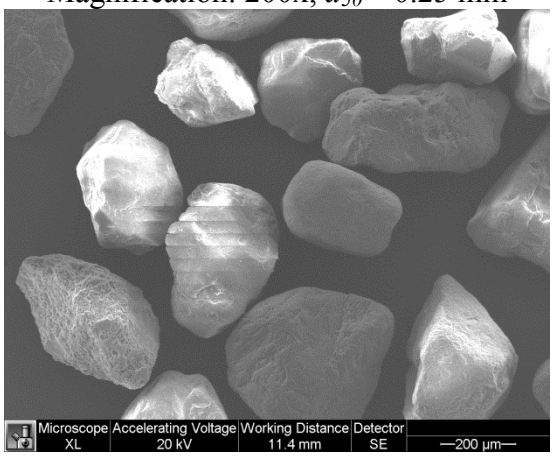

Figure 3.1(d) SIL 4 SEM image;
Magnification: 200x, d_{50} = 0.425 mm

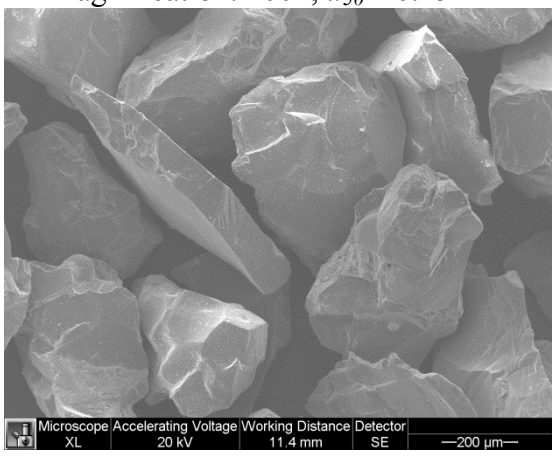

Figure 3.1(e) Aluminum Oxide SEM image;
Magnification: 200x, d_{50} = 0.425 mm

Figure 3.1. SEM images of particles used; Magnification: 200x

3.2.2 Chemicals Used

For proper cleaning of test coupons before and after each experiment, chemical solvents, namely acetone, toluene and a multi-purpose cleaning liquid were used. Table 3.2 shows the properties, composition and WHMIS class of the chemicals that were used in this study.

3.2.3 Test Coupons

The wear test plates (test coupons) used in this study were machined from hot-rolled ASTM A572 GR50 carbon steel plates. The initial dimensions of the source plates were 9.5 mm × 2400 mm × 1200 mm. After the machining processes, the average dimensions of each of the test coupons was 8.0 mm × 100 mm × 80 mm for the large toroid wheels (Wheels A, B and C), as described in Section 3.4.2. For the small toroid wheel (Wheel D), the average dimensions of

Table 3.2. Properties of chemicals used in the present study

Name	Supplier	Properties	Caution
Cleaning Liquid: Fisherbrand Versa – Clean ™	Fisher Scientific	Odourless, Orange in color	Eye Irritant **WHMIS class: D**
Acetone, ReagentPlus, ≥99%	Sigma-Aldrich	Sweet odour, Clear colourless liquid, Volatile	Highly Flammable Liquid, Eye Irritant **WHMIS class: B2, D2B**
Laboratory Grade Toluene, Fisher Chemical	Fisher Scientific	Aromatic, Clear colourless liquid	Flammable Liquid, Very Toxic, Skin Irritant, Storage Code Red **WHMIS class: B2, D2A, D2B**

each test coupons were 8.0 mm × 63.5 mm × 63.5 mm. All of the source materials were purchased from the same manufacturer (U.S. Steel Canada Inc.) to avoid possible inconsistencies in the results due to changes in the material composition. Properties of the carbon steel specimens used in this study are detailed in Appendix A.

3.3 Equipment

3.3.1 Particle Sieve Analyzer

Measurement of particle size and particle size distribution is essential for characterizing the behavior of the slurry and the erosive wear mechanisms. Representative samples were collected from each batch of particles that were used and the size distribution of each sample was obtained by sieve analysis. The sieve analyzer grades the sand particles based on their linear dimensions [43]. In this method, an equivalent sphere size of each particle is measured that can just pass through the square aperture that is the same size as the particles [43]. Figure 3.2 (a) shows the particle sieve analyzer that was used in the present study. The particle sieve analyzer (Brand: W.S. TYLER; Mentor, OH, USA) consists of a nested column of six sieves or meshes oriented in such a manner that the aperture gets smaller for each lower sieve. The stack of sieves is placed in a mechanical shaker, which allows a certain degree of vertical movement of the sieves along with horizontal shaking for a preset time period. The ASTM US standard sieves are usually made of bronze and steel (see Fig. 3.2 (b)). Standard sieves ranging from ASTM # 5 (Aperture: 4000 μm) to ASTM # 200 (Aperture: 74 μm) were used in this study for SIL 1, SIL 4 and gravel particles. The particle size distributions obtained from the sieve analysis are shown in Appendix B.

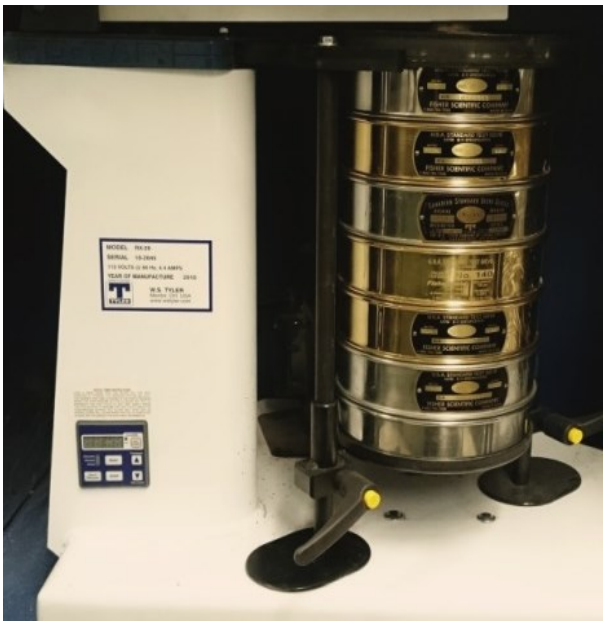

Figure 3.2 (a). Particle Sieve analyzer

Figure 3.2 (b). ASTM US sieves

Figure 3.2. Particle Sieve Analysis using ASTM US sieves

3.3.2 AR-G2 Rheometer

All rheometry measurements in this study were made using an AR-G2 rheometer (TA instruments, Newcastle, DE, USA). Three types of geometries are available for this instrument: concentric cylinder, cone and plate, and parallel plates. The concentric cylinder geometry was used during the viscosity measurement of the carrier fluid samples. The AR-G2 rheometer has a combination of a magnetic thrust bearing and a traditional air-bearing, which increases the accuracy of results of this instrument in comparison to other rheometers [44]. The use of a magnetic thrust bearing allows low viscosity samples over a broad range of conditions to be studied and also allows ultra-low torques to be applied to the sample (see Table 3.3). The rheometer is connected to a smart swap temperature control unit that utilizes deionized water as the circulating cooling fluid and maintains a steady temperature during the measurement. The detailed geometry and calibration of the rheometer is presented in Appendix C.

Table 3.3. AR-G2 technical specifications (CR: Controlled Rate, CS: Controlled Stress)

Minimum Torque Oscillation (CR and CS)	0.003 (μN.m)
Minimum Torque Steady (CR and CS)	0.01 (μN.m)
Maximum Torque	200 (mN.m)
Torque Resolution	0.10 (nN.m)
Angular Velocity Range CR	1.4E-9 to 300 (rad/s)
Thrust Bearing	Magnetic Bearing
Smart Swap Geometry	Standard
Concentric Cylinder	-20 ^{0}C to 150 ^{0}C

3.3.3 Surface Profilometer: Mitutoyo Contracer CV-3100

The surface roughness of the test coupons was measured using a surface profilometer or Contracer (Brand: Mitutoyo; Model: CV-3100H4). It has a motorized Z-axis and the measured values along the X- and Z-axes can be recorded digitally. It was programmed and controlled using the FORMPAK software. The technical specifications of the Mitutoyo Contracer are given in Table 3.4. The steps for FORMPAK programing and measuring the surface roughness of a test coupon are presented in detail in Appendix D.

Table 3.4. Mitutoyo Contracer CV-3100 technical specifications

Measuring Range	X -axis	100 mm
	$Z1$-axis	50 mm
Resolution	X -axis	0.05 μm
	$Z1$-axis	0.2 μm
Angular adjustment	X -axis	$\pm 45^0$
Measuring speed		0.02 – 5 mm/s
Measuring force		30 mN
Probe tip	Material	Carbide
	Radius	25 μm
Straightness deviation		0.8 μm/ 100 mm
Length measurement deviation (at 20^0 C)	X -axis	$\pm(1+0.01L)$ μm; L = forward travel (mm)
	$Z1$-axis	$\pm(2+\|4H\|/100)$ μm; H = Measuring height above horizontal position (mm)

3.4 Toroid Wear Tester (TWT)

3.4.1 Key Elements of the TWT Assembly

The TWT setup consists of the following key elements (see Figure 3.3):

- Four hollow toroid shaped wheels; Outer Diameter: 608 mm,
  Flow channel area: 65 × 60 mm^2 (Wheel A, B, C) and 58 × 60 mm^2 (Wheel D)
- An removable Acrylic Toroid Wheel (ATW); Outer Diameter: 608 mm,
  Flow channel area: 65 × 60 mm^2
- A central shaft powered by one 3 HP motor; Shaft diameter: 40 mm
- A variable frequency drive (VFD)
- An online computer control and monitoring system

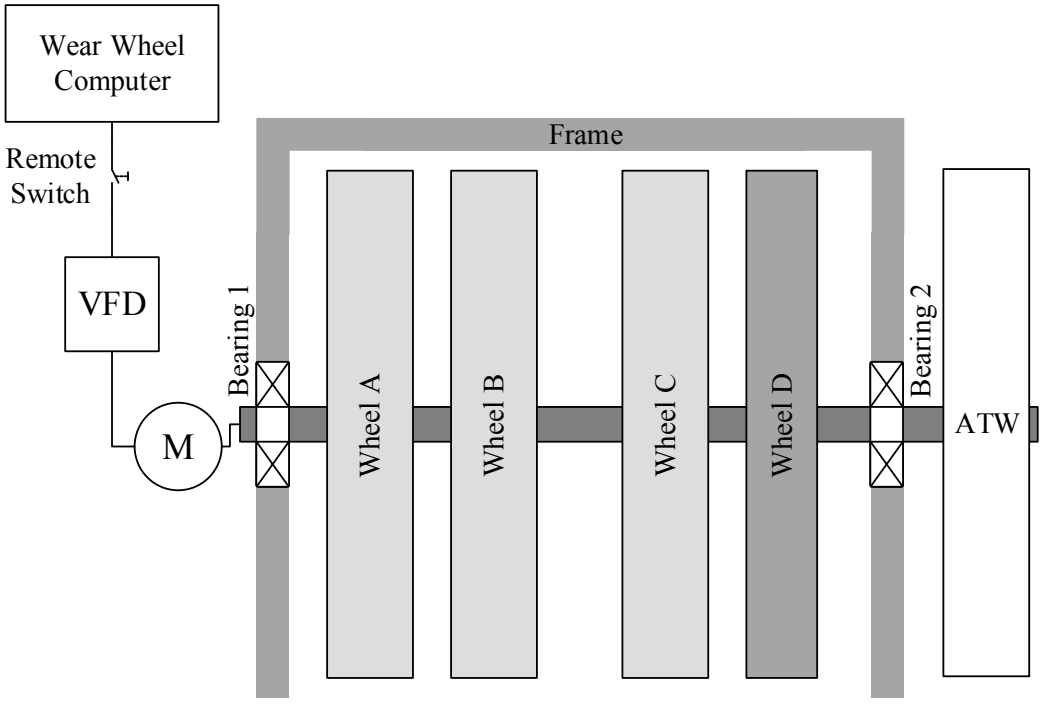

Figure 3.3. Schematic of key elements of Toroid Wear Tester

3.4.2 Toroid Wear Tester (TWT) Design

The TWT has four hollow toroidal shaped wheels labelled A, B, C and D made of stainless steel. Each toroidal wheel has five openings on the outer circumference termed 'coupon windows' (shown in Figure 3.3). To make the coupon windows, firstly, two L-shape stainless steel brackets were welded on the side of the wheel at the desired locations, and then, the top surface of the wheel and the brackets were ground to create a flat surface. In the end, the openings on the flat surfaces were generated by milling operation. The average dimensions of the openings of coupon windows for Wheels A, B, C and Wheel D are 65 × 65 mm^2 and 58 × 58 mm^2, respectively. The test coupons are attached on these coupon windows using a coupon holder with a 0.5 mm thick paper gasket (Manufactuere: Dynoteq, Model: Tesnit® BA-U) in between them. To ensure a perfect sealing, a layer of lubricant (Manufacturer/Supplier: Rust Check) is also applied to the gasket. The gasket is made of synthetic Aramid fiber and Nitrile rubber, and it was selected particularly for its resistivity against water and greasy elements such as the lubricant used.

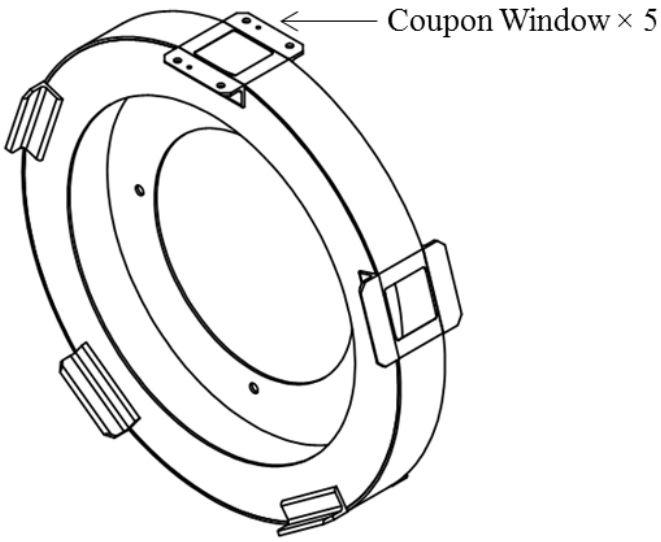

Figure 3.4. Coupon windows on toroid wheel circumference

Each toroid wheel is equipped with one N_2 charging port and one air discharging port, and these ports are located on opposite sides of each toroid wheel to aid N_2 purging before the experiment (See Figure 3.11), which will be discussed later in Section 3.5.4. All toroid wheels are mounted on a central 40 mm diameter shaft. The central shaft rotates in between two bearings (Bearing 1 and Bearing 2 showed in Figure 3.3), which are fixed on the main structural support frame. The central shaft is powered by one 3 HP, 6 pole synchronous motor (Manufacturer: e|Line^{TM} Premium Motors, Model: EL111, Frame: 213T) through a timing belt-pulley drive. To control and maintain the central shaft RPM of the TWT, a VFD system is used. The VFD (Manufacturer: Lenze AC Tech, Model: SMVector) system is hooked up to a computer with a remote toggle switch and is operated either manually or using a computer program, and will be discussed in detail in Section 3.4.4.

Figure 3.5 shows the detailed orthogonal projection of the complete TWT assembly. The entire TWT setup is approximately 5.12 ft long, 2.88 ft wide and 3.52 ft high. The supporting base plate for the motor drive and the central shaft are about 1.2 ft and 2.52 ft high from the ground, respectively. Figure 3.6 shows the complete assembly of the TWT installed in the Pipeline Transport Processes Research Lab at University of Alberta. This figure illustrates the timing belt-pulley drive mechanism that transfers the rotary motion from the motor to the central shaft. Wheels A, B, C, D and the coupon windows on the outer circumference of these wheels are also noticeable in this figure. Some important dimensions of the toroid wheels and shaft size are presented in Table 3.5. The full design drawings are presented in Appendix I.

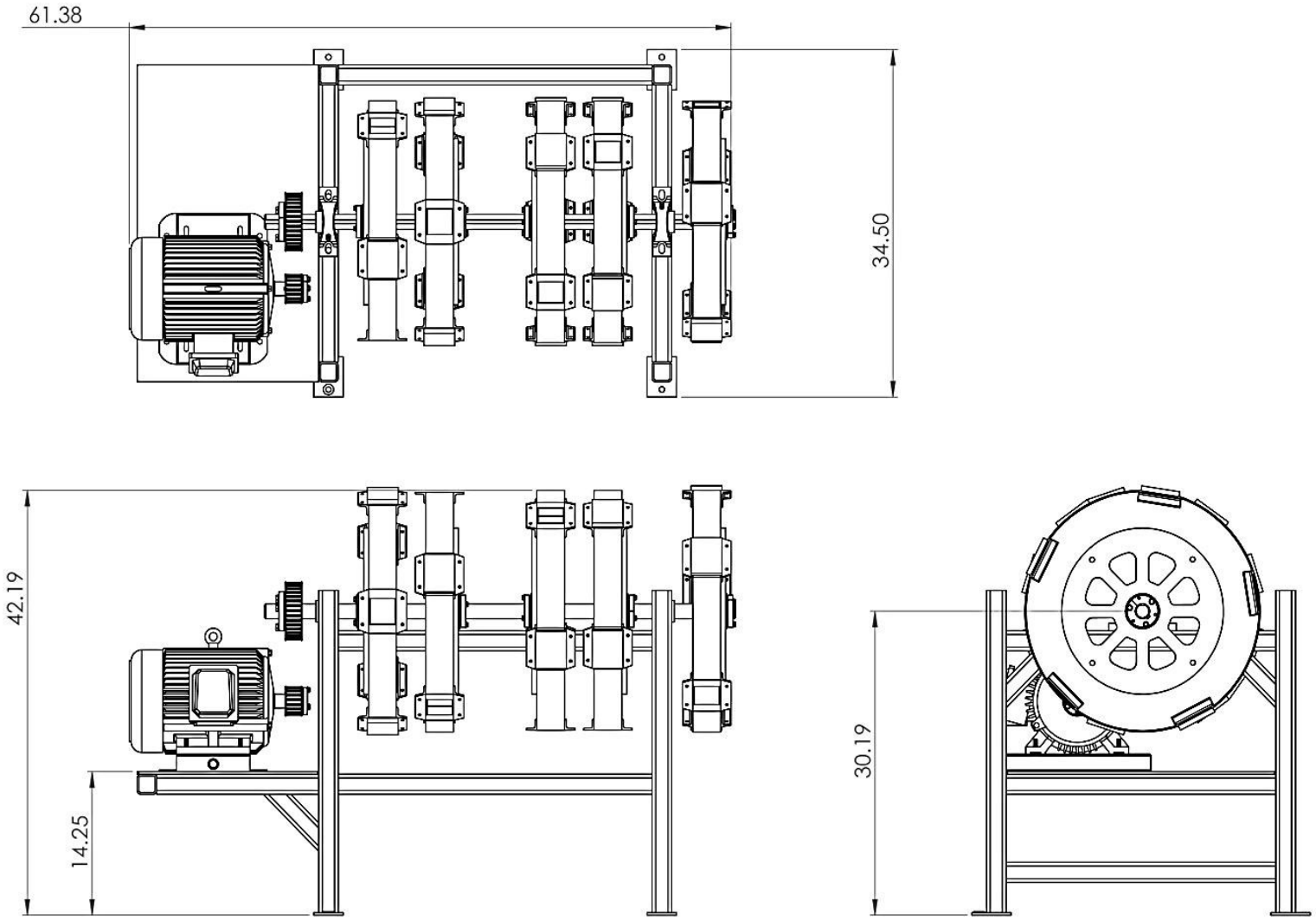

Figure 3.5. Detailed drawing of the TWT assembly (Dimensions are in inches)

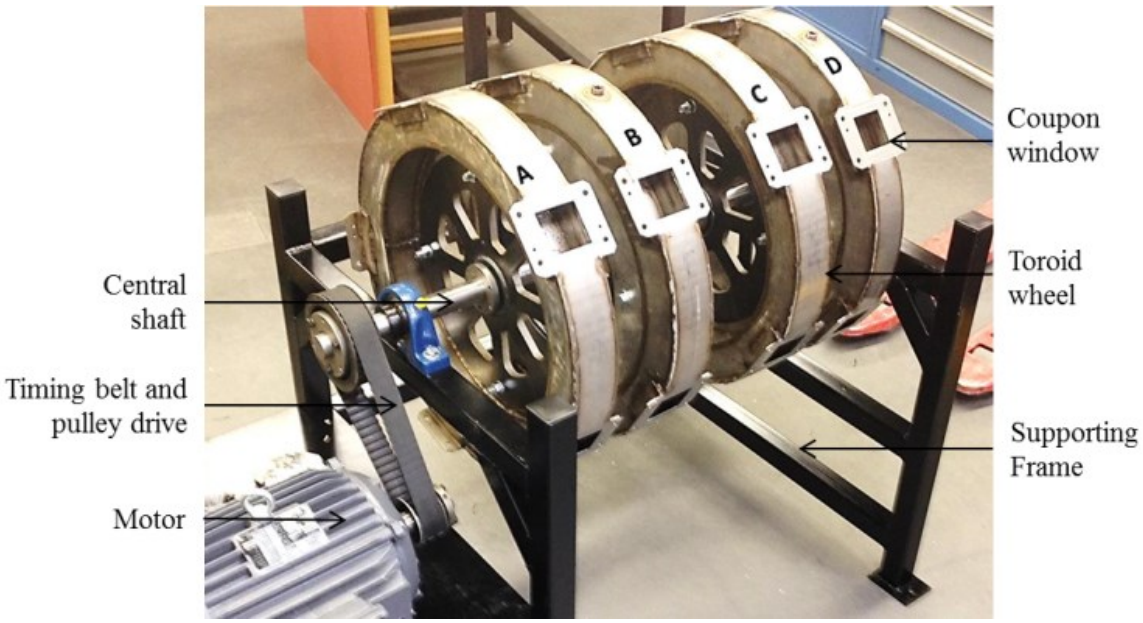

Figure 3.6. Toroid Wear Tester (TWT) assembly

Table 3.5. Important dimensions of the TWT

Item	Dimension (mm)
Wheel outer diameter, OD	604
Channel height, h	60
Channel width (for Wheel A, B, C), w_L	65
Channel width (for Wheel D), w_s	58
Diameter of the central shaft, D_{CS}	40
Length of the central shaft, L_{CS}	1200

3.4.3 Acrylic Toroid Wheel (ATW)

A removable toroid wheel was built with transparent acrylic plastic to observe the flow inside the TWT during operation. Besides observing the slurry flow inside the TWT qualitatively, the ATW reveals the limiting operating conditions and particle-wall contact based correction factors for the TWT, which will be described in Chapter 5. The ATW is dimensionally similar to the larger wear wheels (Wheels A, B and C). The flow channel area of the ATW is 65×60 mm^2. The ATW is mounted on the overhanging part of the TWT central shaft with the help of a self-centered bushing mechanism. The ATW is not equipped with any coupon windows on the outer circumference, rather it has two circular openings on the side walls for slurry charging and discharging. These two openings are kept closed during the flow observation operation using hex-bolts and rubber sealing gaskets. Since the ATW rotates on the same central shaft of the TWT assembly, the VFD control and monitoring option for the ATW is the same as the original TWT. Figure 3.7 shows the ATW, which is rotating at 60 RPM with 2.0 mm gravel particles at 10% volumetric solids concentration.

Figure 3.7. A partial view of the ATW in operation; N = 60 RPM; d_{50} = 2 mm; Cs = 10%

3.4.4 TWT Control Software

The constant speed of the TWT is maintained by the SMVector variable frequency drive (VFD) mentioned earlier, and it is connected to a computer for remote control and monitoring of each material loss experiment. The software for controlling the TWT is called as VWWM (VFD Wear Wheel Main), which is shown in Figure 3.8. It has been designed and developed with the help of the Technical Support Group of Chemical and Materials Engineering Department, University of Alberta and commissioned in the Pipeline Transport Process Research Group's TWT facility. The main purpose of this software is to diagnose the VFD and data logging during the material loss experiment. This software provides the VFD output voltage and current, VFD fault codes, and VFD heatsink temperature for safe and smooth running of a material loss experiment. This software also helps to set the wheel speed, monitors accidental shut down and speed changes of the VFD, and reports an e-mail based alarm to the operators.

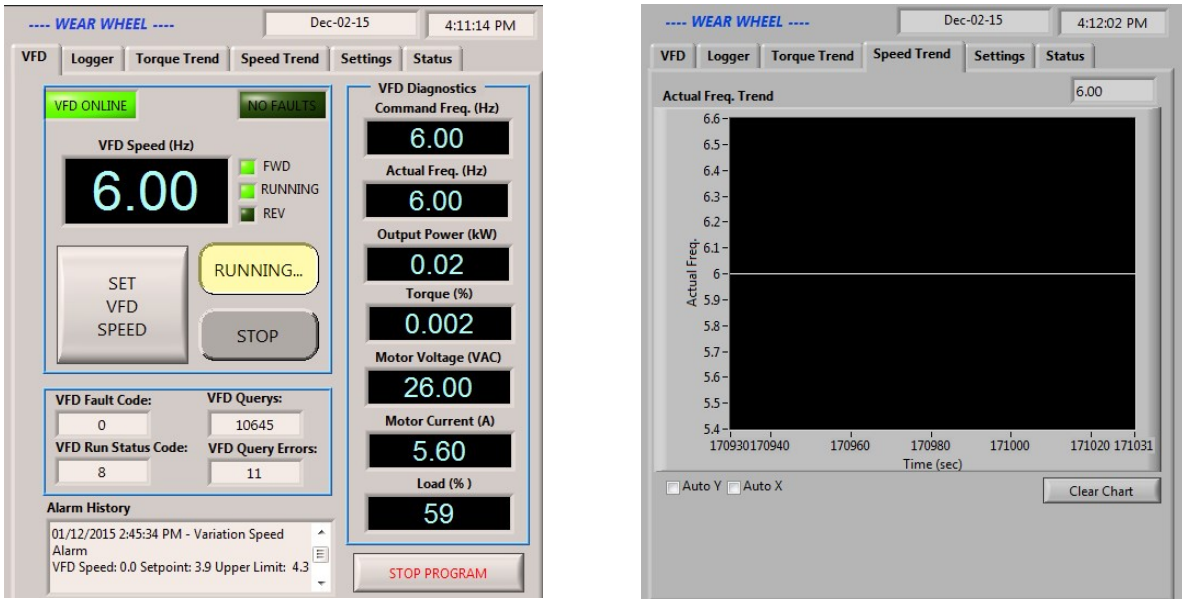

(a) (b)

Figure 3.8. VFD control software; (a) the set parameter window showing the VFD diagnostics data (b) online speed monitoring through operating frequency against time graph

3.5 Procedures

3.5.1 Overview

A simplified overview of the material loss experimental procedure is shown in Figure 3.9. The test coupons are cleaned and weighed before experiment starts (M_1). Then the test coupons are clamped on the coupon window of the TWT. Next, the slurry is charged to fill one-third of the volume of each toroid wheel. Butler *et al.* [45] reported nitrogen (N_2) purging as one of the most efficient way to remove dissolve oxygen from water. Therefore, to minimize the effect of corrosion during the experiment, N_2 was purged inside of each toroid wheel. Purging N_2 through the slurry does not only lower the amount of dissolved oxygen in the slurry, but also replaces existing air from the volume of the TWT not occupied by the slurry. After that, the

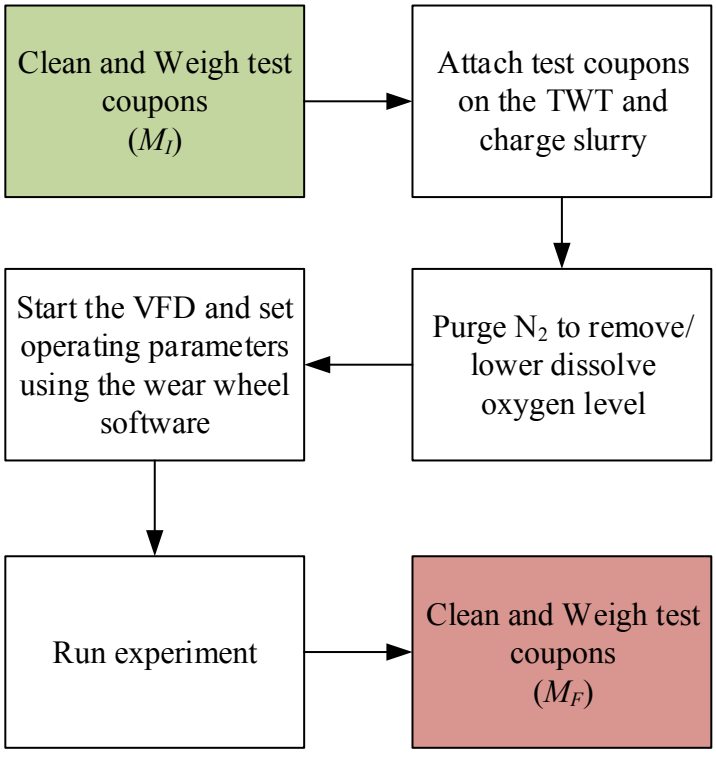

Figure 3.9. Overview of the wear testing procedure using TWT

required wheel speed is set using the VFD, and the TWT is operated for the desired time period. Finally, when an experiment is finished, the test coupons are cleaned and weighed again (M_F) to compare with the initial mass (M_I), and determine the amount of material lost during the experiment. Details of the experimental procedures are presented in the following sections.

3.5.2 Test Coupon Cleaning

The laboratory wear tests are usually done for short time periods and the expected material loss from the test coupon is smaller than compared to an actual pipeline. For this reason, the test coupons are prepared and cleaned carefully before any weight measurement ensuring that minimal weighing errors are caused by any unwanted contamination. For example, the flat test coupons are attached on the coupon windows, and a thin film of liquid lubricant with the paper gasket is used in between them to prevent the slurry leakage during TWT experiments. These lubricants contaminate the un-eroded surface of the test coupons and need to be removed completely before weight measurement after the experiment. Previous studies [8, 11, 13, 15, 28] have reported test coupon cleaning before the weight measurement by rinsing with tap water, with acetone, and drying with a hot air blower or compressed air. In this study, a more comprehensive cleaning methodology was maintained (see Figure 3.10) before and after each material loss experiment so that the gravimetric measurement could accurately represent the material loss due to erosion. The steps for cleaning the test coupons are listed below:

1. Wash the test coupons using tap water to get rid of loose dirt, especially after the wear experiment when the coupon surface is covered with wet sand particles.

2. Make a cleaning solution bath using Versa-Clean ^{TM} and water (mixture ratio 1:10) and immerse the test coupons inside the solution for 30 minutes.

3. After 30 minutes, scrub the test coupon surfaces gently and rinse in tap water to get rid of the dirt and lubricants.

4. Sonicate the test coupons in an ultrasonic De-Ionized (DI) water bath for 5 minutes to wash away the fine particles still adhering to the coupon surfaces.

5. Move the coupons quickly to a fume hood and rinse the coupon surfaces using acetone. Acetone is miscible with water and therefore helps to drive away the water molecules adhered to the coupon surfaces. Leave the coupons in the fume hood for 5 minutes to allow evaporation of acetone.

6. Rinse the coupon surfaces with toluene to get rid of any remaining organic contaminations. Leave the test coupons in the fume hood for 30 minutes to allow evaporation of toluene.

7. Finally, heat the test coupons with a hot air blower for 1-2 minutes to make sure all the toluene is completely evaporated, and then measure the weight.

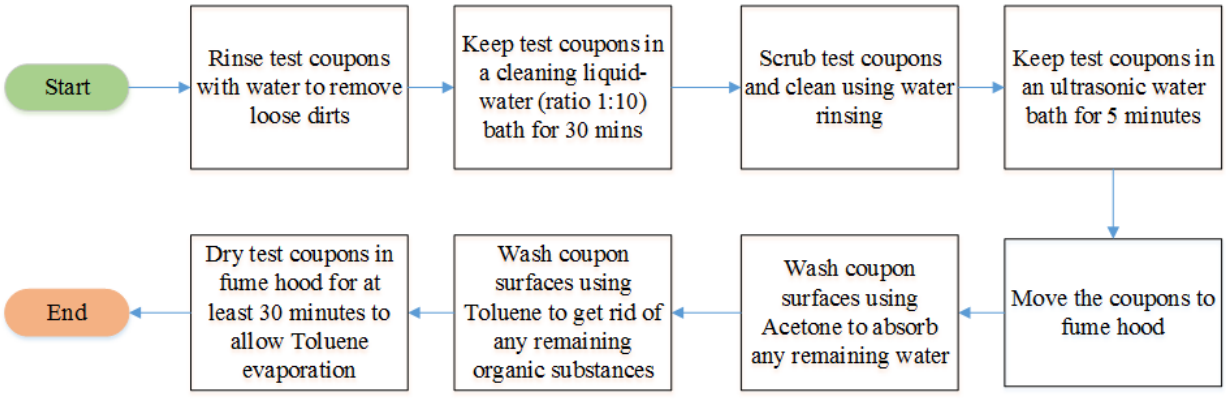

Figure 3.10. Flow chart for test coupon cleaning procedure before and after a wear test

3.5.3 Coupon Weighing

As discussed in Chapter 2, the gravimetric measurement of the TWT test coupons before and after each experiment is one of the simplest yet best methods of material loss measurement. An electronic weighing scale (Brand: A&D Corporation Ltd., Model: FX-3000i) having a resolution of 0.01mg was used in this study to measure the test coupons masses. The measurement procedure of the test coupons is given below:

1. Start the electronic balance, set the sensitivity to medium and tare it to zero. Weigh a 500g standard calibration specimen on the electronic balance, and calibrate the instrument before starting the test coupon weight measurement. The 500g standard calibration specimen was chosen because this is the approximate weight for each of the carbon steel test coupons.
2. Place each test coupon on the weighing scale and record the weight from the display when the data are stable. Measure the weight of each test coupon three times to reduce the uncertainty associated with measurement and data logging.
3. Finally, weigh the 500g standard calibration specimen again to validate the consistency of the measured weight data.

3.5.4 Slurry Charging and N_2 Purging

After recording the initial mass of the test coupons, they are attached to the coupon windows of the TWT. Then the slurry (sand-water mixture) is charged to fill one-third of the volume of a toroid wheel and that wheel is purged with N_2 to eliminate corrosion inside the wheel. The steps for slurry charging and N_2 purging inside the TWT are as follows:

1. Attach four (out of five) test coupons on the coupon windows of the TWT in the following manner:

    - For Wheel A and C: Attach test coupon 1, 3, 2 and 5
    - For Wheel B and D: Attach test coupon 1, 2, 4 and 5

    The attachment of the test coupons is such that the N_2 charging port of each toroid wheel remains at the bottom of the wheel when the open coupon windows (A4, B3, C4 and D3) for each wheel stays on top for the slurry charging.

2. Fill Wheel A and C with the required amount of water through the open coupon window (In this case, window A4 and C4 for Wheel A and Wheel C, respectively). Then, add the calculated amount of sand particles in Wheel A and C through the open coupon window.

3. Insert the Dissolved Oxygen (DO) meter probe inside Wheel A through the open coupon window to measure the initial DO level in the slurry.

4. Open the N_2 charging port for Wheel A, keeping the DO meter probe submerged in the slurry through the open coupon window. Purge N_2 inside the slurry of Wheel A, keeping the discharge pressure of the N_2 cylinder at 5.0 psig. Keep taking DO meter readings continuously during this purging process in order to quantify the amount of oxygen left inside the slurry. The schematic of the N_2 purging is shown in Figure 3.11.

5. When the dissolved oxygen level in the slurry comes down to 1.0 PPM, stop the purging and close the open coupon window using test coupon A4. Normally, it takes about five minutes of N_2 purging for the slurry to get down to a dissolved oxygen level of 1.0.

6. Open the air release port for Wheel A and purge N_2 for another 2-3 minutes to ensure that

the dissolved oxygen level in the slurry is well below 1.0 PPM. The second stage of N_2 purging also drives out any remaining air present in the slurry-unoccupied volume of the wheel. Close the air release port after the N_2 purging.

7. Repeat steps 3-6 to purge N_2 inside Wheel C.
8. Repeat steps 2-7 to add water, and sand inside Wheel B and D, and also to purge N_2 in those wheels as well.
9. Finally, close the N_2 cylinder after finishing the purging, and also close the N_2 charging ports for wheels A, B, C and D.

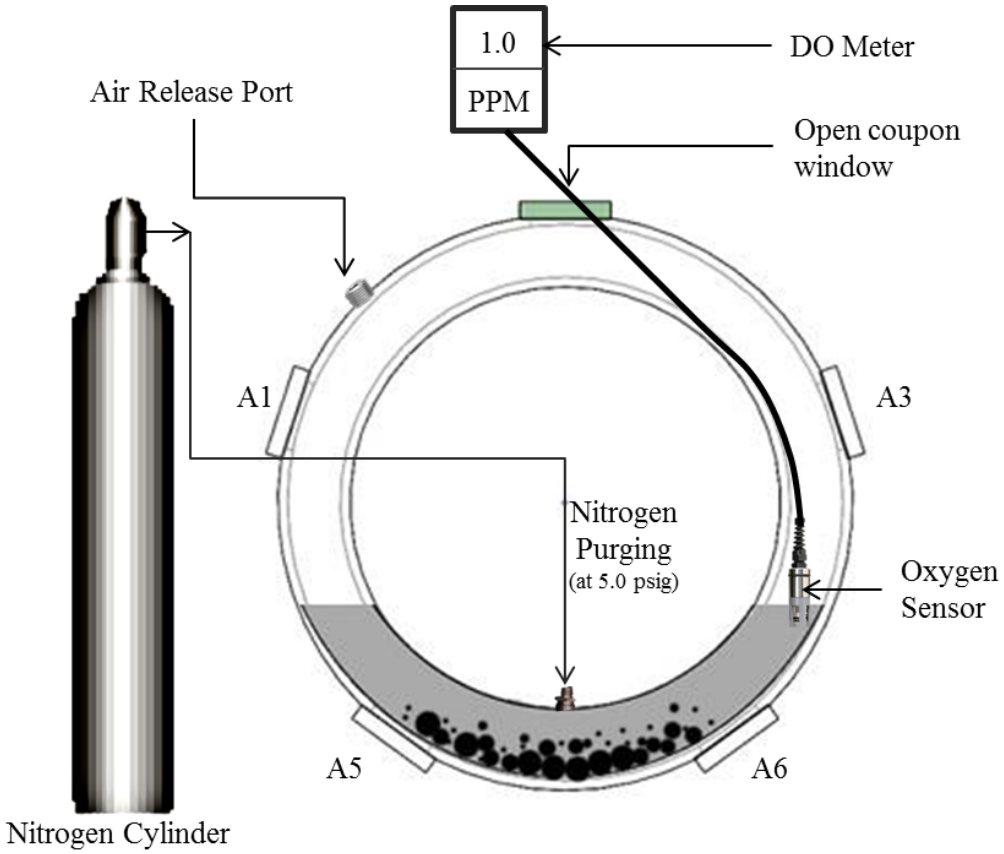

Figure 3.11. Schematic of N_2 purging in the TWT (Wheel A) at 5.0 psig and measuring the *DO* level inside the slurry using DO meter

3.5.5 Starting and Stopping Sequence of the TWT

Starting sequence:

1. Before switching on the power supply, cover the entire TWT set up with a safety cage, to avoid accidents during operation and maintenance of the TWT.
2. Start the main power supply for the VFD and enable remote control of the drive using an on-board toggle switch. The remote control mechanism of the drive is capable of setting operating parameters, data logging, and monitoring the drive performance during experiment.
3. Start the TWT control software, VFDWearWheel_Main. Make sure that the VFD is operating without showing any fault code, in the control software. Start the data logging to record the wheel speed, output voltage and current of the VFD during experiment. Enable the speed variation alert system for the VFD.
4. Set the VFD frequency (Hz) from the software. Confirm the drive frequency and press the 'Start' button in the software to start the TWT experiment.

Stopping sequence:

1. Switch off the speed variation alert system and data logging from the control software.
2. Click on the 'Stop' button to turn off the TWT rotation. Then, shut down the main power for VFD. Then, move the safety cage that is covering the TWT.
3. Open test coupons from all the wheels, rinse them with water and store in the cleaning solution before proceeding to next steps of cleaning described in section 3.4.2. Take

slurry samples from each toroid wheels for rheometry measurements and drain the remaining slurry.

4. Finally wash, clean, and dry all toroid wheels for future experiments.

3.6 Flow Observation using an Acrylic Toroid Wheel (ATW)

For qualitative flow observation, the acrylic toroid wheel (ATW) was attached to the TWT. Qualitative flow observation studies were made using the ATW to determine the limiting operating conditions for the TWT (the slurry carry-over velocity), the presence of sliding bed of particles, and the actual particle-coupon contact time during wear tests. The procedure for the flow observation experiments in the ATW is as follows:

1. Before installing the ATW, make sure the TWT set up is in 'STOP' mode and the main power source for the VFD control is turned off for safety.
2. Install the ATW on the overhanging portion of the main shaft of the TWT with the help of a self-centering bushing and shaft key.
3. Open the circular charging ports of the ATW and charge calculated amount of water and sand to fill one-third volume of the ATW alike the TWT slurry charging, and then seal the charging ports.
4. Turn on the main power for VFD and follow the starting sequence procedures described in section 3.4.5 to start the ATW.
5. Run the ATW at the desired RPM for 1-2 minutes to allow the sand particles to mix with the water, and produce a steady flow situation before observing the flow pattern.

3.7 Data Analysis

In this experiment, the amount of erosion damage was measured in terms of the mass loss of the test coupons. Industrial reports and the literature usually represent erosion damage in terms of thickness of material lost per unit time. To convert the mass loss measurement data to thickness lost, the mass loss data were divided by the density and the eroded area of the test coupons. Then, the thickness lost values (in mm) were divided by the experiment duration (in years) to get the wear rate (mm/year). The steps are shown in the following flow chart:

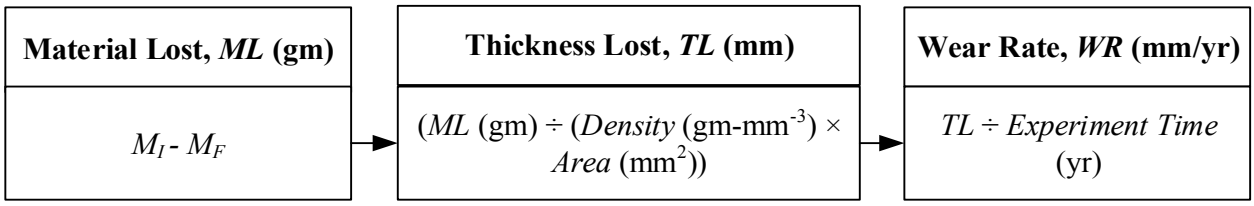

Figure 3.12. Conversion of mass loss to thickness lost per unit time

3.7.1 Sample calculation

A sample of the wear rate calculation is presented in this section. For this sample calculation, mass loss data from a 2.0 mm gravel experiment has been taken. For this particular experiment, Wheel A was partially filled by 2.0mm gravel slurry having 20% (by volume) solids concentration, and ran for 4 days (96 hours) with a slurry replacement interval of 24 hours. Wear rate was calculated from the material loss found from two test coupons, A2 and A4 after the experiment. Details of the sample calculation are as follows:

Time:

Total run time of the experiment, t_{TR} = 96 hours

Total down time of the TWT, t_{DT} = 3 hours

Here, down time indicates the time waste during the slurry replacement.

Total effective run time of the TWT, t_{ERT} = (96-3) hours

= 93 hours

= 1.062×10^{-2} years

Initial Mass (at $t = 0$ hours)**:**

Calibration specimen weight before the TWT experiment, $M_{c,t=o} = 501.29\text{g}$

Initial mass of test coupon A2, $M_{I,A2} = 490.38\text{g}$

Initial mass of test coupon A4, $M_{I,A4} = 493.05\text{g}$

Final Mass (at $t = 93$ hours)**:**

Calibration specimen weight after the TWT experiment, $M_{c,t=93hours} = 501.29\text{g}$

Initial mass of test coupon A2, $M_{F,A2} = 489.71\text{g}$

Initial mass of test coupon A4, $M_{F,A2} = 492.38\text{g}$

Material Lost:

Material lost from test coupon A2, $M_{L,A2}$ = $M_{I,A2} - M_{F,A2} + (M_{c,t=93hours} - M_{c,t=0})$

= $490.38\text{g} - 489.71\text{g} + (501.29\text{g} - 501.29\text{g})$

= 0.67g

Material lost from test coupon A2, $M_{L,A4}$ = $M_{I,A4} - M_{F,A4} + (M_{c,t=93hours} - M_{c,t=0})$

$= \quad 493.05\text{g} - 492.38 + (501.29\text{g} - 501.29\text{g})$

$= \quad 0.67\text{g}$

Conversion to Thickness Lost:

Density of the carbon steel test coupons, ρ $= \quad 0.0078$ g-mm^{-3}

Surface area of the test coupons, A_S $= \quad 4225$ mm^2

Thickness lost from test coupon A2, $T_{L,A2}$ $= \quad \frac{M_{L,A2}}{\rho A_S} = \frac{0.67}{0.0078 \times 4225}$ mm

$= \quad 0.02033$ mm

Thickness lost from test coupon A2, $T_{L,A4}$ $= \quad \frac{M_{L,A4}}{\rho A_S}$

$= \quad \frac{0.67}{0.0078 \times 4225}$ mm

$= \quad 0.02033$ mm

Average thickness lost, $T_{L,avg}$ $= \quad \frac{T_{L,A2} + T_{L,A4}}{2}$

$= \quad \frac{0.02033 + 0.02033}{2}$

$= \quad 0.02033$ mm

Wear Rate:

Wear rate for the carbon steel test coupons (For operating condition: *DO*: <1.0 PPM, d_{50}:2.0 mm, C_S : 20%) $= \quad \frac{T_{L,avg}}{t_{ERT}}$

$= \quad \frac{0.02033}{1.062 \times 10^{-2}}$ mm/year

$= \quad 1.92$ mm/year

3.8 Experimental Program

3.8.1 Qualitative Flow Pattern Study

To determine the optimum slurry volume for each wheel of the TWT, a different volume fraction of the ATW was filled with the slurry and then the ATW was rotated at different speeds. Based on the preliminary observations, one-third volume of the ATW or TWT has been chosen as the optimum slurry volume for material loss experiments. Particles with a d_{50} of 0.250 mm and 2.0 mm were used at different volumetric solids concentrations to prepare the slurries that were used in the ATW experiments at different wheel speeds. Table 3.5 shows the experimental matrix for the ATW flow observation experiments.

Table 3.6. Experimental Matrix for Flow Pattern Study in ATW

Wheel RPM	**Particle Type**	d_{50} **mm**	ρ_s **kg/m^3**	C_s **%**	μ_f **mPa-s**
30 to 90	SIL 1	0.250	2650	5	1.0
				30	
10 to 90	Monosized Pyrex beads	0.250	2650	20	1.0
10 to 90	SRC Gravel	2.0	2650	5	1.0
				10	
				20	

3.8.2 Corrosion control Test

Corrosion is the degradation of material by an electrochemical reaction with its environment, and its synergistic interaction with erosion leads to accelerated material damage [9, 46]. In order to model abrasive wear in industrial slurry pipelines, the effects of erosion, corrosion, and their synergy have to be studied independently and in a controlled way. The focus of this TWT study is the erosion-only sliding bed wear mechanism and therefore, to attain a purely erosive wear experimental condition, it is necessary to remove the dissolved oxygen present in the slurry and in the TWT environment. This was accomplished by N_2 purging as mentioned earlier in this chapter. Measurement of the dissolved oxygen inside the slurries showed that N_2 purging through slurry not only reduces the dissolved oxygen level inside the carrier fluid, but also drives out the remaining two-third volume of air inside the toroid wheels. As a consequence, the effect of corrosion in the TWT is minimized. U.S. Silica slurries were tested in different toroid wheels with and without N_2 purging and the effect of N_2 purging has been quantified. Similar experiments were also conducted with 2.0 mm gravel particles. In both cases, the measured dissolved oxygen level in the slurry was approximately 5.4 PPM before N_2 purging, and after three minutes of N_2 purging, the measured dissolved oxygen level was less than 1.0 PPM. The experimental matrix to understand the effect of dissolved oxygen on test coupon wear is presented in Table 3.7. The terms t_{SRI} and t_{TRT} in Table 3.7 indicates the slurry replacement interval and total run time, respectively. In a separate experiment, one-third of the volume of a toroid wheel has been filled only with water (without any particle) and tested without any N_2 purging. This experiment illustrates and quantifies the severity of corrosion damage on the test coupons in the presence of dissolved oxygen in the slurry. All of these corrosion control experimental results are discussed in Chapter 5.

Table 3.7. Experiment matrix for corrosion control test

Wheel RPM	d_{50} mm	DO PPM	C_s %	t_{SRI} hours	t_{TRT} hours
60	0.250 (US Silica)	5.4	20	24	93
		<1.0		48	
	2.0 (Gravel)	5.5		24	
		<1.0			
	None (Water only)	5.4	0	96	93

3.8.3 Parametric Study in TWT

The study of erosive wear in the TWT is relatively new and very limited data are available in the literature to understand the erosive wear mechanism in the TWT. In order to study erosion damage in industrial slurry pipelines using the TWT, the wear mechanism in the TWT should be characterized. To characterize the wear mechanism, the wear trends found using the TWT are compared with the wear trends reported in previous wear studies using different wear testers i.e. the jet impingement tester, the slurry pot tester, the recirculating pipe loop tester. As discussed in Chapter 2, erosive wear has been reported as a strong function of bulk velocity of the carrier fluid, particle size, shape and concentration in numerous research studies. Some general trends and wear models based on these properties have been reported as well. Therefore, to commission the TWT installed in the PTP group facility and also to analyze the wear performance of the TWT, some parametric studies were completed. Particles with three different d_{50} sizes i.e. 2 mm, 0.425 mm, and 0.250 mm were used at different volumetric solids concentrations during these parametric studies. Most of the experiments were conducted by

keeping the *DO* level below 1.0 PPM to ensure a purely erosion damage on the test coupons. However, in some experiments the *DO* level was kept at 5.4 PPM to analyze the extent of erosion-corrosion wear on the test coupons. Three different wheels speeds of the TWT, namely, 30, 45 and 60 RPM having equivalent linear velocities of 1.0, 1.4 and 1.9 m/s, respectively, were selected based on the preliminary observation in the ATW. Table 3.8 shows the detailed experimental matrix for the parametric study. Mainly, the particle solids concentration of the slurry, the TWT wheel speed, and the particle size and shape parameters were varied during these studies. Analysis and comparison of these experimental results have been presented in Chapter 4.

Table 3.8. Experimental matrix for the TWT parametric study

Wheel RPM	d_{50} **mm**	***DO*** **PPM**	C_s **%**	t_{SRI} **hours**	t_{ERT} **hours**
30	2.0 (Gravel)	6	< 1.0	24	93
		12			
		20			
	0.250 (US Silica)	20	< 1.0	24	186
	0.250 (SIL 1)	20	< 1.0	24	186
45	2.0 (Gravel)	6	< 1.0	24	93
		12			
		20			

Table 3.8 (continued). Experimental matrix for the TWT parametric study

Wheel RPM	d_{50} mm	DO PPM	C_s %	t_{SRI} hours	t_{ERT} hours
60	2.0 (Gravel)	6	<1.0	24	93
		12			
		20	<1.0		
			5.4		
	0.425 (Al_20_3)	20	<1.0		
	0.425 (SIL 4)	20	<1.0		
	0.250 (US Silica)	20	<1.0		
			5.4		
	0.250 (SIL 1)	20	<1.0		

3.8.4 Slurry Replacement Interval (SRI) Experiments

To compare wear rate results with actual pipeline wear data, the absolute wear rate (i.e. wear rate at zero particle degradation) is necessary. To calculate the wear rate at zero particle degradation, the slurry replacement interval (SRI) experiment is essential, which was discussed earlier in Section 2.6.2. SRI experiments were completed for 2 mm gravel, 0.425 mm Al_20_3, 0.425 mm SIL 4 and 0.250 mm U.S. Silica sand particles following the Cooke *et al.* [5] methodology discussed in Chapter 2. Experiments were conducted for about 93 hours in total, changing the slurry at different intervals ranging from 8 hours to 93 hours. The results of each SRI experiment were plotted and then extrapolated by an exponential curve fit to determine the

zero particle degradation wear rate. Chapter 5 contains the detailed results and analyses of the SRI experiments. The experimental matrix for the SRI experiments is given in Table 3.9.

Table 3.9. Experimental matrix for SRI experiments

Wheel RPM	d_{50} **mm**	***DO*** **PPM**	C_s **%**	t_{SRI} **hours**	t_{ERT} **hours**
60	2.0 (Gravel)	20	5.4	8, 12, 24, 48, 96	96
	0.425 (Al_20_3)	20	<1.0	12, 24, 48, 96	
	0.425 (SIL 4)	20	<1.0	12, 24, 48, 96	
	0.25(US Silica)	20	5.4	8, 12, 24, 48, 96	
			<1.0	12, 24, 48, 96	

Chapter 4
Evaluation of the Experimental Setup

4.1 Objective

The performance of the TWT experimental setup is evaluated in this chapter. The evaluation is done not only to verify the data repeatability of the wear tester but also to ensure that errors in the coupon cleaning and weighing procedures do not significantly influence the wear results obtained from the study. In particular, the following parameters are investigated is this chapter:

- Commissioning test of the TWT
- Data repeatability
- Uncertainty analysis

The performance analysis of the TWT is discussed in Section 4.2, which shows the level of confidence in the TWT system reliability and the level of uncertainty on material loss measurements.

4.2 Toroid Wear Tester (TWT) Performance Analysis

4.2.1 Commissioning Tests

After installation of the TWT, the VFD control system was checked thoroughly. Both the manual VFD control and the remote VFD control using the 'VFD Wear Wheel Main' (VWWM) software were checked to ensure smooth operation of the TWT. The RPM of the toroid wheels

Figure 4.1. (a) Rotameter Figure 4.1. (b) Infrared Thermometer

Figure 4.1. Devices used for measuring the TWT RPM and temperature during commissioning tests

and the increase in temperature in the motor drive and bearings during the experiment were selected as two important indicators of the consistency and integrity of the TWT operating system. The VWWM software, which enables operation of the TWT using a computer, directly calculates the RPM from the VFD frequency and displays the RPM during TWT operation. It shows that a constant frequency, and therefore, wheel RPM is maintained during each TWT experiment. The RPM of the TWT was also measured using a rotameter (Brand: Fisher Scientific, see Figure 4.1. (a)) for 116 hours of TWT operation while the wheel speed was set at 60 RPM. Figure 4.2 shows the measured RPM values against time and indicates that a constant RPM is maintained. The small fluctuations in the measured RPM are mainly due to the accuracy of the rotameter, which is 0.04% ±2 digits.

During TWT operation, the motor and bearing temperatures increase. The increase in temperature in the motor and bearings was measured during 116 hours of TWT operation using an infrared thermometer (Brand: Omega, see Figure 4.1. (b)) while the room temperature was

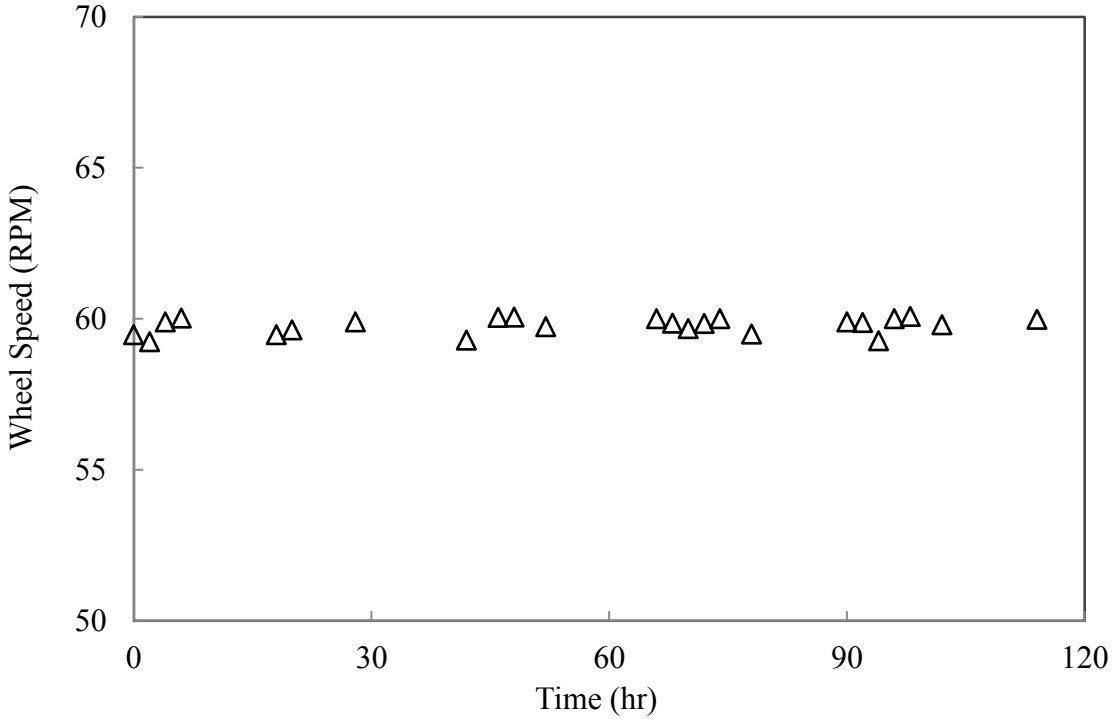

Figure 4.2. TWT speed measured using rotameter; Set parameter, *N* = 60 RPM; Test duration = 116 hrs

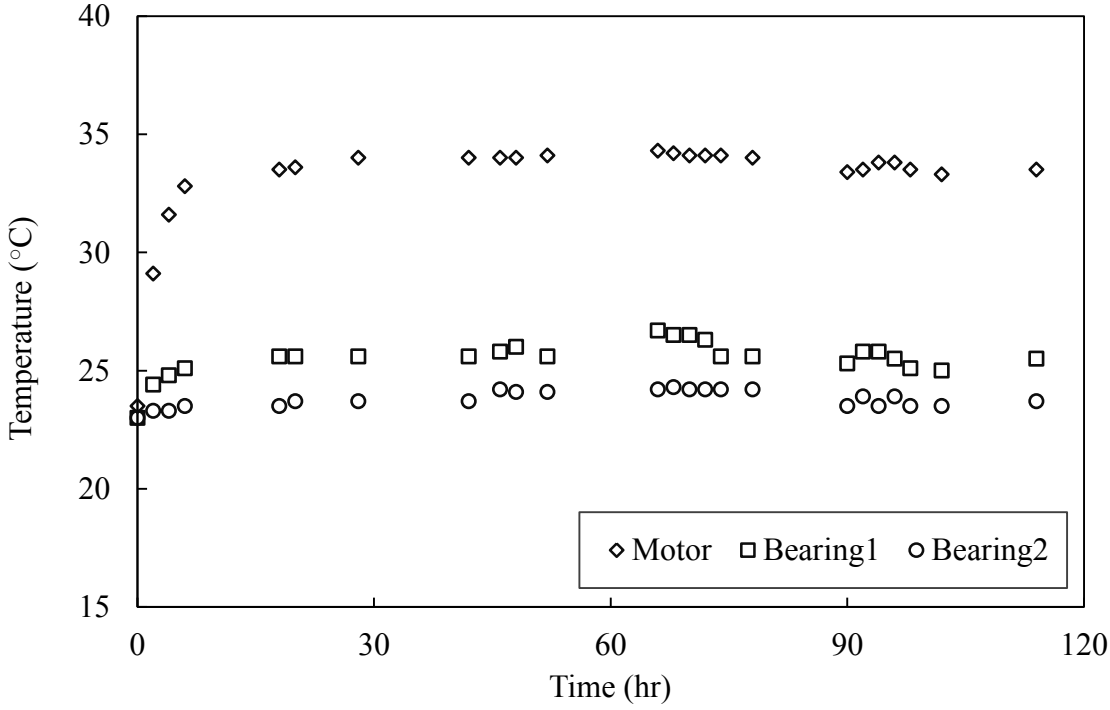

Figure 4.3. Temperature profiles of the motor and bearings of the TWT setup; Room temperature: 23 °C; Test duration = 116 hrs

maintained at 23 °C. The temperature profiles shown in Figure 4.3 indicate that the motor temperature increases by 11 °C within the first 10 hours of operation and becomes steady at about 34 °C. On the other hand, the bearing temperatures increase only by 1 °C to 3 °C within this time period. The final temperatures in the motor and bearings are within the safe working limit and it can, therefore, be concluded that the TWT system can operate at a constant wheel speed without any interruption due to overheating of the motor or the bearing components.

As a part of the commissioning tests, a hydrostatic test was also performed on each toroid wheel, mainly to check for leakage and to check the performance of the motor under the extra load. The four wheels were completely filled with water and were then examined for leaks. The test pressure was kept at the atmospheric pressure, as in the actual operating pressure during wear tests. The TWT was also rotated at different wheel speeds ranging from 10-90 RPM during the hydrostatic test. No leakage or faults were observed during the operation.

4.2.2 Data Repeatability of Material Loss Experiments

Performance analysis of the TWT must be based on an evaluation of the material losses in each toroid wheel at different locations within each toroid wheel, and also by checking whether the TWT setup can produce similar wear results for two or more sets of experiments. Material loss experiments were conducted to evaluate the wear performance of the TWT considering both situations described above. Also, an uncertainty analysis of the gravimetric (weight) measurement was done to identify if the errors associated with the weight measurement device are negligible or not. That uncertainty analysis is also presented in this section.

Data Repeatability of the Test Coupons

To examine the data repeatability of the test coupons, five carbon steel test coupons with similar roughness and material properties were attached to each of the toroid wheels and rotated at 60 RPM for 350 hours with a slurry replacement interval (SRI) of 116 hours. All five coupons attached to each wheel were marked as 1 to 5 with the name of wheel preceding the number, i.e. for wheel A test coupons, the markings were A1, A2, A3, A4, and A5. To check the consistency of the material loss at five different locations on the wheel, the weight loss results of the five test coupons on each toroid wheel were measured during each slurry replacement. The test matrix is given in Table 4.1. Figure 4.4 presents the trend of material loss (Δm) for each test coupon against the operation duration for wheel A, B, C, and D. These graphs show that the rate of material loss in each wheel remains almost constant as the experiment time progresses. It is evident from Figure 4.4 that all the five coupons on each wheel at a similar rate. The maximum difference between material losses of the coupons was found to be approximately 4.5% of the average mass loss after 350 hours of experiment. The relatively small variations in the result may be due to the association of uncontrolled corrosion with the erosion as the experiment was conducted with slurries having a dissolved oxygen level of about 5.4 PPM.

Table 4.1. Experiment Matrix for data repeatability of test coupons

Wheel #	**Wheel Speed, N (RPM)**	**Particle Size, d_{50} (mm)**	**Solids volume concentration, C_s (%)**	**Dissolved Oxygen, DO (PPM)**
A	60	0.250 (SIL 1 sand)	30	5.4
B				
C				
D				

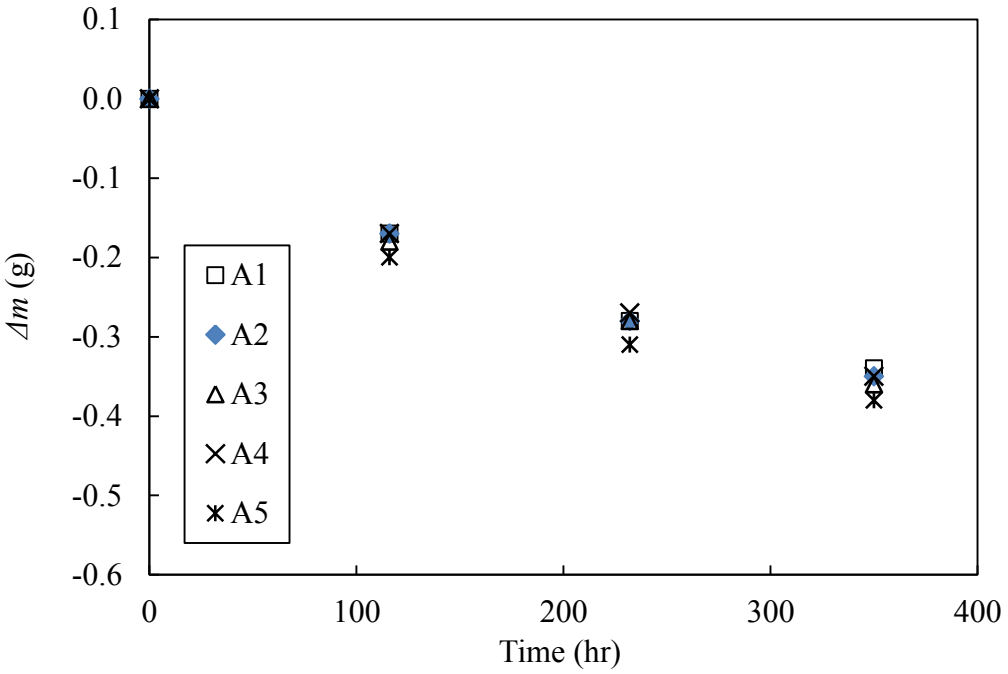

(a) Toroid Wheel A; Flow Channel Area: 65 × 60 mm^2

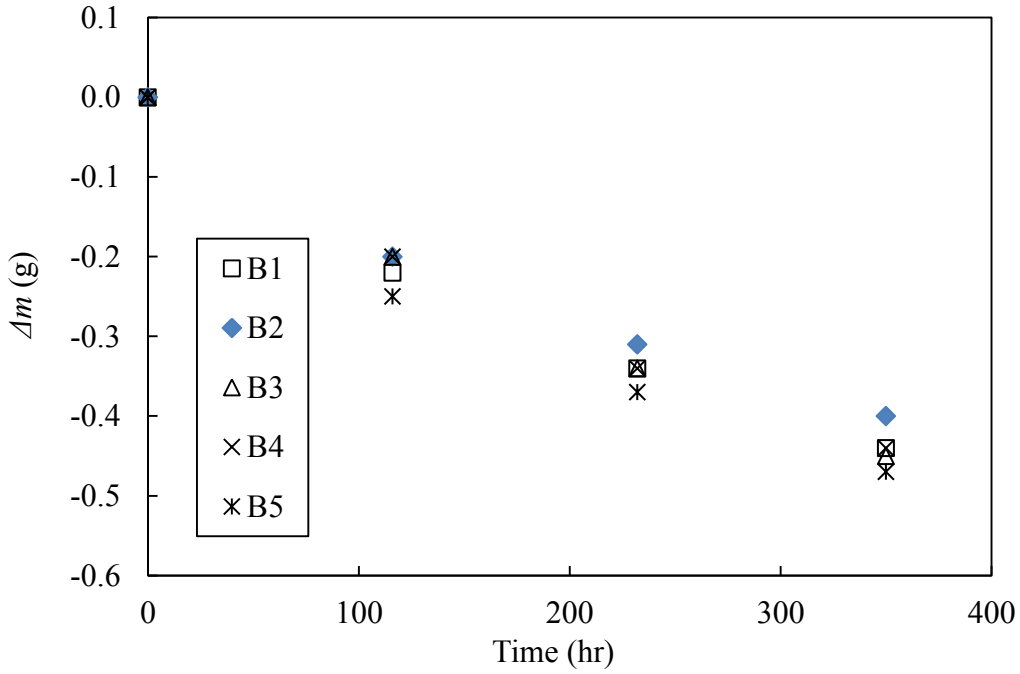

(b) Toroid Wheel B; Flow Channel Area: 65 × 60 mm^2

Figure 4.4. Data repeatability for each coupon on the TWT wheels (Wheel A and B)
***N*=60 RPM; C_s = 30%; SRI = 116 hours; *DO* = 5.4 PPM**

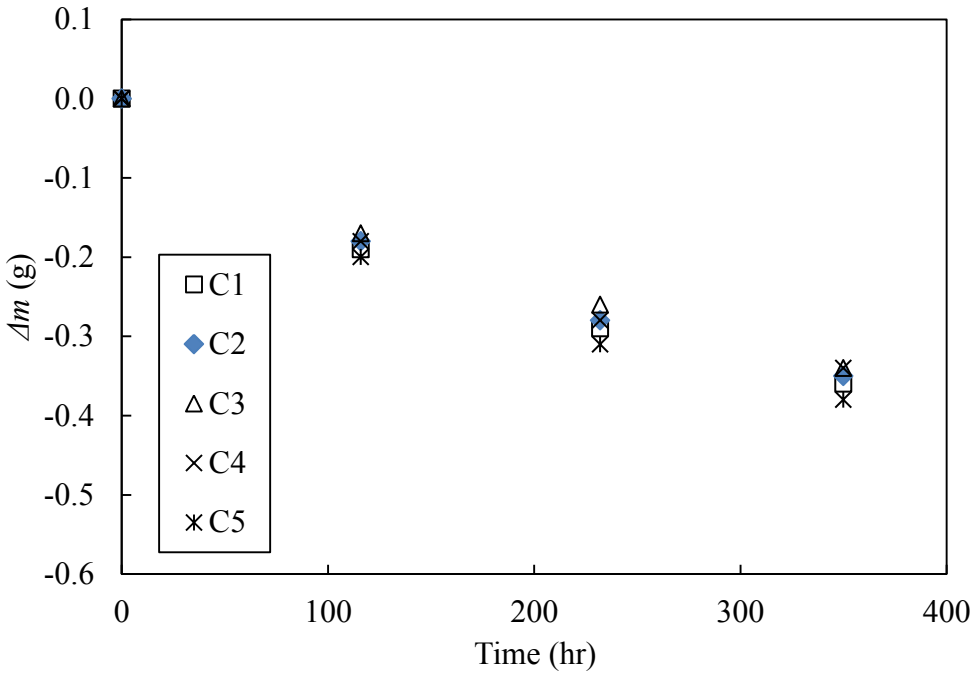

(c) Toroid Wheel C; Flow Channel Area: 65 × 60 mm^2

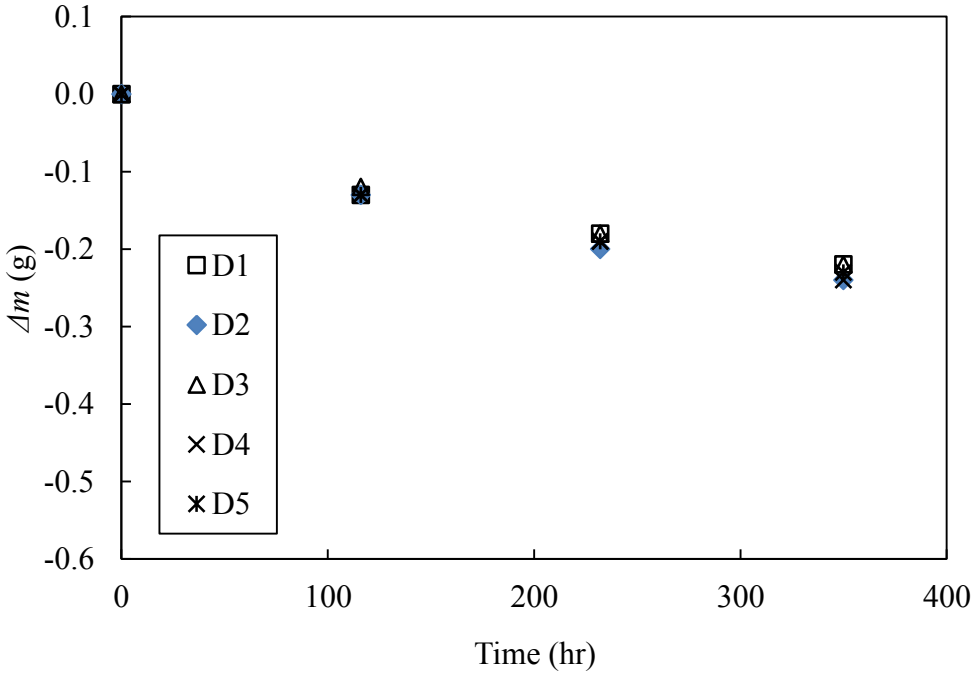

(d) Toroid Wheel D; Flow Channel Area: 58 × 60 mm^2

Figure 4.4. [Continued] Data repeatability for each coupon on the TWT wheels (Wheel C and D)
***N*=60 RPM; C_s = 30%; SRI = 116 hours; *DO* = 5.4 PPM**

Data Repeatability of the TWT

To evaluate the data repeatability of the TWT, two sets of experiments were conducted, keeping the same operating conditions (i.e. particle size, particle volume concentrations, dissolved oxygen level in the slurry and wheel speed). Table 4.2 shows the operating conditions for the two experiments, 'Run#1' and 'Run#2', in detail. In each of the toroid wheels mentioned in Table 4.2, two test coupons were used and the average material loss of those two coupons was converted into wear rate (mm/year) to check repeatability from the two different runs. Figure 4.5 shows the reproducibility of wear data from two different runs for four different slurries: US Silica (0.250 mm), Al_2O_3 (0.425 mm), SIL 4 (0.425 mm), and gravel (2.0 mm). The differences in the wear rates found from these two runs are approximately 5.8%, 9.3%, 10% and 3% of the average material losses for US Silica, SIL 4, Al_2O_3 and gravel particles, respectively. The uncertainty of the balancing scale, which has a precision of 0.01g, does not contribute much to

Table 4.2. Experiment matrix for data repeatability of TWT (for Run#1 and Run#2)

Wheel #	**Wheel Speed (RPM)**	**Particle Size d_{50} (mm)**	**Solids volume concentration, C_s (%)**	**Dissolved Oxygen, *DO* (PPM)**	**Slurry Replacement Interval (hrs)**	**Total Operating Time (hrs)**
A	60	0.425 (Al_2O_3)	20	< 1.0	24	96
B		2.0 (Gravels)				
C		0.425 (SIL 4)				
C		0.250 (US Silica)				

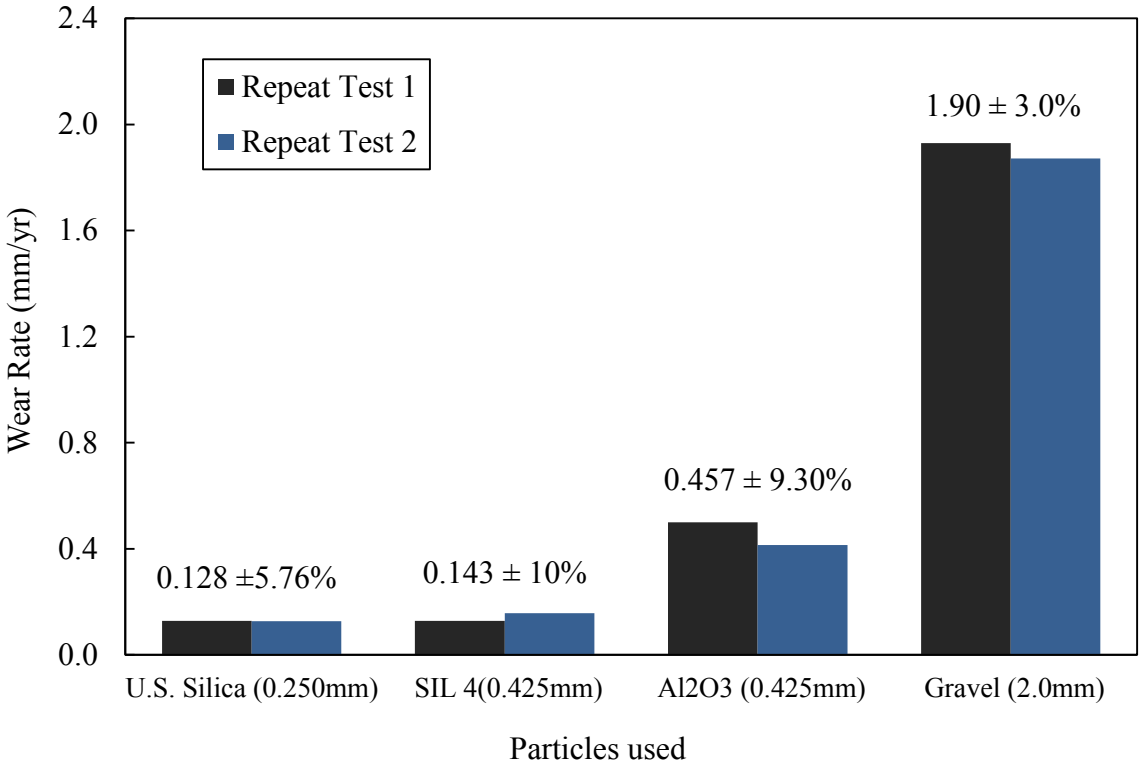

Figure 4.5. Data repeatability from two set of experiments in the TWT for N = 60 RPM; C_s = 20%; SRI = 24 hrs; DO < 1.0 PPM

this error margin, however, the wear rates obtained for smaller particles are significantly less than those obtained using larger gravel particles, and therefore, the measurement uncertainty affects those wear rates more strongly. Figure 4.5 also indicates that the error margin is lower for the 0.250 mm and 2.0 mm particles relative to the 0.425 mm particles. Qualitative flow visualization study inside the TWT indicated that at 60 RPM, the 0.250 mm particles remain completely suspended inside the slurry while the 2.0 mm gravel forms a steady sliding bed of particles at the bottom of the channel. At these two operating conditions, the test coupons experience a consistent wear mechanism, either by the suspended particles or by the sliding bed of gravels, as they pass through the slurry inside the TWT. As a consequence, the deviation between the two sets of repeatability experiments is relatively lower for 0.250 mm U.S. Silica

and 2.0 mm gravel. Qualitative visualization of the 0.425 mm particle slurries suggested a more complex wear mechanism having a mixture of suspended and sliding bed of particles within the TWT, which may have caused higher deviations in the material loss and needs more attention in future studies.

Uncertainty analysis

Uncertainty analysis of the wear rate calculations was performed using a consecutive error propagation method [47] and details of the uncertainty analysis are shown in Appendix E. First, the uncertainties due to the calibration standard and resolution of the instruments, i.e. electronic scale for weighing coupon mass, rotameter for measuring wheel RPM and Vernier caliper for coupon window size measurement, were calculated. Then the propagation of these uncertainties due to mathematical operations performed during the wear rate calculation was determined. Moreover, the effect of uncertainties in velocity and solids concentration on erosive wear rate were determined using a wear model from literature. The uncertainties from the repeatable wear rate experiments using different particles (described earlier in this Chapter) were also calculated. Finally, the combined overall uncertainties of the wear rate were calculated for different particles.

There are two possible sources of uncertainty in the gravimetric measurement of test coupons: the resolution of the electronic scale and the repeatability of the measurements. To determine the uncertainty, the weight of two test coupon samples was measured 35 times, and the standard uncertainty due to the resolution of the electronic scale and repeatability of each measurement were calculated. The average weight of the test coupons was 493.54 g and 498.81 g, respectively. Finally, a combined standard uncertainty of ± 0.00309 g was calculated. Similarly,

the combined standard uncertainty of the rotameter was calculated (±0.0606 RPM) based on the resolution and repeatability tests. The standard uncertainty of coupon window size measurement, using the Vernier caliper, was ±0.00289 mm.

Uncertainties associated with the velocity and the solids concentration were calculated using the propagation of the measurement uncertainties. The calculated uncertainties of the wheel velocity and solids concentration (20 % by volume or 66.7 % by weight) were ±0.00264 m/s and ±0.0000038 % of weight fraction, respectively. The propagation of these uncertainties into wear rate was calculated for four different particles, i.e. US Silica (0.250 mm), SIL 4 (0.425 mm), Al_2O_3 (0.425 mm), and gravel (2.0 mm), using the wear model proposed by Gupta *et al.* [8]:

$$E = 0.223 V^{2.148} d_p^{0.344} C_w^{0.556} \qquad 4.5$$

Where, E indicates the erosion rate, V is the bulk flow velocity, d is the particle size and C_w is the solids concentration (by weight). This wear model was selected because it showed good agreement with the parametric experiments completed during this study, which will be discussed in detail in Chapter 5. The resulting uncertainties found for US Silica, SIL 4, Al_2O_3 and gravel are ±0.00269, ±0.001578, ±0.001578, and ±0.00132 mm/year, respectively.

Finally, the combined standard uncertainties were generated from the individual uncertainty components, i.e. the calculated uncertainty in mass loss measurement, error propagations from uncertainties of velocity and solids concentration measurements, and the calculated uncertainties from the repeatability experiments for different erodent materials. The combined standard uncertainties were divided by the average material loss (mm/yr) for obtaining

the relative overall uncertainty and then multiplied by 2, to ensure a 95% confidence interval. The final calculated relative uncertainties for erosive wear rate study using the TWT using U.S. Silica, SIL 4, Al_2O_3 and gravel are ± 9.23, ± 17.28, ± 11.22, and $\pm 3.95\%$, respectively, with a 95% confidence interval.

Chapter 5
Results and Analysis

5.1 Introduction

In Chapter 4, the commissioning and performance of the TWT were presented, which showed reasonable data reproducibility between different coupons on toroid wheels and between the different wheels of the TWT. This chapter mainly focuses on:

- Qualitative flow pattern analysis
- Corrosion control and parametric study
- Slurry Replacement Interval (SRI) results and analysis
- Strengths and limitations of the TWT
- Comparison of TWT results with existing pipe loop experiment results

The qualitative flow pattern analysis completed using the Acrylic Toroid Wheel (ATW) is presented in Section 5.2, which clearly identifies the necessity of the time correction factors to calculate the wear rate from the material loss data. It is important to determine purely erosion based wear using the TWT so that it can be compared with existing pipe loop results, and Section 5.3 presents test results for controlling corrosion in the TWT by N_2 purging. Wear rates obtained from a series of parametric studies to show the effects of particle diameter, shape and abrasivity and solids concentration are discussed in Section 5.4. Generally, the results of the parametric investigations showed good agreement with results taken from the literature. In the TWT, although the slurry is replaced on a regular interval, the particles degrade over time. It changes

the abrasivity of the slurry and needs to be taken into account to determine the absolute or zero particle degradation wear. Analysis of the zero particle degradation wear rates obtained from the TWT is discussed in Section 5.6. Section 5.7 presents the comparison of the TWT results with some pipe loop experimental results, and limitations of the TWT as a laboratory scale device to simulate an actual pipeline wear situation are discussed.

5.2 Qualitative Flow Pattern Analysis

The Acrylic Toroid Wheel (ATW), which is dimensionally similar to the actual TWT, was used to reproduce and qualitatively observe the exact flow situation inside the TWT. The dimensional details and experimental methodology of using the ATW were explained in Chapter 3. In this section, slurry carry-over, sliding bed physics and particle-coupon contact will be discussed based on qualitative observation of the flow within the ATW. Figure 5.1 illustrates the position terminologies and the direction of rotation considered during the qualitative flow pattern study using the ATW. In all studies reported here, the ATW rotated in the clockwise direction and the vertical 0° position at the bottom of the ATW has been defined as 'Position 0'. The rotating walls move from right to left against the slurry and therefore, the left hand side and right hand side of Position 0 are considered to be the downstream side and the upstream portions of the flow, respectively.

5.2.1 Slurry Carry-Over

The first phase of the flow observation study involved observations of the downstream side of the slurry inside the transparent ATW for slurry carry-over. It has been found that the rotating wall induces a near-wall slurry flow due to the inertial drag in the direction of rotation.

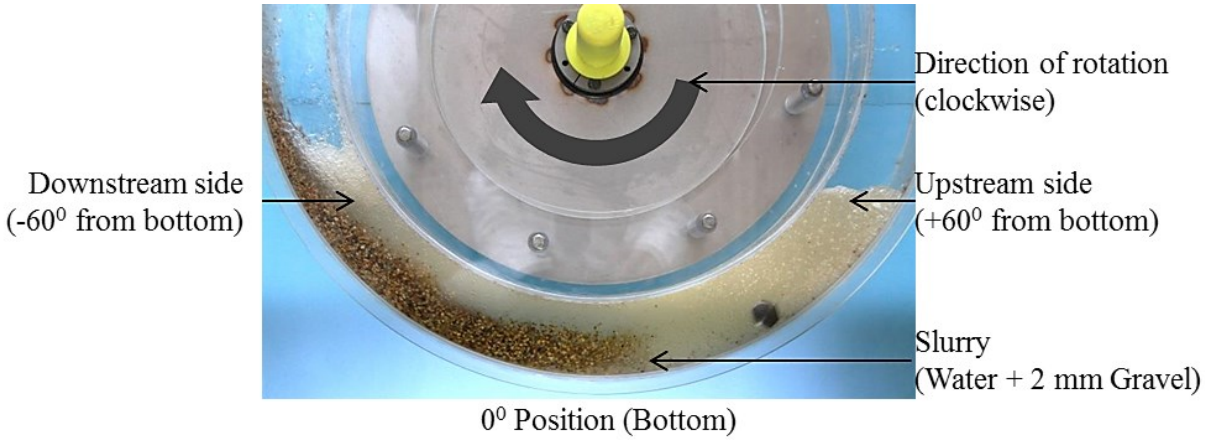

Figure 5.1. Position terminologies for the ATW

As the wheel speed increases, the elevation of the near-wall slurry at the downstream side also increases. At a critical wheel speed, the slurry elevation is so high that it carries all the way to the upstream side of the AWT. The velocity at which slurry carry-over occurs is taken as the maximum operating velocity of the TWT, as reported by Cooke *et al.* [5] and discussed in Chapter 2. Slurry carry-over situations were observed by rotating the ATW at different wheel speeds (ranging from 10 to 90 RPM) and using different particles and solids concentrations. Figure 5.2 shows some photographs of the slurry flow at different wheel speeds, taken during 250 μm SIL 1 sand slurry (30% by volume) experiments. The following observations have been made from these carry-over experiments:

- The test coupons are submerged in the slurry during one-third of each complete revolution. Therefore, the actual particle-coupon contact time is one-third of the entire experiment duration.
- As the wheel speed is increased, differences between the dynamic slurry levels on the downstream side and the upstream side increase, i.e. the slurry starts to be carried along with the outer circumferential wall at the downstream side because of higher inertial drag.

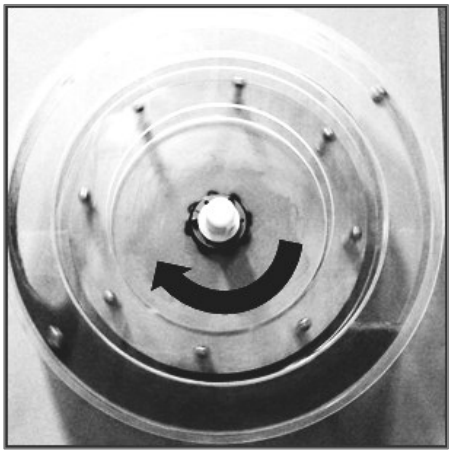

(a) 50 RPM (V = 1.6 m/s)

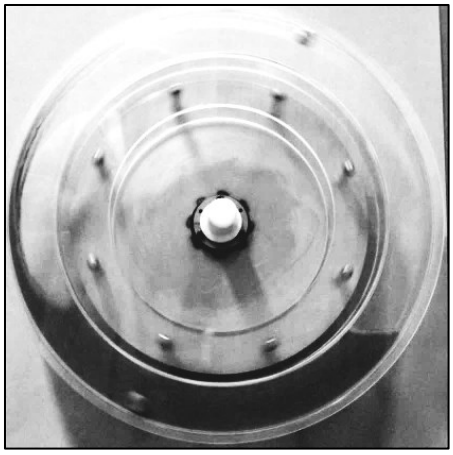

(b) 70 RPM (V = 2.2 m/s)

(c) 90 RPM (V = 2.9 m/s)

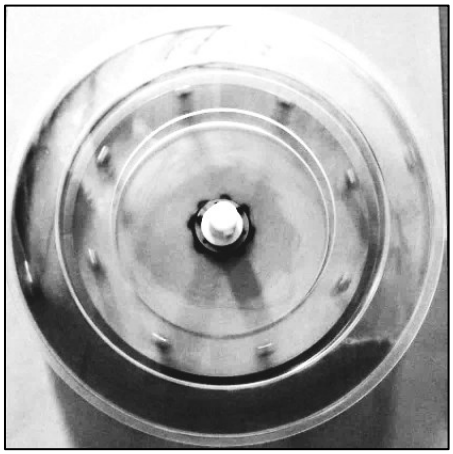

(d) 95 RPM (V = 3.0 m/s)

Figure 5.2. Slurry carry-over observation (in monochrome) study in ATW; d_{50} = 0.250 mm (SIL 1), C_s = 30%, N = 50–95 RPM

- When the wheel speed goes beyond 90 RPM (2.9 m/s), the drag of the SIL 1 sand slurry along the outer wall at the downstream side is such that it is carried with the wall all the way to the upstream side i.e. slurry carry-over is observed (Figure 5.2 (c)). Similar patterns were observed for all slurries irrespective of the particle size and solids volume concentration, and the carry-over wheel speed was found to be between 90 to 95 RPM (2.9-3.0 m/s). At wheel speeds higher than 90 to 95 RPM, the carry-over became continuous.

Based on these observations, 90 RPM (2.9 m/s) has been chosen as the upper velocity limit for the TWT operation (See Appendix F for photographs of other important test conditions). It is also evident from Figure 5.2 that slurries containing small particles, i.e. 250 μm SIL 1 sand, are opaque during the wheel rotation, even at only 5% (by volume) solids concentration. This opacity does not allow the visualization of flow conditions in the ATW.

5.2.2 Sliding Bed Observation

During the TWT rotation, smaller particles in the slurry (sand-water mixture) are suspended in the water and make the water opaque. It was assumed in Chapter 2 that the relatively stationary slurry at the bottom of the TWT forms a sliding bed while the wheel rotates, but because of the slurry opacity, it is impossible to determine if this relatively stationary slurry is heterogeneous (as speculated) or is behaving as a uniform sand-water mixture. Here, the term 'heterogenous' implies that the coarse particles will be likely to settle at the bottom forming a separate layer or bed of sliding particles, as discussed in Chapter 2. To overcome the opacity problem, monosized 250 μm Pyrex beads, both transparent and colored, were used instead of the opaque SIL 1 sand particles, which allowed better visibility in the ATW. Both types of particles were characterized using a scanning electron microscope (SEM), and the SEM images of these particles are presented in Figure 5.3. The mass median diameter (d_{50}) and density of these Pyrex beads are similar to SIL 1 sand particles, i.e. 0.250 mm and 2650 kg/m^3, respectively. Therefore, it is suggested that flow pattern observations using the Pyrex beads represent the SIL 1 slurry flow conditions quite accurately. Experiments similar to the slurry carry-over experiments have been conducted using the Pyrex beads and changing the wheel speed from 10 to 90 RPM.

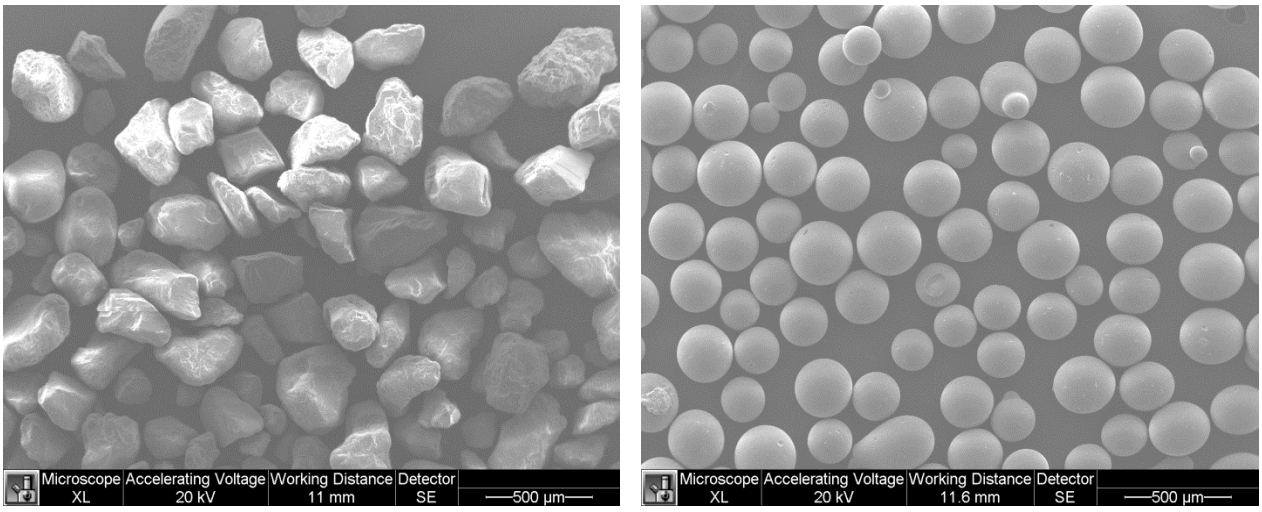

(a) (b)

Figure 5.3. SEM images of (a) SIL 1 sand particles and (b) glass beads; magnification: 100x

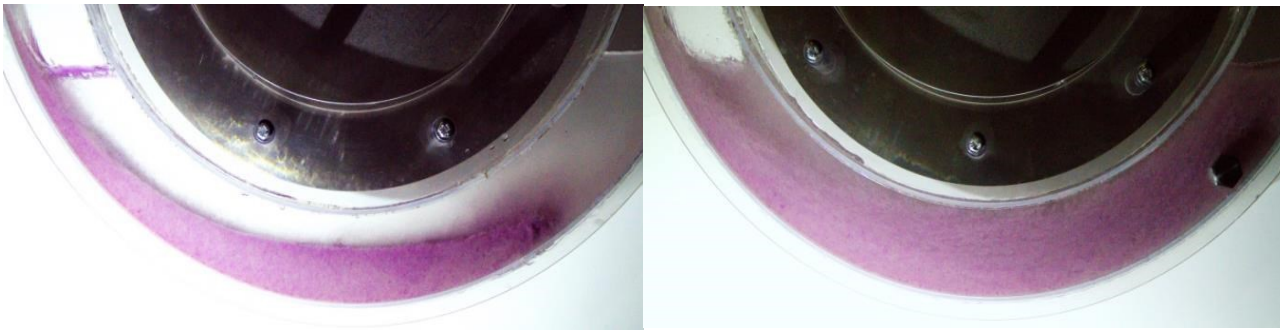

(a) 30 RPM (V = 1.0 m/s) (b) 60 RPM (V = 2.0 m/s)

Figure 5.4. Flow observation using colored glass beads in ATW; d_{50} = 0.250 mm (glass beads), C_s = 20%

Figure 5.4 shows the results obtained using Pyrex beads at two particular wheel speeds, 30 RPM (1.0 m/s) and 60 RPM (1.9 m/s), and the following observations were made:

- A sliding bed of particles was observed at low ATW speeds for the 0.250 mm Pyrex beads. A distinctive settled and slowly moving bed of particles were observed at wheel speeds lower than 30 RPM (Figure 5.4 (a)). The colored beads among the transparent ones worked as particle tracers, and indicated the tumbling action of the sliding bed of Pyrex beads.

- As the ATW speed is increased above 40 RPM (1.3 m/s), the flow regime appears to change from sliding bed to dispersed particle. At an ATW speed of 60 RPM (1.9 m/s), the 0.250 mm particles appear to become completely suspended (Figure 5.4 (b)) due to turbulence and the secondary flow within the carrier fluid, and an almost homogeneous slurry is formed.

- The lower velocity (<30 RPM) ATW flow observation experiments with the Pyrex beads also suggest that during the sliding bed situation, particles are not distributed over the entire slurry wetted area at the bottom of the toroid wheel. The particle distribution over the bottom surface of the toroid is a function of the wheel speed and particle solids concentration. The particle bed moves slowly towards the direction of the flow, and then tumbles back from the downstream side air-water interface. For 20% (by volume) solids concentration of 0.250 mm particles, the actual particle-coupon contact area is approximately 80% of the slurry wetted area, and the thickness of the particle sliding bed at the bottom of the toroid wheel is approximately 65% of the ATW flow channel thickness.

To understand the sliding bed situation and coarse particle behavior inside the TWT, qualitative flow observations were also made using 2 mm gravel and 0.50 mm monosized glass beads in water, for different solids concentrations of the particles (i.e. C_S = 1, 10, and 20% by volume) at different wheel speeds ranging from 10 to 90 RPM. Both radial and tangential distributions of particles inside the slurry were observed during these experiments. Figure 5.5 shows a typical flow observation and the particle sliding bed distribution inside the slurry for 2 mm gravel slurry. Clarity for this slurry flow observation has been attained by first washing the

gravels thoroughly with water to remove most of the fine particles. Qualitative observations of these larger particles indicate that:

- A settled and slowly moving bed of particles exists at the bottom of the ATW at wheel speeds as high as 90 RPM (2.9 m/s) for gravel and at 60 RPM (1.9 m/s) for 500 μm particles. This is mostly because the settling velocity of the larger gravels is much higher than that of the smaller 500 μm particles, and thus they are likely to be less affected by the fluid turbulence [21].
- The bottom layer of the particle bed in contact with the rotating ATW moves slowly in the direction of rotation following the toroid wall, and tumbles back into the middle of the channel from the air-water interface on the downstream side. Therefore, the relative velocity between the settled particles and the rotating ATW in not directly comparable to the relative velocity of a moving sliding bed of particles found in an actual stationary pipeline.

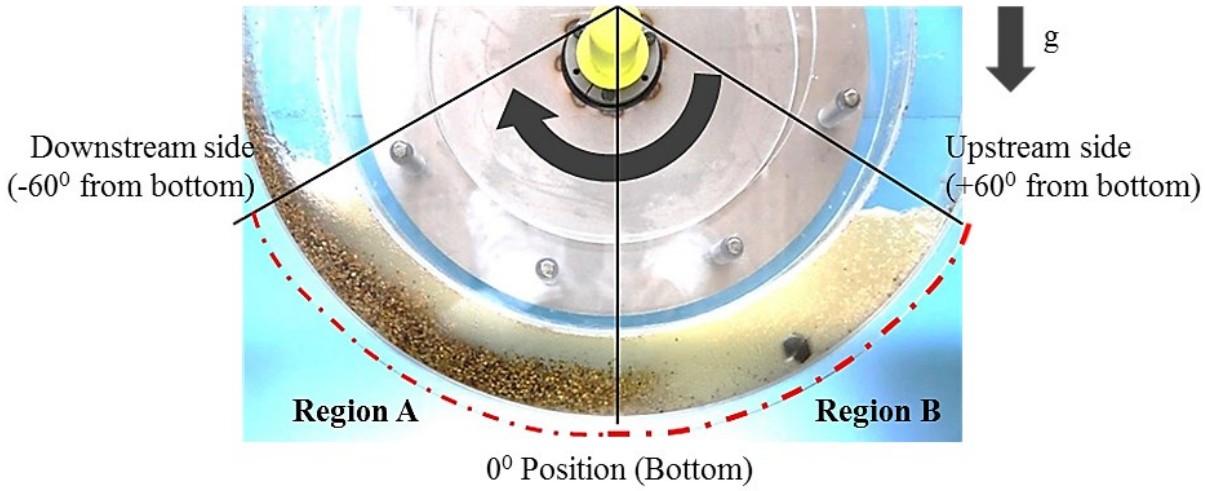

Figure 5.5. Observation of particle distribution inside rotating ATW
***N* = 90 RPM (2.9 m/s); Particle d_{50} = 2 mm; C_s = 10%**

- While larger particles are dragged towards the downstream side of the ATW, the suspended fine particles are more evenly distributed across the whole slurry volume. Based on this observation, the overall slurry volume inside the ATW can be approximately divided into two separate regions, 'Region A' and 'Region B', as shown in Figure 5.5. Region A is on the downstream side (0° to –60° positions), where the sliding bed of particles is apparent, and erosive wear due to the sliding of settled particles against the bottom wall of the toroid is anticipated. Region B is on the upstream side (0° to +60° positions), where a sliding bed of particles is absent, and the erosive wear mechanism may be dominated by the random or directional impingement of particles suspended in the carrier fluid.
- It is evident from Figure 5.5 that coarse particles within the slurry make contact with the bottom of the ATW at a certain portion of the entire slurry wetted area. The particle-wall contact area observed for the 500 μm particles is similar to the contact area for the 250 μm particles, ranging between 60% to 80% of the slurry wetted area at different solids concentrations. The particle-wall contact area observed for the 2 mm gravel is approximately 50% of the entire wetted area. Therefore, a correction factor of 0.5 needs to be taken into account in the wear rate calculation for slurries of large particles (i.e. gravel).

5.3 Corrosion Control using N_2 Purging

Corrosion is identified as one of the probable reasons of additional wear during slurry erosion in a pipeline [9, 46]. The interactions between erosion and corrosion during slurry pipeline wear are complex; both processes supplement each other and a higher overall wear rate is typically obtained [46]. To study the erosion process inside the TWT, corrosion and its synergistic effects with erosion were eliminated by employing purging with N_2, i.e. N_2 gas was purged for five minutes to drive out the dissolved oxygen (*DO*) inside the TWT system. Several experiments were conducted with and without N_2 purging to quantify the effect of dissolved oxygen present inside the slurry in the TWT. Experiments containing only water in the TWT (i.e. particle-free) but with N_2 purging were also conducted to account for the corrosion effects, and to identify the synergistic effect of erosion-corrosion in the presence of high amounts of *DO* . Figure 5.6 shows two test coupons after TWT experiments were conducted with and without N_2

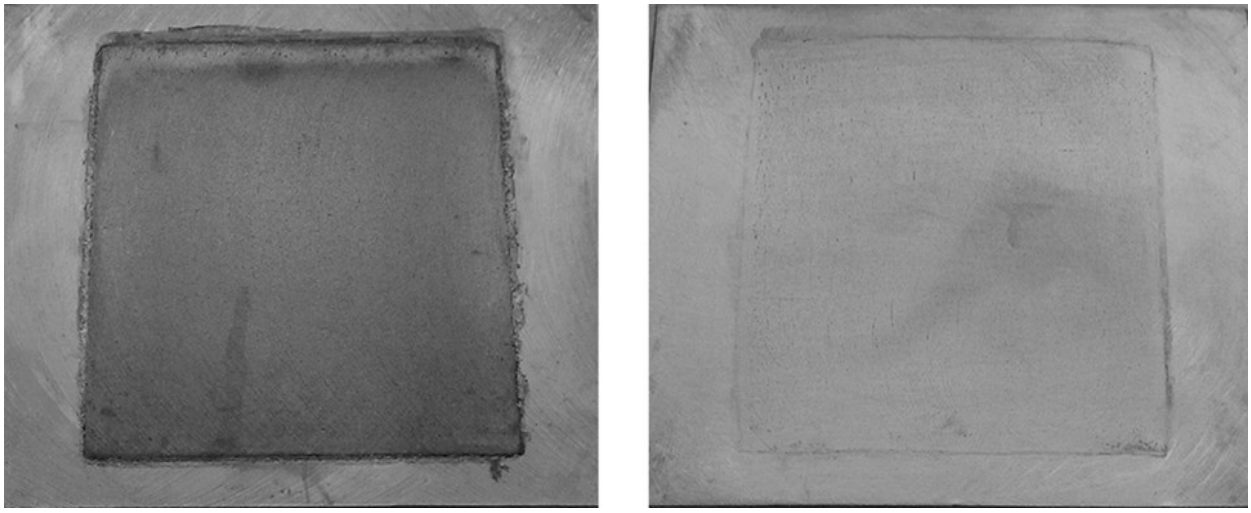

(a) (b)

Figure 5.6. Comparison between (a) erosion-corrosion at *DO* = 5.4 PPM and (b) only erosion affected test coupons at *DO* < 1.0 PPM;
***N* = 60 RPM, d_{50} = 250 micron, Experiment duration: 96 hrs**

purging. Both of the coupons were tested using 250 μm US Silica sand slurry (20% by volume) for 93 hours at 60 RPM. However, for the test coupon shown in Figure 5.6 (a) the slurry was not purged and for the test coupon shown in Figure 5.6 (b) the slurry was purged with N_2. The dark square area in the middle of the carbon steel test coupon in Figure 5.6 (a) indicates severe erosion-corrosion damage, whereas the relatively clearer square area in the middle of the coupon shown in Figure 5.6 (b) represents purely erosive damage. It is obvious from visual inspection that the effect of corrosion and its synergy changes significantly after N_2 purging.

As mentioned in Chapter 3 (Table 3.7), 250 μm US Silica and 2 mm gravel particles have been used during the corrosion control experiments. For both slurries, *DO* inside the TWT was maintained at 5.4 PPM (without N2 purging) and <1.0 PPM (with N2 purging) keeping all other operating parameters identical. Figure 5.7 provides wear results from the aforementioned

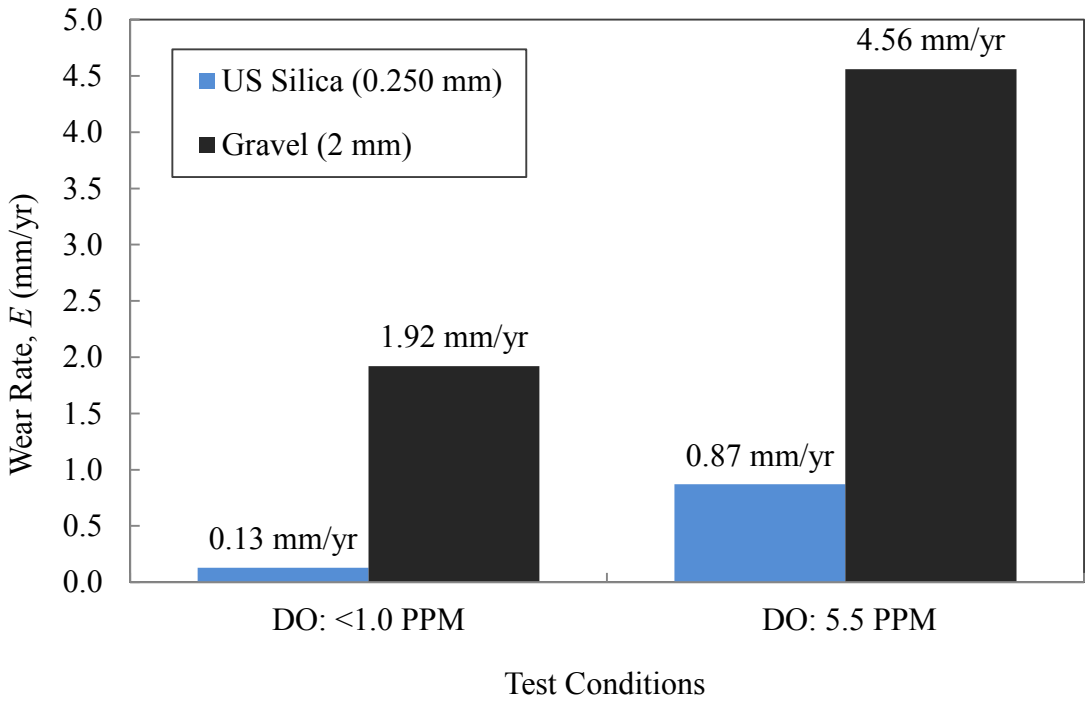

Figure 5.7. Effect of dissolved oxygen on wear rate; N = 60 RPM, C_s = 20%, SRI = 24 hrs;

corrosion control experiments. The blue and black columns in the chart indicate the wear rate calculated for the US Silica and gravel particles, respectively. US Silica sand slurries showed a wear rate of 0.87 mm/year due to the combined effect of erosion and corrosion, which reduced to 0.13 mm/year after lowering the *DO* below 1.0 PPM. For the gravel slurry, wear rate due to erosion-corrosion was found to be 4.56 mm/year, and 1.92 mm/year for the erosion-only test condition, i.e. when *DO* <1.0 PPM. This reduction in the wear rate is mainly due to lack of corrosion and the elimination of its synergistic effect with erosion. The corrosion-only experiment (without the particles and N_2 purging) gave a material loss rate of 0.61 mm/year, and subtraction of this rate from the erosion-corrosion combined wear rate results in 0.26 mm/year and 3.95 mm/year for the US Silica sand and gravel particles, respectively, which are higher than the individual erosive wear rates for these particles. Therefore, it is evident from the TWT experimental results that N_2 purging can be used as an effective method to minimize the corrosion and also the erosion-corrosion synergy in the TWT experiments.

Results obtained from the corrosion control tests were compared with test results available in the literature. Cooke *et al.* [5] experimented with 39 μm gold tailings in a toroid wear tester with the *DO* ranging from 0 to 10 PPM, and reported that the wear rate rapidly increases with increased amount of *DO* in the slurry, up to 2 PPM, and then keeps increasing more slowly with increasing *DO.* Cooke *et al.* [5] reported approximately 60% reduction in the wear rate as the average *DO* level drops from 5.0 PPM to 1.0 PPM. Similar reductions in the wear rate were obtained in the present study. Slurry erosion experiments conducted at *DO* = 5.4 PPM (without N_2 purging) and *DO* <1.0 PPM (after purged with N_2 for five minutes) using 250 μm US Silica sand and 2 mm gravel particles indicate about 57% and 85% reduction in the wear rate, respectively, after the N_2 purging. The *DO* level in the slurry was also measured after these

experiments, which indicated almost zero increase in the *DO* level. It can be concluded that the N_2 purging significantly reduces corrosion in the TWT, and can be used to eliminate and maintain the *DO* level of the slurry below 1.0 PPM during material loss experiments.

5.4 Parametric Study of Erosive Wear using the TWT

The current parametric study is essential to ensure that the results using this TWT are at least qualitatively consistent with previous results reported in the literature. For example, studies using other laboratory scale devices have shown that the erosive wear is dependent upon the bulk flow velocity, particle size and particle solids concentration; and specifically each has a power law relationship with wear rate. In this study, particle solids concentration, wheel speed and particle sizes were varied to determine if similar power law relationships hold true for the TWT.

5.4.1 Effect of Solids Concentration (C_s)

Each test with gravel particles (d_{50} = 2 mm) was conducted for a total of 93 hours. In each test, the mixture was replaced every 24 hours. Three different particle solids concentrations, i.e. 6, 12 and 20% (by volume) were used during these experiments. Experiments were performed at three different rotational speeds: 30, 45 and 60 RPM, having equivalent linear velocities of 1.0, 1.4 and 1.9 m/s, respectively. For these experiments, purely erosive conditions were maintained (DO < 1.0 PPM), and the wear rates were calculated by dividing the material loss with the total experiment time in the TWT, density of material and also by dividing with a particle-coupon contat area correction factor of 0.5 (as discussed in Section 5.2.2). Figure 5.8 shows the effect of solids concentration on the wear rate. It is evident that the wear rate increases with the solids concentration for all three velocities. In all three cases, the experimental data follow a power law.

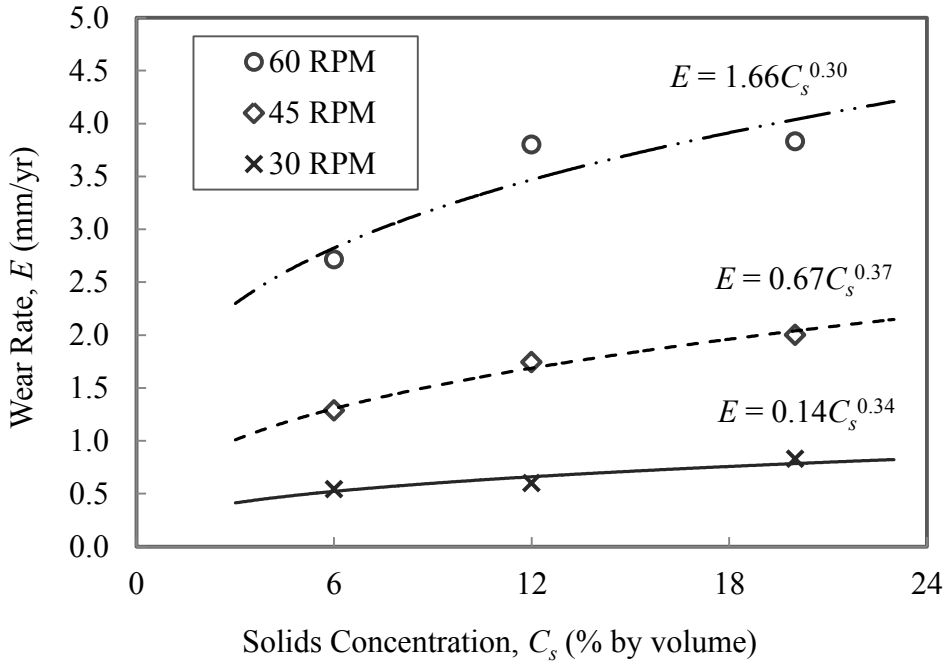

Figure 5.8. Effect of solids concentration (C_s) on wear rate; N = 30, 45 and 60 RPM, SRI = 24 hrs

The calculated exponents from these experiments are 0.34, 0.37 and 0.30 for wheel speeds of 30, 45 and 60 RPM, respectively. Experiments with similar solids concentrations have been reported by previous investigators. For example, Gandhi *et al.* [13] used brass specimens in a slurry pot tester and found the exponent for the solids concentration to be 0.83, and Gupta *et al.* [8] also used a slurry pot and reported the exponent to be 0.556 for mild steel specimens. Cooke *et al.* [5] used a TWT and a power law fit of the experiment data reported by them indicated an exponent of 0.13 for the solids concentration. The current study reports the exponent of solids concentration to be in between the range of values reported by previous researchers. The differences in the exponent within the literature are likely due to differences in the flow hydrodynamics and the properties of target material and particles.

As the solids concentration increases, the thickness of the sliding bed at the bottom of the channel also increases. As discussed earlier in Chapter 2, the increase in the sliding bed thickness has a direct impact on the normal load and corresponding Coulombic friction on the test coupons and it results in an increase in the erosion rate at higher solids concentrations. Flow observations were made with the ATW using 5% and 10% solids concentrations at 30 and 60 RPM, and the change in the sliding bed thickness was analyzed. Figure 5.9 demonstrates the increase in the sliding bed thickness in the ATW, as the solids concentration increases. The average thickness of the sliding bed was measured by calculating the number of pixels along the radial direction, and was normalized in terms of the channel height measured in pixels. The ratio of the change in the sliding bed thickness due to increase in solids concentration has been calculated and compared

(a) 30 RPM; C_s = 5% (by vol)

(b) 60 RPM; C_s = 5% (by vol)

(c) 30 RPM; C_s = 10% (by vol)

(d) 60 RPM; C_s = 10% (by vol)

Figure 5.9. Qualitative observation of change in sliding bed thickness; Slurry: 2.0 mm Gravel + Water

with the calculated wear rate ratio. Table 4.1 shows the comparison between the change in the sliding bed thickness (t_{sb}) and the change in the wear rate. Since the sliding bed thickness increases with higher solids concentration, the ratio of the sliding bed thickness (t_{sb}) at 5 and 10% (by volume) solids concentration is smaller than 1.0, i.e. 0.75 and 0.64 for 30 and 60 RPM wheel speeds, respectively. The corresponding wear rate ratios are 0.82 and 0.72. Applying an exponent of 0.7 to the average sliding bed thickness ratios at 30 and 60 RPM results in a reasonable agreement with the wear rate ratios. However, this exponential fit, based on two data points, is useful for illustrative purposes, but should not be used for calculations until more data can be obtained.

Although a reasonable agreement between the wear rate ratios and the sliding bed thickness ratios was found, the normal load on the test coupons in a TWT is not comparable to an actual pipeline operation. Firstly, the normal load on the coupons varies as the TWT rotates; at the bottom (0° Position) of the TWT, the normal load is maximum, but when the coupons move toward the downstream side of the slurry, the normal load imposed by the weight of particles decrease, unlike an actual pipeline. Also, the test coupons in the TWT experience a discontinuous but repetitive contact with the sliding bed of particles rather than having a

Table 5.1. Comparison between change in sliding bed thickness (t_{sb}) and wear rate (E)

Wheel Speed (RPM)	$\frac{t_{sb-5\%}}{t_{sb-10\%}}$	$\left(\frac{t_{sb-5\%}}{t_{sb-10\%}}\right)^{0.7}$	$\frac{E_{6\%}}{E_{12\%}}$
30	0.75	0.82	0.82
60	0.64	0.73	0.72

continuous contact observed in the pipeline. Secondly, qualitative observations of the slurry flow inside the TWT have indicated a strong back-flow of slurry, which may cause the upper layers of an existing sliding bed to become suspended and therefore, resulting in a decrease in the normal load on test coupons. Although the normal load in a TWT may not be directly comparable to an actual pipeline, the bulk effect of solids concentration on erosion mechanism was noticeably identified; higher solids concentration increase the normal load and the associated Coulombic friction on the test coupons results in a higher amount of slurry erosion.

5.4.2 Effect of Wheel Speed

Tests with 2 mm gravel particles were completed with different solids concentrations, i.e. 6, 12 and 20% (by volume), varying the wheel speed from 30 to 60 RPM. The 2.0 mm gravels has high settling velocity, and was remained as a settled bed at the bottom of the TWT during these experiments. As the wheel speed increases, the relative velocity between the settled 2.0 mm gravels and the test coupon increases. Therefore, it was found that the sliding friction between the gravels and the test coupons results in higher amount of material loss with increasing wheel speed. Figure 5.10 shows the increase in wear rate with wheel speed for 6, 12 and 20% solids concentration and in all three cases, the data follow a power law as mentioned in Chapter 2 (Equation 2.2). The velocity exponents found are 2.3, 2.7, and 2.2 for 6, 12, and 20% solids concentration, respectively. These results show reasonable agreement with reported exponent values by previous researchers [4, 8, 13, 27, 33] as discussed in Chapter 2. In particular, the exponent obtained for the 20% solids concentration (2.2), during this study is within 10% and 3% of the exponents reported by Gandhi *et al.* (2.44) [13] and Gupta *et al.* (2.148) [8], under similar operating conditions. The exponents obtained from the TWT

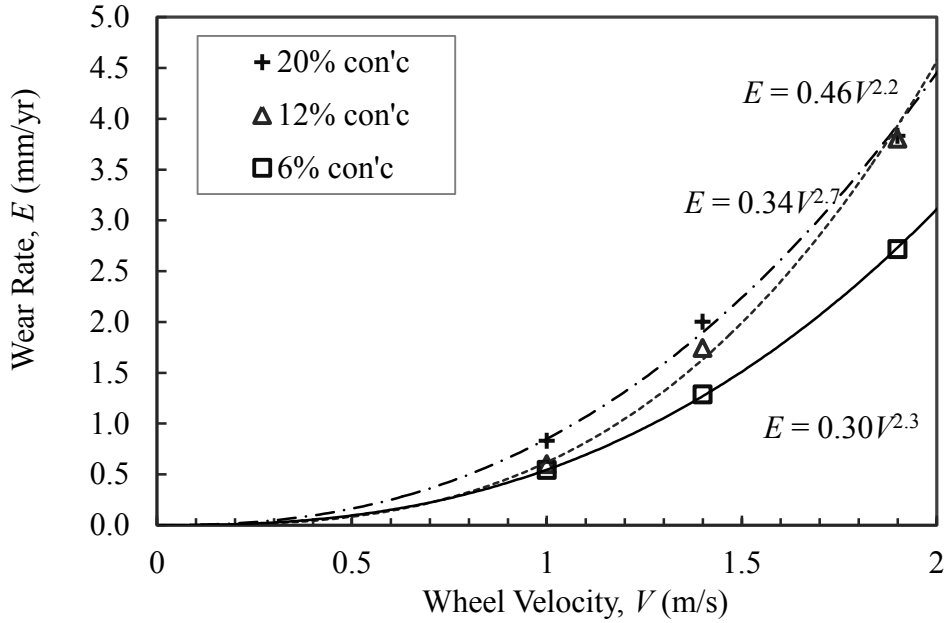

Figure 5.10. Effect of wheel speed on wear rate;
d_{50} = 2.0 mm; C_s = 6, 12 and 20%; *DO* < 1.0 PPM

experiments are also in between the two limiting values for the slurry velocity exponent, i.e. 2.0 and 3.575, reported by Huang *et al.* [4].

The velocity exponents obtained from this study fit the expectation as it is within the range mentioned in the literature [4, 6, 33] involving slurry erosion based on actual pipelines. Also, Goosen *et al*. [6] generally assumed the velocity exponent to be 2.0 considering the particle kinetic energy and the mechanical abrasion as the only wear mechanism in the pipeline. In the TWT, the gravels settle at the bottom and slide over the test coupons generating an almost pure mechanical abrasion equivalent to a pipeline. Therefore, the exponents found in this study (2.2, 2,7, and 2.3) are quite reasonable and indicate the potential of the TWT to simulate slurry pipeline wear mechanisms under specific conditions.

5.4.3 Effect of Particle Size, Shape and Abrasivity

To understand how particle properties affect erosive wear in the TWT, several experiments were conducted in which the particle properties were varied. Experiments were conducted using 2.0 mm gravel, 0.425 mm SIL 4, 0.425 mm Al_2O_3, 0.250 mm SIL 1 and 0.250 mm US Silica at 30 RPM. A wheel speed of 30 RPM was chosen to obtain sliding bed behavior as discussed in Section 5.2.2. Tests at 60 RPM were also conducted using the same slurries. The slurry concentration was kept at 20% (by volume), because at higher concentration the thickness of the sliding bed of gravel particles is too high at the downstream side of the TWT, which blocks the water flow inside the toroid. Figure 5.11 shows the test results for gravel, SIL 4, SIL 1 and U.S. Silica slurries at 30 and 60 RPM. The open markers indicate average wear rates calculated at 30 RPM whereas the solid markers indicate average wear rates at 60 RPM. The figure illustrates that the erosive wear rate in the TWT is a function of the particle size

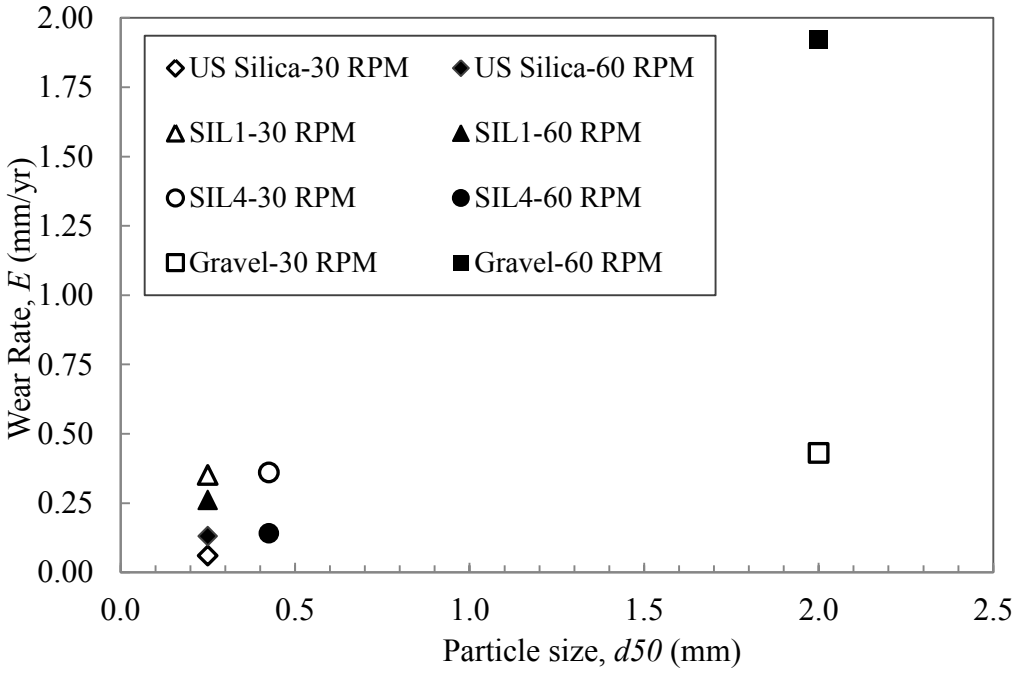

Figure 5.11. Effect of sand particle size on wear rate; N = 30 and 60 RPM, C_s = 20%

and increases with increasing particle diameter. Results obtained for the 2 mm gravel show that as the wheel speed increases, the erosive wear rate increases, but experiments with 0.425 mm and 0.250 mm sands behaved differently. The calculated wear rates found in the 60 RPM experiment are lower than the 30 RPM experimental results, except for the U.S. Silica particles. The major cause of this deviation from the expected trend is the absence of the sliding bed for smaller particles. As indicated earlier, the slurries of smaller particles are heterogeneous at lower speeds (< 40 RPM); as the wheel speed increases, the settled particles begin to disperse in the carrier fluid and remain suspended at 60 RPM. As a result, the erosion mechanism changes from Coulombic friction to either the random or the directional impact of particles, due to turbulence induced flow near the test coupon. This flow regime change alters the effective particle–coupon contact and therefore results in a lower material loss for the 60 RPM tests than the 30 RPM tests. On the other hand, the gravel particles keep sliding at the bottom and the momentum of the sliding particles increases at 60 RPM resulting in greater erosion damage. Therefore, to understand and explain the wear behavior of smaller particles at higher wheel speeds, a better understanding of the flow hydrodynamics inside the TWT is necessary so that the wear mechanism by random or directional impact can be better understood. Another observation from Figure 5.11 is the variation of wear rate between SIL 1 and U.S. Silica sand. Both sand particles have a d_{50} of 0.250 mm, but it is evident that the slurry of SIL 1 particles produces higher wear than the US Silica under otherwise identical operating conditions. To compare the roundness, i.e. the degree of angularity, shape parameters (i.e. sphericity, symmetry and aspect ratio) of these two types of particles were analyzed by dynamic image analysis using a CAMSIZER. A cutoff value of 0.9 has been chosen for the sphericity ($SPHT$) parameter, which suggests that any particle with the $SPHT$ values above 0.9 is round. Other shape parameters, i.e. the symmetry

($Symm$) and aspect ratio (b/l) of particles have also been analyzed using the same cutoff ratio and each parameter showed reasonable similarity for both SIL 1 and U.S. Silica particles as presented in Table 5.2 (See Appendix G for details).

Scanning electron microscopy (SEM) was also used to observe and compare the particle morphology of SIL 1 and US Silica, but no significant differences in the shape of these particles were observed (see Figure 5.12). This implies that the shape factor has very little contribution to their wear characteristics.

Table 5.2. Shape properties of SIL 1 and US Silica sand

Shape Properties	SIL 1		US Silica	
	(%)	Mean	(%)	Mean
Sphericity ($SPHT$ = 0.9)	56.6	0.872	53.8	0.877
Symmetry ($Symm$ = 0.9)	55	0.886	46.2	0.893
Aspect ratio (b/l = 0.9)	98.6	0.709	98.3	0.714

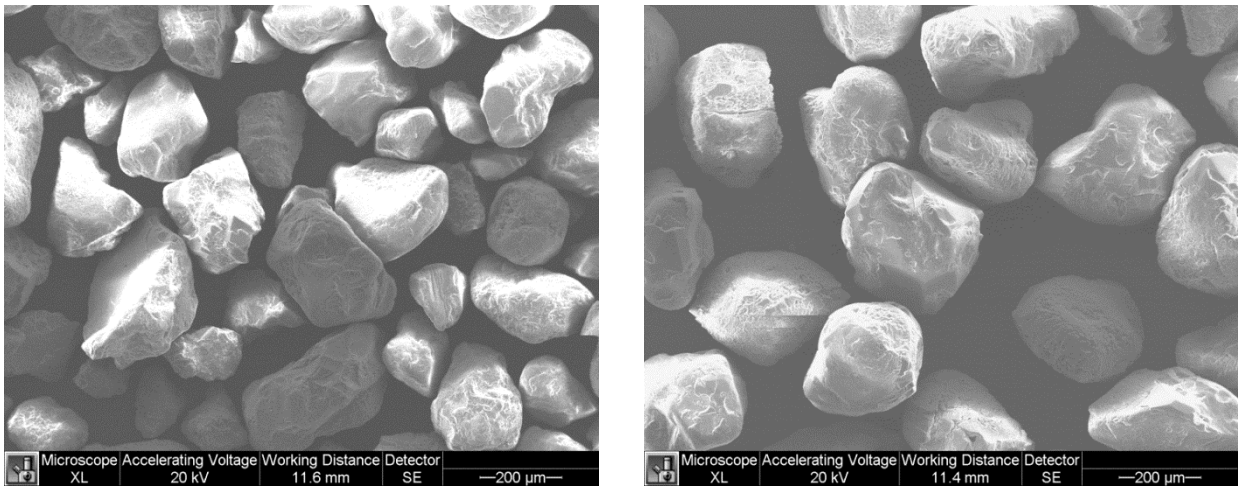

(a) (b)

Figure 5.12. SEM images of (a) SIL 1 sand particles and (b) U.S. Silica; magnification: 200x

However, it can be seen qualitatively from Figure 5.12 that the SIL 1 sand has a wider particle size distribution (PSD) than the US Silica. The CAMSIZER data were also used to determine the particle size distribution of SIL 1 and US Silica sand; the results are presented in Figure 5.13. It is evident that SIL 1 has a wider PSD than the US Silica. As the PSD tends to get wider, the solid concentration in the settled bed (C_{max}) increases [48, 49]. As the C_{max} increases, the number of particle-coupon contacts and effective normal load on the test coupon also increase, which may have resulted the additional material loss rate for the SIL 1 sand. Therefore, it is fair to assume that the PSD has a significant impact on the erosive wear, and needs to be considered alongside particle size and shape factors.

For further analysis of the effect of shape and abrasivity on carbon steel test coupons, material loss experiments have been conducted using SIL 4 sand and Al_2O_3 particle slurries, which have nearly identical d_{50} values (0.425 mm). Figure 5.14 shows the SEM images of SIL 4 and Al_2O_3, from which it is evident that Al_2O_3 is more abrasive than SIL 4. The density and

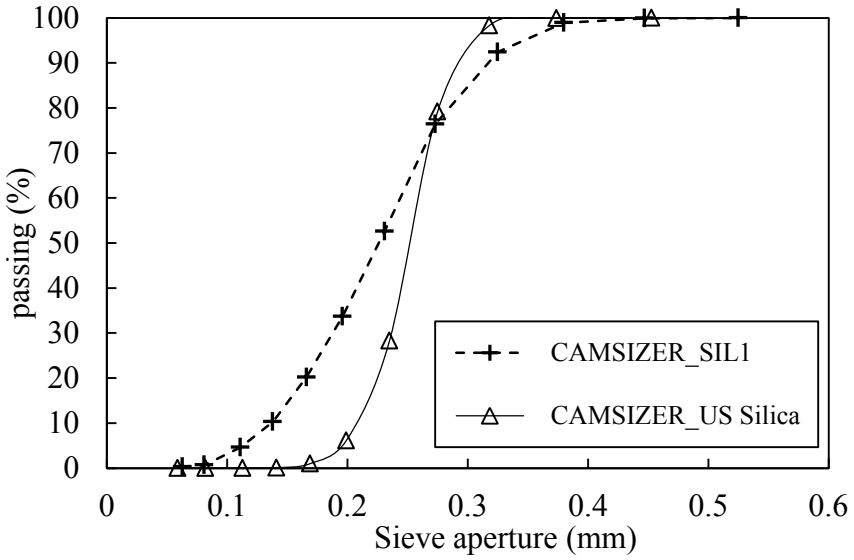

Figure 5.13. Comparison between the particle size distribution of SIL 1 and US Silica

particle hardness of the Al_2O_3 are 3.95 g/cm^3 and 9 (Moh's scale), respectively. These values are higher than those of SIL 4 sand, which has a density and hardness of about 2.65 g/cm^3 and 6 (Moh's scale). Therefore, higher material loss rate was expected for the Al_2O_3 particles. From the experiments, it was found that the test coupons exposed to Al_2O_3 particles wear at a higher rate than with the SIL 4 sand under similar operating conditions. For example, the wear rate obtained for 20% (by volume) Al_2O_3 and SIL 4 sand at 60 RPM was 0.50 mm/year and 0.13 mm/year, respectively.

These findings show that material loss increases with increasing particle size, and also reinforces the hypothesis that in the absence of a sliding bed, the smaller particle may generate a complex wear mechanism within the TWT, and result higher wear may result. From this set of experiments it was also found that the PSD, shape and abrasivity of particles having the same d_{50} all have a significant effect on the wear rate and need further experimental analysis to quantify their effect within the TWT.

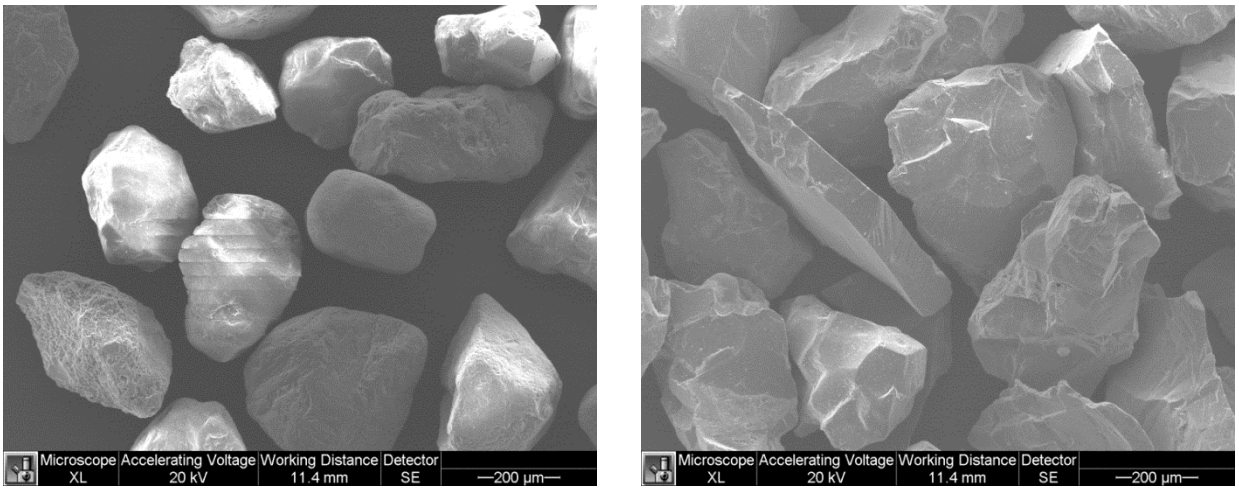

(a) (b)

Figure 5.14. SEM images of (a) SIL 4 sand particles and (b) Al_2O_3 particles; magnification: 200x

5.5 Analysis of Wear Pattern on the Test Coupons

A surface profilometer (Brand: Mitutoyo Contracer) was used to measure the surface roughness of the test coupons before and after the experiments, and the change in the surface roughness was recorded and analyzed. The contracer probe measures the roughness of the test coupons along the Z-axis as the probe travels in X and Y directions. Details of the measurement procedure, including the FORMPAK programming are provided in Appendix E. Comparison between the measured roughness values indicated that the test coupons wear out evenly at all the contact regions except for the leading edge (the leading edge being the first edge of the test coupon that makes contact with the slurry during each rotation). Figure 5.15 shows an example of wear pattern analysis using contracer measurements after an erosion experiment with gravel particles at 60 RPM. The overall experiment time was 93 hours, and the slurry (20% by volume) was replaced every 24 hours. The discrete thicknesses measured using the contracer are plotted on a 3D scatter graph with a cubic interpolation-based best fit surface in Figure 5.15 (a). The contour plot of the best fit surface is shown in Figure 5.15 (b) indicating the zone of highest wear and also the uniformity of wear pattern away from the leading edge. The red region indicates the un-eroded part of the test coupon and the blue region illustrates the zone of highest wear. It is evident from Figure 5.15 (b) that at the zone of highest wear, the thickness change after the experiment is approximately 0.12 mm, whereas most of the test coupon experienced a thickness loss of approximately 0.06 mm (indicated by the yellow region).

From the contour map it can be seen that the material loss near the leading edge of the test coupon is prominent. This phenomenon is referred to as the ‘edge effect’, where additional material loss near the edge reduces the uniformity of the material removed from the test coupon

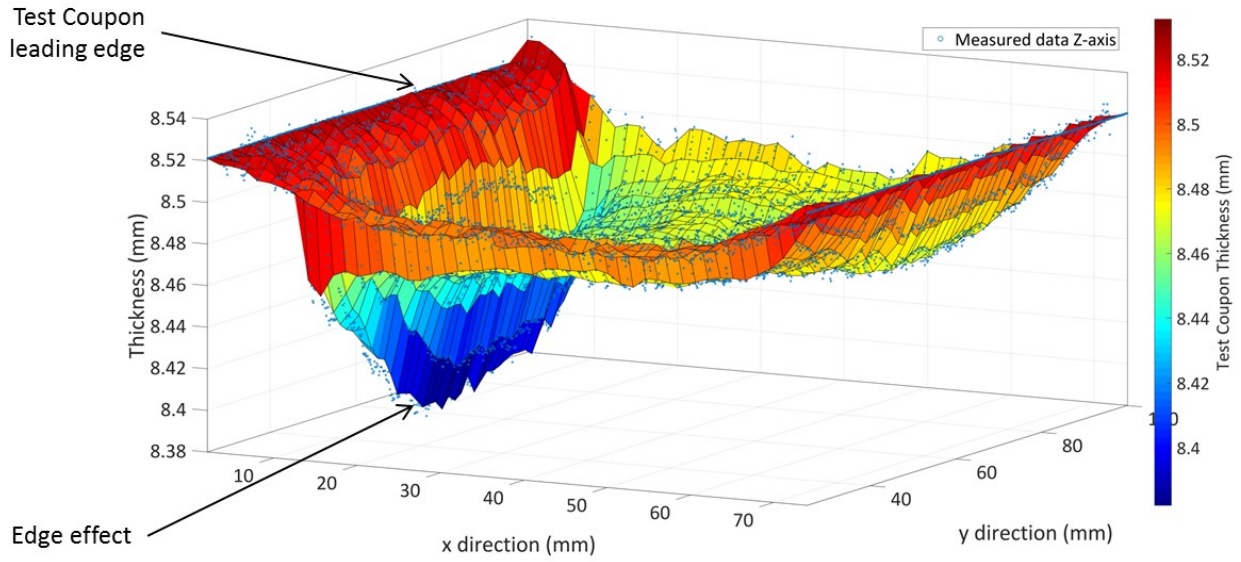

(a) Measured thickness along Z -axis (scatter plot) and best fitted surface plot (jet colormap)

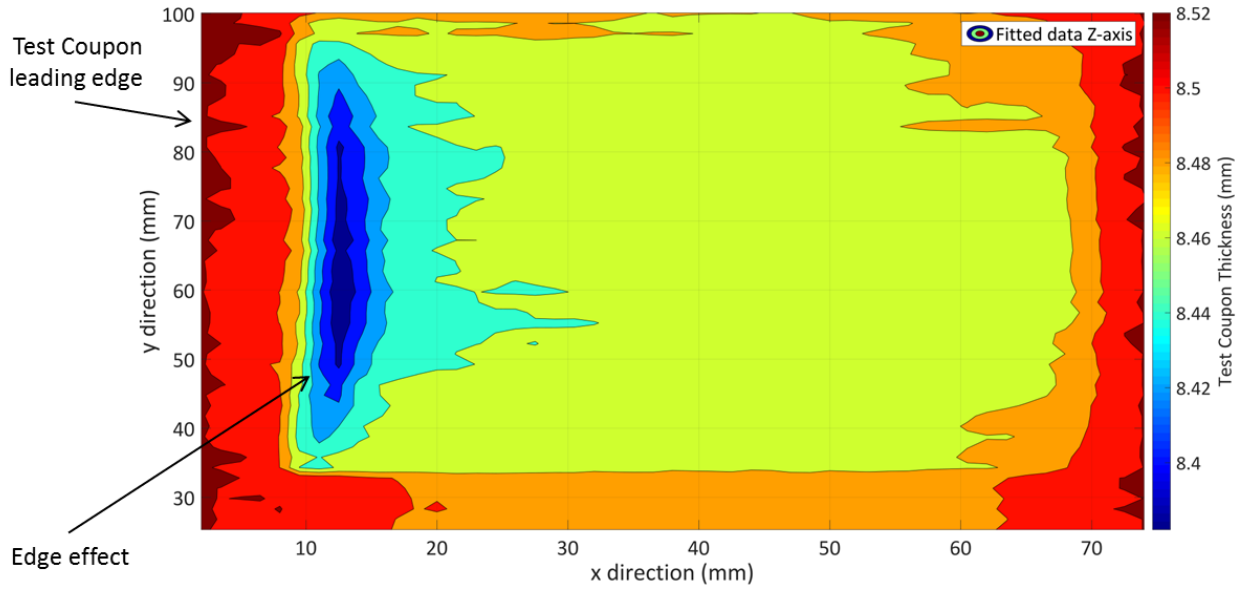

(b) Contour map of the eroded region based on the best fit curve

Figure 5.15. Wear pattern analysis and identification of edge effect using contracer; N = 60 RPM, d_{50} = 2 mm, C_s = 20%, SRI = 24 hours

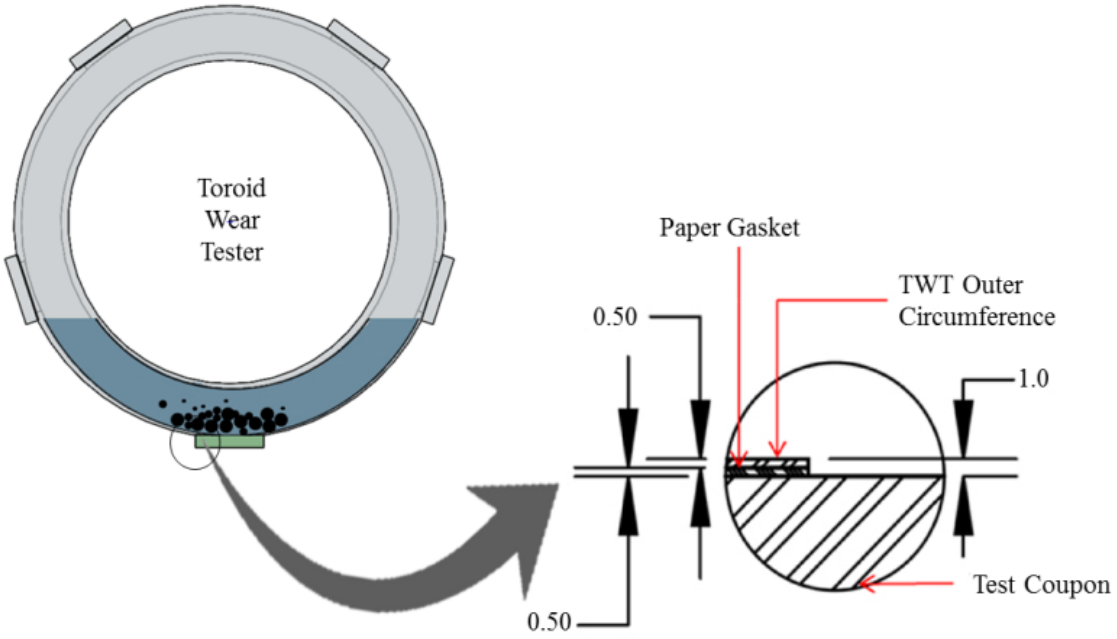

Figure 5.16. Detailed view of the test coupon assembly on the TWT (all dimensions are in mm)

surface. This is a major source of uncertainty in the measured wear rate based on gravimetric measurement. This edge effect is mainly caused by a small step height at the test coupon–coupon window interface. At the coupon window, edge of the toroid wheel outer wall has a step thickness change of about 0.5 mm. Furthermore, a 0.5 mm thick paper gasket is used on the window to seal the contact and then the test coupons are bolted on the coupon windows. As a result, an overall step height of approximately 1.0 mm is produced at the coupon-wheel interface. Figure 5.16 presents a detailed view of one edge of the test coupon during the assembly showing the 1.0 mm step height. When the wheel rotates, the adjacent layer of slurry slides on the test coupons as a loosely packed bed due to inertial drag. The obstruction and sudden change in the flow pattern in the stepped region change the nature of the particle-particle and particle-coupon interactions near the leading edge of the coupons, resulting in a higher abrasive wear at that position.

The contracer data have been plotted along the centerline of the eroded region in the lengthwise direction in Figure 5.17, which shows the wear pattern of the test coupons along the length of the coupon for 45 and 60 RPM at three different solids concentrations. Figure 5.17 illustrates that 80% of the test coupon in the lengthwise direction wears out almost uniformly. The average measured thickness losses in those regions are approximately 0.06 mm and 0.045 mm after 93 hours of slurry erosion, at 60 and 45 RPM, respectively. In comparison to the average values, the material losses found near the leading edge of the coupons are as high as 0.13 mm and 0.06 mm for 60 and 45 RPM, respectively. These results indicate that at the higher speed, i.e. 60 RPM, the edge effect almost doubles the amount of material loss near the leading edge of the test coupons, which becomes less prominent at lower wheel speeds. No significant edge effect was observed near the trailing edge (the trailing edge being the last edge of test coupon that makes contact with the slurry during each rotation); however, some local maximum wear areas were found from the Contracer measurement, i.e. a second local maximum wear region (thickness loss 0.065 mm) was observed from erosion experiments with gravels at 60 RPM and 12% (by volume) solids concentration (see Figure 5.17 (a)). This local maximum wear area near the trailing edge may be due to a combined effect of local turbulence in the flow and particle–particle interactions.

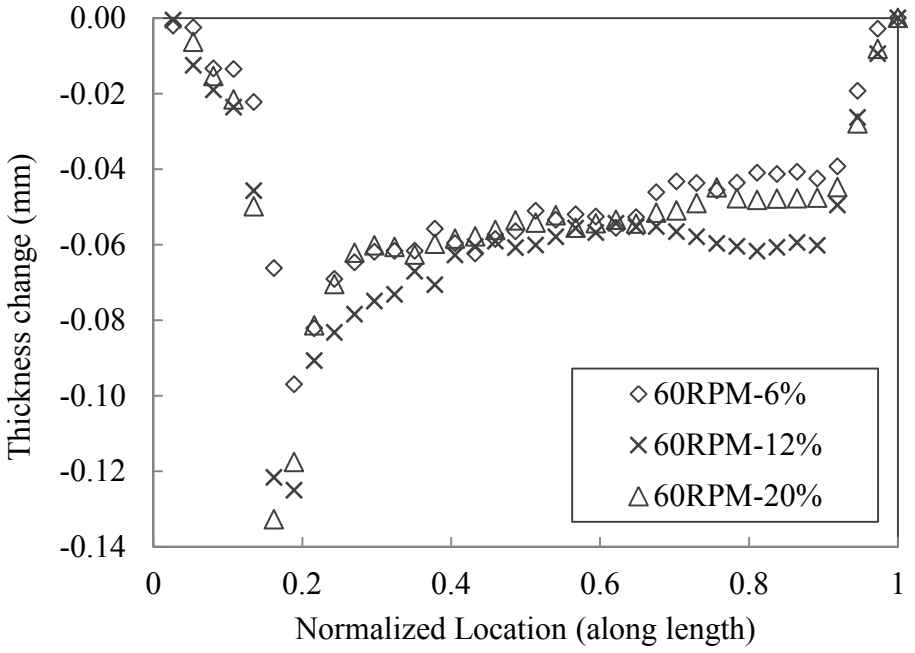

(a)

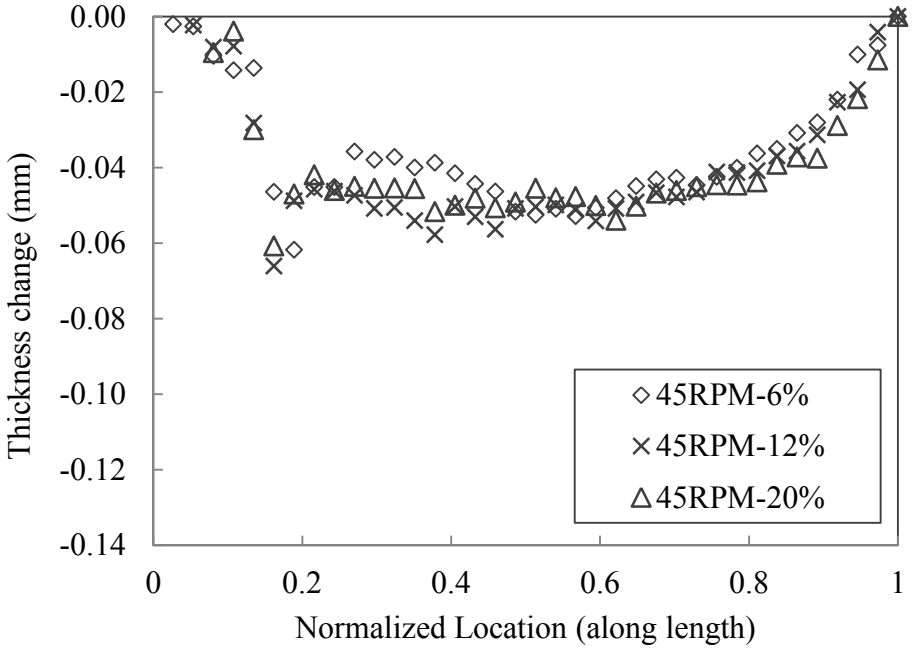

(b)

Figure 5.17. Wear pattern along the centerline (lengthwise) of the test coupons; N = 60 RPM, (b) N = 45 RPM

Figure 5.18 illustrates the wear pattern across the width of the test coupons for similar operating conditions and points out that the material loss across the width of the test coupons is maximum near the center of the coupons and gradually decreases as it approaches towards the edge. The flow channel width of the toroids is similar to the width of the coupons, and the wear locations shown by 20 mm and 100 mm ticks on the x-axis in Figure 5.18 indicate the left and right side wall of the TWT, respectively. It is evident from Figure 5.18 that although the effect of solidsconcentration on material loss is not significant near the center of the test coupons, some inconsistency in the result is present near the side walls of the TWT. Approximately 15% variation in thickness losses was observed between 6% and 20% solids concentration (by volume) slurry at 60 RPM. The variation is approximately 24% between slurries having 12% and 20% solids concentration (by volume) rotating at 60 RPM. Similar trend in the wear pattern was also found for slurries rotating at 45 RPM with different solids concentration, and the variation in thickness losses near wall was higher than that of the 60 RPM results. The inertial drag on the slurry is higher near the boundary, i.e. side wall of the TWT, and this effect combined with the secondary flow near the wall may have caused these irregularities in the results. CFD analysis of an air-water multiphase system in a rotating toroid wheel (without considering any dispersed particles) was completed, and the tangential velocity components on the plane normal to the flow was plotted, details of which will be discussed later in Chapter 6. This swirling flow in the azimuthal direction may be another cause of the inconsistancies in wear pattern near the wall. However, no step height at the coupon-coupon window interface is present near the side wall, except for the 0.5mm step height of the paper gasket, and the loosely packed bed of particles always move parallel to the side of the test coupons. So, no intense edge effect was observed near the side wall of the TWT.

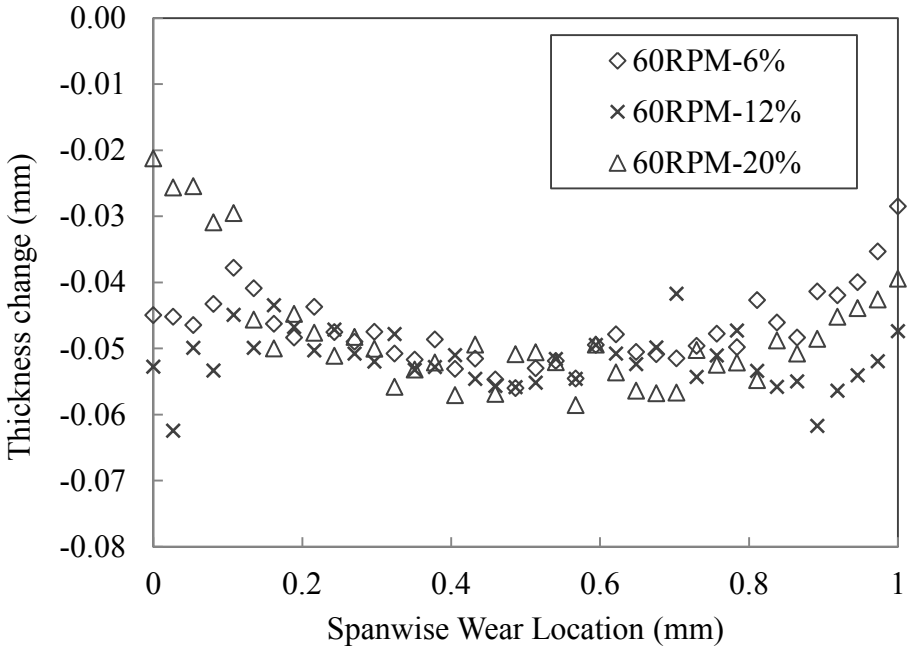

(a)

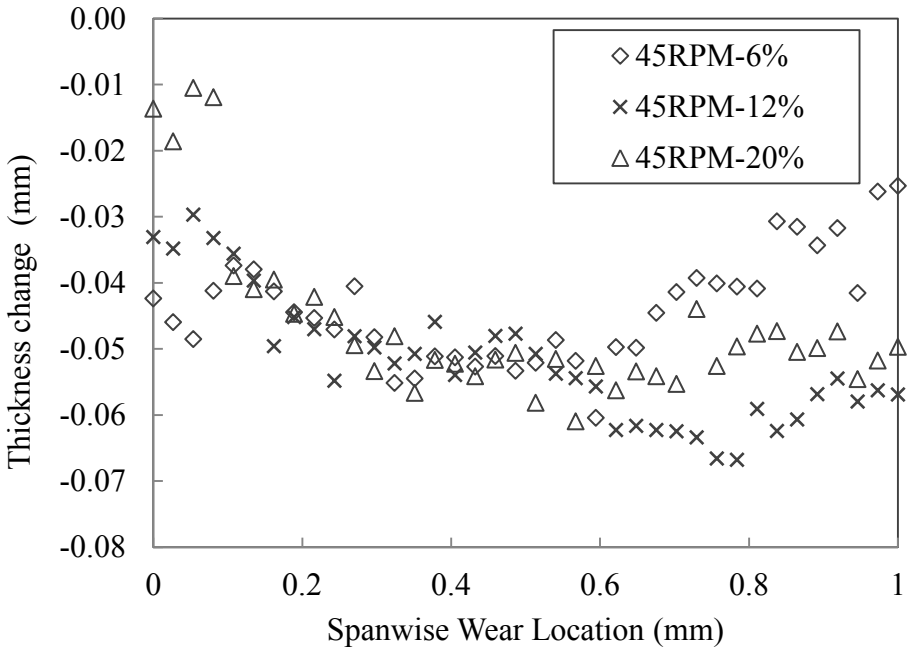

(b)

Figure 5.18. Wear pattern along the centerline (Widthwise) of the test coupons; (a) N = 60 RPM, (b) N = 45 RPM

5.6 Slurry Replacement Interval (SRI) Test

As mentioned in Chapter 2, the slurry replacement interval (SRI) test is mandatory to determine absolute wear rate (the wear rate at zero particle degradation) to compare the material loss data from the TWT with an actual operating pipeline. Tests have been conducted with 2 mm gravel, 0.425 mm Al_20_3 and 0.425 mm SIL 4 sand according to the test matrix described in Chapter 3. In this particular section, the results and analyses of the SRI tests will be presented. Figure 5.19 illustrates the calculated erosive wear from the SRI experiments using 2 mm gravels. Wear rates were calculated and plotted for different SRIs ranging from 8 hours to 96 hours, and then fitted exponentially to the curve:

$$y = a\mathrm{e}^{-bx} + c \qquad 5.6$$

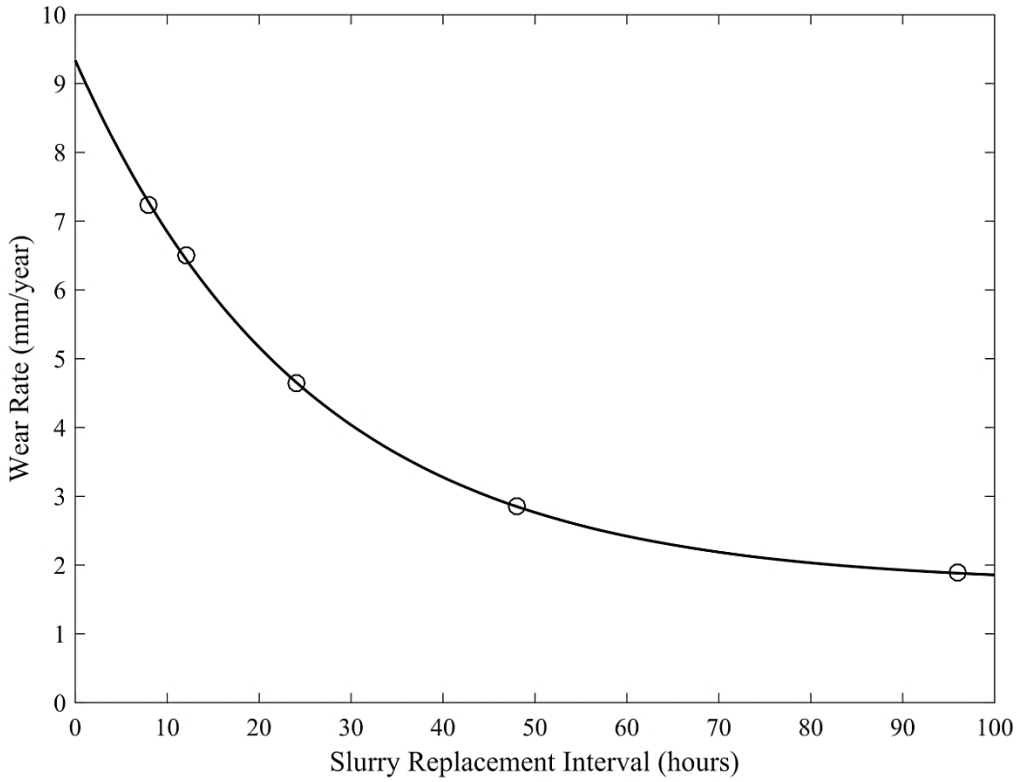

Figure 5.19. Zero particle degradation wear rate for 2 mm gravel; *N* = 60 RPM

Here, y and x indicate the wear rate (mm/year) and SRI (hours), respectively, and a, b and c are constants. A similar trend has been suggested by Cooke *et al*. [5] as discussed in Chapter 2. The fitted curve intersects the y-axis at the point 9.2 mm/year, which indicates the zero particle degradation wear rate for 2 mm gravel particles at the operating conditions specified in Table 3.9 and can be compared with an actual operating pipeline wear data. Experimental results with 0.425 mm Al_20_3 and 0.425 mm SIL 4 sand are also fitted exponentially to Equation 5.1 with a R^2 value of 0.998, and the fitted curves are shown in Figure 5.20. These curve fits also demonstrate the exponentially decreasing trend of the wear rate with SRI. This decreasing trend in the wear rate is caused by particle degradation in the slurry with time.

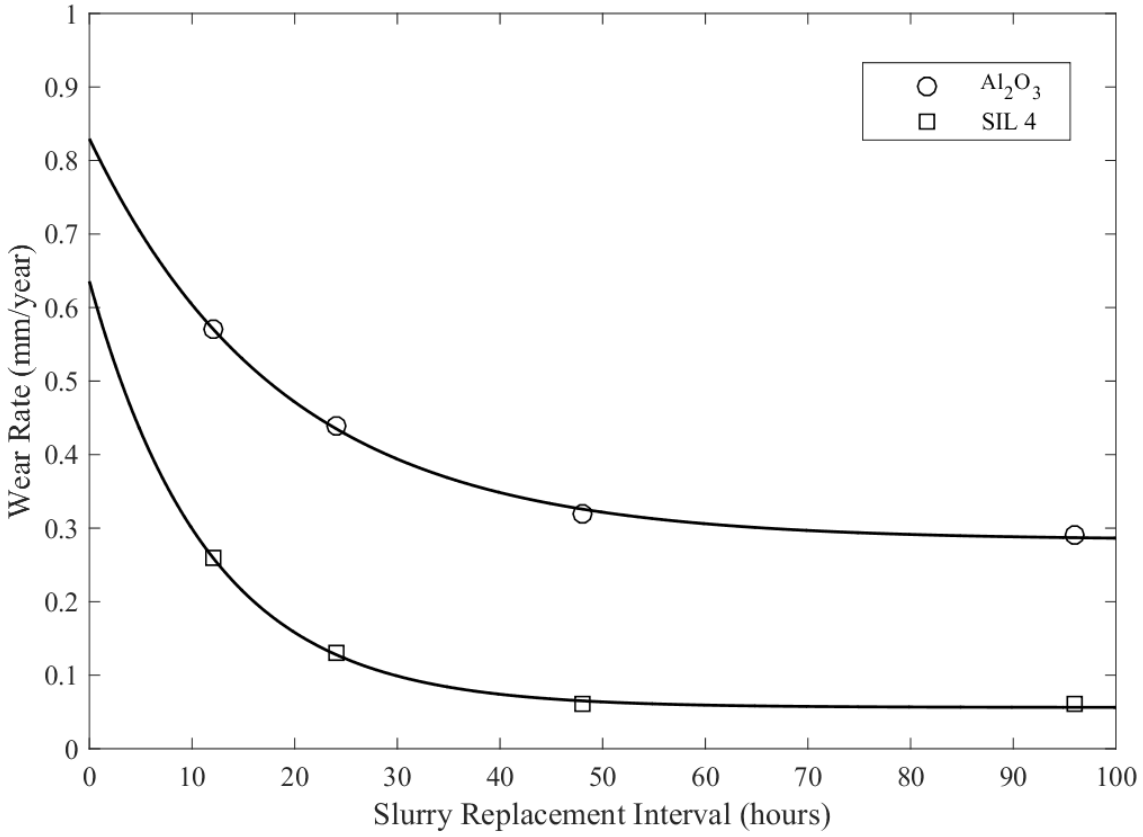

Figure 5.20. Zero particle degradation wear rate for Al_2O_3 and SIL 4; N = 60 RPM

When the TWT rotates, the sharp edges of the particles inside the slurry create an abrasive action on the test coupons, and causes the erosive wear. These sharp edges of the particles get damaged and become rounded with time. In other words, the particles also experience wear and lose their abrasive property with time and therefore the rate of material loss decreases. During this particle degradation process, the 'fines' (d_{50} <44μm) content in the slurry increases and the viscosity of the slurry changes. To understand the severity of particle degradation and the change in viscosity, carrier fluid samples were collected after each SRI experiment, and then filtered using an ASTM 325 mesh (mesh aperture: 0.045 mm) to get rid of the coarse particles. Rheometry analyses of the filtered carrier fluid samples were completed using a concentric cylinder geometry of an AR-G2 rheometer. For the viscosity measurement, each time a carrier fluid sample size of 24 ml was used. The samples were sheared within a range of 0.08 rad/s to 3 rad/s and the torque responses were measured from the rheometer. The

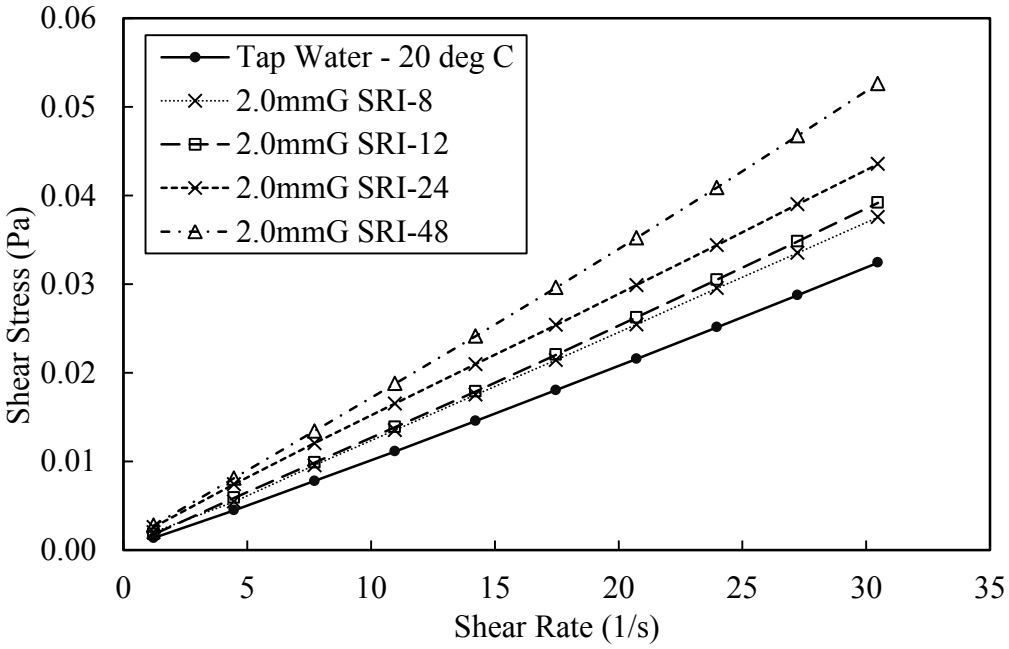

Figure 5.21. Comparison of rheometer results for 2.0 mm gravel slurry samples; SRI = 8, 12, 24, and 48 hours; Temperature = 20 °C

Table 5.3: Viscosity of the 2.0 mm gravel slurry samples measured using AR-G2 rheometer; Temperature = 20 °C

Slurry	Slurry Replacement Interval (hrs)	Viscosity (mPa-s)	Fines concentration (%)
Tap water	n/a	1.05	0
Tap water + 2.0 mm Gravel	8	1.23	0.8
	12	1.28	1.01
	24	1.44	1.67
	48	1.71	2.12

rheogram for each sample has been plotted, and the apparent viscosity has been calculated from the slope of the graph. Figure 5.21 demonstrates a comparison between the rheometer results for 2 mm gravel slurry samples collected after experiments with different SRI. The solid symbols in the figure indicate the rheometer data for tap water at 20 °C that was used as the carrier fluid forthe sand particles during the experiment, while the other markers indicate the rheometer data for carrier fluid samples collected after experiments. It is evident from Figure 5.18 that the viscosity of each sample increases as the SRI increases. The calculated viscosities of the tap water and the carrier fluid samples are presented in Table 5.3 above. The viscosity of the slurry increases about 17% just after 8 hours of operation, and the amount of increase is approximately 63% of the tap water viscosity after 48 hours of operation. The fines concentration in the carrier fluid samples has been measured using a pycnometer and is presented in Table 5.3 as well. These measurements clearly indicate that the fines concentration in the carrier fluid increases with SRI, and therefore the viscosity of the 2.0 mm gravel slurry is not constant, rather increasing with time following a power law relation (see Figure 5.22). However, the change in the fines concentration and sample viscosity is not the same for smaller sand particles or harder particles. Figure 5.23 and 5.24 shows the rheometer results for the SIL 4 sand particles and Al_20_3 particles,

respectively. For the SIL 4 sand, the change in the viscosity is not as profound as for the larger gravel particles, and for the relatively hard Al_20_3 particles, the degradation and the change in viscosity is negligible.

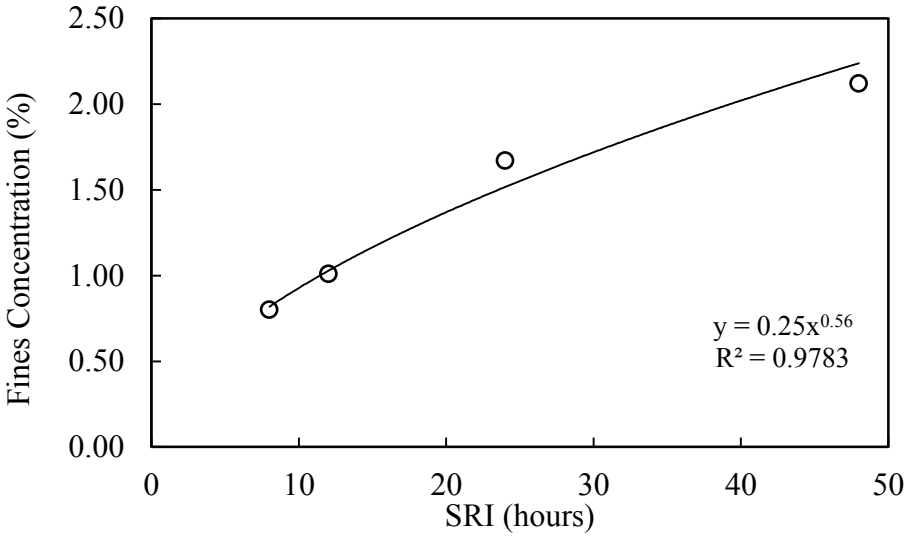

Figure 5.22. Increase in fines concentration in gravel slurry with SRI; d_{50} = 2 mm, C_s = 20%, N = 60 RPM

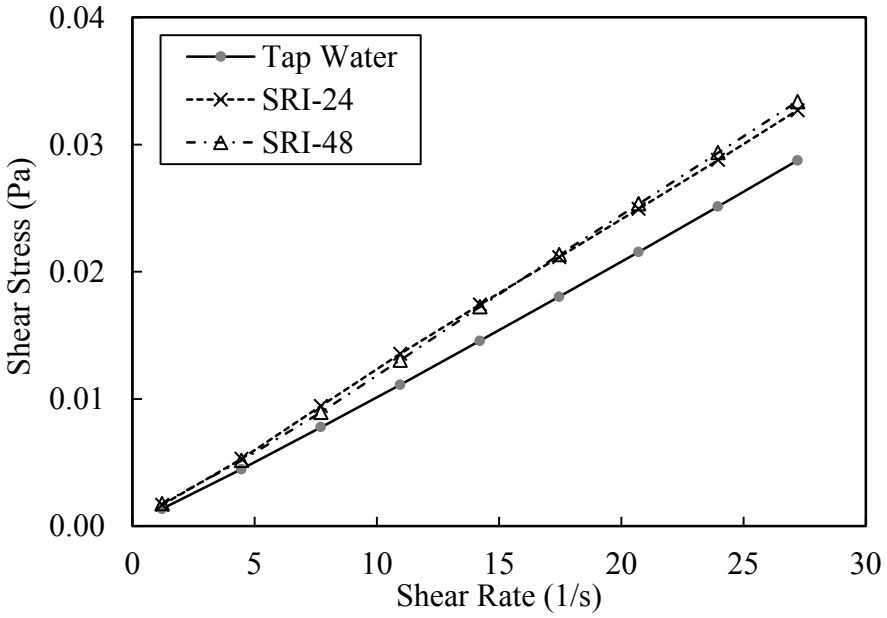

Figure 5.23. Comparison of rheometer results for 0.425 mm SIL 4 slurry samples; SRI = 24 and 48 hours; Temperature = 20 °C

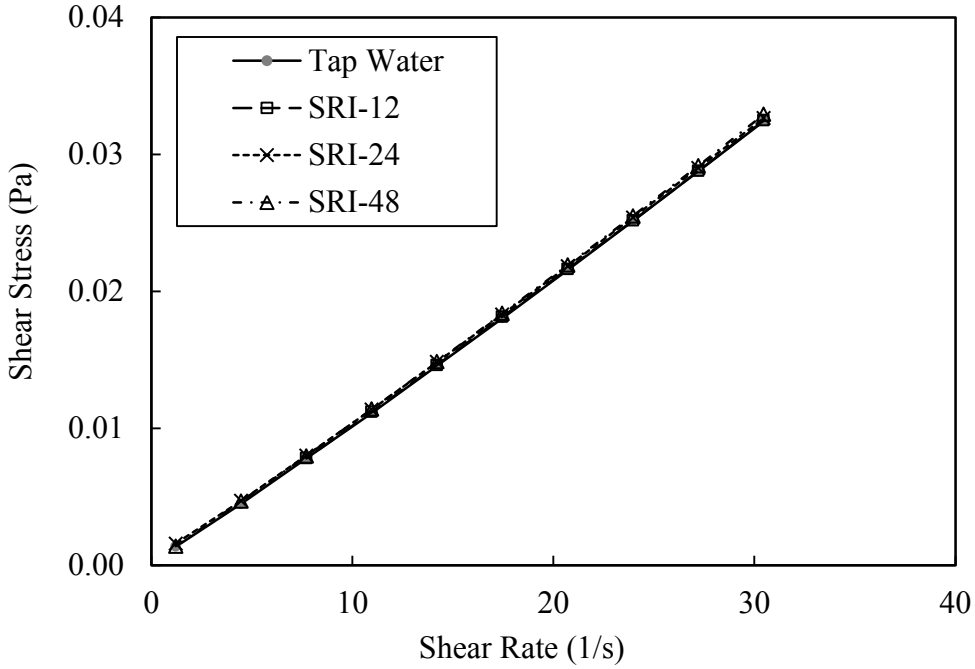

Figure 5.24. Comparison of rheometer results for 0.425 mm Al_20_3 slurry samples; SRI = 12, 24 and 48 hours; Temperature = 20 °C

Contracer analysis was also conducted on the test coupons for the 2 mm gravel SRI experiments. The roughness measurement of the eroded surface is presented in Figure 5.25, and focused on the leading edge region of the test coupons. In this figure, the left edge on $x-$ axis (30 mm) marks the leading edge of the test coupon. Figure 5.25 confirms that the thickness loss from the coupon surface is a function of the SRI. As the SRI increases, the edge effect as well as the erosive wear on the test coupons decreases. It is also noticeable that the edge effect becomes less severe as the SRI increases. For example, material loss at the leading edge of the coupon is about 2.1 and 1.6 times of the average material loss for 8 hours and 48 hours SRI experiments, respectively. The measured thickness of the test coupons using the contracer was converted by integration into volume of material lost and then converted into the mass of material lost. A trapezoidal method was used for the integration. The comparison between mass loss calculated

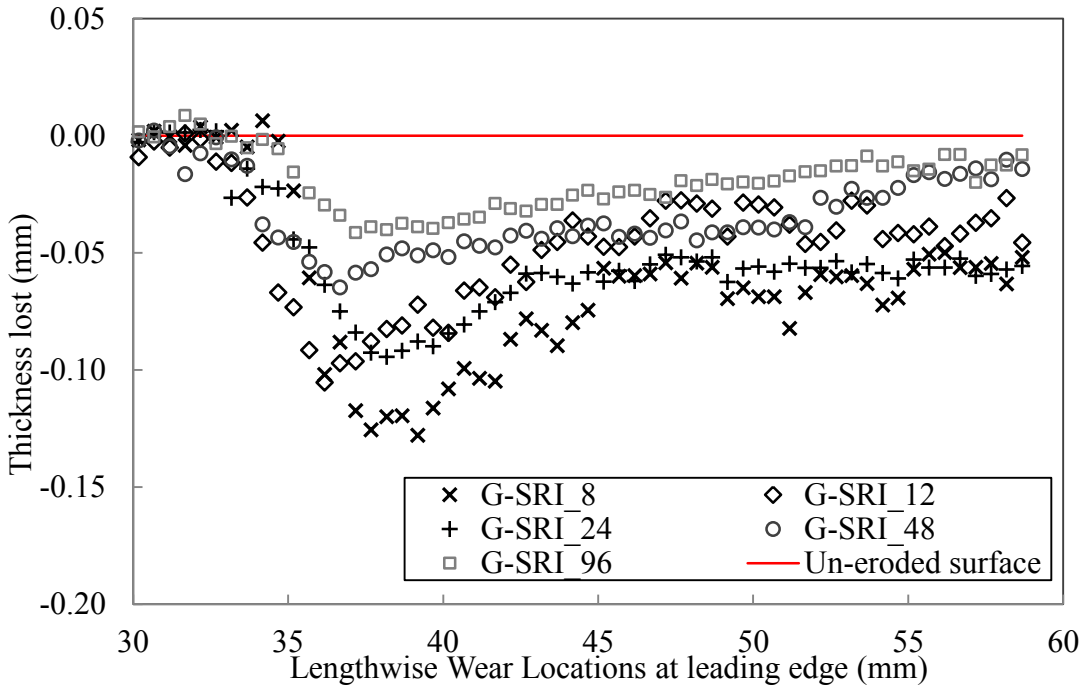

Figure 5.25. Wear patterns at the leading edge of test coupons at different SRI SRI = 8, 12, 24, 48 and 96 hours; d_{50} = 2 mm

from the contracer data and the measured mass loss data is presented in Table 5.4. Differences between these results are within reasonable limits, and indicate that the contracer measurement can be a useful method for calculating material loss at the edge affected region to correct the amount of material loss due to proper erosive wear to compare with pipeline data.

Table 5.4: Comparison between the contracer and material loss measurement

Slurry	Slurry Replacement Interval (hrs)	Measured mass loss (gm)	Mass loss from contracer measurement (gm)	Deviance (%)
Tap water + 2.0 mm Gravel	8	2.37	2.0	15.4
	12	2.13	1.77	17.0
	24	1.61	1.61	0.22
	48	0.98	1.18	20.4
	96	0.62	0.68	10.7

5.7 A preliminary analysis of the potential of the TWT to simulate pipeline wear

5.7.1 Strengths and Limitations of the TWT

During this study, the performance of the TWT was analyzed through commissioning, qualitative flow observation and parametric study of erosive wear. Although the TWT performed well by displaying good conformance with the generally accepted wear trends, under some operating conditions those do not appear to hold, i.e. in the case of tests with smaller particles (0.250 mm) as discussed in Section 5.4.3. Also, the comparison between the experimental results of the TWT and the horizontal recirculating pipe loop [7], under similar operating conditions, showed significant differences, which will be presented in the next section. To make it possible to mitigate these deficiencies and to make the TWT an improved laboratory scale device for pipeline wear testing, the following strength and limitations of the TWT have been identified:

- The particle degradation reported inside the TWT is quite low compared with other existing wear testing devices [5]. However, SRI experiments with different particles have been completed during this study and they suggest that the SRI experiment data can be extrapolated successfully to get the zero particle degradation wear rate to compare results with slurry pipelines.
- The sliding bed of particles is apparent for larger particles at higher RPM, but the smaller 250 μm particles start to form a suspended-particle slurry above 40 RPM. Also, the effective particle-coupon contact area during an experiment is a function of wheel RPM, particle size and solids concentration, which need to be determined and taken into account during the wear rate calculation.

- The sliding bed of particles inside the TWT is not stationary, rather it moves with the TWT outer wall due to the wall friction. As a result, the relative velocity between the sliding bed and toroid wheel is an important control parameter for measurement and scaling of the TWT wear result to compare with pipeline behavior.
- The small step height at the coupon-coupon window interface can introduce severe edge effects, which change the uniformity of the wear pattern on the test coupons. The gravimetric measurement of the test coupons is not enough for a good quantitative prediction of material loss to compare with slurry pipeline erosion. Ultrasonic measurement or contracer measurement is necessary to analyze the wear pattern, and to calculate the average wear rate accurately to compare with pipeline erosion.
- During coarse particle hydrotransport, the solid particles that slide on the bottom pipe wall, transmit a normal stress (σ_{SL}) and causes the Coulombic friction based erosive wear as discussed in Chapter 2. This stress component is proportional to the normal load imposed by the weight of the sliding bed on the test coupon. This normal load enacted by the slowly moving sliding bed in the TWT is not scaled to the actual pipeline condition, and the hydrodynamics of the flow inside the TWT and an actual pipeline are quite dissimilar. Therefore, the normal load on the test coupons should be calculated and scaled to the applicable condition for accurate prediction of the wear rate.

5.7.2 TWT Results vs. Recirculating Pipeloop Results

To see how well the TWT can predict the wear rate compared to a pipeline, 0.425 mm SIL 4 sand particles have been tested in the TWT for different SRIs at 60 RPM (1.9 m/s), and the absolute wear rate was calculated. Among the concerns regarding the TWT measurement stated in the previous section, the absolute wear rate calculated from the TWT experiments was corrected for the actual particle-coupon contact area and the edge effect on the leading edge region. However, no corrections were made for the normal load on the test coupons, the relative velocity between the particles and test coupons, and the effect of hydrodynamics due to the TWT geometry. Figure 5.22 shows the corrected SRI curve for the SIL 4 sand particles, and indicates an absolute wear of 5.0 mm/yr. Material loss experiments under similar operating conditions was conducted earlier by Sadighian *et al.* [7] using a horizontal recirculating pipe loop at the Saskatchewan Research Council (SRC). The uncertainty analysis of the wear rate study using the TWT was completed for SIL 4 sands, which was discussed in Chapter 4 earlier. Based on that analysis, the sensitivity of this extrapolation was analyzed, which is presented in detail in Appendix E. The sensitivity analysis indicated that the corrected zero particle degradation wear rate for SIL 4 sand particle is in between 4.1 mm/year to 5.8 mm/yr, which is approximately ± 17 % within the absolute wear (5.0 mm/year) reported in Figure 5.26.

Sadighian [7] used two pipe test sections having 69 mm and 75 mm diameter, respectively, and measured the erosion rate for different velocities ranging from 2.3 m/s to 3.5 m/s. Comparison between the existing pipe loop results at 2.3 m/s flow velocity and the TWT results at 1.9 m/s wheel velocity is presented in Figure 5.27. The deviation between the results is as high as 50% and it is quite conspicuous in Figure 5.27.

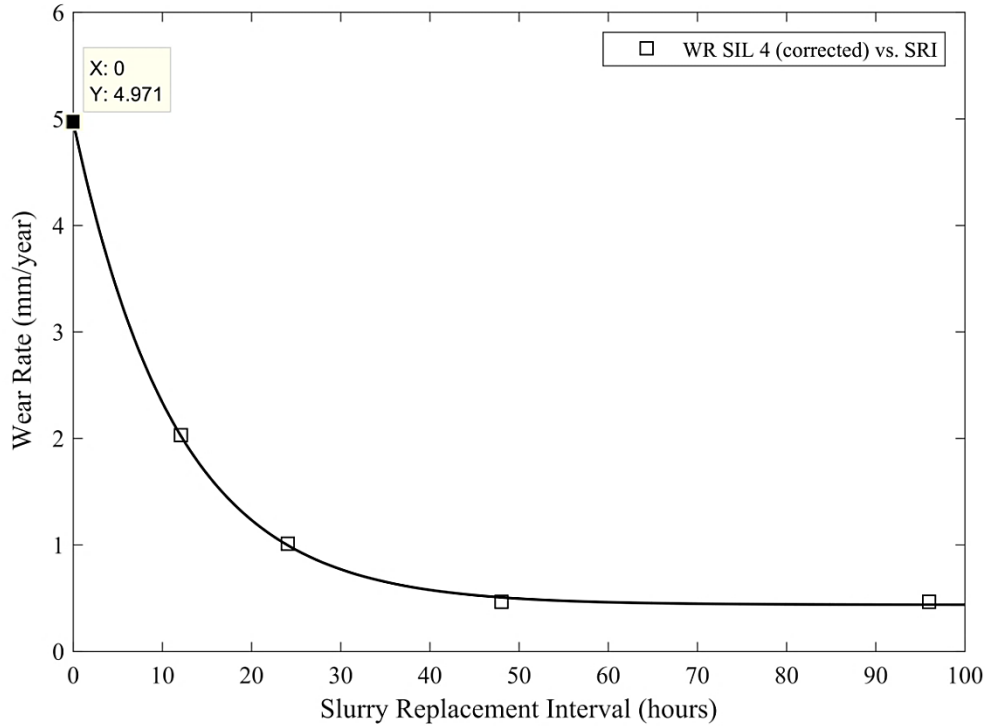

Figure 5.26. Zero particle degradation wear rate for 0.425 mm SIL 4 sand slurry; N = 60 RPM, Particle-Coupon contact area factor = 0.6

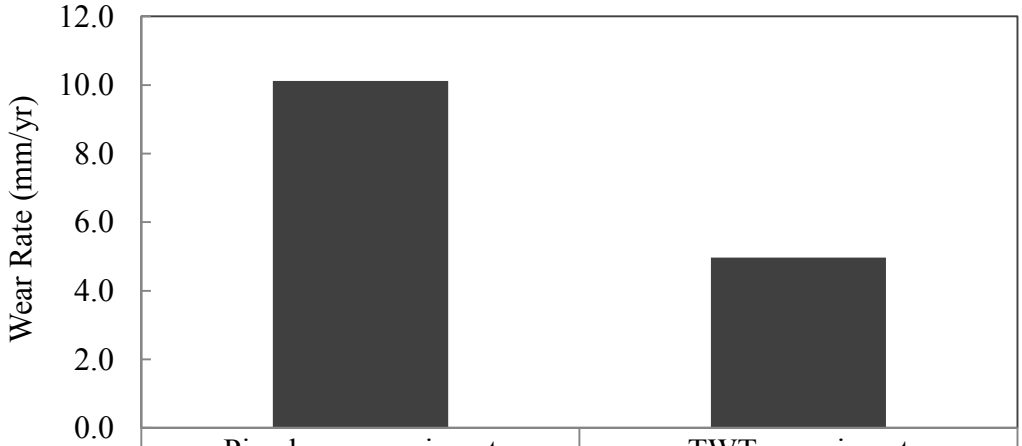

Particle	425 µm SIL 4; C_s = 20%	425 µm SIL 4; C_s = 20%
Velocity	2.3 m/s	1.9 m/s

Figure 5.27. Comparison between the Pipe Loop experiment and the TWT results

One of the major causes of this deviation is the relative velocity between the particles and test coupon. As stated earlier, the sliding bed velocity inside the slurry pipeline and the wheel RPM of the TWT is not directly comparable, and the velocity of particles has a significant effect on the wear rate due to Coulombic friction. Therefore, a detailed study and measurement of the relative velocity between particles and test coupon is of utmost importance, and is highly recommended for future works. Also, the contact load of particles on the bottom wall is different for the pipe loop and the TWT. The hydrodynamics of the TWT is such that a consistent strong backflow of slurry was seen from the qualitative flow observation using the ATW, which will be discussed in Chapter 6 in detail. The presence of this backflow lessens the normal load exerted by the sliding bed on the bottom surface. The TWT rotates in a vertical plane and therefore, the normal load by the sliding bed is 100% only at the instant when the test coupon is in the vertical 0° position at the bottom of the TWT; for other angular positions within the slurry wetted area, only a portion of the sliding bed weight act as the normal load component on the test coupon. Proper quantification and comparison of these differences between the TWT and an actual pipeline is necessary for the erosion modeling and comparison of test results with the pipe loop tester.

5.8 Conclusions

The experimental investigations of this study have shown that the TWT is capable of producing reproducible absolute erosive wear results under controlled dissolved oxygen levels of the slurry. The parametric experimental studies showed reasonable similarity with generally accepted wear trends from existing literature for most slurries. However, the TWT is not at the stage of being the ideal wear test simulator for industrial slurry pipelines, but the major concerns

have been identified. Understanding the hydrodynamics of the slurry, quantifying both the normal load on the bottom surface and a relative velocity between particles and test coupon in the rotating toroid wheel will make a significant improvement to this method.

Chapter 6
CFD Analysis of the Hydrodynamics of an Air-Water Multiphase System in a Rotating Toroid Wheel[1]

6.1 Introduction

Slurry behavior inside a TWT is not identical to a pipeline that transports concentrated coarse particle slurries. In the pipeline, the solids concentration and velocity profiles are asymmetric [20] and coarse particles form a sliding bed which directly affects the pump power requirements, erosion rate and erosion pattern; specifically, the sliding bed contributes significantly to abrasive wear at the pipe invert [50]. The preliminary observations made for the TWT indicated that it induces slurry flow in different directions at the outer/inner walls and at some point within the mixture, producing concentration and velocity gradients in both the radial and tangential directions. The heavier coarse particles tend to settle at the bottom and the smaller particles remain dispersed and suspended. The rotation of the wheel also makes the slurry move along with the wall and tumble down due to gravity after reaching the slurry-air interface at the downstream location. The behavior of the slurry in the rotating toroid wheel is thus more complex and requires advanced fundamental analysis to compare the wear in a pipeline with that obtained in a TWT. As discussed in the previous chapters, it has been observed that under some operating conditions, generally accepted wear trends were found in the TWT experimental studies. However, during experiments with smaller particles (e.g. 0.250 mm particles), the

[1] A version of this chapter has been presented in a conference. Sarker, N.R., Islam, M.A., Sanders, R.S., Fleck, B.A. (2015), 23rd Annual Conference of the CFD Society of Canada, Waterloo.

generally accepted wear trends do not hold. Also, the direct comparison of TWT wear results with the pipe loop wear results shows significant discrepancy. Again, a better fundamental understanding of the hydrodynamics within a TWT is required. The goal of this chapter, then, is on the Computational Fluid Dynamics (CFD) analysis of an air-water multiphase system inside a rotating toroid wheel to predict the velocity field and wall shear stress distribution in the water domain. This is a preliminary step of a more detailed investigation of the slurry hydrodynamics within a TWT.

6.2 Simulations

CFD has been used as a tool to analyze and solve slurry erosion problems by many researchers [46, 51, 52]. The focus of the current study is therefore to explore the CFD analysis of a TWT, which contains air and water at a volumetric ratio of 2:1, and rotates in a vertical plane. The commercial software ANSYS CFX 15.0 has been used in this study. ANSYS CFX has two types of multiphase flow modelling approaches: the Eulerian-Eulerian model and the Lagrangian Particle Tracking model. In this study, the Eulerian-Eulerian modeling approach has been taken as both the air and water phases were treated as continuous phases. As such, the continuity and momentum equations were defined for both phases and appropriate closure relations were utilized to account for the interphase interactions, as discussed below.

6.2.1 Governing Equations

The governing equations of the Eulerian–Eulerian multiphase flow modeling include the continuity and momentum equations for the phases being modeled, and also a volume

conservation equation and a pressure equation as constraints. The continuity equation for a continuous phase $\boldsymbol{\alpha}$ can be written as [53]:

$$\frac{\delta}{\delta t}(r_\alpha \rho_\alpha) + \nabla.(r_\alpha \rho_\alpha \mathbf{U}_\alpha) = \sum_{\beta=1}^{N_p} \Gamma_{\alpha\beta} + S_{MS\alpha} \qquad 6.1$$

Here, r_α, ρ_α and $\mathbf{U}_\alpha$ represent the volume fraction, material density and velocity of phase α, respectively. The terms present on the RHS of Equation 6.1 indicate interphase mass transfer and user specified mass sources, respectively. Since no change in the thermodynamic phase, diffusion of dissolved species, breakup and coalescence phenomena are involved in the current study, both of the terms on the RHS were neglected during the CFD modeling. Neglecting interphase mass transfer terms, the simplified momentum equation for the continuous phase α is given by [53]:

$$\frac{\delta}{\delta t}(r_\alpha \rho_\alpha \mathbf{U}_\alpha) + \nabla.(r_\alpha \rho_\alpha \mathbf{U}_\alpha \mathbf{U}_\alpha)) = -r_\alpha \nabla p_\alpha + \nabla.\bar{\bar{T}}_\alpha + r_\alpha \rho_\alpha g + M_\alpha \qquad 6.2$$

The second term on the RHS in Equation 6.2 is the stress tensor and can be written as [53]:

$$\nabla.\bar{\bar{T}}_\alpha = \nabla.(r_\alpha \mu_\alpha (\nabla \mathbf{U}_\alpha + (\nabla \mathbf{U}_\alpha)^T)) \qquad 6.3$$

Here, μ_α indicates the dynamic viscosity of phase α. The fourth term, M_α on the RHS in Equation 6.2 describes the interfacial momentum transfer term acting on phase α due to presence of other phases [53]. A free surface model was used to resolve the interface between the fluids. Interfacial transfer of momentum between the fluids is dependent on the contact surface

area between the two phases. This is characterized by interfacial area density, $A_{\alpha\beta}$ and for free surface model it is calculated from:

$$A_{\alpha\beta} = |\nabla r_{\alpha}| \tag{6.4}$$

The volume conservation equation simply states that the volume fractions sum to unity and the pressure constraint equation states that all phases present share the same pressure field. Therefore:

$$r_{air} + r_{water} = 1 \tag{6.5}$$

$$p_{air} = p_{water} = p \tag{6.6}$$

6.2.2 Model Definition

A steady state 3D Reynolds Averaged Navier-Stokes (RANS) analysis mode employing the Eulerian-Eulerian modeling approach was utilized in this study. An unstructured 3D mesh containing hexahedral mesh elements was generated using the ANSYS ICEM CFD, and mesh quality parameter evaluations (such as angle, quality, and skewness) were performed. For convergence of the CFD model, the minimum quality and minimum angle of each mesh element should be >0.3 and $>20°$, respectively [54]. For this study, the minimum quality of the mesh elements and minimum angle of the mesh elements were maintained approximately at 0.95 and 80^0, respectively to improve mesh quality and facilitate solution convergence.

The buoyancy activated CFD model considered a closed toroidal domain with a 608 mm outer diameter and 60 mm × 65 mm cross-sectional area as the geometry to be meshed and rotational direction of the toroidal domain has been considered as the axial direction in this

study. Figure 6.1 shows a 3D schematic representation of the toroid wheel domain that has been simulated in this study. Initial volume fractions of air and water in the domain were 0.67 and 0.33, respectively. A standard free surface model was applied because a distinct interface between air and water phases was observed during the Acrylic Toroid Wheel (ATW) experiments. A residual RMS error value of 1e-04 of the solution parameters was chosen as the convergence criteria for the simulation. In the CFD modeling, the flow was considered to be buoyant and to have a strong swirl component in the azimuthal direction as it includes flow in the wall bounded rotating toroid. To account for these conditions, the Reynolds Stress Turbulence models (RSM) were chosen first, because they naturally include the effects due to streamline curvature, buoyancy and secondary flows. Since the use of the $\varepsilon -$ equation with the Reynolds stress models shows deficiencies such as inaccurately predicting flow separation [55],

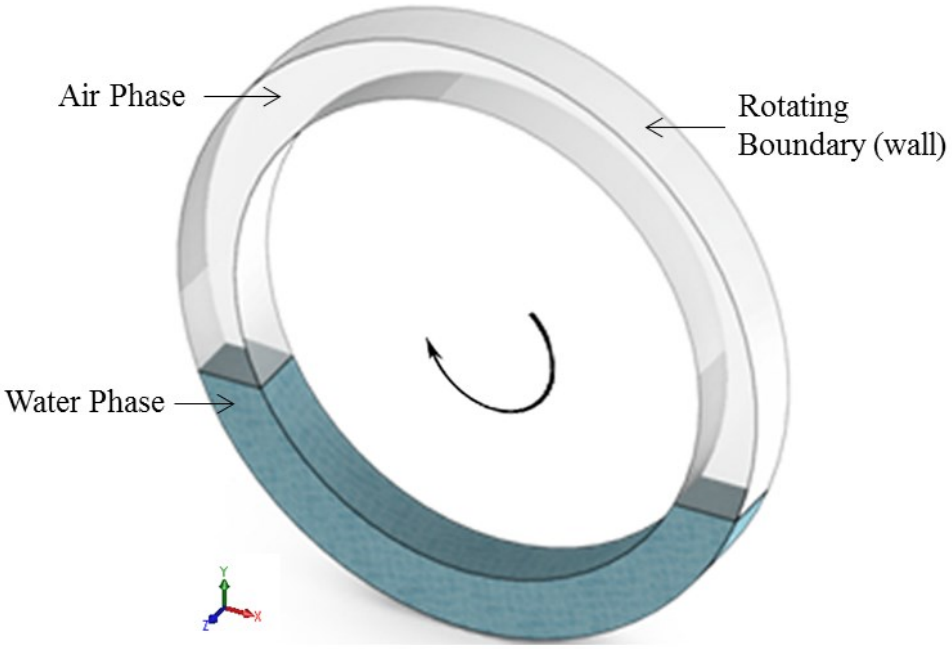

Figure 6.1. 3D schematic of the CFD domain

the $\omega-$ based Baseline (BSL) Reynolds Stress turbulence model with automatic wall treatment was employed in this simulation. Despite having the above mentioned advantages, it was found that the convergence time using the BSL Reynolds Stress model was reasonably high (approximately 30 hours). The shear stress transport (SST) model has similar advantages, and is recommended to overcome deficiencies in the $\omega-$ based Baseline (BSL) Reynolds Stress models [55]. The SST model also showed improved convergence times compared to the BSL-RSM model (approximately 7 hours). Therefore, the SST turbulence model was applied in all the simulations presented in this Chapter. No heat transfer or buoyancy turbulence was considered in the model. A no-slip rotating wall boundary condition was set. Simulations were performed for three different rotational speeds: 30, 60 and 90 RPM, having equivalent linear velocities of 1, 1.9 and 2.9 m/s, respectively.

6.2.3 Mesh Sensitivity Analysis

Mesh sensitivity is an important parameter in evaluating CFD simulations, as it indicates that the CFD modeling is independent of the number of mesh elements used, and also improves the accuracy of the results. Several tests were performed on the computational fluid domains with a number of mesh elements ranging from 38,000 to 1,000,000. The sensitivity analysis showed that about 500,000 hexahedral mesh elements were sufficient to provide a grid independent result. The maximum frictional velocity at the outer circumferential wall of the toroidal domain was chosen as the parameter to be modeled for the sensitivity analysis. The wall frictional velocity (u_*) represents the shear strength at the boundary and can be defined by:

$$u_* = \sqrt{\frac{\tau_{wall}}{\rho}} \qquad 6.7$$

For all simulations in the grid independence test, the convergence of residual error to 1e-04 was ensured. At each new refinement step, the mesh was refined (1.5–2.0 times greater than the previous step) globally to have finer cells throughout the domain and the change in the solution was observed and recorded. The process was repeated until a mesh independent solution was obtained. Figure 6.2 illustrates the variation of maximum wall frictional velocity as the number of mesh elements increases, at 90 RPM (2.9 m/s). The change in the maximum wall friction velocity is higher (about 7%) at lower mesh elements, and becomes negligible (about 0.5%) after 500,000 mesh elements. This indicates a mesh resolution of approximately 500,000 was required to ensure the solution is independent of the mesh; therefore, it was selected as the optimum mesh resolution for further CFD analysis.

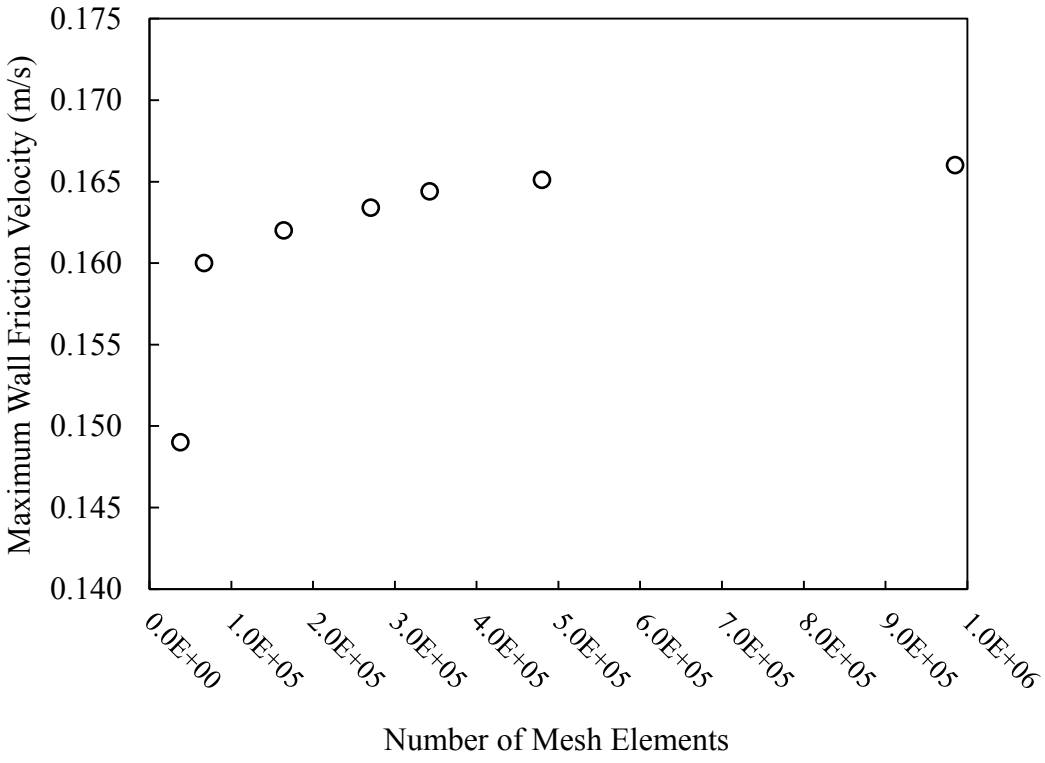

Figure 6.2. Mesh Sensitivity Analysis; N = 90 RPM

6.2.3 Comparison between Experimental and Simulation Observations

Selected CFD simulation results were compared with experimental observations made from a dimensionally similar Acrylic Wear Tester (AWT). The AWT was filled with water to one-third of its volume maintaining the same phase volume fractions as the CFD model and operated at various speeds (30, 60 and 90 RPM). Images of the rotating AWT were captured at 500 frames per second with a high speed camera (FASTEC IMAGING^{TM}, Model: TroubleShooter) and compared with the volume rendered CFD simulation results. A typical image of the AWT experiment is given in Figure 6.3 (a). In this photograph, the separation of water from the outer toroid wall at the downstream side air–water interface (i.e. the interface near the +60° position) is apparent. After the flow separation, the water tumbles back due to gravity and introduces turbulence and back-mixing. Figure 6.3 (b) shows the water velocity vectors obtained from the CFD simulation just below the downstream interface. It can be seen from Figure 6.3 (b) that water inside the toroid wheel flows forward along the rotating wall due to viscous drag until it reaches the air–water interface and then flows backward through the inner core with decreasing magnitude. Also the CFD results for the velocity fields, phasic volume fraction distributions and the wall shear stress within the toroid domain have been analyzed. The qualitative similarity of the simulation results and the actual operations are apparent, particularly at the air-water interfaces. The CFD simulation was also able to predict the water carryover near the outer circumference of the toroid domain, which was also observed during the ATW experiments conducted at higher rotational speeds (e.g. 90 RPM). Figure 6.4 provides the water volume fraction distribution obtained from the CFD simulation conducted for N = 90 RPM. The volume-rendering of water fractions obtained from CFD simulations for lower operating speeds also shows qualitative similarity with the ATW flow observations.

(a) Photograph of the downstream air-water interface during the ATW experiment

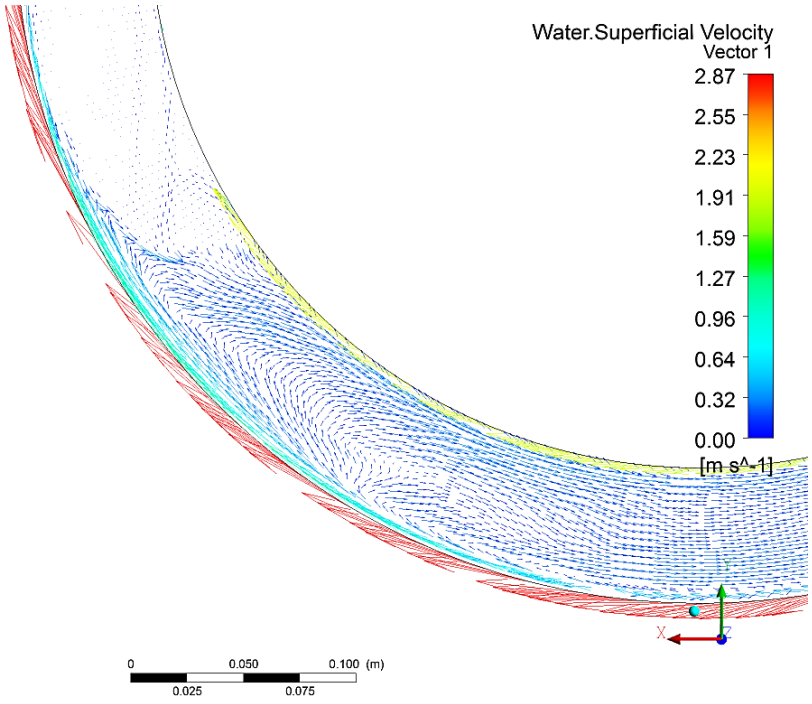

(b) Water velocity vectors at the downstream of water domain

Figure 6.3. Qualitative comparison between the ATW flow observed and CFD simulation at the air – water interface at downstream; N = 90 RPM

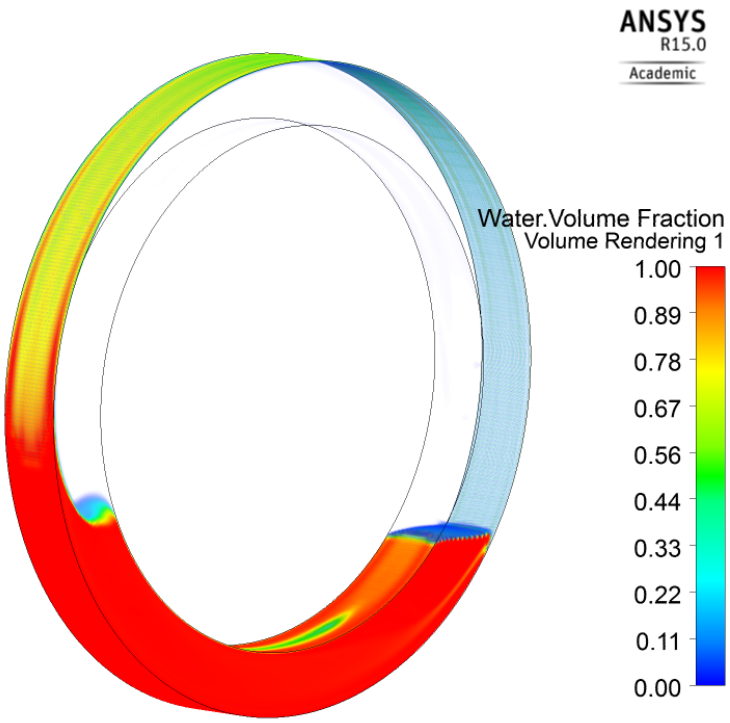

Figure 6.4. Water volume fraction distribution within the toroid domain; N = 90 RPM

6.3 Results and Analysis

To study the TWT hydrodynamics, the velocity field and the wall shear stress parameters have been investigated. Figure 6.5 defines different locations inside the rotating toroid domain (anti-clockwise direction) at which the water velocity profiles were plotted and analyzed in Figures 6.6 through 6.9. Here, Position 0 indicates the bottom of the wheel (6 o'clock position), u_20 is 20° upstream (right) of the bottom, d_20 is at the 20° downstream location of the toroid domain and so forth. Also, the velocity profiles along the channel width were plotted at different radial locations for Position 0. These positions are marked as 0.1 to 0.4 in Figure 6.5, where Positions 0.1 and 0.4 indicate the bottom and top wall of the CFD domain, respectively. Also, Positions 0.2 and 0.3 indicate radial positions at 25% and 75% channel height in the domain, respectively.

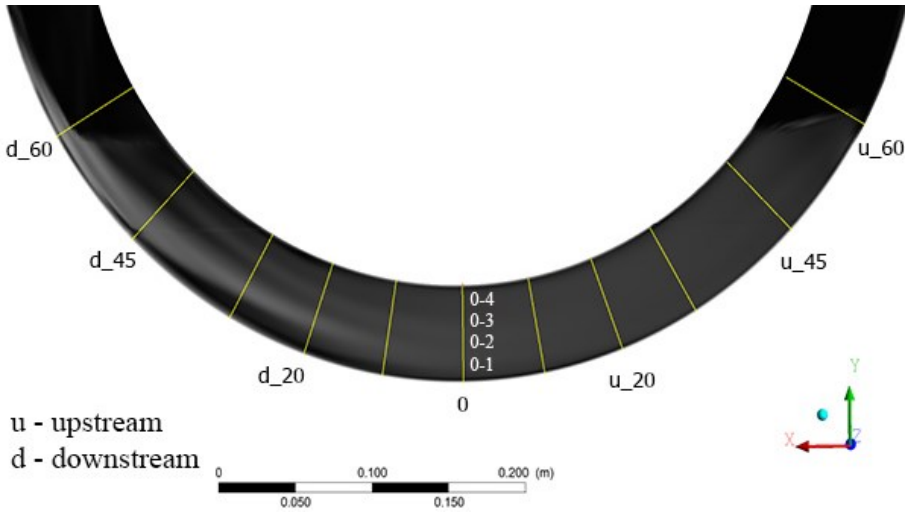

Figure 6.5. Data locations considered in the toroid domain

Figure 6.6 shows a typical water velocity profile in the X-direction at Position 0 with the toroid rotating at 90 RPM. In this figure, V_x indicates water velocity in X-direction. A normalized channel height, *y/H* has been used as the ordinate of Figure 6.6, where *H* indicates the overall height of the flow domain. This figure highlights the counter-current flow situation in the toroid; the positive values of water velocity near the wall indicate induced velocity in the

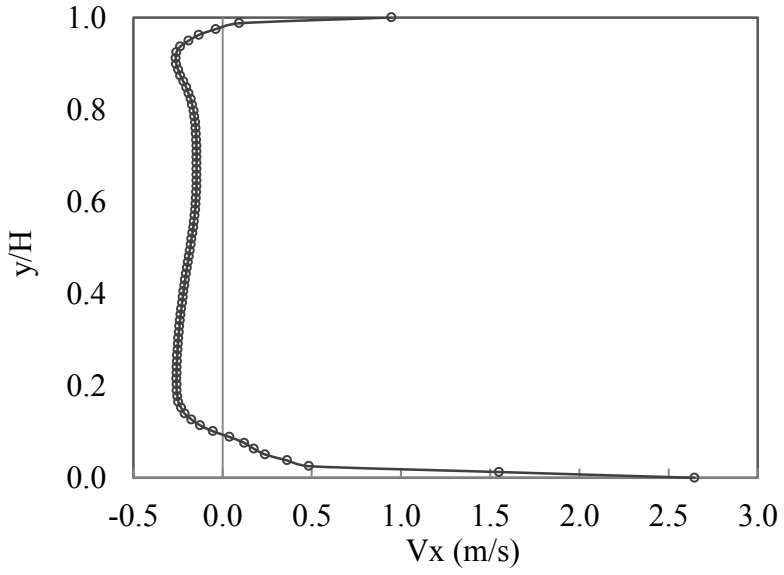

Figure 6.6. X-direction water velocity profile at Position 0; *N* = 90 RPM

direction of rotation and the negative values indicate the backflow of water. Figure 6.7 compares velocity profiles at different angular locations inside the toroid wheel rotating at 90 RPM. It was found that the flow at the upstream is more developed while the downstream side remains unsteady due to the back–mixing. From this figure, it can also be observed that at any channel height, the magnitude of the backflow is greater at downstream locations and it continuously diminishes as water moves to the upstream side. The inflection point, the point in the counter-current flow inside the domain, where the mean water velocity is zero, is closer to the bottom wall at upstream locations and moves away significantly from the bottom wall when one takes downstream locations into consideration. The locations of the inflection points for different angular positions taken from Figure 6.7 are shown in Table 6.1. As the wheel speed increases, the disturbance in the flow field becomes more prominent. Figure 6.8 shows that as RPM increases, the inflection point also moves slightly away from the bottom wall of the TWT.

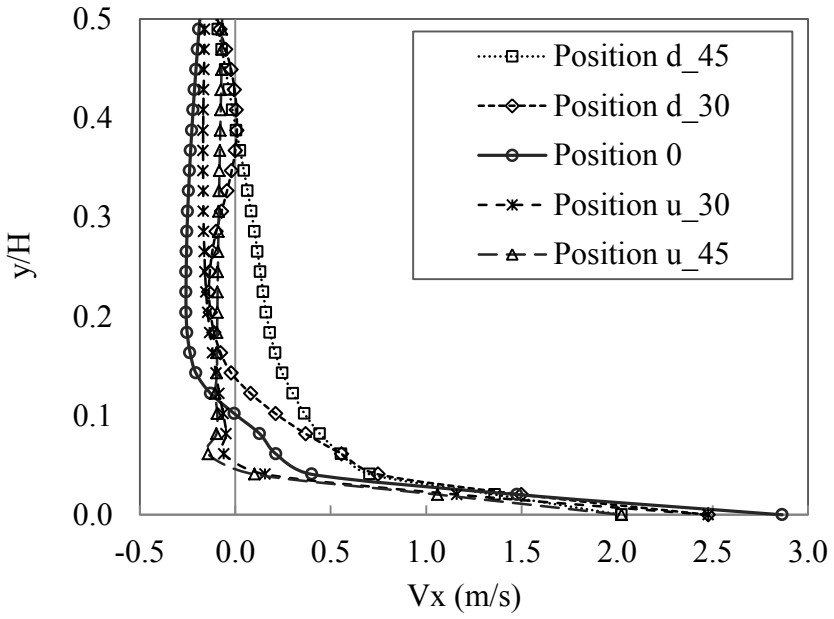

Figure 6.7. X-direction Water velocity profiles at different angular positions; *N* = 90 RPM

Table 6.1. Locations of the inflection point at different angular positions; N = 90 RPM

Angular position	Location of inflection point (*y/H*)
u_45	0.04
u_30	0.05
0	0.10
d_30	0.13
d_45	0.40

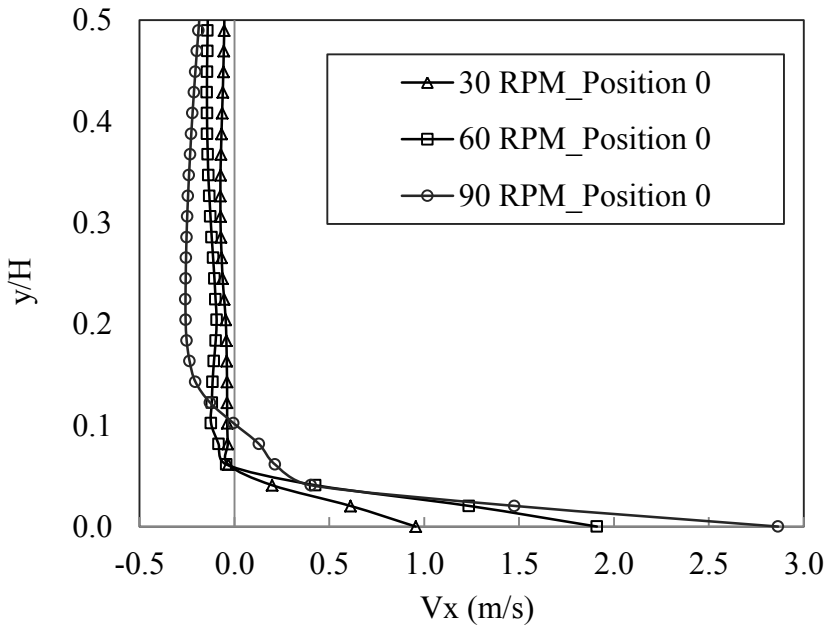

Figure 6.8. Comparison of water velocity profiles at Position 0 for N = 30, 60 and 90 RPM

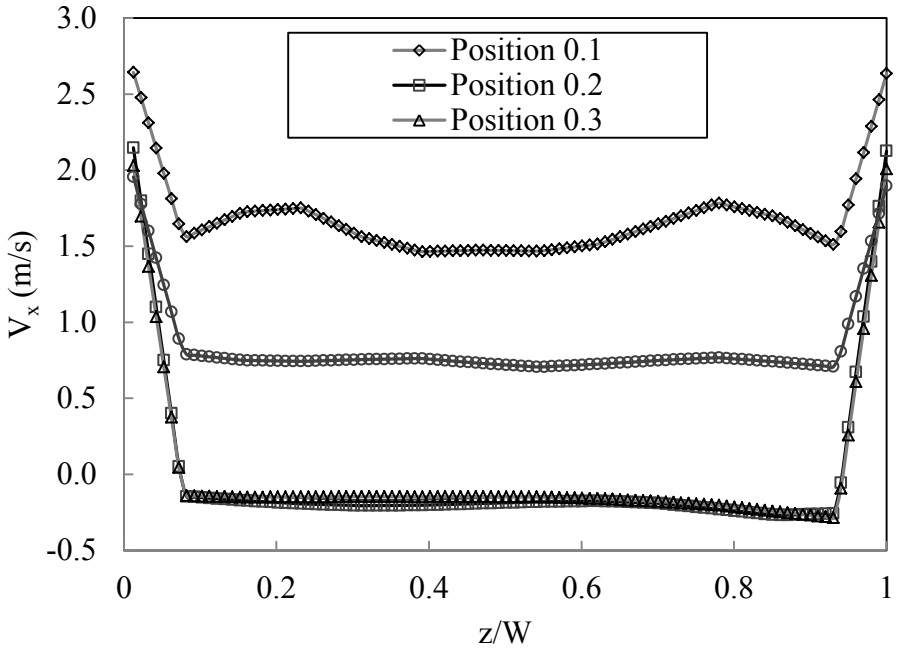

Figure 6.9. Comparison of water velocity profiles at Position 0 for different radial locations; *N* = 90 RPM

Figure 6.9 shows water velocity distributions along the wheel width at Position 0 for four radial positions, i.e. Position 0.1 to 0.4. In this figure, water velocity along the X-direction has been plotted against the normalized channel width (*z/W*) where *W* is the width of the flow domain. Water near the side walls of the toroid (at *z/W* = 0 and *z/W* = 1) flows in the direction of wheel rotation due to viscous drag and water velocities at greater values of radius (*r*) are higher as expected. In the core regions (Positions 0.2 and 0.3, as indicated in Figure 6.5) water flows in the opposite direction as indicated by the negative velocities on the graph. On the basis of the predicted velocity distributions, it can be inferred that TWT may induce a flow near the wall, which will drag the the settled particles at the bottom of the TWT. Consequently, the relative velocity between the settled particles and test coupons in the TWT may not replace the relative velocity between the sliding bed and the slurry pipeline as a direct scaling parameter. Similar observations were made using the AWT as discussed in Chapter 5.

Figure 6.10 shows the YZ-plane view of water carried along the outer wall of the TWT at the downstream location (side view) for different rotational speeds. Figure 6.10 (a) shows the images of water lift (in monochrome) during actual ATW experiments at 30, 60 and 90 RPM. The white area in the photograph indicates the water domain in the ATW, and the greyish region marks the water volume fraction carried along the wall. Figure 6.10 (b) displays the CFD simulation results under similar operating conditions, where the area shown in red denotes 100% water, and indicates the height of the water lift for a specified RPM. It shows that as the RPM increases (which means greater energy input to the water), the higher the water lift along the toroid wall. For example, the water lift is greater at 90 RPM than 30 RPM. Figure 6.10 (b) also shows that the water lift along the side walls of the toroid is higher and basically confirms that 90 RPM is the carry-over speed, which was observed earlier from the qualitative flow observation tests conducted using the ATW.

Figure 6.11 illustrates the wall shear stress distribution at the bottom wall of the toroid tester. The XZ-plane view (bottom view) wall shear stress distribution is shown for different operating speeds. The left and the right end of the plot denote 60° upstream and 90° downstream angular positions relative to Position 0, respectively. It is evident from Figure 6.11 that (i) the wall shear stresses are not uniform on the bottom wall of the toroid, (ii) the shear-affected zone is wider at higher operating speeds, and (iii) average values of the wall shear stress are lower at lower operating speeds. Moreover, the wall shear stress values are almost symmetric relative to Position 0, having a maximum near Position 0. Figure 6.12 has been plotted to illustrate the effect of rotational speed on the shear stresses acting on the bottom wall of the toroid. It shows the variation of the wall shear stress along the centerline of the bottom wall of the toroid tester in the water domain. Positive and negative angular positions indicate, respectively, the downstream

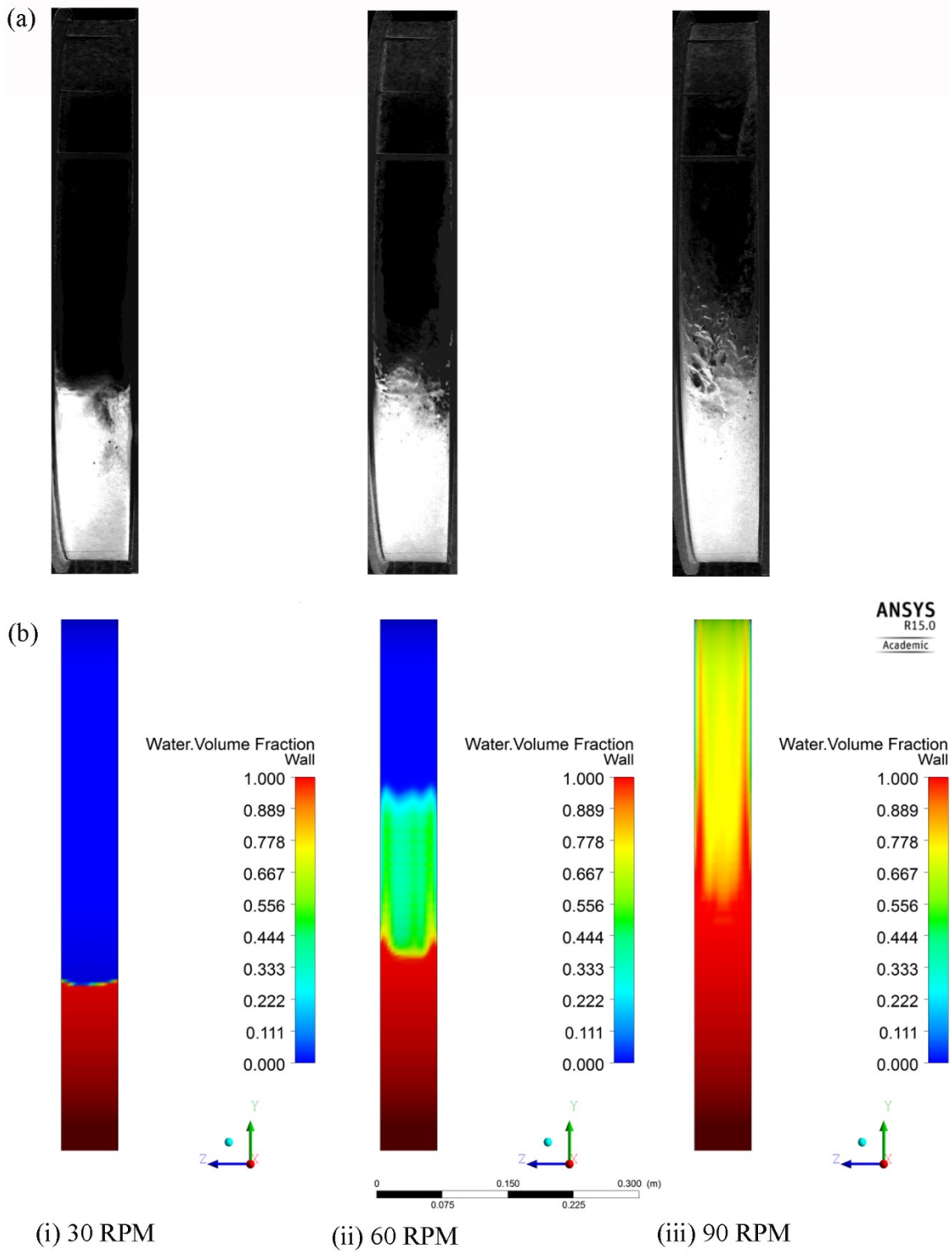

Figure 6.10. Water level along the toroid outer wall at the downstream seen from YZ plane (a) ATW experiment (in monochrome) (b) CFD analysis

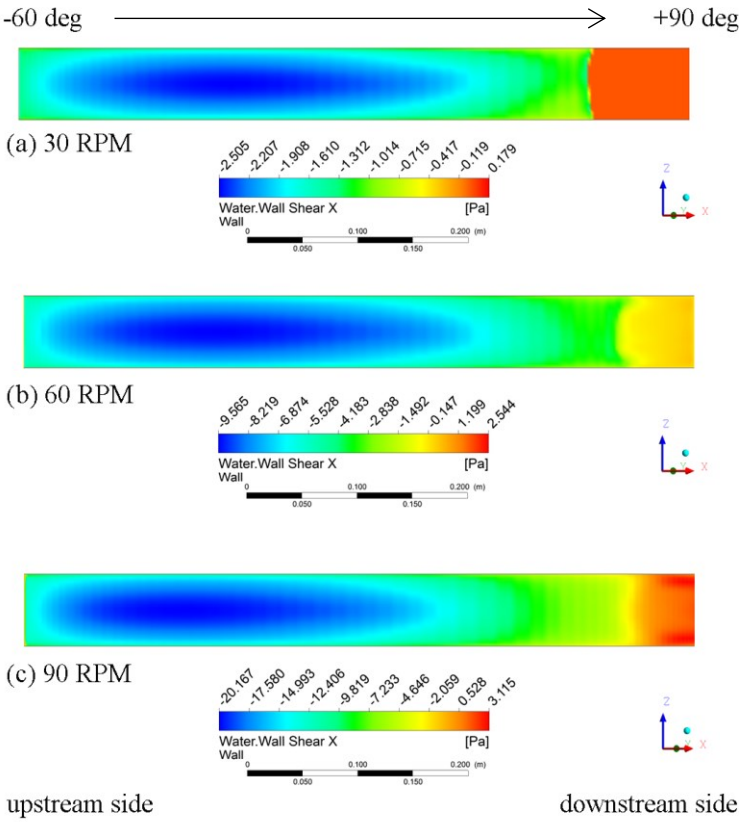

Figure 6.11. Wall shear stress distribution on toroid outer wall seen from XZ plane (bottom view)

and upstream locations relative to Position 0. Different symbols represent different rotational speeds. As shown in Figure 6.12, the maximum shear stress, in an absolute sense, is found at Position 0, and the shear stress distribution is roughly symmetric at this position. As expected, higher rotational speeds lead to higher wall shear stresses.

6.4 Conclusion

The hydrodynamic analysis of an air-water multiphase system in a rotating toroid wear tester has been conducted using an Eulerian-Eulerian based CFD modeling approach. This study is an initial step to understand slurry behavior inside the wear tester. A qualitative comparison of the CFD simulations is made with the flow observed in the acrylic toroid wheel (ATW). The

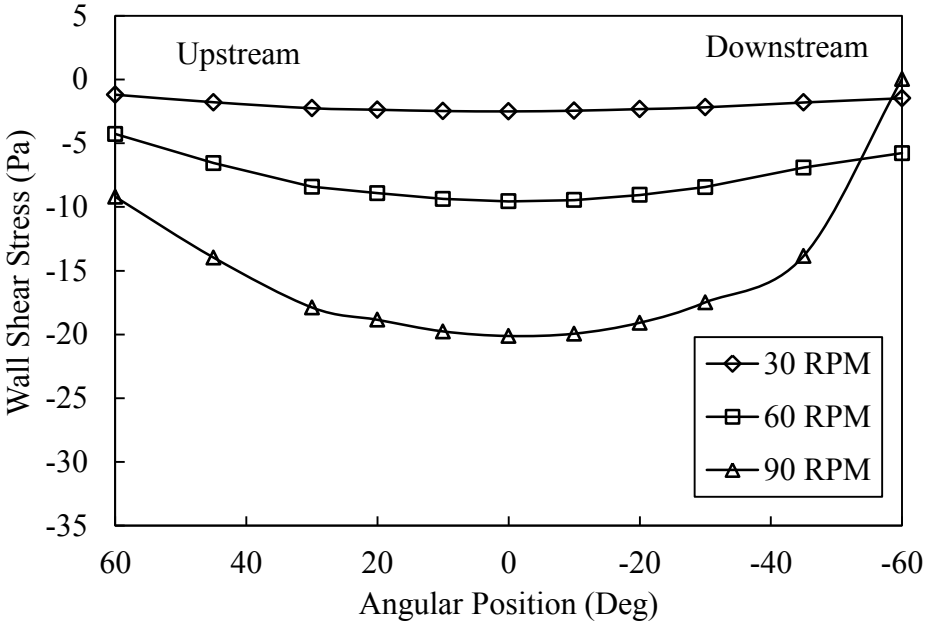

Figure 6.12. Variation of the wall shear stress along the centerline of the bottom wall of the TWT

qualitative similarity of the simulation results and the actual operation was apparent. Velocity distributions obtained from the CFD simulations demonstrate that water flows forward along the rotating wall due to viscous drag until it reaches the air-water interface and then flows backward through the inner core. Moreover, a non-uniform distribution of shear stress at the bottom wall of the toroid is found.

Further CFD analyses with dispersed solids will help improve the understanding of the behavior of slurry inside the toroid wear tester, which will ultimately allow for a quantitative comparison between wear rates measured in a toroid wear tester and those found in operating slurry pipelines.

Chapter 7
Conclusions and Recommendations for Future Work

7.1 Conclusions

The primary objective of this research was to develop a standard methodology for erosive wear analysis using a TWT, under conditions meant to simulate dense slurry flows in a pipeline. A TWT was built, commissioned and checked for data reproducibility using different slurries. Qualitative flow observations were conducted using an acrylic toroid wheel (ATW) to better understand the slurry behavior and particle-coupon contact inside the TWT. Parametric experiments were conducted, varying the particle size, shape and wheel RPM, which have indicated that the TWT results are in qualitative agreement with existing literature, in terms of general wear trends. The slurry replacement interval (SRI) technique was tested, fitted with an exponential model and then extrapolated to determine the absolute wear rate. Strengths and limitations of material loss experiments using the TWT were identified as well.

Qualitative flow observations helped to evaluate the slurry flow behavior and particle-coupon contact mechanism. It was observed that the rotating toroid wall induces a slurry flow near the wall and therefore, smaller particles (i.e. 0.250 mm Pyrex beads) were seen to concentrate towards the direction of rotation. The effective particle-coupon contact area for 0.250 mm particles is about 80% of the slurry wetted area. The distribution of particles was also checked for 0.50 mm beads and 2.0 mm gravels, and the effective particle-coupon contact area found was found to be about 70% and 50% of the slurry wetted area of the wheel, respectively.

The maximum allowable operating speed to ensure a particle sliding bed on the test coupons was found: specifically, 30, 60, and 90 RPM for 0.250 mm beads, 0.50 mm beads, and 2 mm gravels, respectively.

Material loss experiments for carbon steel coupons (ASTM hot rolled A572 GR50) were conducted using particles having a mass median diameter (d_{50}) of 0.250 mm and 0.425 mm, and lumps (gravels) having a mass median diameter of 2.0 mm. The solids concentration in the slurry was varied from 6% to 30% (by volume), and each condition was tested at different wheel speeds, i.e. 30, 45 and 60 RPM. The temperature of the suspending liquid (water) was kept constant during these experiments, i.e. at 22 $^{\circ}$C.

Experiments were conducted during this study in which the particle size, shape, solids concentration and wheel RPM were varied. The findings from the qualitative observations were used to select the operating condtions for the material loss studies and also to calculate the wear rate. The parametric studies using the TWT demonstrated that the material loss rate is a power-law function of the macroscopic parameters like solids concentration and wheel speed. The exponents found for the solids concentration are within the range of 0.30–0.37, and the velocity exponents reported in this study are in between 2.2–2.7. These exponents are close to the values reported in the literature and indicate that the TWT is capable of producing similar wear trends as other laboratory testers as well as pipelines. Experiments conducted with different particle sizes and shapes indicated that wear increases with particle size and angularity, however, the relation is relatively complex and strongly depends on particle-coupon contact mechanism in the TWT, particle size distribution, and particle hardness.

The particle degradation in the TWT over the duration of an experiment and absolute wear rate of the test coupons (extrapolating to zero degradation) were analyzed through the SRI experiments. The SRI experiments indicate that wear rate decreases as the frequency of slurry replacement in the TWT increases. The experimental data were exponentially fitted with an R^2 value of 0.998 and the extrapolations indicate the absolute wear rate. Rheometry analysis of the carrier fluid samples shows that the viscosity of the carrier fluid increases with the SRI. The 'fines' (particles < 44.0 μm) concentration in the slurry samples was measured, which indicates an increase with the SRI as well, implying that the concentration of fines in the carrier fluid increases because of particle degradation, and as a result the viscosity of the carrier fluid increases.

Measurement of the surface roughness of the test coupons confirmed that the material loss is a strong function of the wheel speed. The effect of solids concentration is less prominent; however, near the side walls of the TWT, this effect is quite significant, which is may be due to the secondary flow of the carrier fluid induced by the rotating TWT. A zone of high wear was identified near the leading edge of the test coupons and termed as the 'edge effect', which occurs due to a step height at the coupon-wheel interface and becomes less prominent at lower wheel speeds. The edge effect is also a function of the particle abrasivity; particle abrasivity decreases during higher SRI experiments, and the edge effect decreases as well. For example, the edge effect decreases by 25% when the SRI changes from 8 hours to 48 hours.

CFD analysis of an air-water multiphase system in a rotating toroid was completed as an introductory part of the thorough study of the slurry hydrodynamics within a TWT. Velocity distributions obtained from the CFD simulations demonstrated a near wall flow of water due to

viscous drag. After reaching the air-water interface, the water flows backward through the inner core with decreasing magnitude. Moreover, a non-uniform distribution of shear stress at the bottom wall of the toroid is found.

Overall, the performance of a TWT was analyzed in this study by commissioning, making qualitative flow observations and conducting experimental studies of erosive wear. Corrections in the wear rate calculation were made based on the actual particle-coupon contact and particle degradation, but scaling parameters such as the velocity of the sliding bed of particles relative to the coupons and the normal load on the bottom of the TWT were not compared with an actual pipeline. Hence, the comparison between the experimental results of the TWT and the horizontal recirculating pipe loop, under similar operating conditions, showed significant differences.

7.2 Recommendations for Future Work

The direct comparison of the TWT results with the pipe loop results are not in complete agreement. The qualitative study of TWT hydrodynamics indicated a countercurrent flow within the TWT, which reduces the particle-coupon relative sliding velocity and the normal load exerted by the sliding bed on the bottom surface, unlike an actual pipeline. An initial step for a detailed CFD study was taken in this research, which asks for the continuation of the detailed CFD analysis of the TWT so that a better fundamental understanding of the hydrodynamics within a TWT will result. Also, controlled material loss experiments with proper quantification of particle shape and abrasivity parameters are required. To compare the TWT results with a pipeline and achieve a comprehensive slurry erosion model, the following recommendations are made:

- The sliding velocity of particles relative to the test coupon is required to scale the velocity parameter directly to the pipeline flow situation. To achieve this target, the setup can be configured in such a way that particle image velocimetry (PIV) technique can be applied.
- The normal load on the test coupons imposed by the sliding bed of particles generates a normal stress and is the main reason behind the Coulombic friction based wear mechanism. The normal load is a function of the thickness of the sliding bed and particle properties. Slurry density measurement devices such as Gamma-ray densitometer can be employed to determine the thickness of the bed. Also, ultra-thin integrated force sensors can be employed with the coupons to measure the normal load on the coupon. The variation of the normal loads during the rotation (as the coupon travels within the slurry wetted area) needs to be averaged and scaled to a specific pipeline application for comparison.
- Experiments can be done using test coupons having different dimensions, and the effect of the coupon geometry should be scaled. The Contracer can be employed to measure the surface roughness and interpret the results from the above mentioned experiments.
- Scanning electron microscopy (SEM) and confocal microscopy can be employed to characterize the particle shape and abrasivity before and after controlled material loss experiments. This will improve the understanding of particle degradation, the effect of particle shape and abrasivity parameters on test coupons and eventually lead to the shape factor in a detailed slurry erosion model for industrial pipelines.

- A detailed CFD analysis employing the Eulerian-Eulerian approach should be completed incorporating the particulate phase with the air-water multiphase system in the rotating toroid. It will help in understanding the complex hydrodynamics of the slurry within the TWT and also in understanding particle behaviors near the toroid wall.
- In this study, the viscosity (water, 1.0 mPa-s) of the carrier fluid and the system temperature (22 $^{\circ}$C) of the experiments were kept constant. To compare with actual pipelines and better understand the wear characteristics of the slurries, carrier fluids with different viscosities can be used and an auxiliary temperature control system can be added to the setup which will allow experimenting with higher temperatures.
- Additional experiments should be carried out using sand particle-lump mixtures in the TWT at different concentrations to study the wear characteristics in industrial pipelines. Also, experiments can be conducted by controlling the amount of dissolved oxygen level in the slurry to study the effect of corrosion and erosion-corrosion synergy in pipelines.

References

[1] **H. Bhabra, "Slurry pipeline now goes the distance," *World Pumps*, vol. 2013, no. 6, pp. 38–40, 2013.**

[2] **S. El-sayed, "Measuring wall forces in a slurry pipeline," MSc Dissertation, Dept. of Mechanical Engineering, University of Alberta, 2010.**

[3] **B. Fotty, M., Krantz., J., Been, J., Wolodko, "Development of a pilot-scale facility for evaluating wear in slurry pipeline systems," in *18th International Conference on Hydrotransport*, 2010, pp. 431–443.**

[4] **C. Huang, P. Minev, J. Luo, and K. Nandakumar, "A phenomenological model for erosion of material in a horizontal slurry pipeline flow," *Wear*, vol. 269, no. 3–4, pp. 190–196, 2010.**

[5] **R. Cooke, G. Johnson, and P. Goosen, "Laboratory Apparatus for Evaluating Slurry Pipeline Wear," *Econ. Wear Mater.*, no. March, pp. 1–17, 2000.**

[6] **P. Goosen and I. Malgas, "An Experimental Investigation into Aspects of Wear in Boiler Ash Disposal Pipelines," *14th Int. Conf. slurry Handel. Pipeline Transp.*, no. September, pp. 8–10, 1999.**

[7] **A. Sadighian, "Investigating Key Parameters Affecting Slurry Pipeline Erosion," PhD Dissertation, Dept. of Chemical & Materials Engineering, University of Alberta, 2016.**

[8] **R. Gupta, S. N. Singh, and V. Sehadri, "Prediction of uneven wear in a slurry pipeline on the basis of measurements in a pot tester," *Wear*, vol. 184, no. 2, pp. 169–178, 1995.**

[9] **A. Neville and F. Reza, "Erosion-corrosion of cast white irons for application in the oilsands industry," in *NACE- International Corrosion Conference Series*, 2007.**

[10] **J. Schaan, N. Cook, and R. S. Sanders., "On-Line Wear Measurements for Commercial-scale, coarse-particle slurry pipelines," in *17th International Conference on HYDROTRANSPORT*, 2007.**

[11] **J. I. Ukpai, R. Barker, X. Hu, and A. Neville, "Determination of particle impacts and impact energy in the erosion of X65 carbon steel using acoustic emission technique," *Tribol. Int.*, vol. 65, pp. 161–170, 2013.**

[12] **A. Gnanavelu, N. Kapur, A. Neville, and J. F. Flores, "An integrated methodology for predicting material wear rates due to erosion," *Wear*, vol. 267, no. 11, pp. 1935–1944, 2009.**

[13] **B. Gandhi, S. Singh, and V. Seshadri, "Study of the parametric dependence of erosion wear for the parallel flow of solid–liquid mixtures," *Tribol. Int.*, vol. 32, no. 5, pp. 275–282, 1999.**

[14] **R. M. Summer, "A Review of Pipeline Slurry Erosion Measurements and Research Recommendations," in *Slurry Erosion: Uses, Applications, and Test Methods, ASTM STP 946*, J. E. Miller and F. E. Schmidt, Eds. Philadelphia: American Society for Testing and Materials, 1987, pp. 91–100.**

[15] **R. J. K. Wood and T. F. Jones, "Investigations of sand–water induced erosive wear of AISI 304L stainless steel pipes by pilot-scale and laboratory-scale testing," *Wear*, vol. 255, no. 1–6, pp. 206–218, 2003.**

[16] **R. J. K. Wood, T. F. Jones, J. Ganeshalingam, and N. J. Miles, "Comparison of predicted and experimental erosion estimates in slurry ducts," *Wear*, vol. 256, no. 9–10, pp. 937–947, 2004.**

[17] **L. L. Parent and D. Y. Li, "Wear of hydrotransport lines in Athabasca oil sands," *Wear*, vol. 301, no. 1–2, pp. 477–482, 2013.**

[18] **R. G. Gillies, C. a Shook, and J. Xu, "Modelling Heterogeneous Slurry Flows at High Velocities," *Can. J. Chem. Eng.*, vol. 82, no. October, pp. 1060–1065, 2004.**

[19] **R. G. Gillies and C. a Shook, "Modelling High Concentration Settling Slurry Flows," *Can. J. Chem. Eng.*, vol. 78, no. August, pp. 709–716, 2000.**

[20] **R. G. Gillies, C. a. Shook, and K. C. Wilson, "An improved two layer model for horizontal slurry pipeline flow," *Can. J. Chem. Eng.*, vol. 69, no. 1, pp. 173–178, 1991.**

[21] **R. G. Gillies, "PIPELINE FLOW OF COARSE PARTICLE SLURRIES," University of Saskatchewan, 1993.**

[22] **C. A. Shook and M. C. Roco, *Slurry Flow Principles and Practice*. Stoneham, MA: Butterworth-Heinemann, 1991.**

[23] **M. C. Roco, P. Nair, and G. R. Addie, "Test Approach for Dense Slurry Erosion," in *Slurry Erosion: Uses, Applications, and Test Methods, ASTM STP 940*, J.E. Miller and F. E. Schmidt, Eds. Philadelphia: American Society for Testing and Materials, 1987, pp. 185–210.**

[24] J. Been and F. Ju, "Prediction of Wear of Tailings Pipelines in Oil Sands Slurries."

[25] C. A. Shook and M. C. Roco, *Slurry Flow Principles and Practice*. Stoneham, MA: Butterworth-Heinemann, 1991.

[26] J. G. A. Bitter, "A study of erosion phenomena," *Wear*, vol. 6, no. 3, pp. 169–190, 1963.

[27] A. Elkholy, "Prediction of abrasion wear for slurry pump materials," *Wear*, vol. 84, no. 1, pp. 39–49, 1983.

[28] G. R. Desale, B. K. Gandhi, and S. C. Jain, "Particle size effects on the slurry erosion of aluminium alloy (AA 6063)," *Wear*, vol. 266, pp. 1066–1071, 2009.

[29] H. M. Clark and R. B. Hartwich, "A re-examination of the 'particle size effect' in slurry erosion," *Wear*, vol. 248, no. 1–2, pp. 147–161, 2001.

[30] M. Woldman, E. Van Der Heide, D. J. Schipper, E. van der Heide, T. Tinga, and M. A. Masen, "Investigating the influence of sand particle properties on abrasive wear behaviour," *Wear*, vol. 294–295, pp. 419–426, 2012.

[31] A. Levy and P. Chik, "The effects of erodent composition and shape on the erosion of steel," *Wear*, vol. 89, no. 2, pp. 151–162, 1983.

[32] G. F. Truscott, "A literature survey on abrasive wear in hydraulic machinery," *Wear*, vol. 20, no. c, pp. 29–50, 1972.

[33] A. J. Karabelas, "An Experimental Study of Pipe Erosion by Turbulent Slurry Flow," in *Proceedings of Hydrotransport-5*, 1978.

[34] Y. Oka, K. Okamura, and T. Yoshida, "Practical estimation of erosion damage caused by solid particle impactPart 1: Effects of impact parameters on a predictive equation," *Wear*, vol. 259, no. 1–6, pp. 95–101, 2005.

[35] H. C. Meng and K. C. Ludema, "Wear models and predictive equations: their form and content," *Wear*, vol. 181–183, pp. 443–457, 1995.

[36] Y. I. Oka and T. Yoshida, "Practical estimation of erosion damage caused by solid particle impact," *Wear*, vol. 259, no. 1–6, pp. 102–109, 2005.

[37] S. A. Hashemi, A. Sadighian, S. I. A. Shah, and R. S. Sanders, "Solid velocity and

concentration fluctuations in highly concentrated liquid–solid (slurry) pipe flows," *Int. J. Multiph. Flow*, vol. 66, pp. 46–61, 2014.

[38] S. A. Hashemi, "Velocity and concentration uctuations in concentrated solid-liquid ows," 2013.

[39] D. P. Gillies, "Particle Contributions to Kinematic Friction in Slurry Pipeline Flow," 2013.

[40] S. P. Turchaninov, "Modeling hydroabrasive wear in a toroidal tube," *Sov. Min. Sci.*, vol. 12, no. 6, pp. 620–626, Nov. 1976.

[41] R. C. Worster and D. F. Denny, "Hydraulic Transport of Solid Materials in Pipes," in *Proceedings of the Institution of Mechanical Engineers*, 1955, pp. 563–586.

[42] C. A. Shook, D. B. Haas, W. H. W. Husband, and M. Small, "Relative wear rate determinations for slurry pipelines," *Journal of Pipelines*, vol. 1. pp. 273–280, 1981.

[43] J.F. Richardson, J.H. Harker, and J.R. Backhurst, *Coulson and Richardson's Chemical Engineering: Particle Technology and Separation Processes*, Fifth Edit., vol. 2. Butterworth-Heinemann, 2002.

[44] B. Costello, "The AR-G2 Magnetic Bearing Rheometer," West Sussex, 2005.

[45] I. B. Butler, M. a Schoonen, and D. T. Rickard, "Removal of dissolved oxygen from water: A comparison of four common techniques.," *Talanta*, vol. 41, no. 2, pp. 211–215, 1994.

[46] S. S. Rajahram, T. J. Harvey, and R. J. K. Wood, "Evaluation of a semi-empirical model in predicting erosion–corrosion," *Wear*, vol. 267, no. 11, pp. 1883–1893, 2009.

[47] B. N. Taylor and C. E. Kuyatt, "Guidelines for Evaluating and Expressing the Uncertainty of NIST Measurement Results," *Technology*, no. 1297, p. 2, 1994.

[48] H. Y. Sohn and C. Moreland, "The effect of particle size distribution on packing density," *Can. J. Chem. Eng.*, vol. 46, pp. 162–167, 1968.

[49] K. W. Desmond and E. R. Weeks, "Influence of particle size distribution on random close packing of spheres," *Phys. Rev. E - Stat. Nonlinear, Soft Matter Phys.*, vol. 90, no. 2, pp. 1–6, 2014.

[50] C. A. Shook, M. McKibben, and M. Small, "Experimental investigation of some

hydrodynamic factors affecting slurry pipeline wall erosion," *Can. J. Chem. Eng.*, vol. 68, no. 1, pp. 17–23, 1990.

[51] Y. Zhang, E. P. Reuterfors, B. S. McLaury, S. A. Shirazi, and E. F. Rybicki, "Comparison of computed and measured particle velocities and erosion in water and air flows," *Wear*, vol. 263, no. 1–6 SPEC. ISS., pp. 330–338, 2007.

[52] R. Okita, Y. Zhang, B. S. McLaury, and S. a. Shirazi, "Experimental and Computational Investigations to Evaluate the Effects of Fluid Viscosity and Particle Size on Erosion Damage," *J. Fluids Eng.*, vol. 134, no. June 2012, p. 061301, 2012.

[53] C. Ansys, "ANSYS CFX-solver theory guide," *ANSYS CFX Release*, vol. 15317, no. April, pp. 724–746, 2009.

[54] I. ANSYS, "ANSYS TRAINING MANUAL - APPENDIX A: MESH QUALITY," 2009.

[55] T. D. Canonsburg, "ANSYS CFX-Solver Modeling Guide," vol. 15317, no. April, pp. 724–746, 2009.

Appendix A
Properties of the Carbon Steel Test Coupons

Table A.1. Chemical composition of ASTM A572 GR50 carbon steel specimens

Material	Concentration	Material	Concentration
C	0.06	Mn	0.58
Ti	0.002	Cb	0.034
P	0.009	Mo	0.007
Ca	0.0002	S	0.009
Cu	0.058	Al	0.037
V	0.002	B	0.0002
Si	0.011	Cr	0.062
Ni	0.026		

Table A.2. Mechanical Properties of the ASTM A572 GR50 carbon steel specimens

Tensile strength (MPa)	520
Yield strength (MPa)	442
Elongation	25

Appendix B
Particle Size Analysis: Sieving Data

Table B.1. Sieve analysis data for SIL 1 sand (test 1)

ASTM E-11	Sieve Size	Empty Pan	Cumulative Weight	Weight	% of mass retained	Cumulative % of mass retained
#	µm	gm	gm	gm		
40	425	353.36	365.58	2.23	0.223	0.223
50	300		575.16	209.58	20.959	21.182
60	250		931.48	356.32	35.634	56.816
80	180		1200.76	269.28	26.930	83.746
100	150		1285.33	84.57	8.458	92.204
140	106		1353.3	67.97	6.797	99.001
200	75		-	-	-	-
Pan	0		363.35	9.99	0.999	100
				999.94	100	

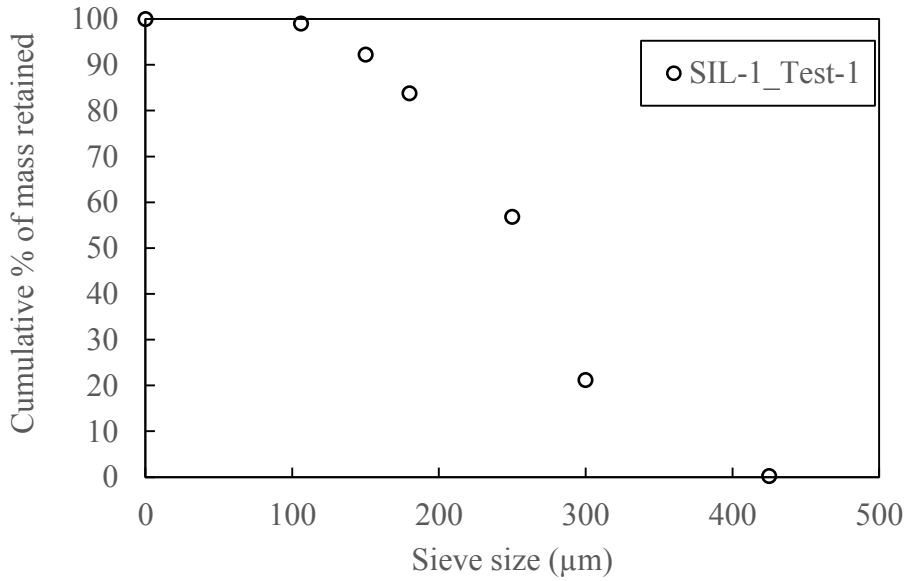

Figure B.1. Sieve analysis of SIL 1 sand (test 1)

Table B.2. Sieve analysis data for SIL 1 sand (test 2)

ASTM E-11	Sieve Size	Empty Pan	Cumulative Weight	Weight	% of mass retained	Cumulative % of mass retained
#	µm	gm	gm	gm		
40	425	353.38	366.31	2.41	0.240	0.240
50	300		620.57	254.26	25.307	25.546
60	250		975.54	354.97	35.330	60.877
80	180		1237.91	262.37	26.114	86.990
100	150		1308.53	70.62	7.029	94.019
140	106		1358.1	49.57	4.934	98.953
200	75					
Pan	0		363.9	10.52	1.052	100
				1004.72	100	

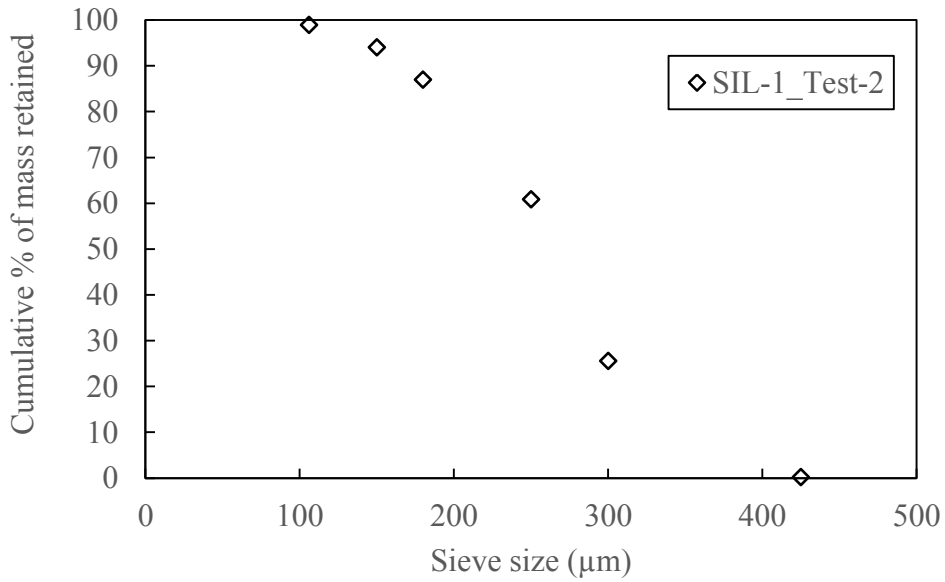

Figure B.2. Sieve analysis of SIL 1 sand (test 2)

Table B.3. Sieve analysis data for SIL 1 sand (test 3)

ASTM E-11	Sieve Size	Cumulative Weight	Weight	% of mass retained	Cumulative % of mass retained
#	µm	gm	gm		
40	400	1.1	1.1	0.0772	0.08
50	297	256.5	255.4	17.9213	18.00
60	250	792.12	535.62	37.5842	55.58
70	210	1011.25	219.13	15.3762	70.96
80	177	1222.89	211.64	14.8507	85.81
100	149	1334.96	112.07	7.8639	93.67
120	125	1399.84	64.88	4.5526	98.23
140	105	1417.86	18.02	1.2645	99.49
170	88	1423.99	6.13	0.4301	99.92
200	74	1424.63	0.64	0.0449	99.97
pan	0	1425.12	0.49	0.0344	100.00
				100.0	

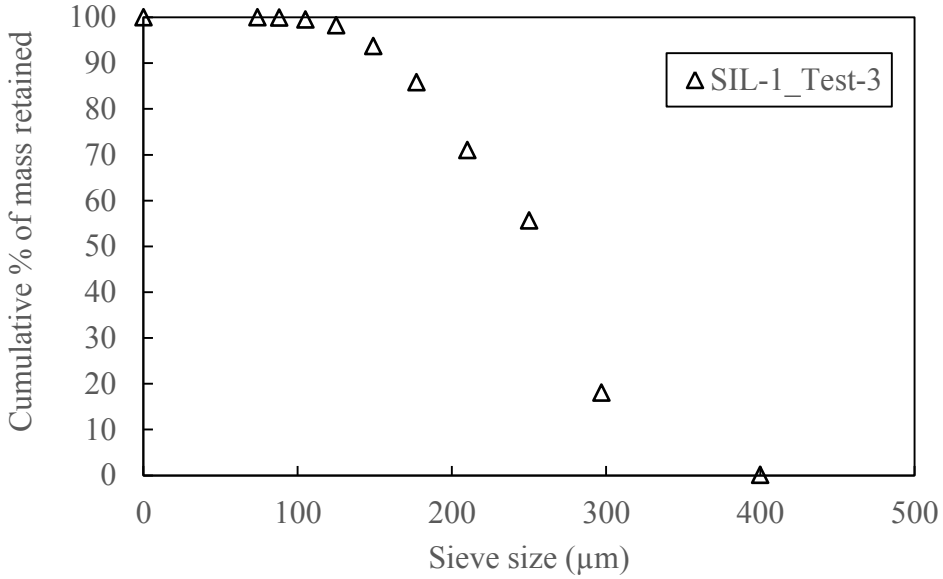

Figure B.3. Sieve analysis of SIL 1 sand (test 3)

Table B.4. Sieve analysis data for SIL 4 sand (test 1)

ASTM E-11	Sieve Size	Empty Pan	Cumulative Weight	Weight	% of mass retained	Cumulative % of mass retained
#	µm	gm	gm	gm		
20	840	353.38	365.74	6.9	0.583	0.583
30	600		421.82	56.08	4.740	5.323
40	425		863.72	441.9	37.350	42.673
50	300		1376.27	512.55	43.321	85.994
60	250		1487.16	110.89	9.373	95.367
80	180		1536.52	49.36	4.172	99.539
Pan	0		358.84	5.46	0.461	100.0
				1183.14	100.0	

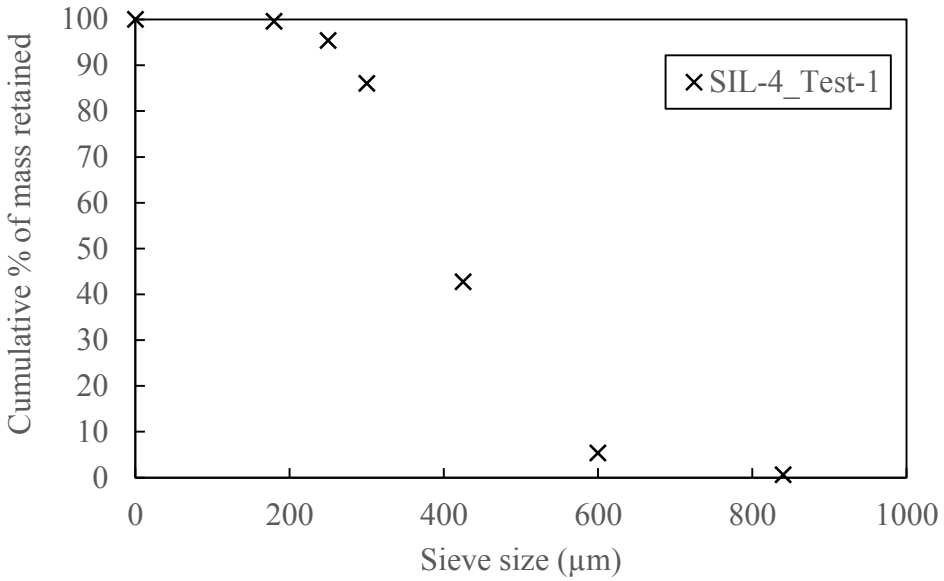

Figure B.4. Sieve analysis of SIL 4 sand (test 1)

Table B.5. Sieve analysis data for SIL 4 sand (test 2)

ASTM E-11	Sieve Size	Empty Pan	Cumulative Weight	Weight	% of mass retained	Cumulative % of mass retained
#	µm	gm	gm	gm		
20	840	353.38	365.83	6.87	0.582	0.582
30	600		415.79	49.96	4.231	4.813
40	425		868.99	453.2	38.379	43.191
50	300		1368.69	499.7	42.317	85.508
60	250		1484.18	115.49	9.780	95.288
80	180		1534.24	50.06	4.239	99.527
Pan	0		358.96	5.58	0.473	100.0
				1180.86	100.0	

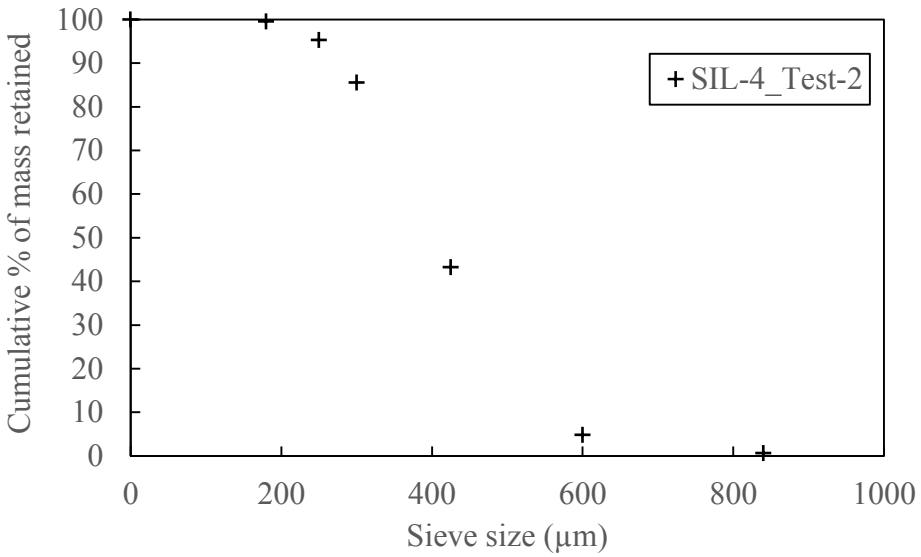

Figure B.5. Sieve analysis of SIL 4 sand (test 2)

Table B.6. Sieve analysis data for gravels (test 1)

ASTM E-11	Sieve Size	Empty Pan	Cumulative Weight	Weight	% of mass retained	Cumulative % of mass retained
#	µm	gm	gm	gm		
5	4000	353.38	0.39	0.39	0.030	0.030
7	2800		188.54	188.15	14.600	14.630
10	2000		758.9	570.36	44.259	58.889
14	1400		1186.57	427.67	33.186	92.076
18	1000		1285.36	98.79	7.666	99.742
20	850		1287.7	2.34	0.182	99.923
PAN	0		1288.69	0.99	0.077	100.000
				1288.69	100.0	

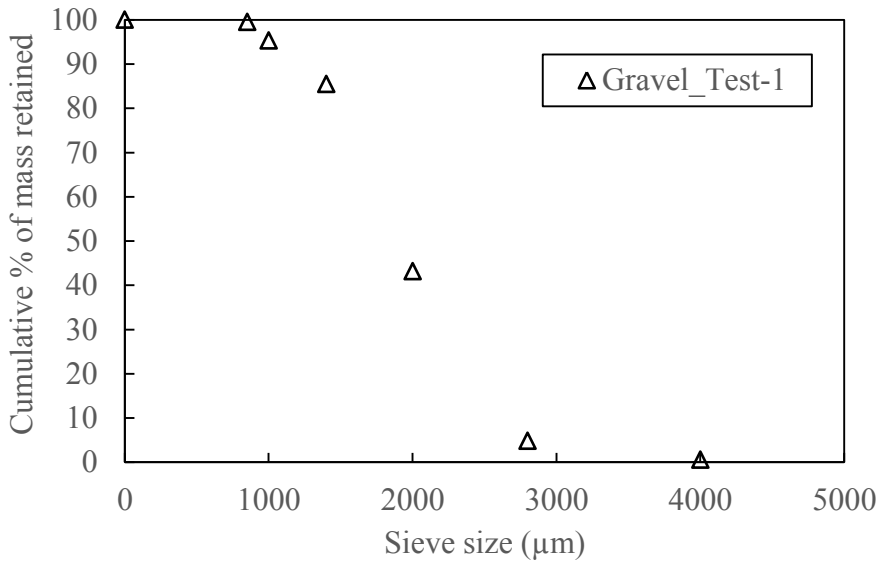

Figure B.6. Sieve analysis of gravels (test 1)

Table B.7. Sieve analysis data for gravels (test 2)

ASTM E-11	Sieve Size	Empty Pan	Cumulative Weight	Weight	% of mass retained	Cumulative % of mass retained
#	µm	gm	gm	gm		
7	2800	353.38	80.06	80.06	7.821	7.821
10	2000		619.06	539	52.653	60.474
14	1400		1001.38	382.32	37.348	97.822
18	1000		1018.62	17.24	1.684	99.506
20	850		1019.66	1.04	0.102	99.607
30	600		1020.42	0.76	0.074	99.682
PAN	0		1023.68	3.26	0.318	100.000
				1023.68	100.000	

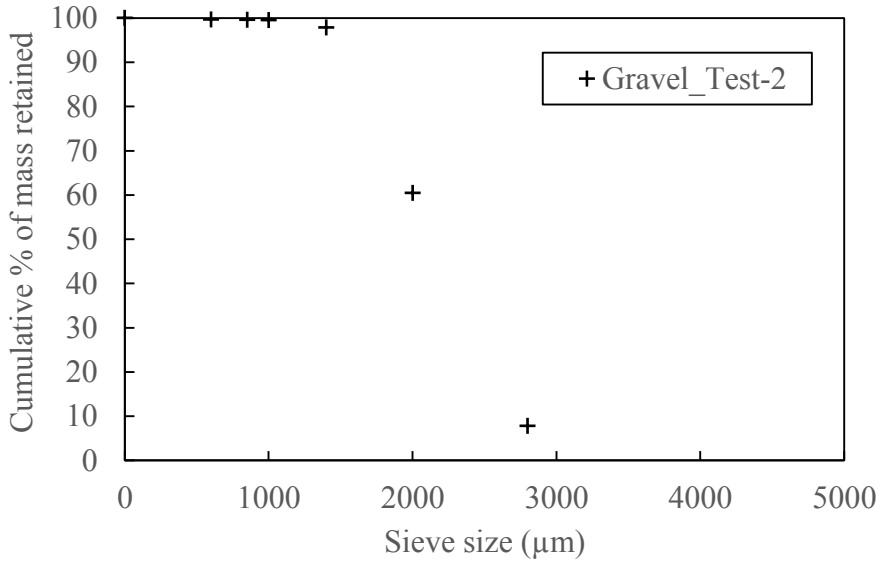

Figure B.7. Sieve analysis of gravels (test 2)

Table B.8. Sieve analysis data for gravels (test 3)

ASTM E-11	Sieve Size	Empty Pan	Cumulative Weight	Weight	% of mass retained	Cumulative % of mass retained
#	µm	gm	gm	gm		
30	595	353.38	0.19	0.19	0.015999	0.015998653
40	400		0.98	0.79	0.066521	0.082519367
50	297		428.99	428.01	36.03991	36.1224318
60	250		1079.14	650.15	54.74486	90.86729539
70	210		1168.44	89.3	7.519367	98.38666218
80	177		1186.75	18.31	1.541765	99.92842708
PAN	0		1187.6	0.85	0.071573	100
				1187.6	100	

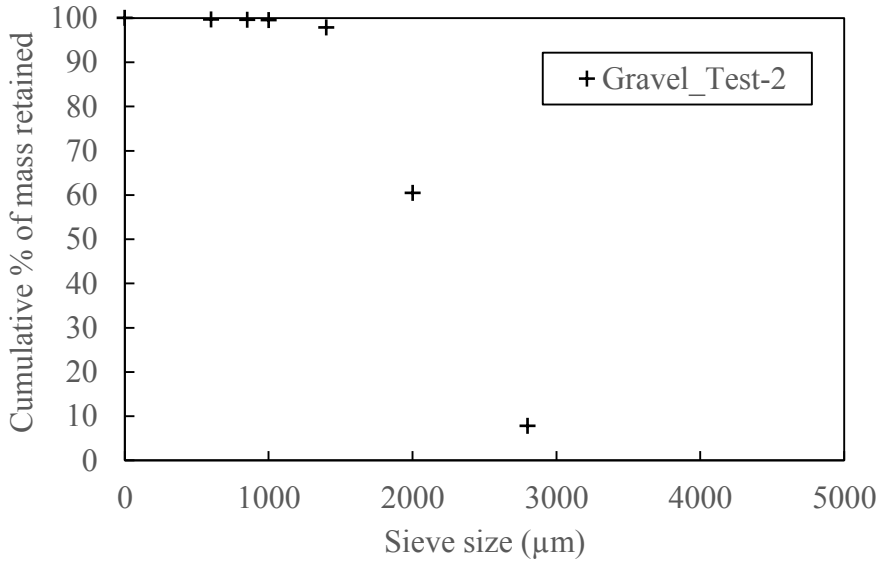

Figure B.8. Sieve analysis of gravels (test 3)

Appendix C
Calibration of the AR-G2 Rheometer and Measured Rheometer Data for SRI Experiments

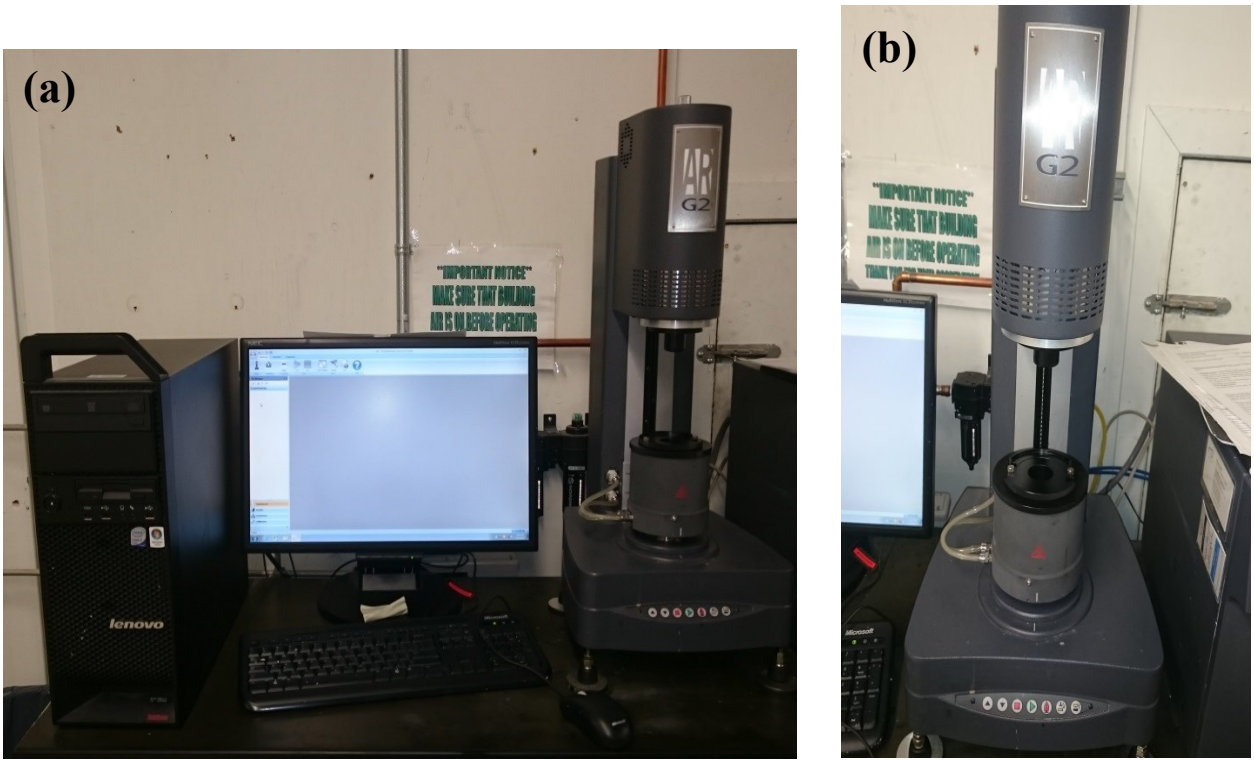

Figure C.1. The AR-G2 Rheometer (a) complete setup (b) the concentric cylinder geometry

Table C.1. AR-G2 concentric cylinder geometry dimensions

Cup diameter (mm)	30.4
Rotor diameter (mm)	28.0
Rotor length (mm)	42.03
Minimum sample size (mL)	22.42
Operating gap (mm)	0.5

Rheometer Calibration Test 1 (N100 Standard Oil)

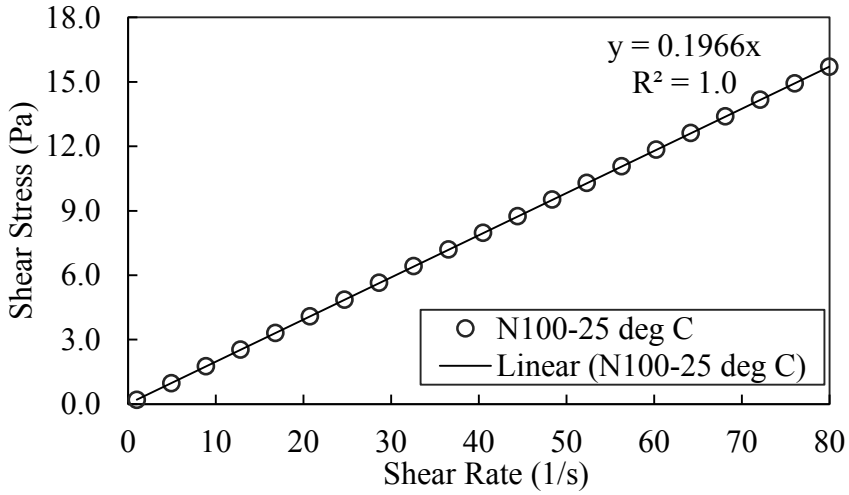

tandard viscosity at 25 °C = 197 mPa.s	Measured viscosity at 25 °C = 196.6 mPa.s

Figure C.2. Calibration test results for AR-G2 rheometer; Sample: N100 Standard oil; Temperature: 25 °C

Table C.2. Calibration Test Data; N100 Standard Oil (Standard viscosity at 25 °C = 197 mPa.s)

Torque (µN.m)	Velocity (rad/s)	Temperature (° C)	Stress (Pa)	Shear rate (1/s)
12.222	0.082	24.997	0.198	1.000
60.237	0.406	25.001	0.978	4.950
108.218	0.730	25.001	1.757	8.900
156.118	1.054	25.001	2.534	12.850
203.987	1.379	24.997	3.311	16.800
251.834	1.703	25.001	4.088	20.750
299.782	2.027	24.997	4.866	24.700
347.645	2.351	25.001	5.643	28.650
395.473	2.675	25.001	6.419	32.600
443.190	2.999	25.001	7.194	36.550
490.949	3.323	25.001	7.969	40.500
538.733	3.647	25.001	8.745	44.450
586.479	3.971	25.006	9.520	48.400
634.238	4.295	25.001	10.295	52.350
681.941	4.620	25.001	11.069	56.300
729.607	4.944	24.997	11.843	60.250
777.320	5.268	24.997	12.617	64.200
824.945	5.592	24.997	13.390	68.150
872.520	5.916	24.997	14.163	72.100
920.232	6.240	25.001	14.937	76.050
967.828	6.564	24.997	15.710	80.000

Rheometer Calibration Test 2 (De-Ionized Water)

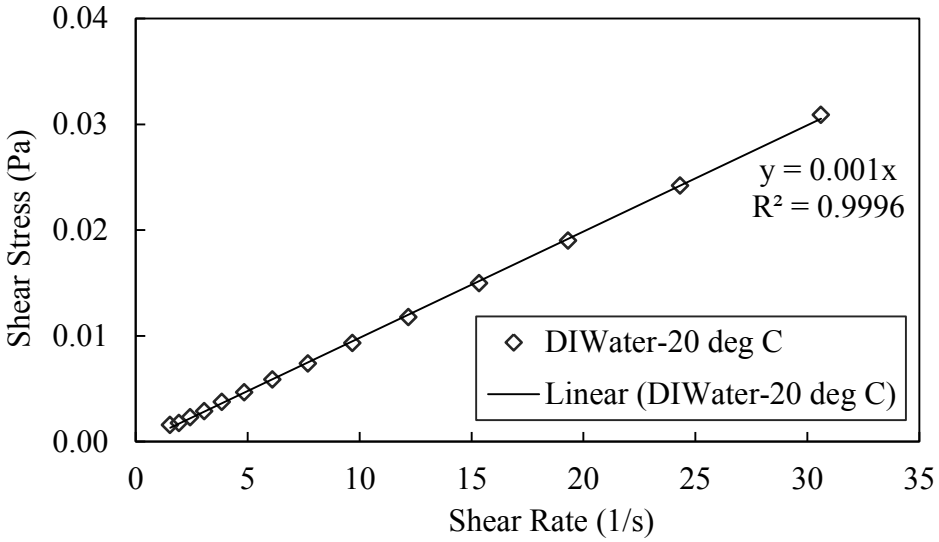

Standard viscosity at 25 °C = 1.0 mPa.s	Measured viscosity at 25 °C = 1.0 mPa.s

Figure C.3. Calibration test results for AR-G2 rheometer; Sample: N100 Standard oil; Temperature: 25 °C

Table C.3. Calibration Test Data; DI Water (Standard viscosity at 20 °C = 1.0 mPa.s)

Torque (µN.m)	Velocity (rad/s)	Temperature (° C)	Stress (Pa)	Shear rate (1/s)
0.094	0.100	21.800	0.0015	1.219
0.095	0.126	21.800	0.0016	1.534
0.108	0.158	21.801	0.0018	1.932
0.142	0.200	21.799	0.0023	2.432
0.176	0.251	21.799	0.0029	3.061
0.231	0.316	21.800	0.0037	3.854
0.285	0.398	21.800	0.0046	4.852
0.361	0.501	21.800	0.0059	6.108
0.453	0.631	21.800	0.0074	7.690
0.573	0.794	21.799	0.0093	9.681
0.724	1.000	21.799	0.0118	12.187
0.921	1.259	21.801	0.0150	15.343
1.170	1.585	21.799	0.0190	19.315
1.489	1.995	21.801	0.0242	24.317
1.902	2.512	21.800	0.0309	30.613

Table C.4. SRI data for 2.0 mm gravel slurry measured using AR G2 rheometer

Carrier Fluid	**Tap Water**		**Tap Water**							
Particle	**N/A**		**Gravel**							
d_{50} (mm)	**N/A**		**2**							
C_s (%)	**N/A**		**20**							
***DO* (PPM)**	**5.5**									
SRI (hr)	**N/A**		**8**		**12**		**24**		**48**	
AR G2 Rheometer Data	Stress	Shear rate	Stress	Shear rate	Stress	Shear rate	Stress	Shear rate	Stress	Shear rate
	(Pa)	(1/s)	(Pa)	(1/s)	(Pa)	(1/s)	(Pa)	(1/s)	(Pa)	(1/s)
	0.00136	1.21862	0.03756	30.46810	0.00178	1.21872	0.00259	1.21874	0.00280	1.21876
	0.00448	4.46863	0.03351	27.21810	0.00589	4.46865	0.00743	4.46864	0.00812	4.46864
	0.00779	7.71850	0.02954	23.96820	0.00987	7.71853	0.01204	7.71863	0.01343	7.71853
	0.01113	10.96850	0.02544	20.71820	0.01387	10.96850	0.01653	10.96850	0.01878	10.96850
	0.01457	14.21840	0.02143	17.46830	0.01789	14.21840	0.02097	14.21840	0.02412	14.21840
	0.01804	17.46830	0.01752	14.21830	0.02203	17.46830	0.02538	17.46830	0.02961	17.46830
	0.02156	20.71830	0.01353	10.96850	0.02623	20.71830	0.02988	20.71830	0.03521	20.71830
	0.02514	23.96820	0.00955	7.71855	0.03050	23.96820	0.03439	23.96820	0.04090	23.96820
	0.02875	27.21810	0.00546	4.46862	0.03482	27.21810	0.03900	27.21810	0.04672	27.21810
	0.03242	30.46800	0.00201	1.21879	0.03918	30.46800	0.04355	30.46800	0.05263	30.46800

Table C.5. SRI data for Al_2O_3 slurry measured using AR G2 rheometer

Carrier Fluid	Tap Water		Tap Water					
Particle	N/A		Al_2O_3					
d_{50} (mm)	N/A		0.425					
C_s (%)	N/A		20					
DO (PPM)	5.5							
SRI (hr)	N/A		12		24		48	
AR G2 Rheometer Data	Stress	Shear rate	Stress	Shear rate	Stress	Shear rate	Stress	Shear rate
	(Pa)	(1/s)	(Pa)	(1/s)	(Pa)	(1/s)	(Pa)	(1/s)
	0.00136	1.21862	0.03247	30.46800	0.00159	1.21874	0.00140	1.21873
	0.00448	4.46863	0.02879	27.21810	0.00470	4.46863	0.00467	4.46865
	0.00779	7.71850	0.02517	23.96820	0.00800	7.71856	0.00797	7.71855
	0.01113	10.96850	0.02163	20.71830	0.01137	10.96850	0.01140	10.96850
	0.01457	14.21840	0.01814	17.46830	0.01484	14.21840	0.01486	14.21840
	0.01804	17.46830	0.01462	14.21840	0.01831	17.46830	0.01839	17.46830
	0.02156	20.71830	0.01119	10.96850	0.02183	20.71820	0.02191	20.71830
	0.02514	23.96820	0.00781	7.71860	0.02539	23.96820	0.02550	23.96820
	0.02875	27.21810			0.02900	27.21810	0.02915	27.21810
	0.03242	30.46800			0.03264	30.46800	0.03292	30.46800

Table C.6. SRI data for SIL 4 sand slurry measured using AR G2 rheometer

Carrier Fluid	Tap Water		Tap Water			
Particle	N/A		SIL 4			
d_{50} (mm)	N/A		0.425			
C_s (%)	N/A		20			
DO (PPM)	5.5					
SRI (hr)	N/A		24		48	
AR G2 Rheometer Data	Stress	Shear rate	Stress	Shear rate	Stress	Shear rate
	(Pa)	(1/s)	(Pa)	(1/s)	(Pa)	(1/s)
	0.00136	1.21862	0.00167	1.21886	0.00178	1.21874
	0.00448	4.46863	0.00530	4.46865	0.00518	4.46865
	0.00779	7.71850	0.00947	7.71854	0.00895	7.71862
	0.01113	10.96850	0.01356	10.96850	0.01306	10.96850
	0.01457	14.21840	0.01743	14.21840	0.01725	14.21840
	0.01804	17.46830	0.02115	17.46840	0.02135	17.46830
	0.02156	20.71830	0.02495	20.71830	0.02535	20.71830
	0.02514	23.96820	0.02880	23.96820	0.02938	23.96820
	0.02875	27.21810	0.03271	27.21810	0.03339	27.21810
	0.03242	30.46800			0.03725	30.46800

Appendix D
Roughness Measurement: Mitutoyo Contracer

FORMPAK Programming:

1. New program (Registering HOME position)

   Register the measurement start position by clicking the icon ‘move’ on the right hand side.

   i. Label name (e.g., HOME POSITION)
   ii. Click on ‘Read Position’
   iii. State of stylus: Move after raising
   iv. Check ‘Register in part program’
   v. Check ‘Absolute’
   vi. Start ‘Movement’
   vii. Save the file as ‘HOME’

2. New program (for MAIN Program: x-macro/x-unit program)
   a. Register the measurement start position by clicking the icon ‘move’ on right hand side.
      i. Label name (e.g., MAIN POSITION)
      ii. State of stylus: Move after raising
      iii. Check ‘Register in part program’
      iv. Check ‘Absolute’
      v. Start ‘Movement’
   b. Settings: ‘Set measuring conditions’
      i. Measurement length: (e.g., 65 mm)
      ii. Measurement pitch: (e.g., 0.5)
      iii. Auto return: Return to measurement start position (Return with stylus raising)
      iv. Click ‘OK’
   c. Settings: ‘Set run condition of the part program’

i. Click ‘Output results’
ii. Check ‘Output measured point data (Text)’
iii. File name setting: Assign name automatically
iv. Click ‘OK’

d. Click ‘Measure’
e. Save the file as ‘MAIN’

3. New program (for CREATING N-PARTS: loop)
   a. File: New of N-Parts
   b. Part program: Register loop start:
      - Lable name: (e.g., Loop)
      - Number of loop (e.g., 37)
      - Step & Repeat
      - Step: Y-axis step: (e.g., 2 mm)
   c. Part program: Register part program (MAIN)
   d. Part program: Register loop end
   e. Part program: Register part program
   f. File: Save part program for N-parts (e.g., Test_Loop)
   g. Part program: Mode change: N-parts part program Run Mode
   h. Run N-P

Measurement steps:

1. Turn on the FORMPAK module.
2. Set the test coupons on the contracer base using the 3-pin positioning.
3. Click on the ‘Run N-P’ button in the FORMPAK module.
4. Allow uninterrupted functioning of the contracer for about one and a half hour.
5. Take off the test coupon from the base after the measurement.

MATLAB Programming: Contracer Data Plot

```
%%  *********** (CONTRACER DATA ANALYSIS) WEAR WHEEL GROUP ***************
%%  ***********************************************************************

%   This Program reads all the numbered *.dat files from CONTRACER
%   measurement and merge the height/depth data into a single matrix.
%   It also sorts the data in a single matrix, plots the thickness
%   measurement and find the best fitted curve based on cubic interpolation
%   scheme. At the end, a contour plot is created based on the fitted data.
%   It also exports the mid-section data (both length-wise and width-wise)
%   for comparison.

%%  Input parameters: measured .dat files, number of data points
%%  along x and y direction

%%  Output: surface plot of the eroded surface, best fitted curve and the
%%  contour map of the eroded surface

%   Developed by:
%   Nitish R Sarker, Graduate Research Assistant, PTP Group
%   Mechanical Engineering | U of A | Final Version Date: NOV 19, 2015

%%  ***********************************************************************

%%  Clear the workspace and command window
    clc;
    clear;

%%  Global Data Matrix

%   Input Parameters
    Nx = input('Insert number of data points along X-direction: ');
    Ny = input('Insert number of data points along Y-direction: ');
    x = zeros(Nx,Ny);

%   Reading all the *.dat files sequencially and taking input into
%   Global Data Matrix

    for k = 1:Ny
        datFileName = sprintf('G%d.dat', k);
            if exist(datFileName,'file')
                %   reading *.dat file from 3rd line after the header
                m = dlmread(datFileName,',',3,0);
                [i,j] = size(m);
                if k == 1
                    for p = 1:i
                        x(p,1) = m(p,1);       % reading x values
                    end
                end
                for q = 1:i
                    x(q,k+1) = m(q,2);         % reading heights
                end
```

```
            else
                % error report
                fprintf('File %s does not exist.\n', datFileName);
            end
    end

 %% Correction Factors from Uneroded Region

    unerod_1 = transpose(x(:,2));
    unerod_2 = transpose(x(:,38));

%%  X and Y directional vectors

    x_values = transpose(x(:,1));           % X direction data vector
    y_values = 1:1:37;                      % Y direction data vector

%% Thickness Parameter Sorting

    for j = 1:numel(y_values)               % Z direction data vector
        for i = 1:numel(x_values)           % with limits
            if i <= 375 && j <= 37
                h(j,i) = x(i,j+1);
            end
        end
    end
    avg_h = mean2(h);                       % Average of thickness data

%% Roughness Parameter Correction

    for j = 1:numel(y_values)
        for i = 1:numel(x_values)
            if i <= 375 && j <= 37
            r(j,i) =    h(j,i)-unerod_1(1,i)+...
                        j*(unerod_1(1,i)-unerod_2(1,i))/37;
            end
        end
    end

%% Thickness Parameter and Axis Value Correction

    for j = 1:numel(y_values)
        for i = 1:numel(x_values)
            if i <= 375 && j <= 37
                r_c(j,i) = abs(avg_h)+r(j,i);
            end
        end
    end

%% Re-format x_values and y_values for Plotting

    for d =1:1:2
        x_values(:,376) = [];
    end
```

```
    y_values = 2*y_values;

%%  Surface plotting

    figure(1);
    surface(interp2(r_c));                  % Plot actual height data
    view(3)                                 % with interpolation
    colormap jet                            % JET colormap used
    alpha(0.9)                              % Transparency 0.9
    camlight HEADLIGHT;
    lighting gouraud


%%  Fit: 'BEST FITTED CURVE BASED ON CUBIC INTERPOLATION'.

    [xData, yData, zData] = prepareSurfaceData( y_values, x_values, r_c );

%   Set up fittype and options.
    ft = 'cubicinterp';

%   Fit model to data.
    [fitresult, gof] = fit( [xData, yData], zData, ft );

%   Create a figure for the plots.
    figure( 'Name', 'Curve Fitting' );

%   Plot fit with data.
    figure(2)
    %p1 = subplot(1,2,1);                   % Optional Sub-plot 1

    % Surface style plotting of the fitted result
    height_fitted = plot( fitresult,'Style','Surface');
    colormap(jet);
    legend(height_fitted,'Fitted data Z-axis','Location','NorthEast' );
    % Label axes
    xlabel ('x direction (mm)','FontName','Calibri','FontSize',12);
    ylabel ('y direction (mm)','FontName','Calibri','FontSize',12);
    zlabel ('Thickness (mm)','FontName','Calibri','FontSize',12);
    cb = colorbar;
    cb.Label.String = 'Test Coupon Thickness (mm)';
    hold on

    %p2 = subplot(1,2,2);                   % Optional Sub-plot 2
    s=4;                                    % Marker size scaler

    % 3D Scatter style plotting of the original data
    height_original = scatter3(xData,yData,zData,s);
    legend(height_original,'Measured data Z-axis','Location','NorthEast');
    % Label axes
    xlabel ('x direction (mm)','FontName','Calibri','FontSize',12);
    ylabel ('y direction (mm)','FontName','Calibri','FontSize',12);
    zlabel ('Thickness (mm)','FontName','Calibri','FontSize',12);
    grid on
    hold off
```

```
%   Make contour plot.

    figure(3)
    height = plot( fitresult,'Style', 'Contour');
    colormap(jet);
    legend( height, 'Fitted data Z-axis',...
           'Measured data Z-axis', 'Location', 'NorthEast' );
    % Label axes
    xlabel ('x direction (mm)','FontName','Calibri','FontSize',12);
    ylabel ('y direction (mm)','FontName','Calibri','FontSize',12);
    cb1 = colorbar;
    cb1.Label.String = 'Test Coupon Thickness (mm)';
    grid on

%%  Mid-section roughness data export

filename = 'data_mid';
xlswrite(filename,r(:,180),3);

xlswrite(filename,(r(20,:))',4);

%% End
```

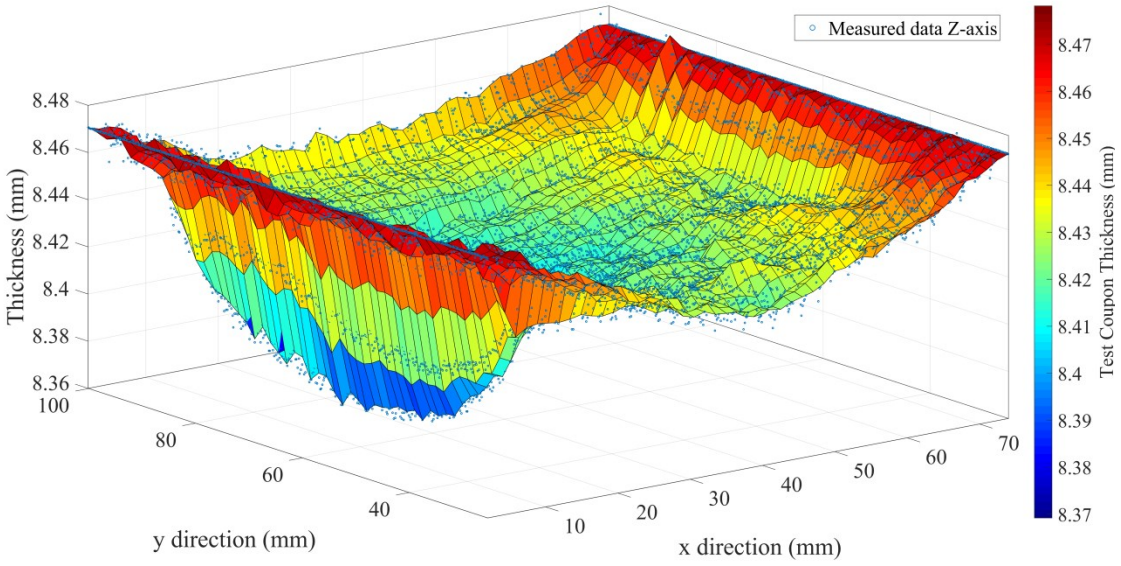

(a) Measured thickness along Z -axis (scatter plot) and best fitted surface plot (jet colormap)

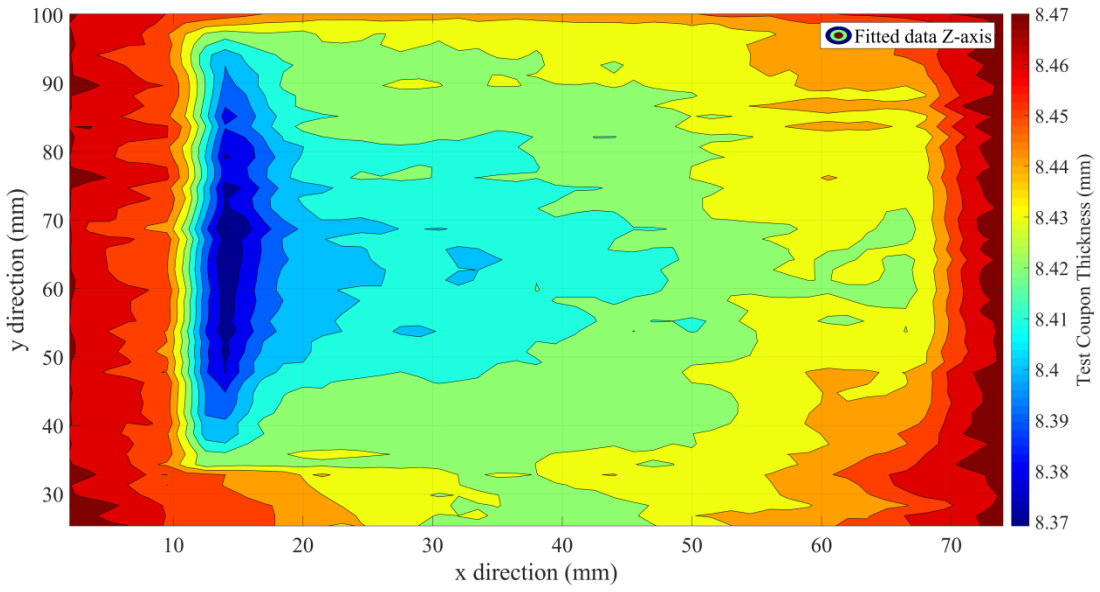

(b) Contour map of the eroded region based on the best fit curve

Figure D.1. Wear pattern analysis and identification of edge effect using contracer; N = 60 RPM, d_{50} = 2 mm, C_s = 6%, SRI = 24 hours

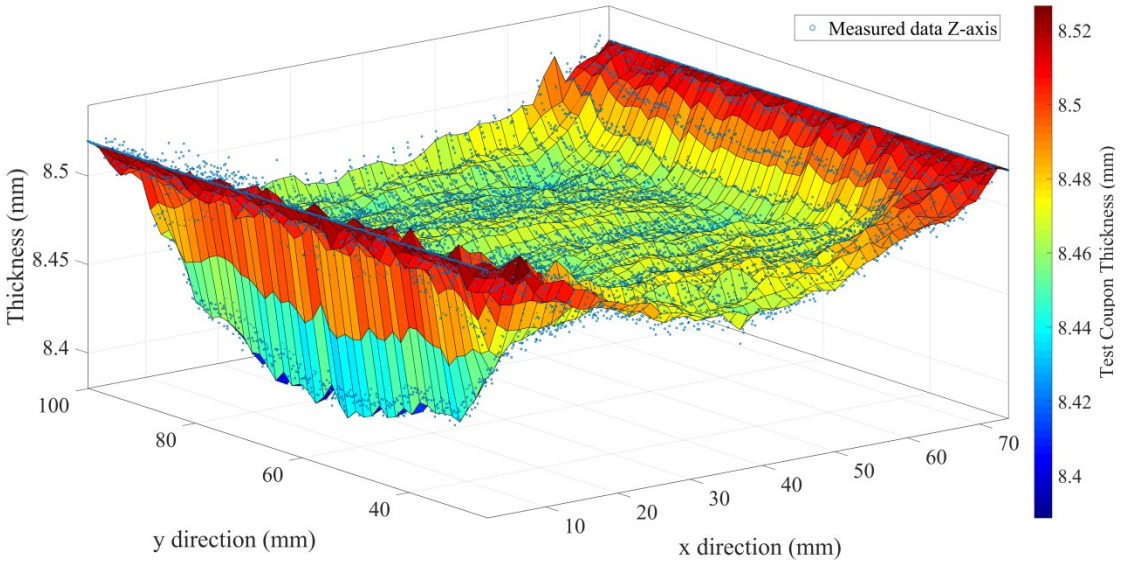

(a) Measured thickness along Z -axis (scatter plot) and best fitted surface plot (jet colormap)

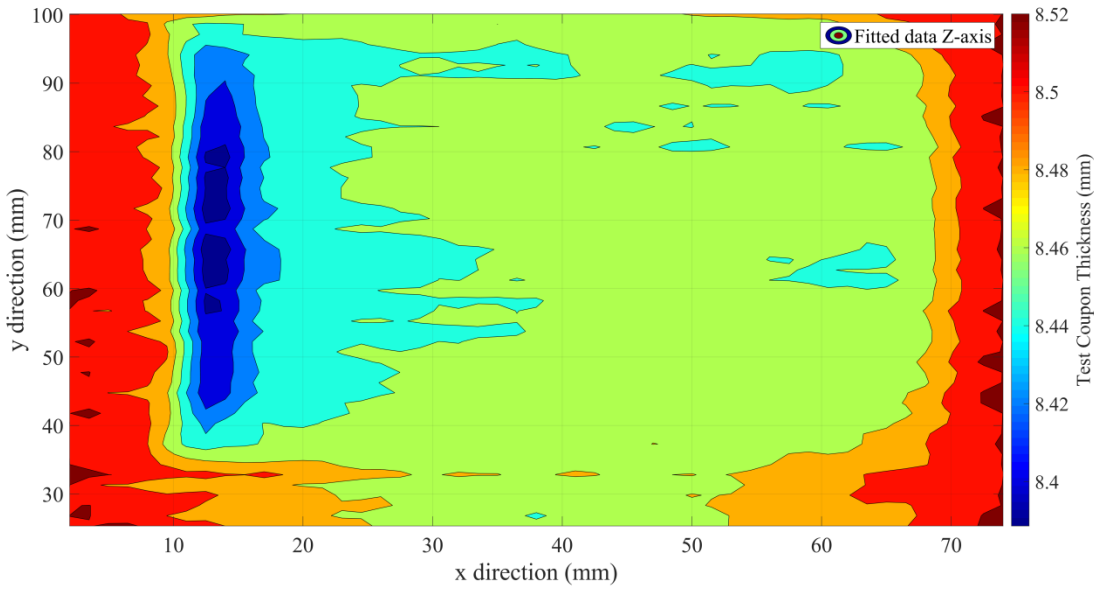

(b) Contour map of the eroded region based on the best fit curve

Figure D.2. Wear pattern analysis and identification of edge effect using contracer; N = 60 RPM, d_{50} = 2 mm, C_s = 12%, SRI = 24 hours

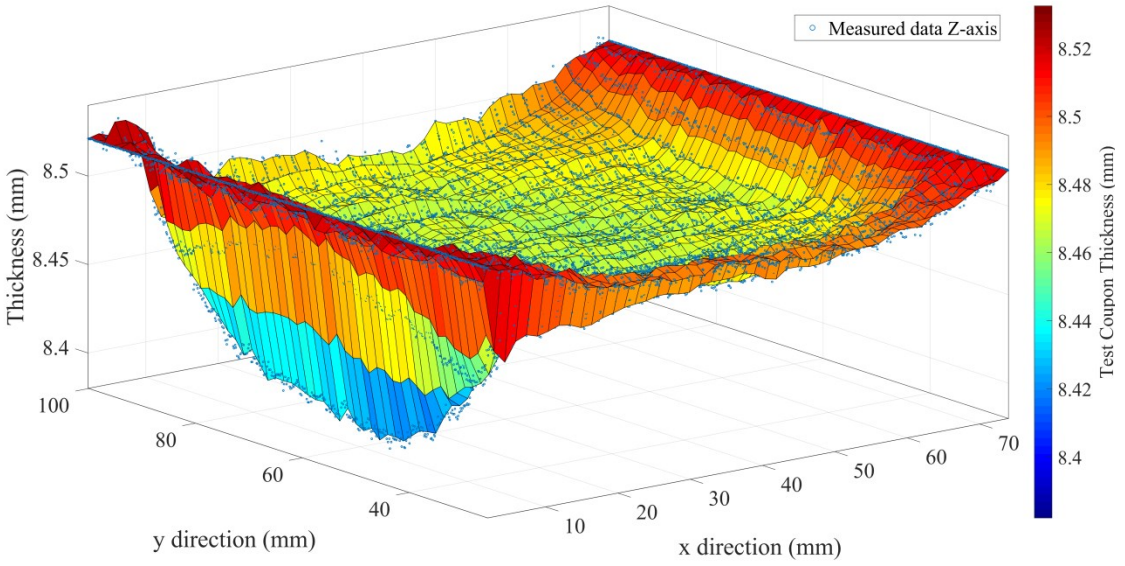

(a) Measured thickness along Z -axis (scatter plot) and best fitted surface plot (jet colormap)

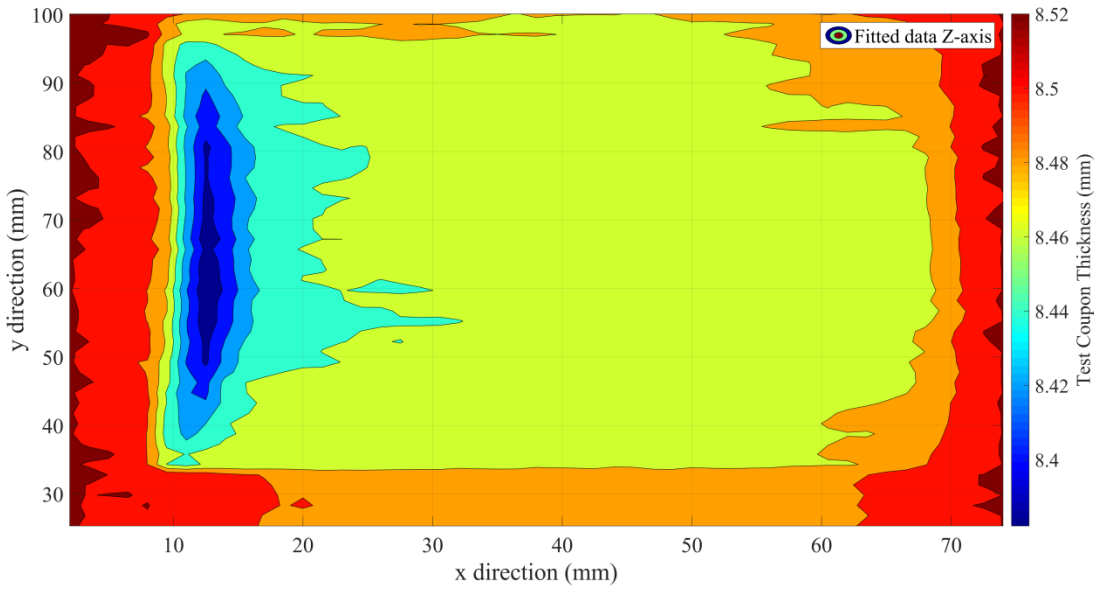

(b) Contour map of the eroded region based on the best fit curve

Figure D.3. Wear pattern analysis and identification of edge effect using contracer; N = 60 RPM, d_{50} = 2 mm, C_s = 20%, SRI = 24 hours

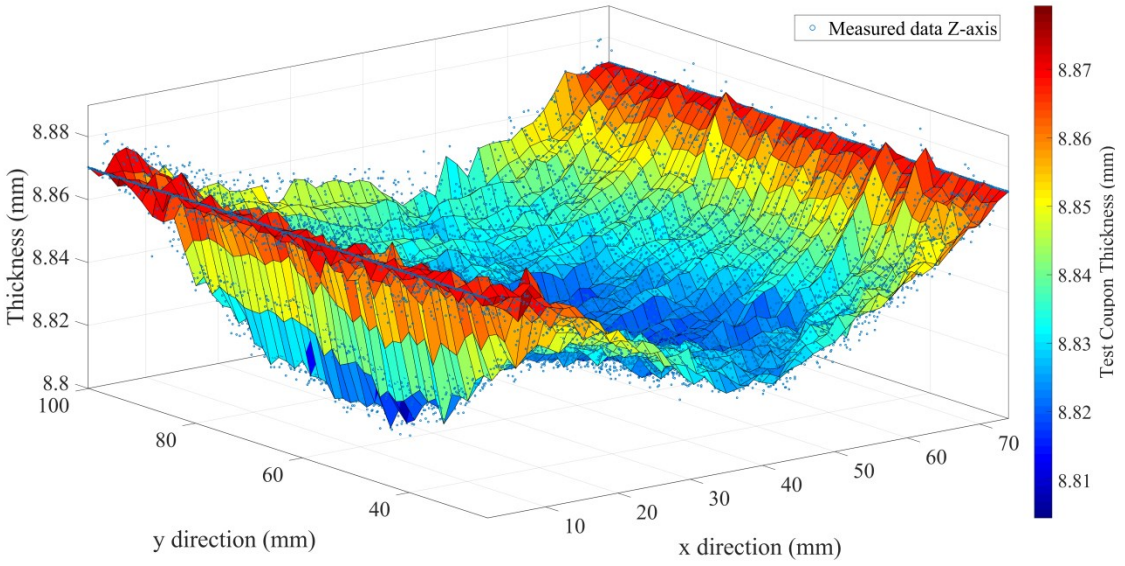

(a) Measured thickness along Z -axis (scatter plot) and best fitted surface plot (jet colormap)

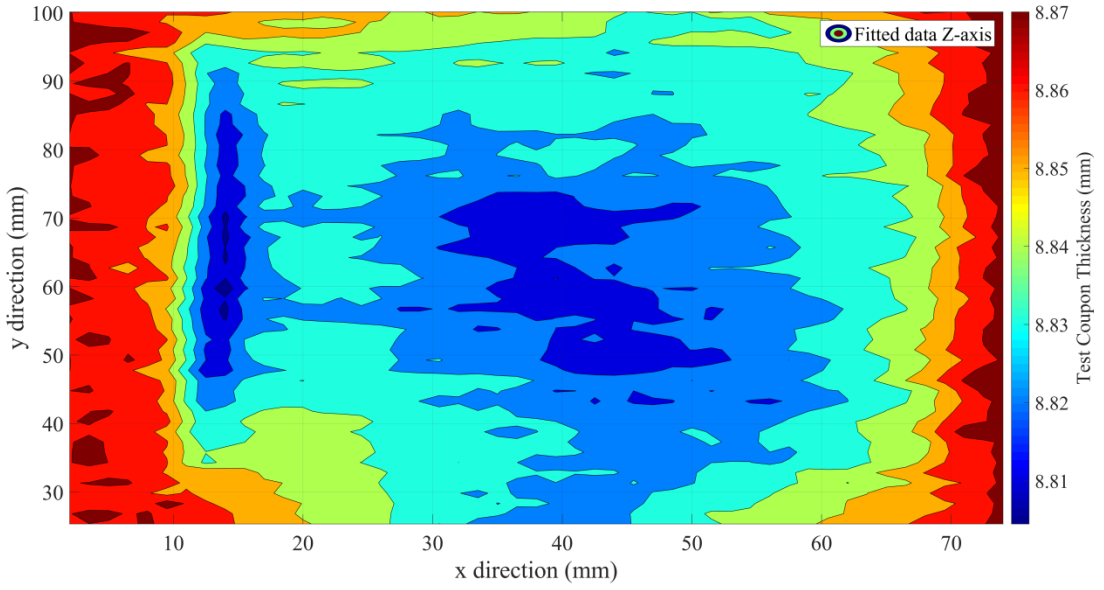

(b) Contour map of the eroded region based on the best fit curve

Figure D.4. Wear pattern analysis and identification of edge effect using contracer; N = 45 RPM, d_{50} = 2 mm, C_s = 6%, SRI = 24 hours

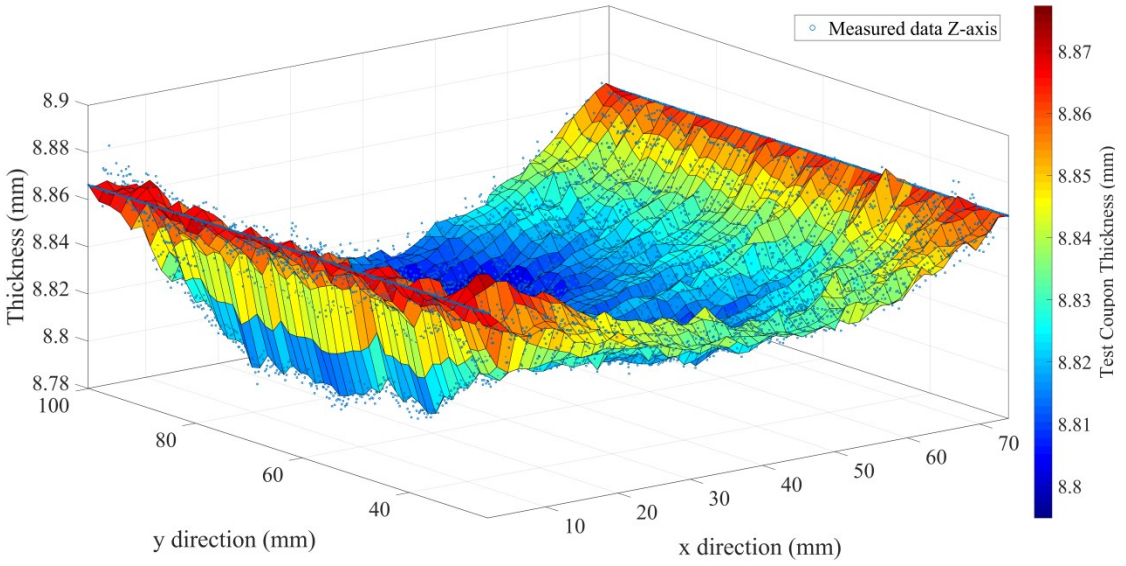

(a) Measured thickness along Z -axis (scatter plot) and best fitted surface plot (jet colormap)

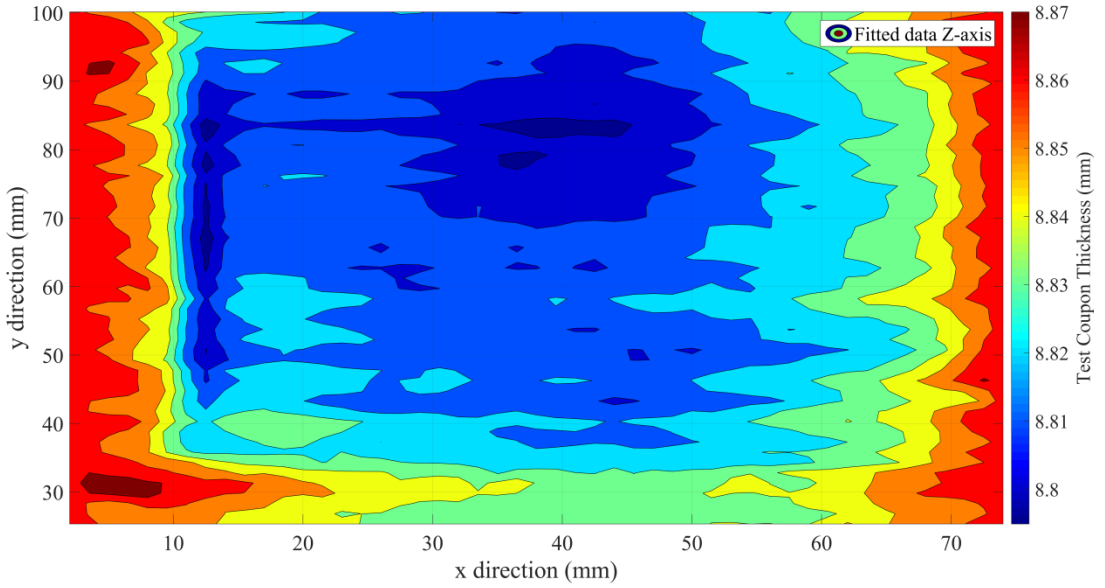

(b) Contour map of the eroded region based on the best fit curve

Figure D.5. Wear pattern analysis and identification of edge effect using contracer; N = 45 RPM, d_{50} = 2 mm, C_s = 12%, SRI = 24 hours

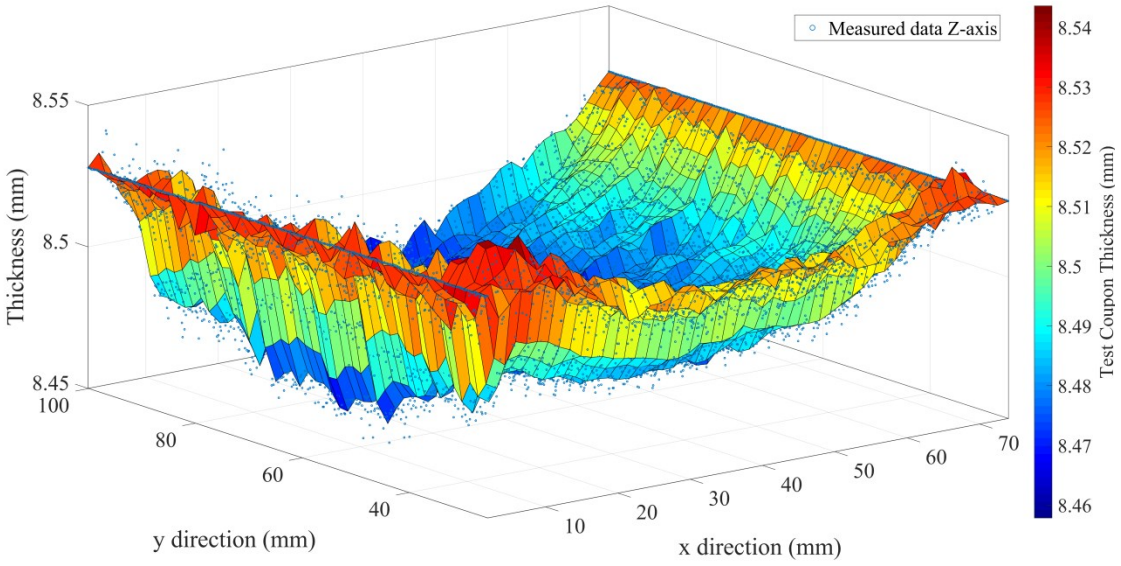

(a) Measured thickness along Z -axis (scatter plot) and best fitted surface plot (jet colormap)

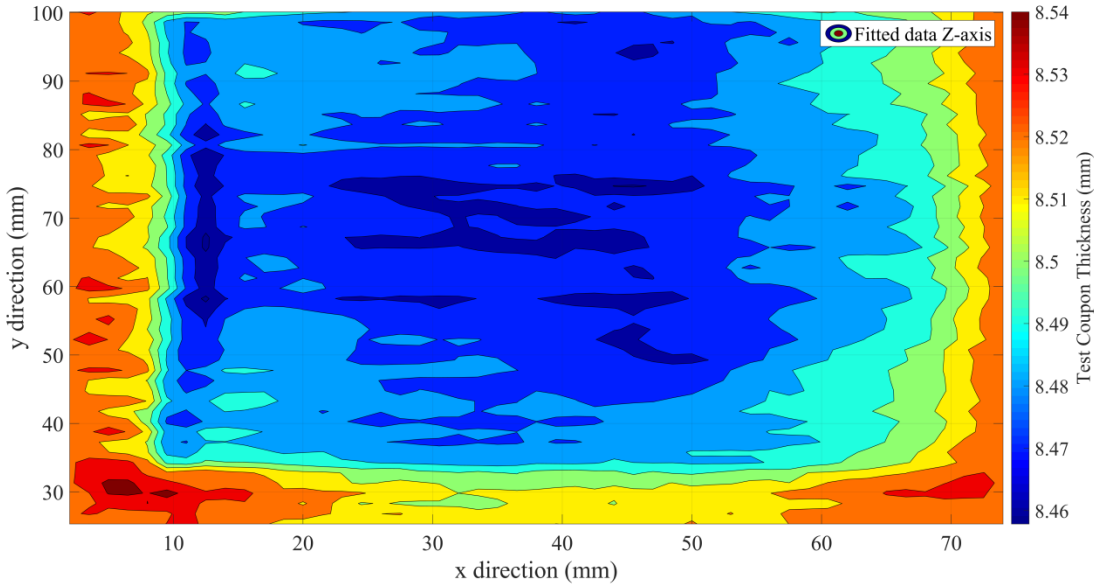

(b) Contour map of the eroded region based on the best fit curve

Figure D.6. Wear pattern analysis and identification of edge effect using contracer; N = 45 RPM, d_{50} = 2 mm, C_s = 20%, SRI = 24 hours

Table D.1. Contracer data along the centerline of the test coupon (in X-direction)

Length-wise positions	Lengthwise			Lengthwise		
	RPM	60		RPM	45	
	Solids Conc'n			Solids Conc'n		
mm	6	12	20	6	12	20
2	-0.00197	-0.00055	0.001146	-0.00199	0.000886	0.001281
4	-0.00255	-0.01249	-0.00631	-0.00259	-0.00223	0.004962
6	-0.01332	-0.01904	-0.01536	-0.01038	-0.00814	-0.00956
8	-0.01349	-0.02358	-0.02162	-0.01418	-0.00785	-0.00388
10	-0.02226	-0.04573	-0.04987	-0.01357	-0.02817	-0.02999
12	-0.06624	-0.12168	-0.13272	-0.04637	-0.06608	-0.06071
14	-0.09701	-0.12502	-0.11758	-0.06176	-0.04879	-0.04703
16	-0.08218	-0.09077	-0.08143	-0.04516	-0.04571	-0.04195
18	-0.06916	-0.08331	-0.07049	-0.04515	-0.04622	-0.04607
20	-0.06473	-0.07846	-0.06214	-0.03575	-0.04734	-0.04499
22	-0.0619	-0.07501	-0.06019	-0.03794	-0.05085	-0.04551
24	-0.06168	-0.07315	-0.06065	-0.03714	-0.05056	-0.04543
26	-0.06165	-0.0671	-0.0627	-0.03993	-0.05408	-0.04555
28	-0.05582	-0.07064	-0.05976	-0.03872	-0.05779	-0.05166
30	-0.05959	-0.06279	-0.05841	-0.04152	-0.0503	-0.04998
32	-0.06237	-0.06054	-0.05786	-0.04431	-0.05302	-0.0481
34	-0.05854	-0.05908	-0.05612	-0.04631	-0.05633	-0.05062
36	-0.05651	-0.06083	-0.05357	-0.0517	-0.05084	-0.04914
38	-0.05109	-0.06017	-0.05423	-0.0525	-0.05036	-0.04546
40	-0.05346	-0.05792	-0.05228	-0.05089	-0.04987	-0.04798
42	-0.05203	-0.05566	-0.05554	-0.05289	-0.05118	-0.0477
44	-0.05261	-0.05681	-0.05439	-0.05068	-0.0541	-0.05002
46	-0.05558	-0.05436	-0.05344	-0.04808	-0.05081	-0.05394
48	-0.05275	-0.0553	-0.0545	-0.04487	-0.04912	-0.05025
50	-0.04612	-0.05525	-0.05155	-0.04306	-0.04664	-0.04677

Table D.1 (continued): Contracer data along the centerline of the test coupon (in X-direction)

Length-wise positions	Lengthwise			Lengthwise		
	RPM	60		RPM	45	
	Solids Conc'n			Solids Conc'n		
mm	6	12	20	6	12	20
52	-0.0433	-0.05659	-0.05101	-0.04266	-0.04775	-0.04609
54	-0.04367	-0.05794	-0.04906	-0.04465	-0.04646	-0.04501
56	-0.04564	-0.05969	-0.04491	-0.04245	-0.04118	-0.04453
58	-0.04362	-0.06043	-0.04777	-0.04004	-0.04129	-0.04465
60	-0.04099	-0.06178	-0.04822	-0.03624	-0.04081	-0.04377
62	-0.04136	-0.06072	-0.04788	-0.03503	-0.03692	-0.03909
64	-0.04074	-0.05947	-0.04773	-0.03083	-0.03563	-0.03721
66	-0.04251	-0.06022	-0.04758	-0.02802	-0.03135	-0.03752
68	-0.03928	-0.04956	-0.04484	-0.02202	-0.02266	-0.02884
70	-0.01925	-0.02631	-0.02789	-0.01001	-0.01937	-0.02176
72	-0.00283	-0.00945	-0.00815	-0.00761	-0.00409	-0.01148
74	0	0	0	0	0	0

Table D.2: Contracer data along the centerline of the test coupon (in Y-direction)

Span-wise positions	Spanwise			Spanwise		
	RPM	60		RPM	45	
	Solids Conc'n			Solids Conc'n		
mm	6	12	20	6	12	20
25.3289	-0.04497	-0.05276	-0.02125	-0.04234	-0.03305	-0.01364
27.3289	-0.04519	-0.06243	-0.02565	-0.04594	-0.03478	-0.01856
29.3285	-0.04647	-0.04992	-0.02545	-0.0485	-0.02968	-0.01048
31.3283	-0.04327	-0.05334	-0.03091	-0.04117	-0.03319	-0.01191
33.3293	-0.03779	-0.04494	-0.02951	-0.03738	-0.03555	-0.03897
35.3277	-0.04092	-0.04992	-0.04565	-0.03797	-0.03962	-0.04096
37.3283	-0.04628	-0.04345	-0.05002	-0.04131	-0.04956	-0.03948
39.3281	-0.04836	-0.04674	-0.04475	-0.04444	-0.04518	-0.04467
41.328	-0.04371	-0.05032	-0.04761	-0.04531	-0.04701	-0.04211
43.3281	-0.04751	-0.04716	-0.05114	-0.04704	-0.05478	-0.04516
45.3288	-0.04897	-0.05078	-0.04824	-0.0405	-0.04807	-0.04942
47.3285	-0.04748	-0.05201	-0.05004	-0.04821	-0.04974	-0.05337
49.3284	-0.05079	-0.04783	-0.05582	-0.05515	-0.05218	-0.04809
51.3284	-0.05169	-0.05323	-0.05322	-0.05446	-0.05071	-0.05664
53.3277	-0.04863	-0.05281	-0.05212	-0.05114	-0.0459	-0.05166
55.3287	-0.05311	-0.05104	-0.05707	-0.05125	-0.05394	-0.05224
57.3286	-0.05154	-0.0546	-0.04944	-0.05268	-0.05054	-0.05414
59.3278	-0.05472	-0.05566	-0.05688	-0.05108	-0.04801	-0.05159
61.3284	-0.05603	-0.05588	-0.05086	-0.05331	-0.04769	-0.05061
63.3286	-0.05301	-0.05519	-0.05061	-0.05209	-0.05074	-0.05813
65.3285	-0.05188	-0.05161	-0.05209	-0.04867	-0.05372	-0.05152
67.3285	-0.05455	-0.05463	-0.05856	-0.05178	-0.05439	-0.06094
69.3288	-0.04948	-0.04948	-0.04944	-0.06043	-0.05568	-0.05256
71.3287	-0.04785	-0.05079	-0.05362	-0.04971	-0.06228	-0.05626

Table D.2 (continued): Contracer data along the centerline of the test coupon (in Y-direction)

Span-wise positions	Spanwise			Spanwise		
	RPM	60		RPM	45	
	Solids Conc'n			Solids Conc'n		
mm	6	12	20	6	12	20
73.3286	-0.05052	-0.05239	-0.05642	-0.04979	-0.06164	-0.05339
75.3291	-0.0509	-0.04988	-0.0568	-0.04455	-0.06224	-0.05413
77.3292	-0.05149	-0.04174	-0.05666	-0.04138	-0.06245	-0.05527
79.3291	-0.0496	-0.05432	-0.05025	-0.03924	-0.06338	-0.04394
81.3294	-0.04779	-0.05107	-0.05249	-0.04008	-0.06659	-0.05255
83.3294	-0.04983	-0.0473	-0.05213	-0.04054	-0.06674	-0.04964
85.3299	-0.04268	-0.05341	-0.0548	-0.04086	-0.05905	-0.04769
87.3299	-0.0461	-0.05584	-0.04881	-0.03067	-0.06242	-0.0473
89.3307	-0.04837	-0.05502	-0.05077	-0.03152	-0.06068	-0.05043
91.3304	-0.04137	-0.06172	-0.04856	-0.03433	-0.05683	-0.04988
93.3298	-0.04195	-0.05639	-0.04522	-0.03169	-0.05445	-0.04733
95.3311	-0.03999	-0.05409	-0.04392	-0.04152	-0.05793	-0.05457
97.3308	-0.03531	-0.05196	-0.04257	-0.02619	-0.05624	-0.05175

Appendix E
Uncertainty and Sensitivity Analysis of the Slurry Erosion Results

Uncertainty in gravimetric measurement:

The resolution of the electronic balance, $R_e = 0.01$ g

The standard uncertainty of the resolution of the electronic balance, $u_{res} = \frac{R_e}{2\sqrt{3}} = 0.0028868$ g

Table E.1. Repeatability of gravimetric measurement of a test coupon

Measurement #	Weight (gm)
1	493.54
2	493.54
3	493.55
4	493.54
5	493.54
6	493.54
7	493.54
8	493.53
9	493.55
10	493.54
11	493.54
12	493.55
13	493.54
14	493.54
15	493.55
16	493.54
17	493.56
18	493.54
19	493.55
20	493.54
21	493.55
22	493.54
23	493.55
24	493.54
25	493.54
26	493.54
27	493.53
28	493.54
29	493.54
30	493.54
31	493.55
32	493.54
33	493.53
34	493.55
35	493.54

Average mass of the coupon, $m_c = 493.5423$ g

Standard deviation of the repeatable mass measurements, $s_m = 0.0064561$ g

The standard uncertainty of the repeatability of the gravimetric measurement, $u_{rep} = \frac{s_m}{\sqrt{35}}$

$= 0.0010913$ g

Therefore,

The combined uncertainty of the gravimetric measurement, $u_g = \sqrt{u_{res}^2 + u_{rep}^2} = 0.00308613$ g

Uncertainty due to coupon-window dimension measurement:

Dimensions of the coupon windows, i.e. the exposed area on the coupon, were measured using a Vernier caliper and uncertainty associated with the resolution of the caliper was calculated.

The resolution of the caliper, $R_c = 0.01$ mm

The standard uncertainty of the resolution of the caliper, $u_{cres} = \frac{R_c}{2\sqrt{3}} = 0.0028868$ mm

Average length of the coupon windows, $L_{cw} = 65.2$ mm

Average width of the coupon windows, $W_{cw} = 66.02$ mm

Average area of the coupon windows, $A_s = 65.2 \times 66.02 = 4304.504$ mm^2

The combined uncertainty of coupon-window area, $u_A = \sqrt{(\frac{\partial A_s}{\partial L_{cw}} \times u_{cres})^2 + (\frac{\partial A_s}{\partial W_{cw}} \times u_{cres})^2}$

$= \sqrt{(W_{cw} \times u_{cres})^2 + (L_{cw} \times u_{cres})^2}$

$= 0.2678569$ mm^2

Uncertainty propagation in thickness loss calculation:

The thickness loss in a test coupon, $T_L = \frac{M_L}{\rho A_s}$

Where, M_L is the mass loss, ρ is the density of the coupon material (7800 kg/m^3) and A_s is the coupon surface area.

Uncertainty in material loss (using gravimetric measurement), $u_{\Delta g} = \sqrt{u_g^2 + u_g^2} = 0.0410575$ g

The propagated uncertainty in thickness loss calculation, $u_T = \sqrt{(\frac{\partial T_L}{\partial M_L} \times u_{\Delta g})^2 + (\frac{\partial T_L}{\partial A_s} \times u_A)^2}$

$= \sqrt{(\frac{1}{\rho A_s} \times u_{\Delta g})^2 + (\frac{-M_L}{\rho A_s^2} \times u_A)^2}$

Table E.2. Uncertainty propagation in thickness loss calculation (after 93 hours experiment)

Particle (d_{50})	**Avg. Mass loss, M_L (g)**	**Thickness loss, T_L (mm)**	**Standard uncertainty, u_T (mm)**
Gravel (2.0 mm)	0.67	1.9955e-08	1.30e-10
Al2O3 (0.425 mm)	0.14	1.4892e-09	2.59e-13
SIL 4 (0.425 mm)	0.05	4.1698e-09	9.27e-14
US Silica (0.250 mm)	0.045	1.3403e-09	8.34e-14

Uncertainty propagation in erosion rate calculation:

The resolution of the time measurement, $R_t = 0.5 \text{ min } = 9.513 \times 10^{-07}$ year

The standard uncertainty of time measurement resolution, $u_t = \frac{R_t}{2\sqrt{3}} = 5.4923 \times 10^{-07}$

The experiment time, $t = 93 \text{ hour} = 0.01062 \text{ year}$

The propagated uncertainty in wear rate calculation, $U_E^1 = \sqrt{(\frac{\partial E}{\partial T_L} \times u_{T_L})^2 + (\frac{\partial E}{\partial t} \times u_t)^2}$

$= \sqrt{(\frac{1}{t} \times u_{T_L})^2 + (\frac{-T_L}{t^2} \times u_t)^2}$

Table E.3. Uncertainty propagation in wear rate calculation

Particle (d_{50})	**Avg. Mass loss, M_L (g)**	**Standard uncertainty, U_E^1 (mm/yr)**
Gravel (2.0 mm)	0.67	1.30e-10
Al2O3 (0.425 mm)	0.14	2.59e-13
SIL 4 (0.425 mm)	0.05	9.27e-14
US Silica (0.250 mm)	0.045	8.34e-14

Uncertainty propagation in velocity calculation:

From Table H.1 (Appendix H),
The average measured RPM of the wheel, $N = 59.78$ RPM
The standard deviation of the measurement, $s_{rm} = 0.266478$ RPM

The standard uncertainty of the measurement, $u_{rm} = \frac{s_{rm}}{\sqrt{25}} = 0.053296$ RPM

The resolution of the tachometer, $R_{rres} = 0.1$ RPM

The standard uncertainty of the resolution of the tachometer, $u_{rres} = \frac{R_r}{2\sqrt{3}} = 0.02886$

The combined standard uncertainty of the tachometer, $u_r = \sqrt{u_{rres}^2 + u_{rm}^2} = 0.060612$ RPM

Radius of the TWT wheel, $r = 0.304$ m
Resolution of the measurement scale, $R_s = 0.001$ m

The standard uncertainty of the resolution of the scale, $u_s = \frac{R_s}{2\sqrt{3}} = 0.000289$ m

Velocity of the wheel, $v = \frac{2\pi Nr}{60}$

The propagated uncertainty of the calculated velocity, $u_v = \sqrt{(\frac{\partial v}{\partial N} \times u_r)^2 + (\frac{\partial v}{\partial r} \times u_s)^2}$

$$= \sqrt{(\frac{2\pi r}{60} \times u_r)^2 + (\frac{2\pi N}{60} \times u_s)^2}$$

$$= 0.002644 \text{ m/s}$$

Uncertainty propagation in solids concentration calculation:

Resolution of the graduated cylinder to measure carrier fluid volume, $R_{gc} = 10 \text{ cc} = 10 \text{ g}$

The standard uncertainty of the carrier fluid volume measurement, $u_{gc} = \frac{R_{gc}}{2\sqrt{3}} = 2.886751 \text{ g}$

The uncertainty of the gravimetric measurement of sand, $u_g = 0.00308613 \text{ g}$

Combined uncertainty in volume measurement of slurry, $u_v = \sqrt{u_{gc}^2 + u_g^2} = 2.886753 \text{ g}$

Solids concentration (by weight), $C_s^w = \frac{m_p}{m_s}$,

Where, m_p and m_s are the mass of the particles and slurry, respectively.

The propagated uncertainty of the calculated solids concentration (by weight),

$$u_{c_s^w} = \sqrt{(\frac{\partial C_s^w}{\partial m_p} \times u_g)^2 + (\frac{\partial C_s^w}{\partial m_s} \times u_v)^2}$$
$$= \sqrt{(\frac{1}{m_s} \times u_g)^2 + (\frac{-m_p}{m_s^2} \times u_v)^2}$$
$$= 0.000377$$
$$= 0.0000038\,\% \text{ of weight fraction}$$

Propagation of uncertainty over Erosion Rate:

The propagation of uncertainty on erosion rate due to the standard uncertainty of particle solids concentration and velocity was calculated using the erosion model proposed by Gupta *et al.* [8]:

$$E_w = 0.223 v^{2.148} d^{0.344} (C_s^w)^{0.556}$$

The propagated uncertainty over erosion rate is $U_E^2 = \sqrt{(\frac{\partial E_w}{\partial v} \times u_v)^2 + (\frac{\partial E_w}{\partial C_s^w} \times u_{c_s^w})^2}$,

Where,

$$\frac{\partial E_w}{\partial v} = 0.4790 v^{1.148} d^{0.344} (C_s^w)^{0.556}$$

$$\frac{\partial E_w}{\partial C_s^w} = 0.1239 v^{2.148} d^{0.344} (C_s^w)^{0.444}$$

Table E.4. Uncertainty propagation over erosion rate

Particle (*d50*)	$\frac{\partial E_w}{\partial v}$	$\frac{\partial E_w}{\partial C_s^w}$	**Propagated uncertainty,** U_E^2 **(mm/yr)**
Gravel (2.0 mm)	1.014183536	0.521925575	0.002688
Al2O3 (0.425 mm)	0.595289236	0.306351529	0.001578
SIL 4 (0.425 mm)	0.595289236	0.306351529	0.001578
US Silica (0.250 mm)	0.495967936	0.25523817	0.001315

Uncertainty in repeatability experiments:

Table E.5. Uncertainty in repeatability experiments using different particles

	Gravel (2.0 mm) mm/yr	Al_2O_3 (0.425 mm) mm/yr	SIL 4 (0.425 mm) mm/yr	US Silica (0.250 mm) mm/yr
Sample 1	1.86	0.49	0.14	0.114
Sample 2	2.0	0.51	0.17	0.143
Sample 3	1.83	0.43	0.14	0.130
Sample 4	1.92	0.4	0.11	0.130
Average	1.90	0.457	0.143	0.13
Standard Deviation	0.075	0.0512	0.0245	0.0117
Uncertainty U_E^3	0.0375	0.0256	0.0122	0.0059

Overall uncertainty in erosion rate experiments using the TWT:

Uncertainties and propagation of uncertainties calculated for mass measurement, velocity and solids concentration effect, and repeatability were combined together to calculate the overall uncertainty in predicting erosive wear rate using the TWT and then multiplied with 2, to ensure a 95% confidence level.

The overall uncertainty is $U_E = \sqrt{(U_E^1)^2 + (U_E^2)^2 + (U_E^3)^2}$

Table E.6. Overall uncertainty in erosion rate experiments using the TWT

Particle (*d50*)	Avg. Material Loss (mm/yr)	Overall Uncertainty, U (mm/yr)	Relative Overall Uncertainty, U (%)	Relative Overall Uncertainty, U (%) (within 95% confidence bounds)
Gravel (2.0 mm)	1.900	± 0.037596	± 1.977985	± 3.956
Al_2O_3 (0.425 mm)	0.457	± 0.025666	± 5.612252	± 17.281
SIL 4 (0.425 mm)	0.143	± 0.012349	± 8.640736	± 11.225
US Silica (0.250 mm)	0.130	± 0.005998	± 4.613677	± 9.227

Sensitivity analysis of the SRI curve fit:

SRI experiments have been conducted to determine the zero particle degradation wear by fitting with an exponential equation:

$$y = a\mathrm{e}^{-bx} + c$$

Sensitivity analyses of the extrapolations have been completed based on the uncertainties calculated above. Uncertainties in the wear rate calculation were applied on the SRI experimental results and the maximum and minimum points of intercept at zero SRI were analyzed.

Table E.7. Maximum and Minimum wear rates from SRI experimental data based on calculated relative uncertainty

Gravels (2.0 mm)				
SRI (hr)	WR (mm/yr)	Relative Uncertainty (%)	Maximum WR (mm/yr)	Minimum WR (mm/yr)
8	7.1	± 3.96	7.38116	6.81884
12	6.37	± 3.96	6.622252	6.117748
24	4.56	± 3.96	4.740576	4.379424
48	2.79	± 3.96	2.900484	2.679516
96	1.85	± 3.96	1.92326	1.77674
Al_2O_3 (0.425 mm)				
SRI (hr)	WR (mm/yr)	Relative Uncertainty (%)	Maximum WR (mm/yr)	Minimum WR (mm/yr)
12	0.569608	± 11.22	0.633518	0.505698
24	0.43816	± 11.22	0.487321	0.388998
48	0.321317	± 11.22	0.357369	0.285265
96	0.29226	± 11.22	0.325051	0.259468
SIL 4 without any area correction (0.425 mm)				
SRI (hr)	WR (mm/yr)	Relative Uncertainty (%)	Maximum WR (mm/yr)	Minimum WR (mm/yr)
12	0.26	± 17.2	0.30472	0.21528
24	0.13	± 17.2	0.15236	0.10764
48	0.06	± 17.2	0.07032	0.04968
96	0.06	± 17.2	0.07032	0.04968

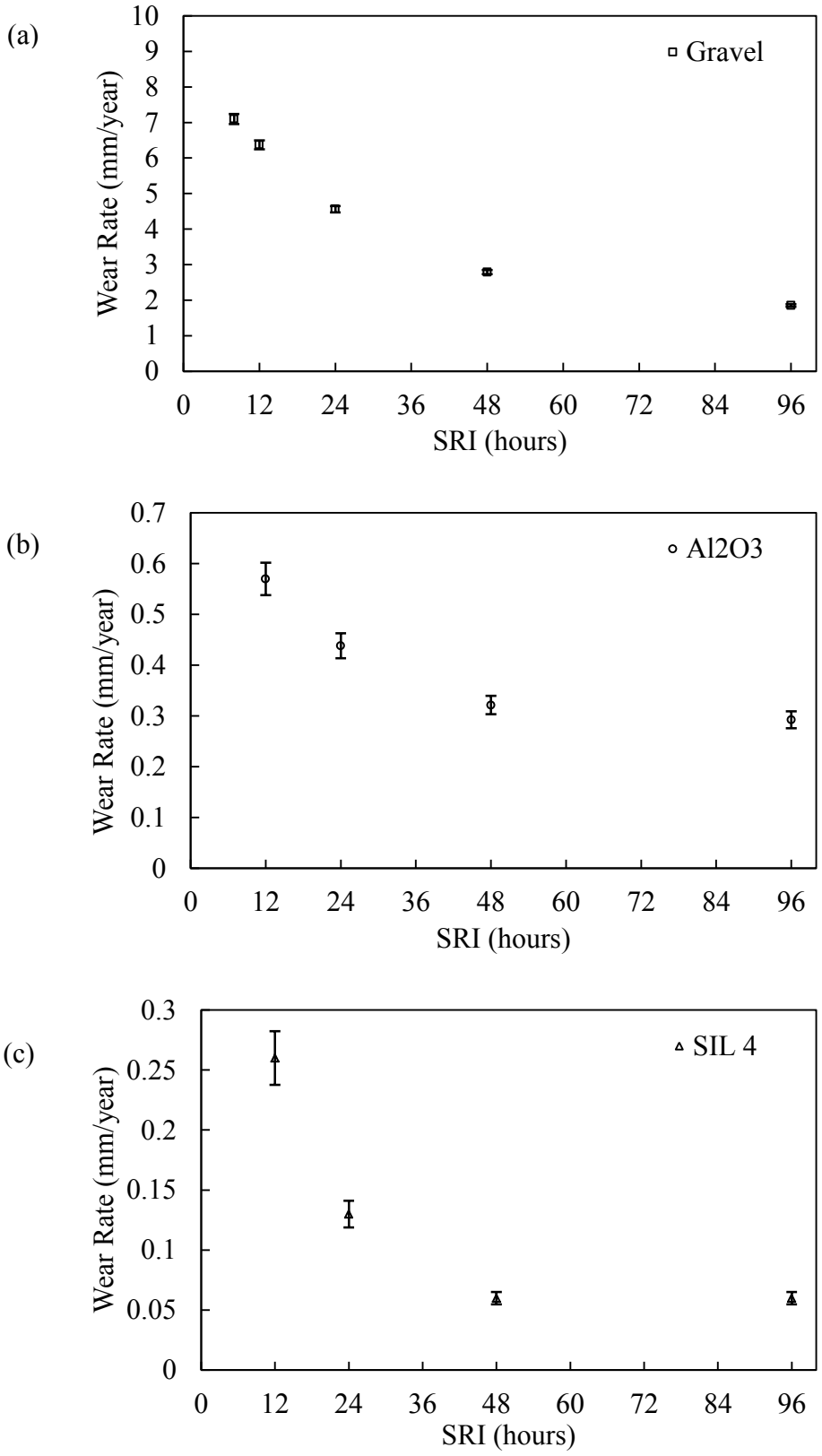

Figure E.1. SRI experimental data with calculated uncertainty

SIL 4 data after correction done for area and pipe loop diameter:

Table E.8. Maximum and Minimum wear rates from SIL 4 SRI experimental data based on calculated relative uncertainty (after area and diameter correction)

SRI (hr)	WR (mm/yr)	Relative Uncertainty (%)	Maximum WR (mm/yr)	Minimum WR (mm/yr)
12	2.02839866	± 17.2	2.377283	1.679514
24	1.01419933	± 17.2	1.188642	0.839757
48	0.468092	± 17.2	0.548604	0.38758
96	0.468092	± 17.2	0.548604	0.38758

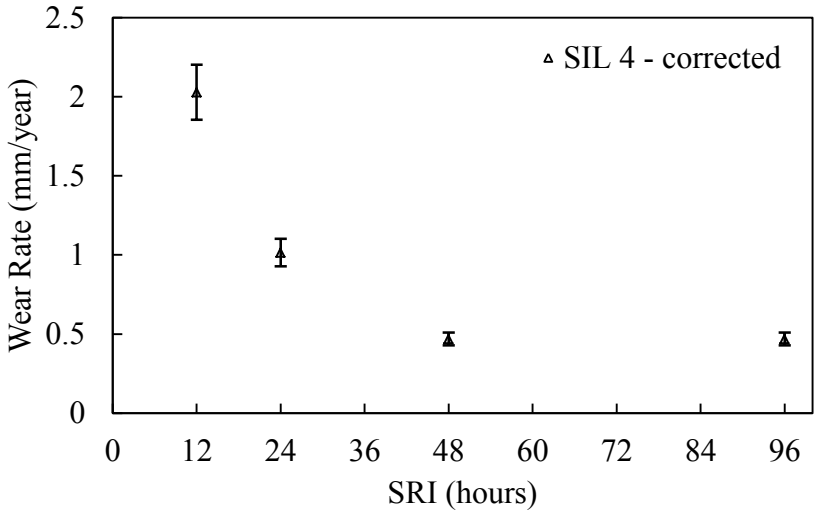

Figure E.2. Corrected SRI experimental data for SIL 4 sand particles with calculated uncertainty

After the area correction (from qualitative flow observation) and the pipe loop diameter correction (to compare with Sadighian *et al.* [7] pipe loop data) the calculated uncertainties (± 17.2% within 95% confidence bound) were applied on the experimental data to determine the maximum and minimum possible wear rate (Table G8, Figure G2). Different combinations of the maximum and minimum calculated wear rate were fitted exponentially and a range of the intercepts were observed as a part of the sensitivity analysis of the extrapolation. The highest and lowest intercept found from the sensitivity analyses are 5.836 and 4.115 mm/yr, respectively,

which are shown in Figure G3 in comparison with the actual intercept (4.97 mm/yr) based on the true experimental data. These maximum and minimum intercepts are approximately ± 17.3% of the actual extrapolation.

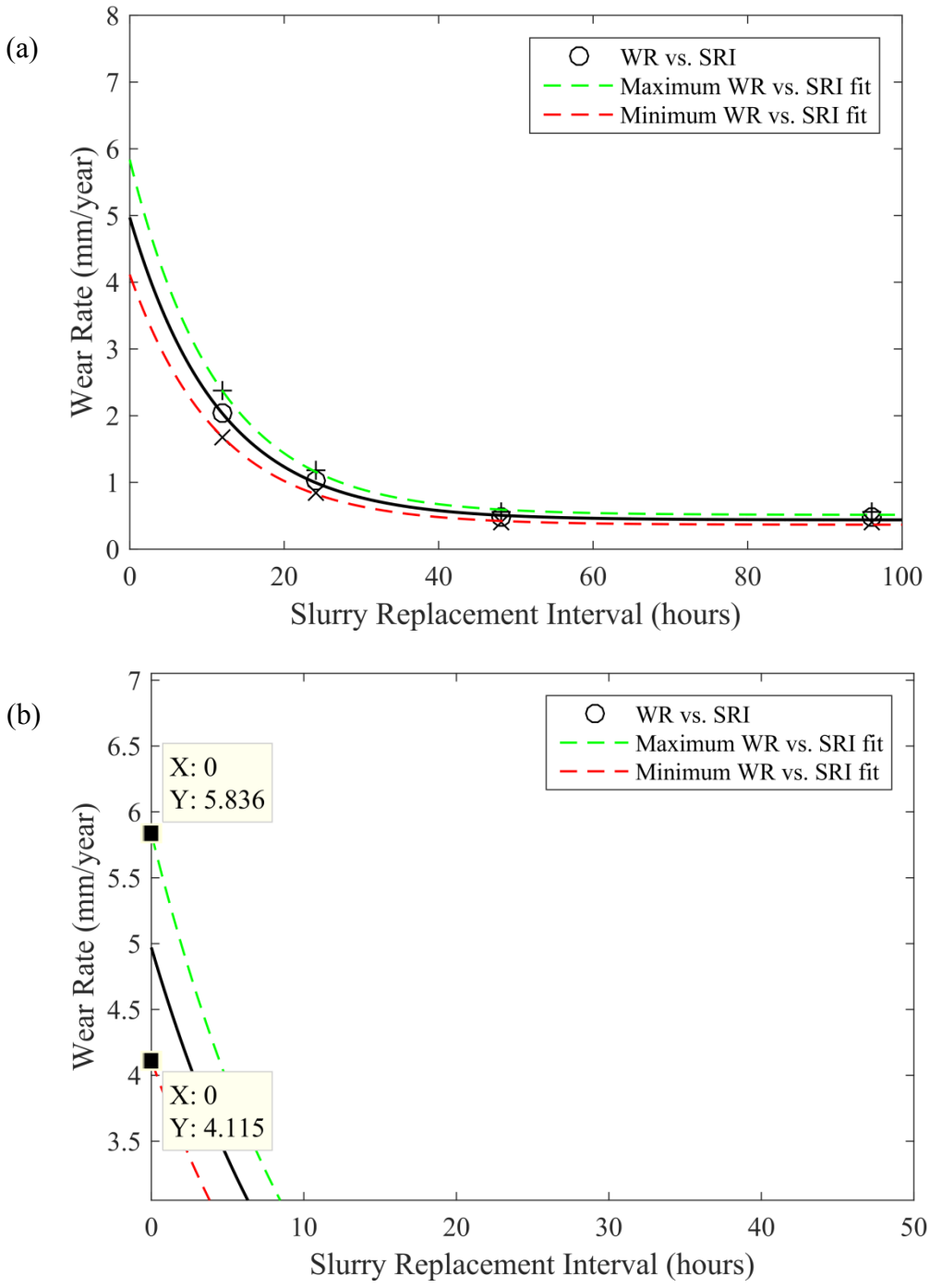

Figure E.3. (a) Sensitivity analysis of the corrected SIL 4 SRI experimental data (b) zoomed in view of the maximum and minimum intercepts at zero SRI

Appendix F
Qualitative Flow Pattern Analysis

Water only:

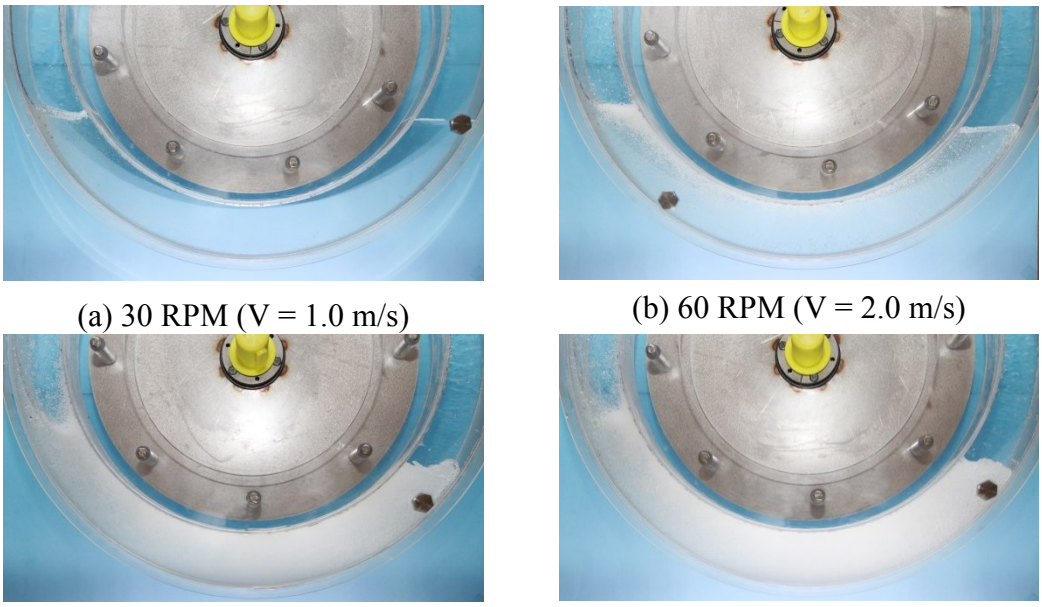

(a) 30 RPM (V = 1.0 m/s) (b) 60 RPM (V = 2.0 m/s)

(c) 90 RPM (V = 2.9 m/s) (d) 100 RPM (V = 3.2 m/s)

Figure F.1. Slurry flow pattern analysis using the ATW; Water only, C_s = 0%, N = 30–100 RPM

LM 125 Sand (d_{50} = 0.125 mm), C_s = 30%:

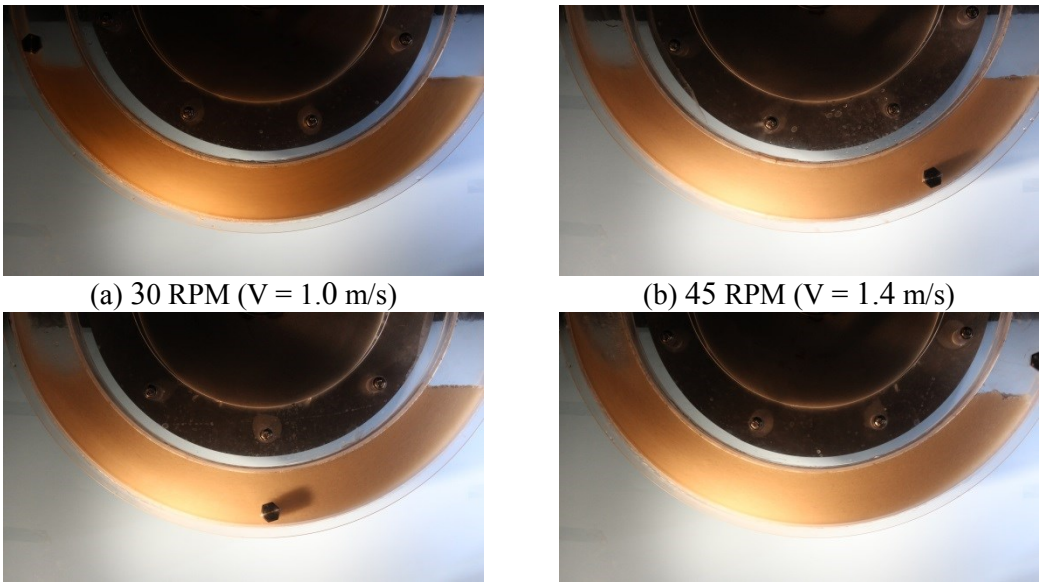

(a) 30 RPM (V = 1.0 m/s) (b) 45 RPM (V = 1.4 m/s)

(c) 60 RPM (V = 2.0 m/s) (d) 90 RPM (V = 2.9 m/s)

Figure F.2. Slurry flow pattern analysis using the ATW; d_{50} = 0.125 mm (LM 125), C_s = 30%, N = 30–90 RPM

Gravel (d_{50} = 2 mm), C_s = 1% :

(a) 30 RPM (V = 1.0 m/s)

(b) 60 RPM (V = 2.0 m/s)

(c) 90 RPM (V = 2.9 m/s)

(d) 100 RPM (V = 3.2 m/s)

Figure F.3. Slurry flow pattern analysis using the ATW; d_{50} = 2 mm (Gravel), C_s = 1%, N = 30–100 RPM

Gravel (d_{50} = 2 mm), C_s = 5% :

(a) 30 RPM (V = 1.0 m/s)

(b) 60 RPM (V = 2.0 m/s)

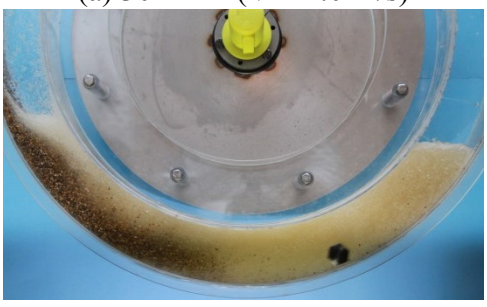

(c) 90 RPM (V = 2.9 m/s)

(d) 100 RPM (V = 3.2 m/s)

Figure F.4. Slurry flow pattern analysis using the ATW; d_{50} = 2 mm (Gravel), C_s = 5%, N = 30–100 RPM

Gravel (d_{50} = 2 mm), C_s = 10% :

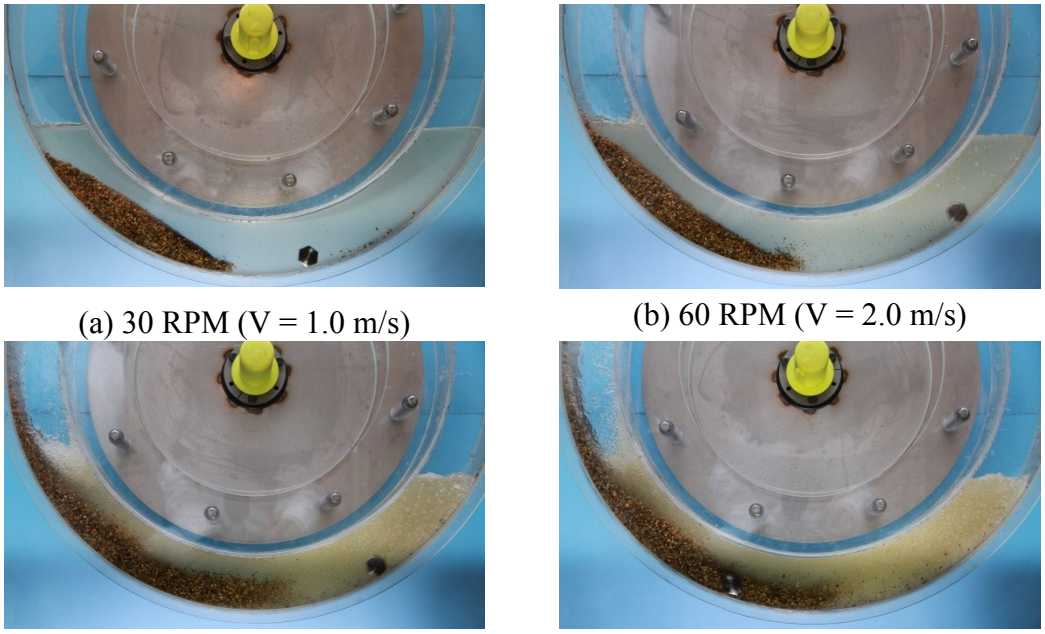

(a) 30 RPM (V = 1.0 m/s)

(b) 60 RPM (V = 2.0 m/s)

(c) 90 RPM (V = 2.9 m/s)

(d) 100 RPM (V = 3.2 m/s)

Figure F.5. Slurry flow pattern analysis using the ATW; d_{50} = 2 mm (Gravel), C_s = 10%, N = 30–100 RPM

Pyrex beads (d_{50} = 0.5 mm), C_s = 10% :

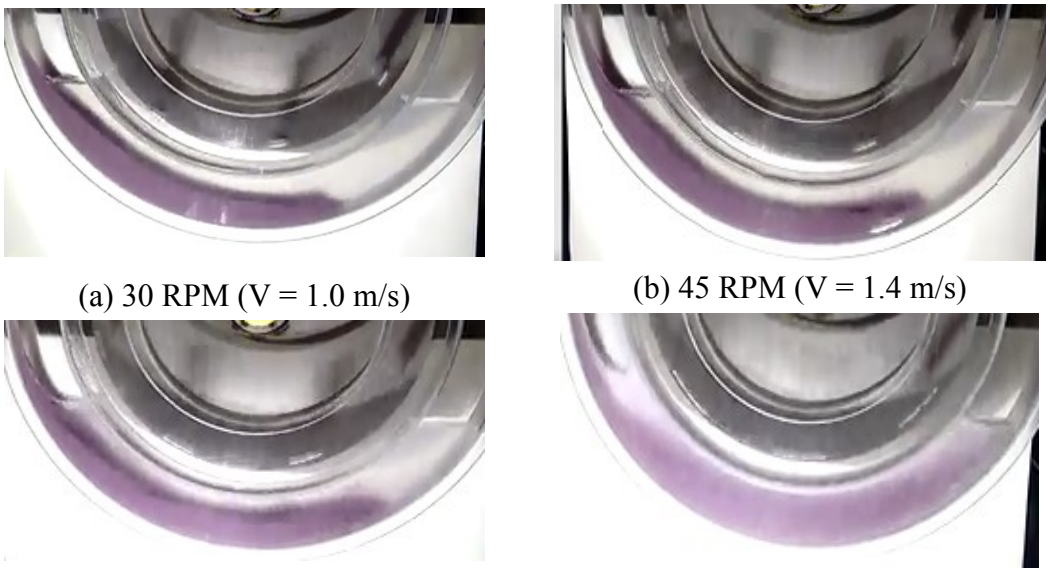

(a) 30 RPM (V = 1.0 m/s)

(b) 45 RPM (V = 1.4 m/s)

(c) 60 RPM (V = 2.0 m/s)

(d) 90 RPM (V = 2.9 m/s)

Figure F.6. Slurry flow pattern analysis using the ATW; d_{50} = 0.5 mm (Pyrex beads), C_s = 10%, N = 30–100 RPM

Appendix G
Particle Shape Analysis: CAMSIZER® Data

Table G.1. CAMSIZER® data for SIL 1 sand

Size class	[mm]	ASTM(+)	No(-)	retained [%]	passing [%]	xc_3 [mm]	xc_min_3 [mm]	xc_max_3 [mm]	$SPHT_3$	$Symm_3$	b/l_3	$Conv_3$
0	0.075	PAN	#200	0.3	0.3	0.073	0.063	0.085	0.903	0.87	0.666	0.999
0.075	0.09	#200	#170	0.4	0.7	0.095	0.081	0.113	0.89	0.873	0.658	0.998
0.09	0.125	#170	#120	3.9	4.6	0.129	0.111	0.153	0.889	0.881	0.678	0.998
0.125	0.15	#120	#100	5.7	10.3	0.158	0.138	0.186	0.892	0.886	0.701	0.997
0.15	0.18	#100	#80	9.9	20.2	0.19	0.166	0.223	0.884	0.887	0.706	0.996
0.18	0.212	#80	#70	13.5	33.7	0.225	0.196	0.264	0.881	0.889	0.715	0.994
0.212	0.25	#70	#60	18.9	52.6	0.265	0.231	0.309	0.88	0.89	0.725	0.993
0.25	0.3	#60	#50	23.8	76.4	0.311	0.273	0.361	0.877	0.889	0.736	0.992
0.3	0.355	#50	#45	16	92.4	0.367	0.325	0.422	0.873	0.887	0.753	0.99
0.355	0.425	#45	#40	6.5	98.9	0.425	0.38	0.484	0.865	0.882	0.768	0.987
0.425	0.5	#40	#35	1	99.9	0.502	0.447	0.572	0.829	0.861	0.769	0.98
0.5	0.6	#35	#30	0.1	100	0.582	0.525	0.654	0.801	0.829	0.794	0.974
0.6	0.71	#30	#25	0	100	0.667	0.608	0.719	0.638	0.725	0.866	0.955
1	1.18	#18	#16	0	100	1.136	1.085	1.168	0.963	0.926	0.86	1
1.18	1.4	#16	#14	0	100	1.444	1.305	1.651	0.861	0.866	0.752	0.99
1.4	1.7	#14	#12	0	100	0	0	0	1	0	0	0
1.7	2	#12	#10	0	100	0	0	0	1	0	0	0
2	4	#10	#5	0	100	0	0	0	1	0	0	0
4	1000	> #5		0	100	0	0	0	1	0	0	0

Sphericity	**Q_3 (SPHT=0.9) [%]**	**56.6**
Symmetry	**Q_3 (Symm=0.9) [%]**	**55.0**
Aspect ratio	**Q_3 (b/l=0.9) [%]**	**98.6**
Mean value of SPHT	**Mean value $SPHT_3$**	**0.872**
Mean value of Symm	**Mean value $Symm_3$**	**0.886**
Mean value b/l	**Mean value b/l_3**	**0.709**

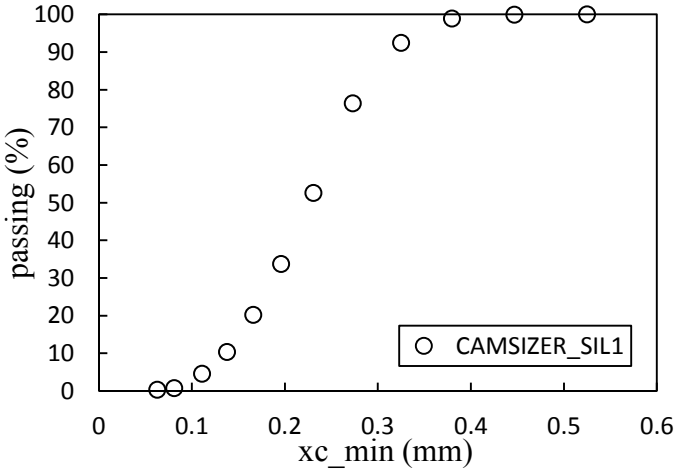

Table G.2. CAMSIZER® data for US Silica sand

Size class	[mm]	ASTM(+)	No(-)	retained [%]	passing [%]	xc_3 [mm]	xc_min_3 [mm]	xc_max_3 [mm]	$SPHT_3$	$Symm_3$	b/l_3	$Conv_3$
0	0.075	PAN	#200	0	0	0.089	0.059	0.147	0.681	0.824	0.431	0.997
0.075	0.09	#200	#170	0	0	0.123	0.082	0.193	0.688	0.822	0.437	0.994
0.09	0.125	#170	#120	0	0	0.17	0.113	0.26	0.694	0.833	0.43	0.994
0.125	0.15	#120	#100	0.1	0.1	0.208	0.141	0.311	0.72	0.862	0.439	0.992
0.15	0.18	#100	#80	0.9	1	0.234	0.169	0.326	0.776	0.877	0.499	0.993
0.18	0.212	#80	#70	5.1	6.1	0.255	0.199	0.33	0.831	0.889	0.581	0.994
0.212	0.25	#70	#60	22.2	28.3	0.279	0.235	0.335	0.877	0.898	0.675	0.995
0.25	0.3	#60	#50	50.9	79.2	0.309	0.275	0.352	0.899	0.901	0.753	0.994
0.3	0.355	#50	#45	19.1	98.3	0.354	0.318	0.4	0.884	0.886	0.779	0.99
0.355	0.425	#45	#40	1.6	99.9	0.442	0.374	0.52	0.761	0.797	0.717	0.965
0.425	0.5	#40	#35	0.1	100	0.555	0.453	0.66	0.569	0.664	0.688	0.92
0.5	0.6	#35	#30	0	100	0.687	0.54	0.86	0.395	0.626	0.638	0.865
0.6	0.71	#30	#25	0	100	0.845	0.652	1.116	0.292	0.565	0.6	0.855
0.71	0.85	#25	#20	0	100	1.091	0.811	1.49	0.284	0.611	0.553	0.809
0.85	1	#20	#18	0	100	1.187	0.898	1.49	0.245	0.614	0.612	0.783
1	1.18	#18	#16	0	100	1.48	1.098	1.893	0.248	0.475	0.629	0.772
1.18	1.4	#16	#14	0	100	1.774	1.218	1.941	0.133	0.499	0.768	0.695
1.4	1.7	#14	#12	0	100	2.283	1.611	3.826	0.083	0.597	0.405	0.689
1.7	2	#12	#10	0	100	0	0	0	1	0	0	0

Sphericity	**Q_3 (SPHT=0.9) [%]**	**53.8**
Symmetry	**Q_3 (Symm=0.9) [%]**	**46.2**
Aspect ratio	**Q_3 (b/l=0.9) [%]**	**98.3**
Mean value of SPHT	**Mean value $SPHT_3$**	**0.877**
Mean value of Symm	**Mean value $Symm_3$**	**0.893**
Mean value b/l	**Mean value b/l_3**	**0.714**

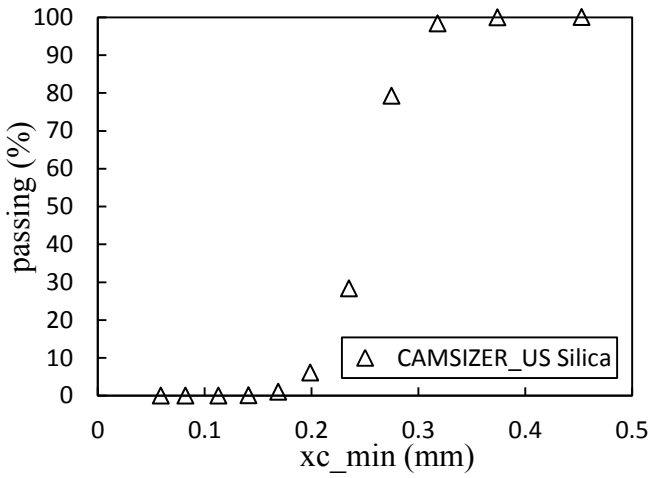

Appendix H
TWT Commissioning and Wear Test Results

Commissioning phase results (Temperature and RPM Data of the TWT):

Table H.1. Temperature and wheel speed monitoring data during commissioning

	Motor Temperature	**Bearing 1 Temperature**	**Bearing 2 Temperature**	**Wheel Speed**
Time	T1	T2	T3	N
(hours)	(°C)	(°C)	(°C)	(RPM)
0	23.5	23	23	59.47
2	29.1	24.4	23.3	59.23
4	31.6	24.8	23.3	59.89
6	32.8	25.1	23.5	60.02
18	33.5	25.6	23.5	59.47
20	33.6	25.6	23.7	59.63
28	34	25.6	23.7	59.89
42	34	25.6	23.7	59.29
46	34	25.8	24.2	60.04
48	34	26	24.1	60.05
52	34.1	25.6	24.1	59.73
66	34.3	26.7	24.2	60
68	34.2	26.5	24.3	59.85
70	34.1	26.5	24.2	59.67
72	34.1	26.3	24.2	59.84
74	34.1	25.6	24.2	60
78	34	25.6	24.2	59.49
90	33.4	25.3	23.5	59.89
92	33.5	25.8	23.9	59.87
94	33.8	25.8	23.5	59.26
96	33.8	25.5	23.9	60
98	33.5	25.1	23.5	60.07
102	33.3	25	23.5	59.79
114	33.5	25.5	23.7	59.98
116	31.1	25.6	23.5	60.02

Data repeatability experiment results:

Table H.2. Data repeatability results for test coupons

Coupon ID	Time					SRI	Sand	Δm	Δm
	0 hr	116 hr	232 hr	350 hr	Δm (g)	hr		(g/100h)	(mm/yr)
Wheel A									
A1	772.43	772.26	772.15	772.09	0.34	116	30% SIL1	0.097	0.26
A2	776.58	776.41	776.30	776.23	0.35			0.100	0.27
A3	779.93	779.75	779.65	779.57	0.36			0.103	0.27
A4	778.17	778.00	777.90	777.82	0.35			0.100	0.27
A5	777.69	777.49	777.38	777.31	0.38			0.109	0.29
Wheel B									
B1	778.38	778.16	778.04	777.94	0.44	116	30% SIL1	0.126	0.33
B2	778.44	778.24	778.13	778.04	0.40			0.114	0.30
B3	777.58	777.38	777.24	777.13	0.45			0.129	0.34
B4	776.54	776.34	776.20	776.10	0.44			0.126	0.33
B5	779.37	779.12	779.00	778.90	0.47			0.134	0.36
Wheel C									
C1	778.56	778.37	778.27	778.20	0.36	116	30% SIL1	0.103	0.27
C2	779.10	778.92	778.82	778.75	0.35			0.100	0.27
C3	778.16	777.99	777.90	777.82	0.34			0.097	0.26
C4	779.58	779.40	779.30	779.24	0.34			0.097	0.26
C5	776.36	776.16	776.05	775.98	0.38			0.109	0.29
Wheel D									
D1	394.24	394.11	394.06	394.02	0.22	116	30% SIL1	0.063	0.17
D2	390.49	390.36	390.29	390.25	0.24			0.069	0.18
D3	394.25	394.13	394.07	394.03	0.22			0.063	0.17
D4	393.48	393.35	393.29	393.24	0.24			0.069	0.18
D5	393.56	393.43	393.37	393.33	0.23			0.066	0.17

Table H.3. Data repeatability results of the TWT

Coupon ID	Particle	d_{50}	*Cs*	m_i	m_f	Δm	Experiment duration	SRI	Δm	Δm
		(mm)	(%)	(g)	(g)	(g)	(hr)	(hr)	(g/100h)	(mm/yr)
RUN#1										
C2	US Silica	0.25	20	494.93	494.87	0.09	192	24	0.048043	0.127706
C4				493.68	493.62	0.09			0.048043	0.127706
Standard Weight (500 g)				501.37	501.4					
C2	SIL 4	0.425	20	494.36	494.31	0.05	96	24	0.053763	0.142912
C4				492.98	492.94	0.04			0.043011	0.11433
Standard Weight (500 g)				501.34	501.34					
A2	Al_2O_3	0.425	20	492.19	492.02	0.17	96	24	0.182796	0.485902
A4				491.75	491.57	0.18			0.193548	0.514485
Standard Weight (500 g)				501.34	501.34					
B3	Gravel	2	20	491.41	490.76	0.65	96	24	0.698925	1.857861
B5				492.39	491.69	0.7			0.752688	2.000773
Standard Weight (500 g)				501.34	501.34					
RUN#2										
C1	US Silica	0.25	20	491.52	491.5	0.04	96	24	0.043011	0.11433
C3				491.04	491.01	0.05			0.053763	0.142912
Standard Weight (500 g)				501.23	501.25					
C2	SIL 4	0.425	20	491.91	491.85	0.06	96	24	0.064516	0.171495
C4				492.12	492.07	0.05			0.053763	0.142912
Standard Weight (500 g)				501.37	501.37					
A2	Al_2O_3	0.425	20	491.98	491.83	0.15	96	24	0.688172	1.829278
A4				491.82	491.68	0.14			0.72043	1.915026
Standard Weight (500 g)				501.37	501.37					
B3	Gravel	2	20	489.64	489	0.64	96	24	0.698925	1.857861
B5				490.47	489.8	0.67			0.752688	2.000773
Standard Weight (500 g)				501.37	501.37					

Corrosion control experiment results:

Table H.4. Corrosion control test results in the TWT

Coupon ID	Slurry	d_{50}	Cs	m_i	m_f	Δm	Experiment duration	SRI	Δm	Δm
		(mm)	(%)	(g)	(g)	(g)	(hr)	(hr)	(g/100h)	(mm/yr)
A1	US Silica + Water + Air	0.25	20	501.1	500.8	0.32	96	24	0.344086	0.914639
A3				491.8	491.53	0.29			0.311828	0.828892
B1	Water + Air	0.25	20	492.43	492.22	0.23	96	24	0.247312	0.657397
B3				490.96	490.78	0.2			0.215054	0.57165
C1	US Silica + Water + N_2	0.25	20	491.52	491.5	0.04	96	24	0.043011	0.11433
C3				491.04	491.01	0.05			0.053763	0.142912
Standard Weight (500 g)				501.23	501.25					

Parametric test results (Effect of wheel speed and solids concentration without contact area correction):

Table H.5 (a). Parametric test results using 2.0 mm gravel in the TWT at 60 RPM

Coupon ID	Particle	d_{50}	Cs	m_i	m_f	Δm	Experiment duration	SRI	Δm	Δm
		(mm)	(%)	(g)	(g)	(g)	(hr)	(hr)	(g/100h)	(mm/yr)
Wheel Speed, N = 60 RPM										
A2	Gravel	2	20	490.38	489.71	0.67	96	24	0.72043	1.915026
A4				493.05	492.38	0.67			0.72043	1.915026
B3			12	489.6	488.93	0.67		24	0.72043	1.915026
B5				491.77	491.11	0.66			0.709677	1.886443
C2			6	494.26	493.77	0.49		24	0.526882	1.400541
C4				492.37	491.91	0.46			0.494624	1.314794
Standard Weight (500 g)				501.29	501.29					

Table H.5 (b). Parametric test results using 2.0 mm gravel in the TWT at 45 RPM

Coupon ID	Particle	d_{50}	Cs	m_i	m_f	Δm	Experiment duration	SRI	Δm	Δm
		(mm)	(%)	(g)	(g)	(g)	(hr)	(hr)	(g/100h)	(mm/yr)
Wheel Speed, N = 45 RPM										
A2	Gravel	2	20	491.55	491.2	0.36	96	24	0.387097	1.028969
A4				492.02	491.69	0.34			0.365591	0.971804
B3			12	493.27	492.98	0.3		24	0.322581	0.857474
B5				492.06	491.76	0.31			0.333333	0.886057
C2			6	493.96	493.74	0.23		24	0.247312	0.657397
C4				492.06	491.85	0.22			0.236559	0.628814
Standard Weight (500 g)				501.29	501.3					

Table H.5 (c). Parametric test results using 2.0 mm gravel in the TWT at 30 RPM

Coupon ID	Particle	d_{50}	Cs	m_i	m_f	Δm	Experiment duration	SRI	Δm	Δm
		(mm)	(%)	(g)	(g)	(g)	(hr)	(hr)	(g/100h)	(mm/yr)
Wheel Speed, N = 30 RPM										
A2	Gravel	2	20	493.81	493.66	0.15	96	24	0.16129	0.428737
A4				492.48	492.34	0.14			0.150538	0.400155
B3			12	491.33	491.23	0.1		24	0.107527	0.285825
B5				493.76	493.65	0.11			0.11828	0.314407
C2			6	494.08	493.98	0.1		24	0.107527	0.285825
C4				492.32	492.23	0.09			0.096774	0.257242
Standard Weight (500 g)				501.29	501.3					

Parametric test results (Effect of particle size and shape):

Table H.6 (a). Parametric test results using different particle sizes in the TWT; N = 60 RPM

Coupon ID	Particle	d_{50}	Cs	Wheel speed	m_i	m_f	Δm	Experiment duration	SRI	Δm	Δm
		(mm)	(%)	(RPM)	(g)	(g)	(g)	(hr)	(hr)	(g/100h)	(mm/yr)
A2	SIL 1	0.25	20	60	491.79	491.63	0.19	192	24	0.101423	0.269601
A4					490.22	490.07	0.18			0.096085	0.255411
Standard Weight (500 g)					501.37	501.4					
C2	US Silica	0.25	20	60	494.93	494.87	0.09	192	24	0.048043	0.127706
C4					493.68	493.62	0.09			0.048043	0.127706
Standard Weight (500 g)					501.34	501.34					
C2	SIL 4	0.425	20	60	491.91	491.85	0.06	96	24	0.064516	0.171495
C4					492.12	492.07	0.05			0.053763	0.142912
Standard Weight (500 g)					501.37	501.37					
B3	Gravel	2	20	60	491.41	490.76	0.65	96	24	0.698925	1.857861
B5					492.39	491.69	0.7			0.752688	2.000773
Standard Weight (500 g)					501.34	501.34					

Table H.6 (b). Parametric test results using different particle sizes in the TWT; N = 30 RPM

Coupon ID	Particle	d_{50}	Cs	Wheel speed	m_i	m_f	Δm	Experiment duration	SRI	Δm	Δm
		(mm)	(%)	(RPM)	(g)	(g)	(g)	(hr)	(hr)	(g/100h)	(mm/yr)
C1	SIL 1	0.25	20	30	494.12	493.88	0.25	192	24	0.133452	0.354738
C3					492.69	492.45	0.25			0.133452	0.354738
Standard Weight (500 g)					501.4	501.41					
C2	US Silica	0.25	20	30	494.42	494.39	0.04	192	24	0.021352	0.056758
C4					489.12	489.09	0.04			0.021352	0.056758
Standard Weight (500 g)					501.4	501.41					
B3	SIL 4	0.425	20	30	492.94	492.82	0.13	192	24	0.145251	0.386103
B5					490.23	490.12	0.12			0.134078	0.356403
Standard Weight (500 g)					501.47	501.48					
A2	Gravel	2	20	30	493.81	493.66	0.15	96	24	0.16129	0.428737
A4					492.48	492.34	0.14			0.150538	0.400155
Standard Weight (500 g)					501.29	501.3					

Slurry Replacement Interval (SRI) experiment results:

Table H.7. SRI test results for 2.0 mm gravels; N = 60 RPM

Coupon ID	d_{50}	Cs	m_i	m_f	Δm	Experiment duration	SRI	Δm	Δm
	(mm)	(%)	(g)	(g)	(g)	(hr)	(hr)	(g/100h)	(mm/yr)
A1	2	20	498.93	496.59	2.34	96	8	2.638106	7.012535
A3			501.5	499.1	2.4			2.70575	7.192343
A5			496.48	493.73	2.75			3.100338	8.241227
Standard Weight (500 g)			501.23	501.23					
B1	2	20	499.22	497.08	2.14	96	12	2.412627	6.413173
B3			495.95	493.84	2.11			2.378805	6.323269
B5			494.37	491.93	2.44			2.750846	7.312216
Standard Weight (500 g)			501.23	501.23					
C1	2	20	499.59	498.02	1.6	96	24	1.709402	4.543881
C3			498.68	497.13	1.58			1.688034	4.487082
C5			501.3	499.69	1.64			1.752137	4.657478
Standard Weight (500 g)			501.23	501.26					
B1	2	20	498.17	497.27	0.93	96	48	0.99359	2.641131
B3			498.11	497.18	0.96			1.025641	2.726328
B5			500.76	499.73	1.06			1.132479	3.010321
Standard Weight (500 g)			501.23	501.26					
C1	2	20	490.4	489.77	0.63	96	96	0.710259	1.88799
C3			496.43	495.81	0.62			0.698985	1.858022
C5			488.16	487.56	0.6			0.676437	1.798086
Standard Weight (500 g)			501.23	501.23					

Table H.8. SRI test results for 0.425 mm Al_2O_3 particles; N = 60 RPM

Coupon ID	d_{50}	Cs	m_i	m_f	Δm	Experiment duration	SRI	Δm	Δm
	(mm)	(%)	(g)	(g)	(g)	(hr)	(hr)	(g/100h)	(mm/yr)
A2	0.425	20	501.2	501.01	0.21	96	12	0.230769	0.613424
A4			491.68	491.52	0.18			0.197802	0.525792
Standard Weight (500 g)			501.24	501.26					
B3	0.425	20	489.7	489.57	0.15	96	24	0.164835	0.43816
B5			490.55	490.42	0.15			0.164835	0.43816
Standard Weight (500 g)			501.24	501.26					
C2	0.425	20	493.35	493.26	0.11	96	48	0.120879	0.321317
C4			500.92	500.83	0.11			0.120879	0.321317
Standard Weight (500 g)			501.24	501.26					
A2	0.425	20	491.6	491.55	0.1	96	96	0.104712	0.278342
A4			491.46	491.4	0.11			0.115183	0.306177
Standard Weight (500 g)			501.23	501.28					

Table H.9. SRI test results for 0.425 mm SIL 4 sand particles; N = 60 RPM

Coupon ID	d_{50}	Cs	m_i	m_f	Δm	Experiment duration	SRI	Δm	Δm
	(mm)	(%)	(g)	(g)	(g)	(hr)	(hr)	(g/100h)	(mm/yr)
A2	0.425	20	492.03	492	0.08	96	12	0.087146	0.231649
A4			490.34	490.29	0.1			0.108932	0.289561
Standard Weight (500 g)			501.25	501.3					
C2	0.425	20	494.36	494.31	0.05	96	24	0.053763	0.142912
C4			492.98	492.94	0.04			0.043011	0.11433
Standard Weight (500 g)			501.34	501.34					
C2	0.425	20	492.61	492.64	0.02	96	48	0.020942	0.055668
C4			493.11	493.14	0.02			0.020942	0.055668
Standard Weight (500 g)			501.23	501.28					
B3	0.425	20	489.1	489.13	0.02	96	96	0.020942	0.055668
B5			492.22	492.25	0.02			0.020942	0.055668
Standard Weight (500 g)			501.23	501.28					

Corrected SRI results for SIL 4 sand particles:

The particle-coupon contact correction factor (from ATW observation), $A_C = 0.7$

The hydraulic diameter of the TWT, $d_h^{TWT} = 63mm$

The hydraulic diameter of the pipe loop, $d_h^{pipeloop} = 85mm$

The diameter correction to compare the TWT result with the pipe loop, $D_C = \left(\frac{d_h^{pipeloop}}{d_h^{TWT}} \right)^2$

$$= \left(\frac{85}{63} \right)^2 = 1.82$$

Table H.10. Corrected SRI test results for 0.425 mm SIL 4 sand particles; *N* = 60 RPM

SRI	Mass Loss	Total Run Time	Total Down Time	Total Effective Run Time		Thickness Loss	Particle-Coupon Contact Area Correction Factor	Pipeloop Dia Correction Factor	Corrected Thickness Loss
	Δm	t_{TR}	t_{DT}	t_{ERT}	Δm	T_L	A_C	D_C	$T_{L(corr)}$
(hr)	(g)	(%)	(g)	(g)	(g/100h)	(hr)			(mm/yr)
12	0.09	96	4.2	91.8	0.098039	0.260604925	0.7	1.82	2.02839866
24	0.045	96	4.2	91.8	0.048387	0.12862114			1.01419933
48	0.02	96	0.5	95.5	0.020942	0.055668487			0.468092
96	0.02	96	0.5	95.5	0.020942	0.055668487			0.468092

Exponential curve fitting using MATLAB:

```
function [fitresult, gof] = createFit(SRI, WR)
%CREATEFIT(SRI,WR)
%  Create an exponential best fit using the SRI vs. WR data.
%
%  Data for the best fit:
%      X Input : Slurry Replacement Interval (SRI)
%      Y Output: Wear Rate in mm/year (WR)
%  Output:
%      fitresult : a fit object representing the exponential fit.
%      gof : structure with goodness-of fit info.


%% Fit: 'exponential fit'.
[xData, yData1] = prepareCurveData(SRI, WR);

% Set up fittype and options.
ft = fittype( 'exp2' );
opts = fitoptions( 'Method', 'NonlinearLeastSquares' );
opts.Display = 'Off';
opts.Lower = [-Inf -Inf -Inf 0];
opts.StartPoint = [0.528576218726667 -0.0815908887061707 0.0624524996012027
0];
opts.Upper = [Inf Inf Inf 0];

% Fit model to data.
[fitresult, gof] = fit( xData, yData1, ft, opts );

% Plot fit with data.
figure( 'Name', 'Exponential fit' );
e = plot(xData,yData1,'ks');
axis ([0 100 0 20])
e.MarkerSize = 8;
hold on
h = plot(fitresult,'k-');
h.LineWidth = 1.3;
legend( 'WR vs. SRI', 'Location', 'NorthEast' );
% Label axes
xlabel 'Slurry Replacement Interval (hours)'
ylabel 'Wear Rate (mm/year)'
grid off
hold on
```

Appendix I
Full Design Drawings

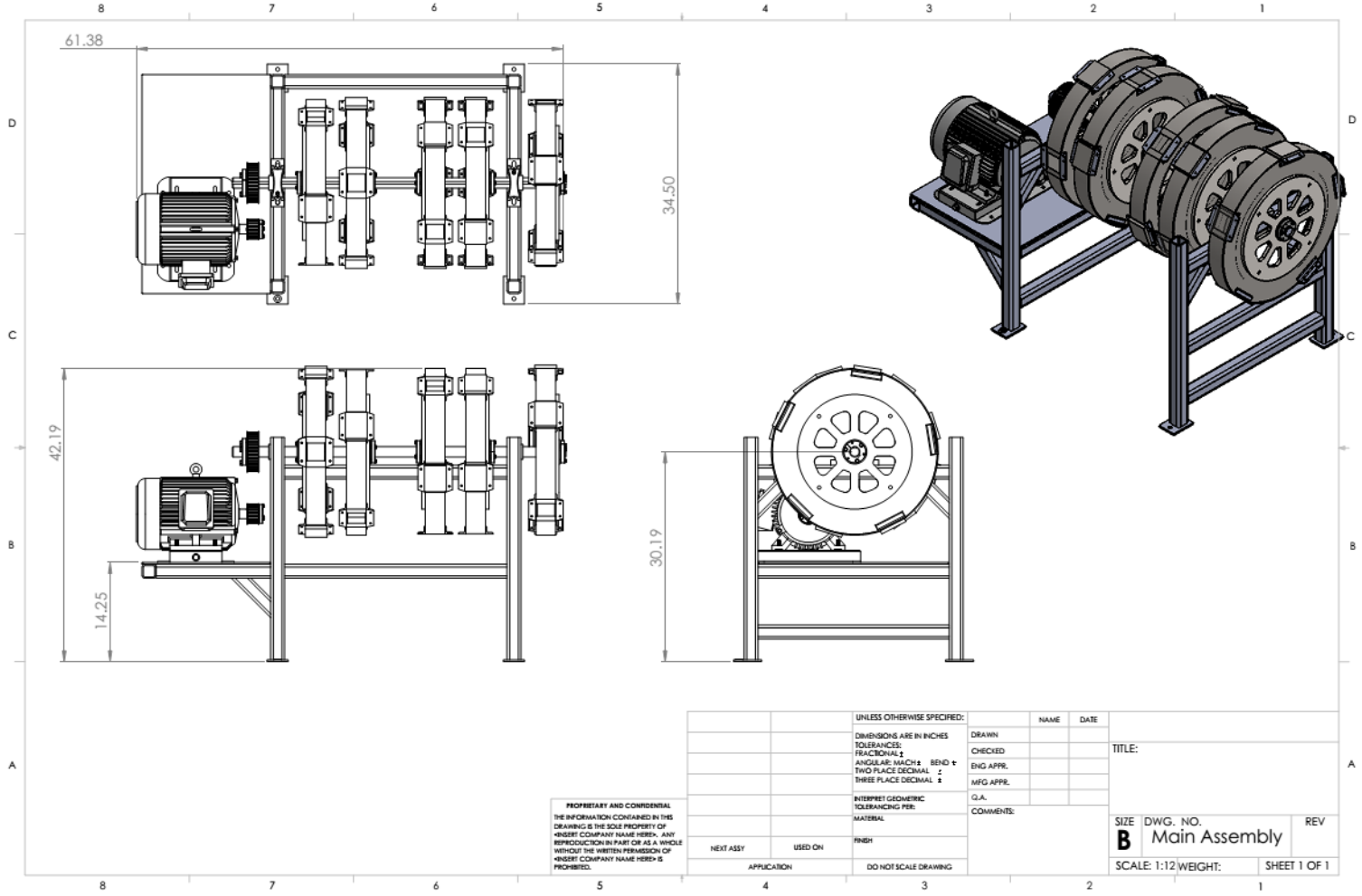

Figure I.1. Main Assembly of the Toroid Wear Tester (TWT)

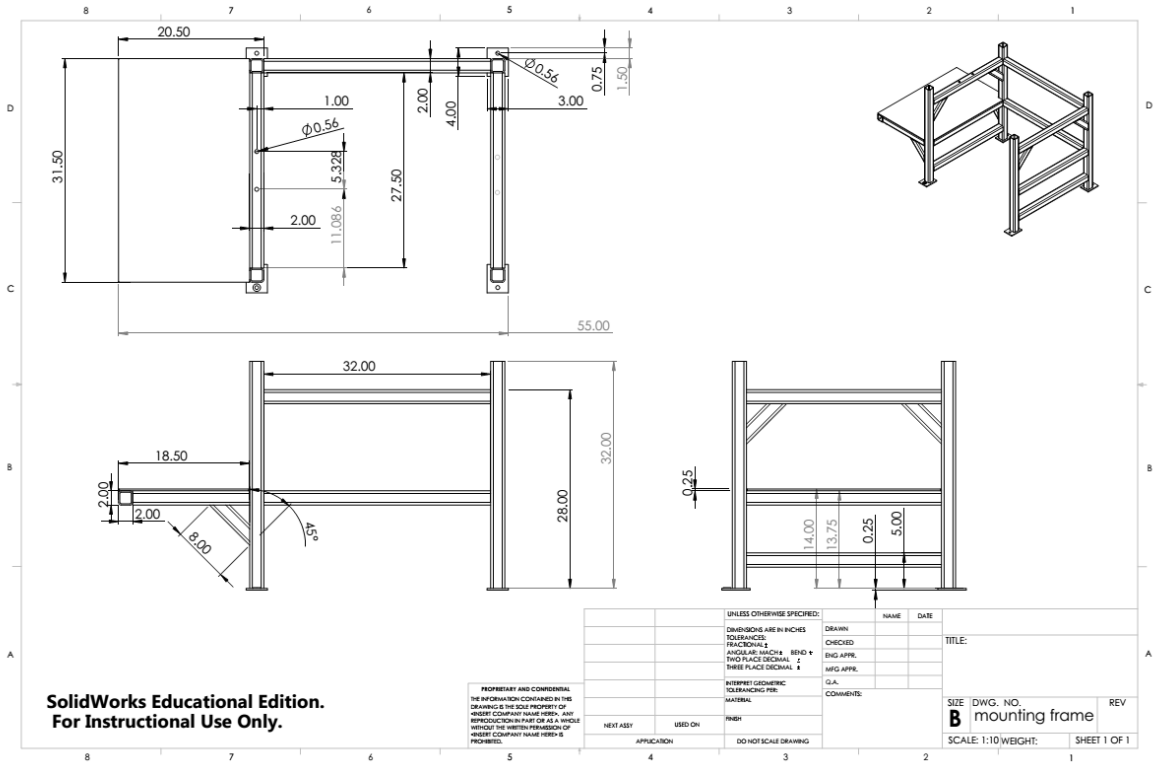

Figure I.2. Mounting Frame of the Toroid Wheels and the Motor

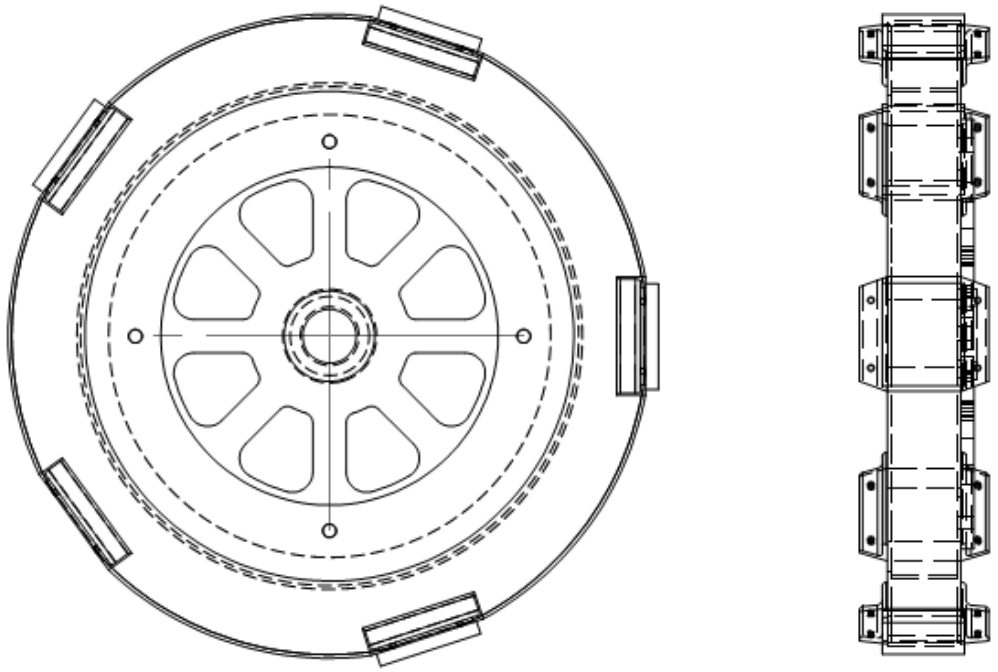

Figure I.3. Front and RHS view of a Toroid Wheel Assembly

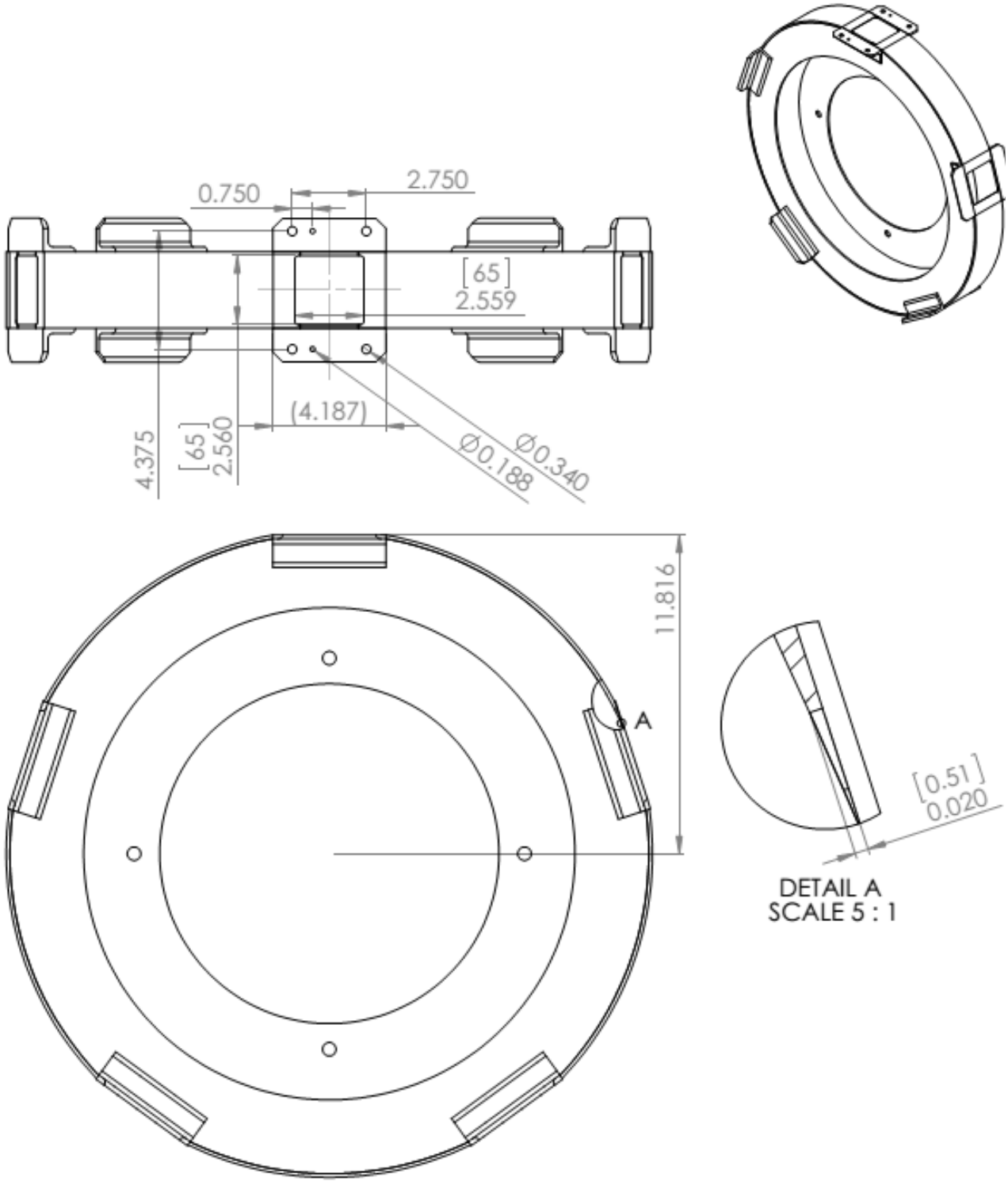

Figure I.4. Detailed Dimensions of the Toroid Wheel (A,B, and C) with the Cuts

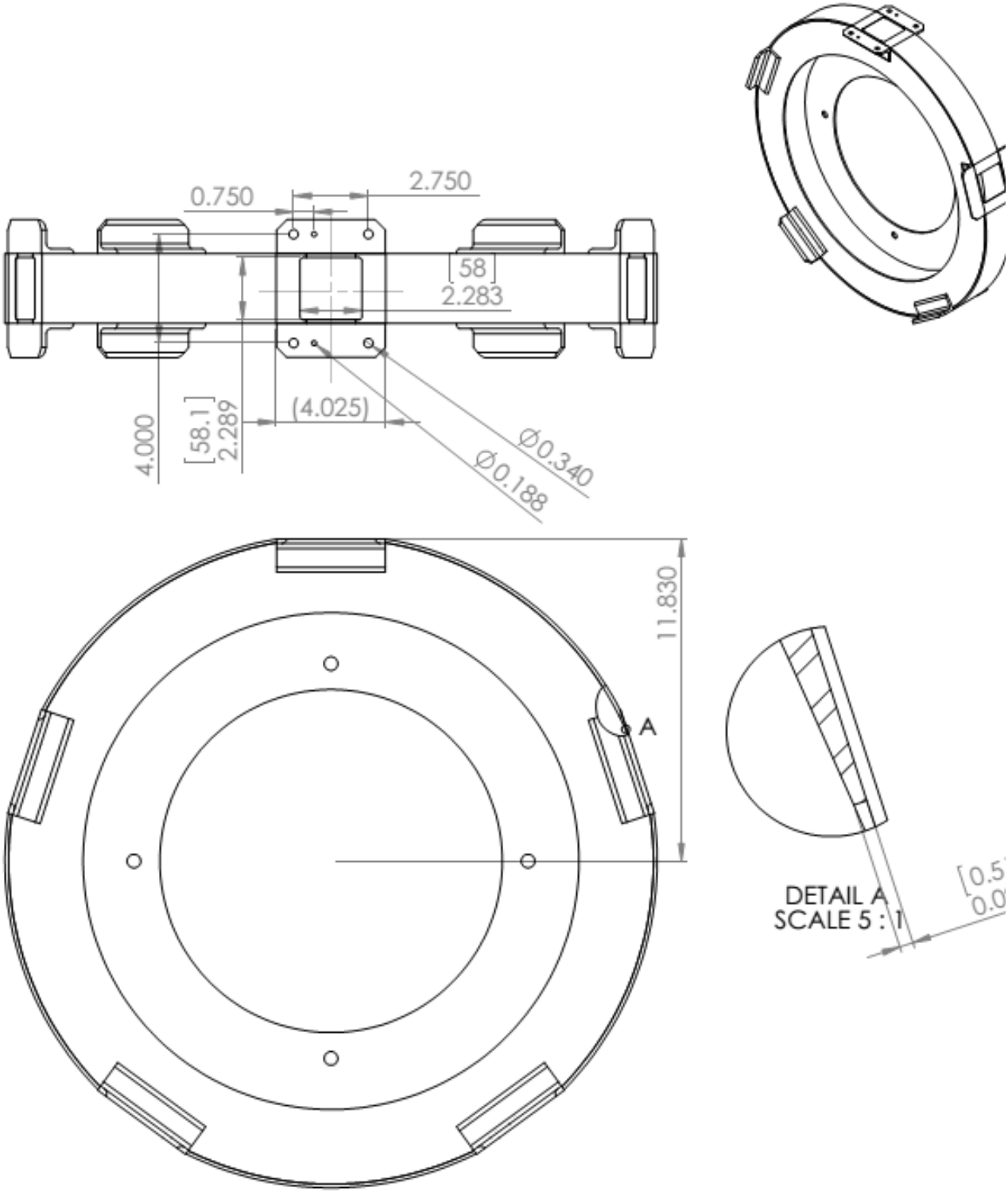

Figure I.5. Detailed Dimensions of the Toroid Wheel D with the Cuts

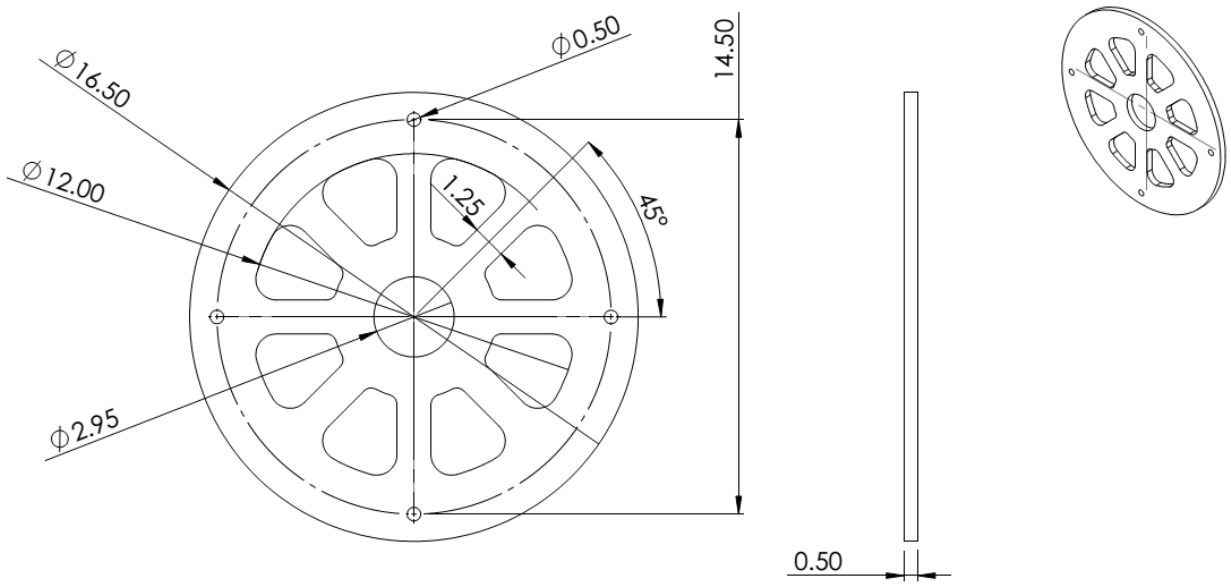

Figure I.6. Detailed Dimensions of the Toroid Wheel Drive Plate

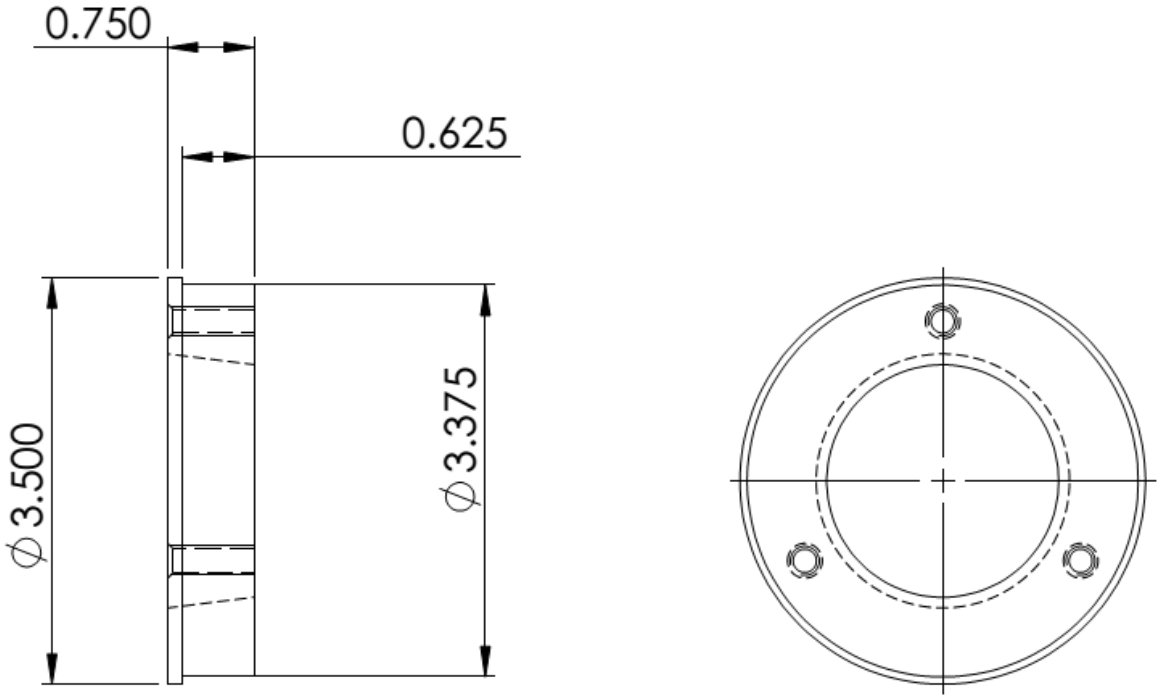

Figure I.7. Detailed Dimensions Weld on Hub